

Isolated Performance at Mach Numbers From 0.60 to 2.86 of Several Expendable Nozzle Concepts for Supersonic Applications

*Richard J. Re, Bobby L. Berrier, and William K. Abeyounis
Langley Research Center, Hampton, Virginia*

The NASA STI Program Office ... in Profile

Since its founding, NASA has been dedicated to the advancement of aeronautics and space science. The NASA Scientific and Technical Information (STI) Program Office plays a key part in helping NASA maintain this important role.

The NASA STI Program Office is operated by Langley Research Center, the lead center for NASA's scientific and technical information. The NASA STI Program Office provides access to the NASA STI Database, the largest collection of aeronautical and space science STI in the world. The Program Office is also NASA's institutional mechanism for disseminating the results of its research and development activities. These results are published by NASA in the NASA STI Report Series, which includes the following report types:

- **TECHNICAL PUBLICATION.** Reports of completed research or a major significant phase of research that present the results of NASA programs and include extensive data or theoretical analysis. Includes compilations of significant scientific and technical data and information deemed to be of continuing reference value. NASA counterpart of peer-reviewed formal professional papers, but having less stringent limitations on manuscript length and extent of graphic presentations.
- **TECHNICAL MEMORANDUM.** Scientific and technical findings that are preliminary or of specialized interest, e.g., quick release reports, working papers, and bibliographies that contain minimal annotation. Does not contain extensive analysis.
- **CONTRACTOR REPORT.** Scientific and technical findings by NASA-sponsored contractors and grantees.

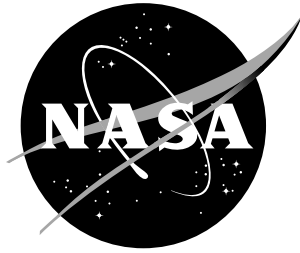
- **CONFERENCE PUBLICATION.** Collected papers from scientific and technical conferences, symposia, seminars, or other meetings sponsored or co-sponsored by NASA.
- **SPECIAL PUBLICATION.** Scientific, technical, or historical information from NASA programs, projects, and missions, often concerned with subjects having substantial public interest.
- **TECHNICAL TRANSLATION.** English-language translations of foreign scientific and technical material pertinent to NASA's mission.

Specialized services that complement the STI Program Office's diverse offerings include creating custom thesauri, building customized databases, organizing and publishing research results ... even providing videos.

For more information about the NASA STI Program Office, see the following:

- Access the NASA STI Program Home Page at <http://www.sti.nasa.gov>
- E-mail your question via the Internet to help@sti.nasa.gov
- Fax your question to the NASA STI Help Desk at (301) 621-0134
- Phone the NASA STI Help Desk at (301) 621-0390
- Write to:
NASA STI Help Desk
NASA Center for Aerospace
Information
7121 Standard Drive
Hanover, MD 21076-1320

NASA / TP-2001-211259



Isolated Performance at Mach Numbers From 0.60 to 2.86 of Several Expendable Nozzle Concepts for Supersonic Applications

Richard J. Re, Bobby L. Berrier, and William K. Abeyounis
Langley Research Center, Hampton, Virginia

National Aeronautics and
Space Administration

Langley Research Center
Hampton, Virginia 23681-2199

November 2001

Acknowledgments

The research presented in this report is the result of the cooperative effort of the Allison Gas Turbine Division, which at the time of the tests was part of the General Motors Corporation, and the Langley Research Center. The design and development of the nozzle concepts were conducted by Allison as was the fabrication of the nozzles. The model buildup, calibrations, testing, and data reduction were conducted by the staff of the former Propulsion Aerodynamics Branch of the Langley Research Center.

Available from:

NASA Center for AeroSpace Information (CASI)
7121 Standard Drive
Hanover, MD 21076-1320
(301) 621-0390

National Technical Information Service (NTIS)
5285 Port Royal Road
Springfield, VA 22161-2171
(703) 605-6000

Summary

Investigations have been conducted in the Langley 16-Foot Transonic Tunnel (at Mach numbers from 0.60 to 1.25) and in the Langley Unitary Plan Wind Tunnel (at Mach numbers from 2.16 to 2.86) at an angle of attack of 0° to determine the isolated performance of several expendable nozzle concepts for supersonic nonaugmented turbojet applications. The effects of centerbody base shape, shroud length, shroud ventilation, cruciform shroud expansion ratio, and cruciform shroud flap vectoring were investigated. The nozzle pressure ratio range, which was a function of Mach number, was between 1.9 and 11.8 in the 16-Foot Transonic Tunnel and between 7.9 and 54.9 in the Unitary Plan Wind Tunnel. Discharge coefficient, thrust-minus-drag, and the forces and moments generated by vectoring the divergent shroud flaps (for Mach numbers of 0.60 to 1.25 only) of a cruciform nozzle configuration were measured.

Nozzle configurations with a concave centerbody base had a discharge coefficient about 2 percent higher than nozzle configurations with a convex centerbody base for nozzle pressure ratios above 3.0. The shortest nozzle had the best thrust-minus-drag performance at Mach numbers up to 0.95 but was approached in performance by other configurations at Mach numbers of 1.15 and 1.25. At Mach numbers above 1.25, the cruciform nozzle configuration having the same expansion ratio (2.64) as the fixed geometry nozzles had the best thrust-minus-drag performance. Ventilation of the fixed geometry divergent shrouds to the nozzle external boattail flow generally improved thrust-minus-drag performance at Mach numbers from 0.60 to 1.25, but decreased performance above a Mach number of 1.25. When the cruciform nozzle shroud flaps were positioned for combined pitch and yaw vectoring at subsonic and transonic speeds, significant aerodynamic and propulsive forces and moments were generated that may be utilized for vehicle control. For shrouds having the same expansion ratio, thrust-minus-drag comparisons at typical mission high and low altitude engine operating pressure ratios indicated that the short nozzle had the best thrust-

minus-drag performance at Mach numbers from 0.60 to 1.25. At Mach numbers from 2.16 to 2.86, the cruciform nozzle had the best thrust-minus-drag performance.

Introduction

Compact, nonaugmented turbojet powered payloads designed to cruise at supersonic speeds after being air or rocket launched would initially operate subsonically and then accelerate through the transonic speed range to reach cruise speed. A payload capable of being air launched and perhaps carried internally in an aircraft must be compact, light, and as economical (i.e., it is a consumable) as possible. This means some compromises in performance and efficiency for all components, including the nozzle, are acceptable to obtain simplicity of design. However, use of a simple fixed geometry nozzle, optimized for a supersonic cruise Mach number, can result in large overexpansion losses at off-design Mach numbers and at low nozzle pressure ratios. This can result in poor thrust-minus-drag performance in the subsonic/transonic speed range, which in some cases could be insufficient for acceleration through that speed range. For efficient thrust-minus-drag performance with a turbojet engine over this broad spectrum of speeds, the logical nozzle installation would have variable geometry to maintain fully expanded exhaust flow as ambient Mach number changes. The engine operating pressure ratio depends on Mach number and ranges from about 2 at subsonic speeds to about 50 at supersonic speeds. However, if at all possible, it is preferable to use a fixed geometry nozzle if adequate thrust-minus-drag performance can be obtained for acceleration through the transonic speed range.

Utilization of a nonaugmented turbojet engine for propulsion conceptually permits incorporation of the aft portion of the turbine centerbody as part of a convergent-divergent nozzle flow path. That is, the absence of an afterburning duct section for reheating the flow ahead of the nozzle throat means the throat can occur as far forward as the annular area between the turbine centerbody outer

surface and the duct wall. This throat location results in a short exhaust flow path and was selected as the starting point for the design of five fixed geometry nozzle (shroud) concepts and one simplified variable geometry nozzle concept. The concepts consisted of nozzles with long and short fixed geometry shrouds (with and without axially venting the divergent section to ambient flow); a fixed geometry shroud with annular venting to ambient flow in the divergent section; and a simplified variable geometry nozzle with four moveable flaps in a cruciform cross-sectional shaped divergent shroud. All the nozzles had an axisymmetric internal body representing the rear portion of a turbine centerbody with either a concave or convex base geometry.

The purpose of this investigation was to determine the internal performance and isolated thrust-minus-drag of the nozzle concepts statically and over a Mach number range from 0.60 to 2.86 for a range of nozzle pressure ratios. For testing purposes, the nozzles were attached to a generic strut mounted test pod through which high pressure air passed to simulate the propulsion system exhaust. The test pod was axisymmetric in shape with the forward portion attached directly to the strut support system. Forces and moments were measured only on the aft (metric) portion of the test pod, which included the nozzle, using a six-component force balance to attach that portion of the model to the forward (nonmetric) portion of the test pod.

Symbols and Abbreviations

AF	balance axial force, lb
A_e	nozzle exit area, in ²
A_t	nozzle geometric throat area, 10.816 in ²
a	cruciform shroud flap position (see fig. 4(f)); with all four flaps in this position nozzle expansion ratio is 2.92
b	cruciform shroud flap position (see fig. 4(f)); with all four flaps in this position nozzle expansion ratio is 2.64

C_p	local pressure coefficient, $(p - p_\infty)/q_\infty$
c	cruciform shroud flap position (see fig. 4(f)); with all four flaps in this position nozzle expansion ratio is 1.90
D_f	calculated skin friction drag of metric portion of model forward of nozzle connect station, lbf
D_p	calculated pressure drag of boattailed portion of model forward of nozzle connect station, lbf
d	cruciform shroud flap position (see fig. 4(f)); with all four flaps in this position nozzle expansion ratio is 1.27
d_m	model maximum diameter, 7.340 in.
d_{nc}	model diameter at nozzle connect station (Sta. 54.760), 6.758 in.
F	measured thrust (at $M = 0$), lbf
F_i	ideal isentropic gross thrust, $w_p \left\{ \frac{R_j T_{t,j}}{g^2} \left(\frac{2\gamma}{\gamma - 1} \right) \left[1 - \left(\frac{P_a}{P_{t,j}} \right)^{(\gamma-1)/\gamma} \right] \right\}^{1/2}, \text{ lbf}$
F_r	resultant thrust (at $M = 0$) or resultant force (wind-on), $\sqrt{F^2 + NF^2 + SF^2}$, lbf
$F - D$	measured thrust-minus-drag (at $M > 0$), lbf
g	gravitational constant, 32.174 ft/sec ²
M	free-stream Mach number
NF	normal force (in vertical plane perpendicular to model axis, positive upwards), lbf
NPR	nozzle pressure ratio, $p_{t,j}/p_a$ for $M = 0$ or $p_{t,j}/p_\infty$ for $M > 0$
PM	pitching moment, in-lb

p	local pressure, psi	w_p	measured flow rate, lbf/sec
p_a	ambient pressure, psi	x	axial distance measured from nozzle connect station, Sta. 54.760 (positive downstream), in.
$p_{t,j}$	average jet total pressure, psi		
$p_{t,\infty}$	free-stream total pressure, psi	YM	yawing moment, in-lb
p_∞	free-stream static pressure, psi	y	vertical distance measured from model centerline, in.
q_∞	free-stream dynamic pressure, psi	z	distance of pressure orifices in axial nozzle vent from shroud exterior surface, in.
R	radius, in.		
R_j	gas constant for air, 1716 ft ² /sec ² -°R	16FT TT	Langley Research Center 16-Foot Transonic Tunnel
R_N	free-stream Reynolds number per foot		
r	radial ordinate from model centerline, in.	γ	ratio of specific heats for air, 1.3997
		Δ	incremental value
r_{\max}	maximum radial ordinate of centerbody, 2.202 in.	δ_p	pitch vector angle for nozzle with cruciform shroud, $\tan^{-1} NF/F$ for $M = 0$ or $\tan^{-1} NF/(F - D)$ for $M > 0$, deg
rad	radius	δ_y	yaw vector angle for nozzle with cruciform shroud, $\tan^{-1} SF/F$ for $M = 0$ or $\tan^{-1} SF/(F - D)$ for $M > 0$, deg
SF	side force (in horizontal plane perpendicular to model axis, positive to right), lbf	ϕ	meridian angle measured from top of model (0°), clockwise when looking upstream, deg
Sta.	Station: distance from tip of model nose as installed in 16-Foot Transonic Tunnel (see fig. 2), in.		
$T_{t,j}$	jet total temperature, °R		
$T_{t,\infty}$	free-stream total temperature, °R	Subscripts:	
TE	trailing edge of nozzle shroud	adj	vectored cruciform nozzle data adjusted for geometric, installation, and flow asymmetries
typ	typical		
UPWT	Langley Research Center Unitary Plan Wind Tunnel	aero	cruciform nozzle vectored flap aerodynamic (jet off) contribution
w_i	ideal flow rate,	jet	cruciform nozzle vectored flap jet contribution
	$p_{t,j} A_t \left\{ \frac{g^2 \gamma}{R_j T_{t,j}} \left[\left(\frac{2}{\gamma + 1} \right)^{(\gamma+1)/(\gamma-1)} \right] \right\}^{1/2}, \text{ lbf/sec}$	u	cruciform nozzle flaps in 2a + 2d positions, unvectored

un	indicates uncertainty range for parameter
v	cruciform nozzle flaps in 2a + 2d positions, vectored

Apparatus and Methods

Wind Tunnels

The investigation was conducted in the Langley Research Center 16-Foot Transonic Tunnel (ref. 1) and the Langley Research Center Unitary Plan Wind Tunnel (ref. 2). The 16FT TT is a single return, continuous air exchange, atmospheric wind tunnel with an octagonal test section having slots at the wall vertices. The distance between opposite walls is 15.5 ft. Test section cross-sectional area is 199.15 ft². The tunnel has a speed range capability from Mach number 0.20 to 1.30.

The high speed tests ($M \geq 2.16$) were conducted in the low speed test section of the UPWT, which is a variable-pressure, continuous-flow facility. The rectangular test section is 16 ft² in cross section and 7 ft in length. An asymmetric sliding-block type nozzle is used to expand the flow to the test section and is capable of providing continuous test section Mach number variation from 1.50 to 2.90.

The nominal free-stream conditions in the two facilities for this investigation are summarized in table 1.

Test Pod and Support Systems

Photographs showing the model test assemblies in the 16FT TT and UPWT test sections are presented in figure 1, and a cross-sectional schematic of the sting-strut supported model as installed in the 16FT TT is presented in figure 2. The axisymmetric forebody was nonmetric (not attached to the force measuring balance) and extended back to model Sta. 40.890. The forebody nose had an ogive shape to reduce the strength of the external flow expansion around the forebody shoulder (nose-to-cylindrical cross

section intersection). The cylindrical portion (7.340 in. in diameter) of the forebody was reduced in length by 5.76 in. (see fig. 2) for the tests in the UPWT to avoid impingement on the nozzle boattail surface of wall reflected shocks originating at the model nose (Sta. 5.760 for UPWT tests). At the end of the forebody (Sta. 40.890) there was a 0.10 in. wide gap to prevent contact between the nonmetric forebody and the metric afterbody. This gap was spanned by a free floating flexible strip in an annular groove to inhibit flow into or out of the model interior. A portion of the metric afterbody was of the same 7.340 in. diameter (up to Sta. 49.210) as the forebody. Between Sta. 49.210 and 54.760 the afterbody diameter was reduced from 7.340 in. to 6.758 in. at a half angle of 3°. Sta. 54.760 is referred to as the nozzle connect station for purposes of discussion in this report.

In both wind tunnels an external high-pressure air system provided a continuous flow of clean, dry air for propulsion simulation at a controlled stagnation temperature of about 530°R in the model instrumentation section. The air was supplied through the support strut (see fig. 2) by six tubes, collected in a high pressure plenum located in the model forebody, and was then routed aft. The air was then discharged radially into a low-pressure plenum through eight multi-holed sonic nozzles equally spaced around the aft portion of the high pressure plenum. This arrangement is intended to minimize the forces imposed by the transfer of axial momentum as the air passes from the nonmetric high pressure plenum to the metric low pressure plenum. Two flexible metallic bellows serve as flow seals and compensate for axial forces caused by pressurization.

In the 16FT TT, the nozzle centerline was located on the test section centerline. The centerline of the sting portion of the sting-strut support system was 22.0 in. below the test section centerline. The sting was 2 × 6 in. in cross section with top and bottom capped by half cylinders of 1-in. radius (fig. 2). The strut portion was swept 45° and was 5 percent thick streamwise with a chord of 20 in. In the UPWT, which has a

4-ft by 4-ft test section, an identical strut support (no sting) was used and was mounted directly to the test section sidewall (fig. 1(c)) in the horizontal centerline plane of the test section. The length of the strut put the model centerline 3 in. past the vertical centerline plane of the test section.

Nozzles

Nozzle Design Considerations

The primary requirement for efficient nozzle thrust performance at a supersonic Mach number is that the nozzle divergent section have sufficient area ratio (A_e/A_t) to expand the engine exhaust flow to ambient pressure. However, a turbojet powered configuration having a fixed geometry nozzle optimized for supersonic performance would encounter its most critical phase of operation in the transonic speed range where it must produce sufficient thrust to overcome the drag rise and accelerate to supersonic speed. Since air launched payloads are usually consumables and are carried in or on other air vehicles, their cost, weight, and size become important factors in the trades to be made against aerodynamic performance during the design process. As shown in figure 3 (from ref. 3), a payload designed to cruise at a high supersonic Mach number would require the nozzle to operate at nozzle pressure ratios from about 2 when launched subsonically to over 50, depending on the supersonic cruise Mach number. Since mechanical complexity generally accompanies the ability to change nozzle area ratio, and complexity is directly related to cost, optimizing area in this manner for a broad range of flight conditions would not be the desirable approach unless absolutely necessary. In effect, cost considerations drive the design to a fixed geometry nozzle with a large area ratio capable of producing high thrust efficiency at the cruise Mach number and engine operating pressure ratio. With this as the starting point for nozzle performance, it becomes imperative to determine, and try to improve, the off-design performance of what is essentially a nozzle designed for supersonic cruise. The large area ratio nozzle

would, based on the known performance characteristics of divergent nozzles operating well below their design point, not have good thrust performance at the low pressure ratios required at subsonic/transonic Mach numbers because of flow overexpansion effects. In actual operation, flow separation from the overexpanded divergent nozzle walls usually results in significantly higher thrust performance than would be expected. The extent of this beneficial separation is not accurately predictable without testing and is dependent to some degree on nozzle internal contour. For example, use of an empirical relationship arrived at in reference 4 from the correlation of some scale model nozzle data allows estimation of a minimum value of nozzle thrust recovery to be made from analytically determined peak and overexpanded thrust ratios for a given geometry. However, the author of reference 4 observed that thrust recovery for an actual nozzle at overexpanded conditions will almost always be higher than the empirical estimate since such items as leakage, discontinuities, and flow profiles generally encourage more flow separation in the divergent section.

The possibility of improving the thrust performance of fixed geometry, overexpanded, convergent-divergent nozzles at subsonic and transonic Mach numbers by ventilation of the divergent portion of the nozzle to external conditions was indicated by the investigation of reference 5. The nozzles were vented (slotted) longitudinally from the throat to the exit so that the external flow on the nozzle boattail and the internal flow (or separated internal flow regions) could communicate through whatever pressure differential might exist between them. The results of reference 5 indicate that ventilating the divergent portion of a nozzle having an expansion ratio (A_e/A_t) of 2.24 significantly improved thrust ratio at overexpanded conditions (statically and at Mach numbers from 0.8 to 1.2 at low nozzle pressure ratios). When a nozzle pressure ratio of about 8.0 was reached, the thrust improvement disappeared and some thrust ratio loss was evident. However, the ventilated nozzle was not tested at its original supersonic design

Mach number, so the magnitude of thrust ratio loss due to ventilation at fully expanded cruise conditions was not determined.

Nozzle Models

Six nozzle shroud concepts were designed for air-breathing nonaugmented turbojet applications at supersonic speeds. Shroud geometry is defined by the sketches shown in figure 4 and by the coordinates provided in tables 2 through 5. Five of the shroud designs (figs. 4(a) through (e) and tables 2 through 4) had fixed axisymmetric geometry and an area ratio of 2.64 (design nozzle pressure ratio of 17.1). The fixed geometry shroud design variables consisted of length, internal contour, and venting to the free stream. The sixth shroud design (fig. 4(f)) incorporated a simplistic variable geometry having four flaps forming a cruciform cross-sectional area. On this nozzle, the flaps were capable of movement in two-dimensional channels in the divergent shroud integrated into the basic axisymmetric flow path. In the simplest form, the flaps would be fixed in place in a low expansion ratio position using explosive bolts, and at some higher Mach number (probably near supersonic cruise), the explosive bolts would be activated and the four flaps would move outward (due to internal pressure loads or springs) to provide a higher, more optimum nozzle expansion ratio. Another possible mode of operation would be to allow the flaps to free-float and self-adjust to various expansion ratios depending on the internal/external load balance on the flaps. In either case, the four flap positions provided for this configuration (see fig. 4(f)) would be useful to help determine the most beneficial conditions for explosive bolt activation and/or define the nozzle performance envelope. In the most complex form, the four nozzle flaps would be independently actuated (controlled) to provide a more continuous optimization of expansion ratio. With the four flaps in their second most open position (position b) in the channels, this shroud also had an area ratio of 2.64 (same as the fixed geometry nozzle designs). Unequal deflection of each of the four flaps to one of the four available positions could be used to provide intermediate area ratios (figs. 1(a) and

1(b)) or a limited amount of thrust vectoring if the flaps were independently actuated.

The two unvented fixed geometry axisymmetric shrouds differed in length (figs. 4(a) and (c)) but had identical internal geometry up to an x/d_{nc} of 0.236 (compare tables 2 and 3). The short shroud length, as measured from the nozzle connect station, was approximately 75 percent that of the long shroud with internal divergence in both shrouds being terminated at the exit at a half angle of 11° relative to the nozzle centerline. The internal contour of the short shroud was derived to encourage shroud flow separation at low overexpanded nozzle pressure ratios and to minimize shock losses near design nozzle pressure ratio (fully expanded flow conditions). The cruciform shroud was approximately 22 percent longer than the fixed long shroud and had the same internal geometry up to an x/d_{nc} of 0.319.

The nozzles with axially vented shrouds (fig. 1(c) and figs. 4(b) and (d)) were the same pieces of hardware used for the unvented nozzles shown in figures 4(a) and (c). The slots were machined after all the unvented nozzle configurations had been tested in both wind tunnels. The venting was intended to allow the higher pressure air on the external boattail to flow into the low pressure or separated area of the overexpanded shroud to improve nozzle performance at off-design conditions by increasing the pressure in the overexpanded area and perhaps encourage earlier separation without recourse to the complexities of variable geometry.

The nozzle shroud with the annular venting (fig. 1(d) and fig. 4(e)) had the same overall length as the long fixed geometry shroud (fig. 4(a)). It also had the same internal flow path geometry as the long fixed geometry shroud up to an x/d_{nc} of 0.448, which is the location of the trailing edge of the forward portion of the shroud (compare tables 2 and 4(a)). Details of the annular slot shape can be obtained from the differences between the coordinates presented in table 4 for the forward and aft shroud components. The locations and geometry of the six lenticular

(double convex circular arc cross sections) shaped struts that span the annular slot and support the aft portion of the shroud are shown in figure 4(e). The amount of shroud area opened to flow from the nozzle boattail was approximately the same for all three vented nozzles. The area ratio of the annular shroud was also 2.64.

The six shrouds were tested with centerbodies that represented the aft portion of a turbine having either a convex base or a concave (truncated and recessed) base (fig. 4(a) and table 5). The nozzle geometric throat ($A_t = 10.816 \text{ in}^2$) was in the shape of a cone frustum whose slant height was defined by connecting the aft point of the concave centerbody ($x/d_{nc} = 0.12726$) to the closest point on the shroud internal surface. All nozzle configurations had identical internal flow path geometry up to the geometric throat so that all changes in either shroud or centerbody geometry occurred in the divergent portion of the flow path. With a given centerbody, some of the shrouds had identical internal nozzle geometry for some distance downstream of the geometric nozzle throat as can be seen by comparing coordinates for the fixed geometry shrouds in tables 2, 3, and 4.

Instrumentation

A six-component force balance was used to measure the combined external (aerodynamic) and internal (thrust) forces and moments on the model downstream of Sta. 40.890. Jet total pressure was measured with sets of four pressure probes mounted on three of the six centerbody support struts in the constant area annular duct section ahead of the nozzle centerbody (which represented the aft portion of a turbine centerbody, see fig. 2). Jet total temperature was measured with two thermocouples at approximately the same location as the total pressure probes. Mass flow in the high pressure air system was calculated from pressure and temperature measurements made in calibrated critical flow venturis external to the model.

The fixed geometry nozzle shroud surfaces had internal and external static pressure orifices

located as described in tables 6 and 7. It should be noted that, for ease of fabrication, neither the internal nor external shroud orifices were installed in a row (i.e., at a given meridian angle). Four (those near the nozzle geometric throat) of the 10 centerbody static pressure orifices were also not on the same meridian angle as the 6 orifices closest to the centerbody axis of symmetry (see table 8).

Static pressures on the internal nozzle surfaces, where high pressure levels were anticipated, and at the metric break station were measured on individual differential pressure strain-gauge transducers. On the aft portion of the divergent section of the shroud and on the model external surface, where lower levels of static pressure were expected, measurements were made using electronic pressure scanning units housed in the model forebody.

Data Reduction

Approximately 50 frames of data, recorded at a rate of 10 frames per second, were taken for each data point; average values were used in all computations.

The balance measurements are initially corrected for model weight tares and balance interactions. Although the bellows arrangement was designed to eliminate pressure and momentum effects on the balance readings, small bellows tares on all components still exist. These tares result from a small pressure difference between the ends of the bellows when internal velocities are high and also from small differences in the spring constants of the forward and aft bellows when the bellows are pressurized. As discussed in reference 6, these bellows tares were determined by testing calibration nozzles with known performance over a range of nozzle pressure ratios while applying force and moment loadings that simulate the ranges expected for the test nozzles. The balance data were then corrected for these tares in a manner similar to that discussed in references 6 and 7.

The corrected balance forces and moments are transferred to the body axis of the metric portion

of the model. In the 16FT TT the pitch attitude of the nonmetric forebody relative to gravity was determined from a calibrated attitude transmitter located in the model nose. The aerodynamic angle of attack of the metric portion of the model was determined by applying terms for afterbody deflection under load (balance bending) and for test section flow angularity to the nonmetric forebody angle measured by the attitude transmitter. The test section flow angularity used in setting the metric afterbody at an angle of attack of 0° in the 16FT TT was 0.1° , which is the average of measurements made during tests of similar models. In the UPWT the model was mounted from the sidewall at a geometric angle of attack of 0° and no flow angularity adjustment was made.

Nozzle discharge coefficient (w_p/w_i) is the ratio of measured weight flow to ideal weight flow, where ideal weight flow is based on jet total pressure ($p_{t,j}$), total temperature ($T_{t,j}$), and nozzle throat area (A_t). Nozzle discharge coefficient is then a measure of the ability of the nozzle to pass mass flow. Thrust ratio (F/F_i) or thrust-minus-drag ratio ($(F - D)/F_i$) is obtained by dividing the corrected axial force, measured by the balance at a given nozzle pressure ratio and Mach number, by the ideal thrust. For static (wind-off) conditions, this is a measure of the ability of the nozzle to convert the supplied mass flow into an axial (thrust) force. For wind-on conditions it is a measure of the net axial force resulting from the combination and interaction of aerodynamic and nozzle thrust forces. Resultant force ratio (F_r/F_i) is obtained by dividing the resultant force from the corrected force balance measurements along the three body axes (i.e., axial (F) or ($F - D$), normal (NF), and side (SF)) by ideal thrust. The nonaxial force components (NF and SF) can arise as a result of external aerodynamics, asymmetric flow separation in the divergent portion of the nozzle, and vectoring the cruciform nozzle flaps to turn the flow. Vector angles in the pitch and yaw planes (δ_p and δ_y) are defined as $\delta_p = \tan^{-1} (NF/F)$ and $\delta_y = \tan^{-1} (SF/F)$ for $M = 0$, and

$$\delta_p = \tan^{-1} (NF/(F - D)) \text{ and } \delta_y = \tan^{-1} (SF/(F - D)) \text{ for } M > 0.$$

The data contained in this report were obtained from three separate wind tunnel entries, which necessitated gathering instrumentation and building up the test apparatus three times. Proper test technique required that the instrumentation for each test entry be calibrated and that the appropriate balance force and moment tares be determined each time. The nozzles were tested first in the 16FT TT and then in the UPWT. During the UPWT test entry the long and short unvented shrouds were tested and then modified in a machine shop to create the axially vented shrouds (without vent wall pressure orifices) and retested. After the UPWT entry six pressure orifices were installed in the axial vent walls of the two shrouds. Then a second entry into the 16FT TT was made to test the axially vented shrouds and some cruciform nozzle configurations with additional shroud flap settings. Because of the multiple test entries, the wide range of pressure transducer capacities used, and the multiple determinations of the balance force and moment tares, a concise determination of uncertainty bands is not practical. However, a discussion of the force balance and pressure transducer accuracy is contained in appendix A.

The force balance derived data in the body of this report represent the measured performance for the entire metric afterbody of the model. Isolated nozzle-only performance data can be obtained by applying adjustments for the skin friction and pressure drag on that portion of the metric afterbody forward of the nozzle connect station. Simple calculations have been made of the two aforementioned adjustments and are discussed in appendix B. However, it is not necessary to include these adjustments in the data when the various nozzle configurations are compared since the adjustments are unaffected by nozzle efflux at a given Mach number and are independent of nozzle configuration. The adjustments will be of use if the absolute level of performance for a particular nozzle is desired at a specific nozzle operating condition.

Tests

Data were obtained in the 16FT TT (which is an atmospheric wind tunnel) at static conditions and Mach numbers from 0.60 to 1.25, and in the UPWT at static conditions (with the tunnel circuit pumped down to a low ambient pressure) and at Mach numbers of 2.16, 2.50, and 2.86. Nominal values of the free-stream test conditions for each facility are presented in table 1. Only nominal values and ranges of test conditions are presented since the ability to maintain identical test conditions from day to day and configuration to configuration was limited by variations in atmospheric conditions (16FT TT) and the addition of jet mass flow to the tunnel airstream (pumping capacity at UPWT). It should be noted that model Reynolds number with a given nozzle installed would be computed using a different model length (see fig. 2) for tests conducted in the 16FT TT than in the UPWT. The shorter model (nose) was used in the UPWT to avoid impingement on the model of wall reflected shocks that originate at the model nose at the lowest UPWT Mach number of 2.16.

Model angle of attack was held constant at 0° for the investigation. The nozzles were tested at nozzle pressure ratios within the range from 1.9 to 11.8 in the 16FT TT at subsonic and transonic Mach numbers, and within the range from 7.9 to 54.9 in the UPWT at the three high supersonic Mach numbers. To ensure a turbulent boundary layer over the model, a 0.1 in. wide transition strip of No. 100 carborundum particles was fixed 1.5 in. downstream of the tip of the model nose in the 16FT TT tests. In the UPWT tests, a 0.1 in. wide transition strip of No. 50 carborundum particles was fixed 1.2 in. downstream of the tip of the model nose.

Presentation of Results

The results of this investigation are presented graphically as the variation of discharge coefficient (w_p/w_i), thrust ratio (F/F_i), thrust-minus-drag ratio ($(F - D)/F_i$), normal force ratio (NF/F_i), side force ratio (SF/F_i), pitch vector angle (δ_p), and yaw vector angle (δ_y) with nozzle

pressure ratio (NPR). For a given nozzle configuration, internal ($p/p_{t,j}$) and external (C_p) pressure data are presented for each Mach number. Pressure data for some intermediate nozzle pressure ratios have been omitted for graphical clarity. No pressure data are presented for the cruciform nozzle configurations since only centerbody pressures were obtained.

In general, the 16FT TT data are presented separately from the UPWT data since some changes in figure scales were appropriate. The wide range of NPR tested in the UPWT made it desirable to compress the NPR scale for presentation purposes. A change in the C_p (pressure coefficient) scale for the two speed ranges was also appropriate because of the larger variations of external pressures that occurred in the NPR range applicable to the subsonic and transonic speeds. In addition, the subsonic and transonic external pressure (C_p) data scale for the axially vented long shroud configurations was changed to accommodate the low pressures measured on the walls of the vents. Some centerbody pressure data are not presented since the pressures overran the instrumentation capability at high NPR.

The experimental data and comparisons of the performance of the various nozzle configurations are presented in the following figures:

Figure

Nozzle performance characteristics for the nozzle with \tilde{N}

Long unvented shroud	5
Long axially vented shroud	6
Long annularly vented shroud	7
Short unvented shroud	8
Short axially vented shroud	9
Cruciform shroud with flaps in position a.....	10
Cruciform shroud with flaps in position b.....	11
Cruciform shroud with flaps in position c.....	12

Cruciform shroud with flaps in position d.....	13
Cruciform shroud with flaps in position 2a + 2b	14
Cruciform shroud with flaps in position 2a + 2c	15
Cruciform shroud with flaps in position 2a + 2d	16
Cruciform shroud with flaps in position 2a + 2d, vectored	17
Nozzle internal and external pressure data with \tilde{N}	
Long unvented shroud with concave centerbody base	18
Long unvented shroud with convex centerbody base	19
Long axially vented shroud with concave centerbody base	20
Long axially vented shroud with convex centerbody base	21
Long annularly vented shroud with concave centerbody base	22
Long annularly vented shroud with convex centerbody base	23
Short unvented shroud with concave centerbody base	24
Short unvented shroud with convex centerbody base	25
Short axially vented shroud with concave centerbody base	26
Short axially vented shroud with convex centerbody base	27
Comparison of nozzle thrust-minus-drag performance for \tilde{N}	
Configurations having shrouds with same expansion ratio	28

Cruciform shroud configuration with flaps in various positions	29
Various shroud configurations at nozzle operating NPR	30
Cruciform shroud configuration adjusted vector angles with flaps in position 2a + 2d at nozzle operating NPR	31

Discussion

Discharge Coefficient

Long and Short Axisymmetric Nozzles

Discharge coefficients were generally in the range between 0.91 and 0.94 at nozzle pressure ratios above 3.0 for the long and short axisymmetric nozzles at all Mach numbers tested (see figs. 5 through 9). For a given configuration, discharge coefficient varied little as nozzle pressure ratio was increased above 3.0. Where data were available for comparison for a given nozzle shroud geometry, discharge coefficient was about 0.02 higher with the concave centerbody base than with the convex centerbody base above a nozzle pressure ratio of 3.0 (see fig. 5).

At nozzle pressure ratios between 2.0 and 3.0, all nozzles with the concave centerbody base experienced an increase in discharge coefficient between 0.03 and 0.05 before reaching a nearly constant level for the remainder of the nozzle pressure ratio range (see fig. 5(a)). Venting the divergent portion of the nozzle shrouds to external flow had no noticeable effect on discharge coefficient (compare fig. 5 with figs. 6 and 7). This result was expected since all the venting was well downstream of the throat and all the data were obtained at nozzle pressure ratios above the choked condition (sonic flow at the throat). Above the choked condition, mass flow is affected only by throat area and the geometry upstream of the throat.

Centerbody and shroud internal surface pressure measurements indicate that the consistent differences in discharge coefficient that occurred

for the two centerbodies (e.g., fig. 6(a)) are a result of differences in the location and nozzle pressure ratio at which sonic flow ($p/p_{t,j} = 0.5283$) occurred on the centerbody. For example, when the wind-off centerbody pressure data for the two axially vented long nozzle configurations are compared (figs. 20(a) and 21(a)), projection of the location of the first occurrence of sonic flow onto the nozzle centerbody sketch shows that sonic flow occurs on the base of the concave centerbody (at $r/d_{nc} = 0.20$), and in the annular flow passage downstream of the geometric throat location on the convex centerbody (at $r/d_{nc} = 0.24$). Since sonic flow occurs at the same location on the shroud for both centerbody configurations this indicates that the shape of the sonic line between the shroud and concave centerbody surfaces is distorted or angled and results in a larger effective throat area than for configurations with the convex centerbody. A larger effective throat area would explain the consistently higher discharge coefficients obtained for configurations having the concave centerbody at nozzle pressure ratios of 3.0 and above.

The first indication of sonic flow on the centerbodies in these same wind-off centerbody pressure distributions occurs at a nozzle pressure ratio of about 4.5 on the concave centerbody and at a nozzle pressure ratio of about 2.5 on the convex centerbody. Examination of the discharge coefficient data of figure 6 indicates that these nozzle pressure ratios approximate the nozzle pressure ratios above which discharge coefficient becomes constant for each of the configurations.

Cruciform Nozzles

Discharge coefficients were generally in the range between 0.91 and 0.95 at nozzle pressure ratios above 3.0 for the cruciform nozzle configurations at all Mach numbers tested (see figs. 10 through 17). For a given configuration, discharge coefficient varied little with increasing pressure ratio above 3.0. For a cruciform nozzle with a given shroud flap position, discharge coefficient was about 0.02 higher with the concave centerbody base at nozzle pressure ratios

above 3.0 where data for comparison were available (e.g., fig. 10). As nozzle pressure ratio was increased from 2.0 to 3.0, discharge coefficient increased for most of the configurations with the concave centerbody base. This increase in discharge coefficient decreased in magnitude as the shroud flap angle was decreased (smaller nozzle exit area) until the d position was reached (fig. 13) where the discharge coefficient was essentially flat for the entire nozzle pressure ratio range.

Effect of Centerbody Base Geometry on Thrust-Minus-Drag Performance

The pressure levels on the centerbody bases were greater than the capacity of the pressure instrumentation selected for some of the static, subsonic, and transonic test conditions. Therefore, in figures 18 through 27, there are some nozzle pressure ratios at which no local pressure ratios are presented on the centerbody plots.

Long Unvented Shroud

The thrust-minus-drag ratio data of figure 5 show the effect of nozzle centerbody geometry at a given Mach number over the range of nozzle pressure ratios. In the subsonic/transonic speed range the thrust-minus-drag performance of the configuration with the concave centerbody base was generally higher than the performance of the configuration with the convex centerbody base at Mach numbers equal to or greater than 0.95.

The largest effects of centerbody base geometry occurred at Mach numbers of 0.60 and 0.90, where $(F - D)/F_i$ for the configuration with the concave centerbody base decreased abruptly by about 0.06 relative to the configuration with the convex centerbody base at nozzle pressure ratios above 5 and 4, respectively. At low nozzle pressure ratios, the nozzles of the current study are greatly overexpanded (exit area too large) and, at subsonic speeds, the internal flow is separated from the shroud internal surface. As is generally the case with greatly overexpanded nozzles, the thrust performance at nozzle pressure ratios well below that for fully expanded flow is better when

the flow is separated than it would be if the flow were attached. This is illustrated in figure 5(a) where there is an abrupt decrease in thrust-minus-drag ratio at Mach numbers of 0.60, 0.80, 0.90, and 0.95 when the nozzle pressure ratio reaches a value where flow attaches to the overexpanded divergent shroud. The shroud internal pressure distributions of figures 18(c) through (f) and figures 19(c) through (f) indicate flow attachment at the nozzle pressure ratios at which the thrust-minus-drag ratio abruptly decreases. This flow behavior in a greatly overexpanded nozzle is typified by the occurrence of an additional thrust-minus-drag performance peak at some nozzle pressure ratio below that for fully expanded flow conditions.

The shroud internal pressure data of figures 18 and 19 can be used to show that the difference in thrust-minus-drag ratio performance between configurations with the concave and convex centerbody bases at Mach numbers of 0.60 and 0.90 is a result of the different shroud flow conditions. For example, at a Mach number of 0.60, the shroud internal pressure data indicate that at a nozzle pressure ratio of 6.0 the internal flow is attached to the shroud for the configuration with the concave centerbody base (fig. 18(c)) and is separated from the shroud for the configuration with the convex centerbody base (fig. 19(c)). The difference in local pressure ratio ($p/p_{t,i}$) between the configurations is approximately 0.08 and occurs between an x/d_{nc} of 0.32 and 0.62. Computation of the incremental axial force due to that pressure differential on the projected axial area of the shroud in that x/d_{nc} range results in a thrust-minus-drag ratio increment of about 0.067. Comparison of the thrust-minus-drag ratios in figure 5(a) for the two configurations at a Mach number of 0.60 and a nozzle pressure ratio of 6.0 indicates that this is the order of magnitude of the performance difference. A similar computation was made at a Mach number of 0.90 and a nozzle pressure ratio of 5.0 and yielded a thrust-minus-drag ratio increment of 0.062.

There is also an indication in the centerbody pressure distributions of figures 18 and 19 of

lower pressures over a portion of the convex centerbody base. However, the lower pressures are present at all Mach numbers and apparently do not act over a large enough projected area to show an effect on the thrust-minus-drag data. It is not known why the thrust-minus-drag ratio data (fig. 5(a)) and pressure data (figs. 18(d) and 19(d)) at the intermediate subsonic Mach number of 0.80 do not also indicate the persistence of fully separated internal flow for the configuration with the convex centerbody to a higher nozzle pressure ratio than the configuration with the concave centerbody base.

Long Axially Vented Shroud

The thrust-minus-drag ratio data of figure 6 indicate that the configuration with the convex centerbody base generally had higher performance than the configuration with the concave centerbody base by about 0.01 to 0.02 in $(F - D)/F_i$ at subsonic Mach numbers. Comparison of pressures on the shroud internal surface for the two different centerbody geometries (figs. 20 and 21, (c) through (f)) does not show a difference in pressure level that would explain the source of the difference in performance. At supersonic Mach numbers, the centerbody geometry effects on thrust-minus-drag performance are smaller.

Long Annularly Vented Shroud

The thrust-minus-drag ratio data of figure 7(a) indicate that there was no significant difference in performance due to centerbody base geometry at subsonic and transonic Mach numbers. No comparison can be made at the high supersonic Mach numbers since data were not obtained for this shroud configuration with the convex centerbody in the UPWT.

Short Unvented Shroud

The thrust-minus-drag ratio data of figure 8 indicate that the effect of centerbody base geometry on performance was small over the range of nozzle pressure ratio at subsonic speeds but that the configuration with the convex base

had slightly higher performance at subsonic speeds and the configuration with the concave base generally had higher performance at supersonic speeds. Examination of the pressure distributions on the internal surface of the shroud (figs. 24 and 25) indicates that the nozzle internal flow was separated from the shroud surface from an x/d_{nc} of about 0.32 to the nozzle exit for all the subsonic and transonic Mach numbers over the range of nozzle pressure ratios investigated.

Short Axially Vented Shroud

The thrust-minus-drag ratio data of figure 9(a) indicate that in general there was no significant effect of centerbody base geometry on nozzle performance at subsonic speeds but the configuration with the concave base generally had slightly higher performance at transonic speeds. At Mach numbers of 2.16 and 2.50 (fig. 9(b)) at low nozzle pressure ratios, the configuration with the convex centerbody base had higher performance before dropping down to a constant $(F - D)/F_i$ level of about 0.88. The configuration with the concave base showed a similar drop in performance at a Mach number of 2.16. The reason for this behavior is not readily evident from comparison of the pressure data of figures 26 and 27, (i) and (j), although there appears to be an indication of separated flow between x/d_{nc} of 0.32 and 0.50 in figures 26(i), 27(i), and 27(j) that is not present in figure 26(j).

Cruciform Shroud

Thrust-minus-drag ratio data for a given cruciform shroud configuration with both centerbody base configurations were obtained with the flaps in positions a and b. The subsonic and transonic data of figures 10(a) and 11(a) indicate that at Mach numbers above 0.60 the configuration with the concave centerbody base generally had better thrust-minus-drag performance by varying amounts than the configuration with the convex centerbody base over the nozzle pressure ratio range. At Mach number 0.60, the configuration with the flaps in position a (fig. 10(a)) generally had higher performance with the concave centerbody base at

nozzle pressure ratios above 5.0. With the flaps in position b (fig. 11(a)), the performance of the configuration with the concave centerbody base was higher over the nozzle pressure ratio range tested except at a nozzle pressure ratio of 4.0 at a Mach number of 0.60. At the three high supersonic Mach numbers, the configuration with the flaps in position b (fig. 11(b)) and the convex centerbody base had the best performance over the nozzle pressure ratio range by amounts up to a maximum of about 0.015 in $(F - D)/F_i$. Data were not obtained in the UPWT for the cruciform shroud with the flaps in position a and the convex centerbody base. The lack of pressure instrumentation on the cruciform shroud precludes any attempt to explain differences measured by the force balance using pressure measurements.

Effect of Shroud Configuration on Thrust-Minus-Drag Performance With Concave Centerbody Base

Comparisons of the thrust-minus-drag performance of the model with the six different nozzle shrouds and the concave centerbody base are shown in figure 28. The cruciform shroud configuration selected for these comparisons has the flaps in position b so that its expansion ratio (2.64) is the same as the five configurations with fixed geometry shrouds at the design nozzle pressure ratio of 17.1. The comparisons shown in figure 29 are for the cruciform nozzle with the various shroud flap positions and the concave centerbody.

Thrust Ratio for Nozzles Having Same Expansion Ratio at Static Conditions

Statically (fig. 28(a)) at low nozzle pressure ratios (below the nozzle design pressure ratio of 17.1), the two short shroud configurations had the best performance while at the high nozzle pressure ratios, above 18.0, they had the poorest performance. Comparison of the pressure data of figures 18(a) and 24(a) indicates the higher thrust ratios for the short shroud nozzle at the low nozzle pressure ratios are a result of higher pressure on the centerbody base and slightly

higher pressure over the divergent surface of the shroud. The configuration with the cruciform shroud had the worst thrust performance at low nozzle pressure ratios and the best thrust performance at nozzle pressure ratios above 14.0.

The data of figure 28(a) also show that for the short shroud nozzles, the axial vents had a negligible effect on thrust ratio below a pressure ratio of 5 and above a pressure ratio of 30. However, in the range of nozzle pressure ratios from 10 to 30, the axial vents improved performance. Comparison of the internal pressures on the shroud walls of these two configurations (figs. 24(b) and 26(b)) indicates that the vents produced higher pressures (which will reduce drag) on the wall of the overexpanded shroud downstream of the minimum internal diameter of the shroud in this nozzle pressure ratio range. The axial vents in the long shroud nozzle configuration decreased thrust ratio performance by about 0.02 over the range of low nozzle pressure ratios (top of fig. 28(a)). At the high pressure ratios (bottom of fig. 28(a)), there was a smaller decrease in performance. At a nozzle pressure ratio of about 9.0, the axial vents substantially improved thrust ratio performance; however, only a single data point indicates this at the start of the high nozzle pressure ratio sweep. No significant differences in the shroud internal pressure distributions of figures 18(a) and (b) and figures 20(a) and (b) indicate the source of any of these thrust ratio differences except at a nozzle pressure ratio of 10 where the vented shroud showed higher wall pressures.

Statically, the annularly vented shroud gave thrust ratio performance comparable to the long unvented shroud at nozzle pressure ratios below 3.5. At nozzle pressure ratios between 3.5 and 20, the nozzle with the annular vented shroud had the higher performance. A comparison of internal pressure distributions on the shroud walls in this pressure ratio range (figs. 18(b) and 22(b)) indicates the wall pressures were higher on the

annularly vented shroud in the separated region. Above a nozzle pressure ratio of 20, the annular vent caused a small decrease in performance.

Wind-on Thrust-Minus-Drag Ratio for Nozzles Having Same Expansion Ratio

The wind-on thrust-minus-drag ratio data of figure 28 show that the configuration with the axially vented short shroud generally had the best performance at Mach numbers through 1.25. Above Mach number 1.25 (fig. 28(e)) the configuration with the cruciform shroud (b flaps) had the best performance above a nozzle pressure ratio of 16.0 at all three Mach numbers while the two short shroud configurations had the poorest performance at all nozzle pressure ratios. The cause of the wind-on performance differences can generally be determined if the shroud internal pressure distributions are compared (for the shrouds that have internal pressure orifices). For example, at a Mach number of 2.86 and a nozzle pressure ratio of about 40, the data of figure 28(e) show that there is a difference in thrust-minus-drag ratio of 0.038 between the configurations with the long and short unvented shrouds. Examination of the shroud internal surface pressures of figures 18(k) and 24(k) shows that the long unvented shroud had a considerably higher level of pressure over the rearmost portion of the shroud (internal and external). cursory calculations of the axial forces on the projected areas of the diverging portions of the two shrouds downstream of an x/d_{nc} of 0.3 indicate that there is about a 0.042 difference in thrust-minus-drag ratio attributable to the internal pressure distribution differences in this area. Similar comparisons show that the drop in thrust-minus-drag ratio for the configuration with the long unvented shroud above a nozzle pressure ratio of 5.0 at a Mach number of 0.60 (fig. 28(b)), which does not occur with the short unvented shroud, is attributable to a sudden decrease in shroud internal surface pressures between $x/d_{nc} = 0.3$ and 0.7 (figs. 18(c) and 24(c)). This decrease in

shroud internal pressure at nozzle pressure ratios of 6 or greater is probably caused by a jet plume reattachment on the long shroud that does not occur on the short shroud.

Effect of Flap Position on Thrust-Minus-Drag Performance for Nozzle With Cruciform Shroud and Concave Centerbody Base

The cruciform shroud was designed so that the moveable flaps could be set for four discrete expansion ratios (i.e., flap positions a, b, c, and d as described in the table of fig. 4(f)). The nozzle was tested with the flaps set for these four nozzle expansion ratios over the Mach number range and the data are included in figure 29. It was also possible to assemble the cruciform nozzle at expansion ratios between the four symmetrical flap design expansion ratios by setting the four individual flaps in different positions. To this end, some intermediate expansion ratio configurations (the two flaps in one plane were set in one of the four positions and the two flaps in the other plane were set in another of the four positions) were investigated statically at high nozzle pressure ratios and at the three high supersonic Mach numbers and the data are included in figure 29.

Thrust Ratio for Nozzle With Flaps Set for Various Expansion Ratios at Static Conditions

Statically, the cruciform nozzle thrust ratio performance (fig. 29(a)) is generally as would be expected. That is, at the lowest pressure ratios, the configurations with the low expansion ratios had the best performance while at the highest nozzle pressure ratios, the configurations with the high expansion ratios had the best performance. In the low nozzle pressure ratio range (top of fig. 29(a)), the nozzle configurations with the flaps in position b and in position c experienced an abrupt drop in thrust ratio performance at nozzle pressure ratios of 2.5 and 4.0, respectively. These drops in thrust ratio and the recovery afterward in the low nozzle pressure ratio range are characteristic of separated internal flow in an overexpanded nozzle attaching itself to the diverging shroud walls as the nozzle pressure ratio is increased. A

performance drop probably also occurs for the nozzle with the flaps in the a position (highest expansion ratio tested) at a nozzle pressure ratio above the maximum tested at static conditions. This flow condition in a highly overexpanded nozzle often results in two thrust ratio peaks at both static and wind-on conditions as discussed previously. The one exception to the general performance trend with increasing expansion ratio occurred in the high nozzle pressure ratio range where the configuration with two flaps in position a and two flaps in position d had a significantly lower thrust ratio (by about 0.02) than the configuration with all four flaps in position c despite having a slightly higher expansion ratio.

Wind-on Thrust-Minus-Drag Ratio for Nozzle With Flaps Set for Various Expansion Ratios

The thrust-minus-drag data of figures 29(b) through (e) show the gradual improvement in performance with increasing Mach number for the configurations with the high expansion ratios until at a Mach number of 0.95 the peak performance of the nozzle with the flaps in position c is the same as with the flaps in position d at a nozzle pressure ratio of about 7.5. As Mach number is increased above 0.95, the peak nozzle performance with the flaps in position d decreases while the nozzles with higher expansion ratios continue to improve in performance. At the highest Mach number (2.86) and highest nozzle pressure ratio of this investigation, the thrust-minus-drag ratio of the lowest expansion ratio nozzle is about 0.06 lower than that of the three highest expansion ratio nozzles. The poorer performance of the configuration with two flaps in position a and two flaps in position d relative to the configuration with four flaps in position c, observed statically (fig. 29(a)), did not significantly change with Mach number (fig. 29(e)).

Since there were no pressure orifices in the cruciform shroud, there are no pressure data available to determine the source of performance changes that occurred as flap position was changed. However, the trends noted for varying

expansion ratio, Mach number, and nozzle pressure ratio are typical of conventional convergent-divergent nozzles as discussed previously.

Effect on Nozzle Thrust-Minus-Drag Performance of Positioning Flaps in Cruciform Shroud for Vectoring

As noted previously, each cruciform shroud flap could be set independently in any one of four positions (fig. 4(f)). This capability was exercised during the investigation by setting two adjacent flaps in position a and the other two adjacent flaps in position d so that a combined pitch and yaw thrust vectored configuration was created with flap geometric thrust vector angles of 9.62° in both planes. To provide a baseline unvectored nozzle having the same expansion ratio as the vectored configuration, the shroud was also assembled with one pair of opposite flaps set in position a and the other pair of opposite flaps set in position d. The centerbody with the convex base was utilized for both of these nozzle configurations and data were obtained at Mach numbers from 0 to 1.25 and are presented in figure 17.

It should be noted that the thrust-minus-drag and resultant force ratios for the nozzle with the vectored shroud geometry were significantly higher than those with the unvectored shroud geometry at Mach numbers of 1.15 and 1.25 at all nozzle pressure ratios (figs. 17(a) and (b)). At Mach numbers from 0.60 to 0.95 thrust-minus-drag performance was also better for the vectored nozzle at attached flow conditions (above a nozzle pressure ratio of 4.0). This was an unexpected result since thrust vectored nozzles generally have turning losses which result in lower thrust performance when compared to an unvectored nozzle. The absence of pressure instrumentation on the cruciform shroud limits the ability to explain these performance differences by analyzing differences in local shroud pressures. Comparison of the centerbody base pressures (not presented herein) for the vectored and unvectored nozzles did show that there was no effect of vectoring on the centerbody pressures. This result

leads to the conclusion that the source of the performance differences arises from differences in overexpansion effects on the internal surfaces of the shroud. It is likely that some of the internal flow remained attached to the unvectored nozzle shroud wall downstream of the area ratio for fully expanded flow causing a thrust loss, and that when adjacent flap pairs were set in the same position for vectoring this in some way acted as a mechanism to reduce, or prevent, overexpansion losses on the divergent flaps of the shroud.

The fixed geometry portion of the cruciform nozzle (i.e., that portion of the shroud ahead of the moveable flaps) has an expansion ratio of 1.273, which corresponds to a nozzle pressure ratio of 4.44 for fully expanded flow. Up to this nozzle pressure ratio the internal flow should separate symmetrically from the internal surfaces of the fixed portion of the shroud (before reaching the flaps) and no significant vectoring forces should be generated by the internal flow. Therefore, the only vector forces that should occur below a nozzle pressure ratio of 4.44 would be due to external aerodynamic forces acting on the vectored flaps. The data of figures 17(c), (e), and (g) show a break in the data trends with nozzle pressure ratio above a nozzle pressure ratio of 4, indicative of flow becoming attached to the vectored flaps at Mach numbers from 0.60 to 0.95. At the lowest nozzle pressure ratios, the jet-on and jet-off vector angles and force and moment ratios are a measure of the effect of small model internal and external geometric and flow asymmetries combined with data distortion resulting from ratioing the variables to small values of thrust.

The thrust vectoring characteristics of this nozzle (figs. 17(c), (e), and (g)) are similar to those of an overexpanded nozzle in which vectoring is initiated downstream of the throat (refs. 8 and 9). The magnitude of the measured vector angles shown in figures 17(c) and (e) indicate that this nozzle concept has the potential to provide forces and moments that may be useful for vehicle control. In order to separate the aerodynamic contribution of the vectored flaps and the vectored jet contribution from the

measured vector angles, the measured jet-off contribution was removed from the measured jet-on vector angles. This was done with the assumption that the measured jet-off (aerodynamic) normal and side forces at a given Mach number remained constant over the nozzle pressure ratio range. These jet-off forces and the jet-on thrust-minus-drag forces measured at each Mach number and nozzle pressure ratio were then used to calculate a jet-off contribution to vector angle as shown in figures 17(d) and (f). These jet-off vector angles are then subtracted from the measured jet-on vector angles to obtain the vector angle contribution of the jet (top portion of figs. 17(d) and (f)). The nonzero jet-off vector angle values for the unvectored configuration in figures 17(d) and (f) (solid symbols) are assumed to be due to a combination of the effect of the forward support strut flow field, model misalignment, and tunnel flow asymmetries.

In order to compensate for the effects of the aforementioned geometric and flow asymmetries, the vector angle data of figures 17(d) and (f) were adjusted using the equations shown in figure 31(a). These results (fig. 31(a)) show the variation with nozzle pressure ratio of the adjusted vector angles and the aerodynamic and jet portions of the total angle. The symbols indicate the nozzle pressure ratios at which the data for the calculations were obtained from figure 17. As would be expected, the aerodynamic effect of deflecting the flaps for vectoring is the largest portion of the vector angle up to the nozzle pressure ratio 4.44 since little internal flow turning (or asymmetric flow separation) should occur in the axisymmetric divergent portion of the nozzle ahead of the variable flaps.

Comparison of Nozzle Performance at Representative Engine Operating Pressure Ratios

In order to make a meaningful comparison of performance for these nozzle concepts in a particular mission application, it is necessary to know the operating pressure ratios for the nozzles at various flight conditions. The mission engine operating pressure ratios over the Mach number

range at high and low altitudes for these nozzle concepts were presented in reference 3 and are reproduced in figure 3 for the Mach number range of this investigation.

The variations of discharge coefficient and thrust-minus-drag ratio with Mach number at the nozzle operating conditions for high and low altitudes shown in the table in figure 3 are presented in figure 30 for the various shroud configurations with the concave centerbody base. The variations with Mach number at the nozzle operating conditions of cruciform nozzle vector angles adjusted for geometric and flow asymmetries and the jet-on and jet-off vectoring increments due to deflecting the shroud flaps are presented in figure 31(b) for the nozzle with the convex centerbody base. Although the data presented in figures 30 and 31(b) are from interpolations, they are represented by symbols to indicate the nozzle Mach numbers at which the interpolations were made.

Discharge Coefficient

As previously noted, discharge coefficients for the fixed shroud nozzle configurations with the concave centerbody were generally constant above a nozzle pressure ratio of 3.0 (the constant discharge coefficient value ranged between 0.90 and 0.94 depending on nozzle configuration). At nozzle pressure ratios between 2.0 and 3.0, discharge coefficient increased by between 0.03 and 0.05 before reaching the nearly constant level of the higher nozzle pressure ratio range.

The variation of discharge coefficient with Mach number for the six nozzle configurations having the same expansion ratio with the concave centerbody is presented in figure 30(a) for the high and low altitude nozzle operating pressure ratios. The drop off in discharge coefficient at the lower subsonic Mach numbers for the low altitude condition results from the lower nozzle operating pressure ratios. Above a Mach number of 0.90, nozzle discharge coefficient was between 0.93 and 0.94 for all five fixed shroud configurations. In figure 30(b) the variation of discharge coefficient with Mach number for seven

cruciform shroud nozzle configurations with the concave centerbody is presented for the high and low altitude nozzle operating pressure ratios. Once again there is some drop off in discharge coefficient at the lower Mach numbers for some configurations. Discharge coefficient was between 0.94 and 0.95 for all cruciform shroud configurations at Mach numbers higher than 0.80.

As noted earlier, a discharge coefficient of 0.96 was selected during the design process to size the nozzle exit area at supersonic cruise conditions. The data obtained during this investigation at high supersonic speeds indicate that measured nozzle discharge coefficient was between 0.93 and 0.95 for all shroud configurations with the concave centerbody at high and low altitude nozzle operating pressure ratios.

Thrust-Minus-Drag Ratio

In figure 30(a) the variation with Mach number of thrust-minus-drag ratio for six different shroud configurations having the same expansion ratio with the concave centerbody is presented at the high and low altitude nozzle operating pressure ratios. As can be seen from both the high and low altitude mission conditions, the short axially vented shroud gave the best thrust-minus-drag performance at Mach numbers up to 1.25. However, at the high supersonic Mach numbers, the nozzle with the cruciform shroud had the best thrust-minus-drag performance while the short axially vented shroud had the poorest performance. Of the five fixed shroud configurations (excludes the cruciform nozzle), the long annular vented shroud nozzle had the highest performance at high Mach numbers. Comparison of the high altitude thrust-minus-drag trends with Mach number at transonic speeds for the various nozzles indicates that the nozzle with the cruciform shroud will probably surpass the performance of all the other fixed geometry nozzle configurations at Mach numbers greater than 1.25.

The variation of thrust-minus-drag ratio with Mach number for seven cruciform shroud

configurations with the concave centerbody is presented in figure 30(b) for high and low altitude nozzle operating pressure ratios. At subsonic and transonic speeds only nozzle configurations with all four shroud flaps in the same position were tested while at the three high supersonic speeds; nozzle configurations with intermediate expansion ratios, obtained by setting one pair of opposite shroud flaps at a different position than the other pair, were also tested. As would be expected, the best thrust-minus-drag performance at the low subsonic Mach numbers was obtained with all the flaps in position d, that is, at the lowest nozzle expansion ratio. As Mach number (and nozzle operating pressure ratio) increased, the underexpansion losses for the lowest expansion ratio configuration (position d) became too large and the flap position c nozzle configuration, with its incrementally higher expansion ratio, provides the best performance. This performance crossover point occurs at approximate Mach numbers of 1.05 and 1.25 for the high and low altitude missions, respectively. Eventually, the underexpansion losses for the flap position c nozzle configuration become too large and the b flap nozzle configuration, with its incrementally higher expansion ratio, provides the best performance. This performance crossover occurred at approximate Mach numbers of 2.3 and 2.5 for the high and low altitude missions, respectively. For the Mach numbers of the current investigation, the flap position a nozzle configuration (largest expansion ratio tested) never provided the highest performance. However, it is expected that a performance crossover would also occur for this configuration at some higher Mach number. These results indicate, as would be expected, that the ability to change expansion ratio by varying the cruciform shroud flap angles allows thrust-minus-drag ratio to be maximized as Mach number is increased.

Cruciform Nozzle Vectoring

In order to obtain nozzle vector angles without the small contributions of model geometric asymmetries, internal flow asymmetries, model installation effects, and tunnel flow asymmetries (shown in the vector angles of figs. 17(c) and (e)),

the aerodynamic (flap deflection effect, jet-off) and vectored thrust (jet) increments have been separated from the measured data. The adjusted vector angles and the aerodynamic and jet vector angle contributions at subsonic/transonic speeds of the cruciform nozzle with two adjacent shroud flaps in the a position and the other two adjacent shroud flaps in position d have been calculated using the equations shown in figure 31(a) and are presented as a function of nozzle pressure ratio.

The adjusted pitch and yaw vector angles and vector angle increments are presented in figure 31(b) for the high and low altitude nozzle operating pressure ratios. The resulting calculated data indicate that positioning the flaps for vectoring in the cruciform shroud can produce significant forces away from the axial (thrust) direction at subsonic/transonic speeds, which can be utilized for vehicle control or maneuver. At the high altitude nozzle operating pressure ratios, nearly constant values of adjusted pitch and yaw thrust vector angle were calculated at Mach numbers from 0.60 to 1.25. These adjusted vector angles, which include the aerodynamic (external) effect of deflecting the flaps 9.26° in both the pitch and yaw planes, exceed the shroud flap geometric thrust vector angle by between 0.5° and 2.0° depending on Mach number. If the internal (jet) vector contributions to the adjusted vector angles are compared to the geometric vector angle they are found to be between 1.0° and 2.3° less than the 9.26° geometric vector angle, depending on Mach number, as might be expected due to jet turning losses. At the low altitude nozzle operating pressure ratios of the lower Mach numbers where the internal flow separates from the nozzle wall ahead of the flapped portion of the shroud, the adjusted and jet vector angles were more dependent on Mach number than was the case for the high altitude mission.

Conclusions

Investigations have been conducted in the Langley 16-Foot Transonic Tunnel (at Mach numbers from 0.60 to 1.25) and in the Langley Unitary Plan Wind Tunnel (at Mach numbers from 2.16 to 2.86) to determine the isolated

performance of several expendable nozzle concepts for nonaugmented turbojet powered supersonic applications. The effects of centerbody base shape, shroud length, shroud ventilation, cruciform shroud expansion ratio, and cruciform shroud flap vectoring were investigated. The results of the investigation indicate the following conclusions:

1. For those shroud configurations tested with both a concave and convex centerbody base the configurations with the concave centerbody base had a discharge coefficient that was about 0.02 higher at nozzle pressure ratios above 3.0. However, discharge coefficient for the concave base configurations dropped off between 0.03 and 0.05 at lower nozzle pressure ratios.

2. Ventilation of the overexpanded divergent shroud to the boattail (external) flow generally improved thrust-minus-drag performance at subsonic and transonic Mach numbers but decreased performance at Mach numbers above 1.25. The performance improvements were a result of earlier separation in the overexpanded shroud and an increased pressure in the separated region.

3. For nozzles having the same expansion ratio, the short, axially vented nozzle had the best thrust-minus-drag performance over the nozzle pressure ratio range at Mach numbers up to 0.95 but was approached in performance by other configurations at Mach numbers of 1.15 and 1.25. At Mach numbers above 1.25, the cruciform nozzle had the best thrust-minus-drag performance.

4. The nozzle with the cruciform shroud had the highest thrust-minus-drag ratios of all the nozzles at all Mach numbers when the flaps were positioned to give expansion ratios close to those required for fully expanded flow.

5. When the cruciform nozzle shroud flaps were positioned for combined pitch and yaw vectoring at subsonic and transonic speeds, significant aerodynamic and propulsive forces and moments were generated that may be utilized for vehicle control or maneuver.

Appendix A

Instrumentation and Calibration Accuracies

No documented uncertainty data were available for the model instrumentation and calibration standards at the time of these investigations. However the calibration standards were routinely checked as a standard practice and all the tunnel and model instrumentation were maintained to the same levels of accuracy as are currently used.

All the individual pressure transducers (housed outside the tunnel circuit) that measured internal model pressures were calibrated within specified accuracy ranges before each test using standard calibration equipment. Electronically scanning pressure modules (housed in the model forebody) were used to measure model external pressures and many of the internal pressures in low pressure regions. The dominant contributor to the accuracy of the electronically scanning pressure modules is the effect of test section temperature variation. As a tunnel run progressed, test section temperature changed with time or Mach number, especially in the 16FT TT. The modules were calibrated during the run as necessary, based on the comparison of known pressures that were monitored both by the electronic modules and accurate pressure transducers outside the tunnel circuit. The

estimated accuracy of the pressure measuring instrumentation attached to the various model orifices (as identified in the sketches of fig. 32) is presented in table 9.

The laboratory calibration of the force balance was used in the data reduction with various correction factors added to account for model installation and propulsion simulation system effects. There are two major contributors to the balance installation effects. One is the combined effect of flexing and pressurization of the metallic bellows that pass the high pressure air for the propulsion simulation system from the nonmetric to the metric portion of the model. The second is the restraint of pressure tubing crossing from the nonmetric portion of the model to the metric portion of the model. These effects were determined before each test by applying combinations of known loads to the model (jet-on and jet-off) with standard calibration nozzles installed in place of the test nozzles.

Estimates of the accuracy of the installed balance force and moment measurements are presented in table 10 along with uncertainty data for test section flow parameters and for parameters associated with the high pressure jet flow. The uncertainty data were estimated as the root-sum-square of the individual contributions with 95-percent confidence and were obtained from subsequent tests that used the same instrumentation.

Appendix B

Adjustments to Thrust-Minus-Drag Data

The thrust-minus-drag data presented in this report represent the performance of the entire metric portion of the model as installed in the wind tunnels with a force correction applied for the pressure differential between the pressures measured at the metric break and free-stream static pressure. If the data are needed as isolated nozzle-only performance data it can be adjusted by applying increments for the skin friction and pressure drag on that part of the metric afterbody forward of the nozzle connect station (Sta. 54.760).

The portion of the metric afterbody forward of the nozzle connect station is far enough ahead of the nozzle exit so that variation in nozzle pressure ratio has no measurable effect on the drag of that part of the afterbody. Since model angle of attack was not varied during the investigation, the pressure distribution over the boattailed portion of the model ahead of the nozzle connect station remained a constant for a given Mach number. Therefore, to represent the contribution of the portion of the metric afterbody forward of the customer connect station, a single value of skin friction drag and a single value of pressure drag

can be calculated for each free-stream Mach number.

The skin friction drag forward of the nozzle connect station was calculated using the approach of reference 10. The pressure drag of the boattailed portion of the afterbody forward of the nozzle connect station (see fig. 4(a)) was computed from static pressures measured on that portion of the afterbody. Eighteen pressure orifices were arranged in equal rows of six on the top, one side, and bottom of the boattail. Weighted axially projected areas were computed for each orifice for the pressure force computation. The boattail pressures used for this computation are not presented in this report.

The results of the friction and pressure drag computations are presented in figure 33 and have been ratioed to ideal thrust (F_i) so that they are in a nondimensional form compatible with the thrust-minus-drag ratio data of this report. Since the calculated drag contributions are a constant at each Mach number and are independent of the nozzle configuration installed, they have no effect on any of the conclusions drawn in the discussion of this report when the various nozzles are compared. Application of the computed friction and pressure drag to obtain isolated nozzle-only data affects only the level of performance at a given Mach number and nozzle pressure ratio.

References

1. Capone, Francis J.; Bangert, Linda S.; Asbury, Scott C.; Mills, Charles T. L.; and Bare, E. Ann: *The NASA Langley 16-Foot Transonic Tunnel Historical Overview, Facility Description, Calibration, Flow Capabilities, and Test Capabilities*. NASA TP-3521, 1995.
2. Jackson, Charlie M., Jr.; Corlett, William A.; and Monta, William J.: *Description and Calibration of the Langley Unitary Plan Wind Tunnel*. NASA TP-1905, 1981.
3. Baker, V. D.; Kwon, O.; Vittal, B. V. R.; and McKain, T. F.: *Expendable Supersonic Exhaust Nozzle Concepts*. AIAA-89-2927, July 1989.
4. Kuchar, A. P.: *Variable Convergent-Divergent Exhaust Nozzle Aerodynamics. Aerothermodynamics of Gas Turbine Engines*, AFAPL-TR-78-52, U.S. Air Force, 1978, Ch. 14.
5. Leavitt, Laurence D.; and Bangert, Linda S.: *Performance Characteristics of Axisymmetric Convergent-Divergent Exhaust Nozzles With Longitudinal Slots in the Divergent Flaps*. NASA TP-2013, 1982.
6. Staff of Propulsion Aerodynamics Branch: *A User's Guide to the Langley 16-Foot Transonic Tunnel Complex, Revision 1*. NASA TM-102750, 1990. (Supersedes NASA TM-83186, compiled by Kathryn H. Peddrew, 1981.)
7. Mercer, Charles E.; Berrier, Bobby L.; Capone, Francis J.; and Grayston, Alan M.: *Data Reduction Formulas for the 16-Foot Transonic Tunnel, NASA Langley Research Center, Revision 2*. NASA TM-107646, 1992. (Supersedes NASA TM-86319, Rev. 1.)
8. Wing, David J.; and Asbury, Scott C.: *Static Performance of a Cruciform Nozzle With Multiaxis Thrust-Vectoring and Reverse-Thrust Capabilities*. NASA TP-3188, 1992.
9. Re, Richard J.; and Leavitt, Laurence D.: *Static Internal Performance Including Thrust Vectoring and Reversing of Two-Dimensional Convergent-Divergent Nozzles*. NASA TP-2253, 1984.
10. Frankl, F.; and Voishel, V.: *Friction in the Turbulent Boundary Layer of a Compressible Gas at High Speeds*. NACA TM 1032, 1942.

Table 1. Nominal Free-Stream Test Conditions

M	Facility	$p_{t,\infty}$, psi	p_∞ , psi	q_∞ , psi	$T_{t,\infty}$, °R	R_N
0.0	16FT TT	14.7	14.7		Atm.	
0.0	UPWT	0.6 to 1.3	0.6 to 1.3		525 to 555	
.60	16FT TT	14.7	11.54	2.93	556 to 595	3.0×10^6 to 3.3×10^6
.80			9.67	4.33	582 to 620	3.5×10^6 to 3.8×10^6
.90			8.72	4.95	588 to 626	3.6×10^6 to 3.9×10^6
.95			8.25	5.21	582 to 629	3.6×10^6 to 4.0×10^6
1.15			6.48	6.00	607 to 635	3.7×10^6 to 4.0×10^6
1.25			5.69	6.22	598 to 637	3.7×10^6 to 4.1×10^6
2.16	UPWT	9.4	.93	3.04	582 to 588	2.0×10^6
2.50		11.1	.65	2.85	584 to 590	
2.86		13.4	.46	2.60	584 to 588	

Table 2. Internal Geometry of Long Unvented Shroud

x/d_{nc}	r/d_{nc}	x/d_{nc}	r/d_{nc}	x/d_{nc}	r/d_{nc}
0	0.44555	0.20278	0.36233	0.46564	0.35951
.00745	.44537	.20408	.36157	.47027	.36116
.01488	.44491	.20587	.36054	.47431	.36262
.02232	.44424	.20704	.35985	.48238	.36540
.02973	.44319	.20892	.35876	.49099	.36829
.03712	.44183	.21077	.35769	.50015	.37132
.04450	.44029	.21194	.35701	.50988	.37446
.05185	.43847	.21332	.35623	.52020	.37776
.05919	.43643	.21492	.35531	.53112	.38113
.06653	.43420	.21677	.35425	.54269	.38455
.07388	.43175	.21893	.35300	.55488	.38798
.08123	.42909	.22143	.35158	.56774	.39143
.08860	.42621	.22431	.34993	.58127	.39482
.09599	.42308	.22764	.34803	.59544	.39806
.10341	.41972	.23144	.34587	.61020	.40155
.11087	.41610	.23579	.34339	.62557	.40505
.11829	.41224	.24072	.34059	.64151	.40864
.12197	.41006	.24629	.33742	.65798	.41231
.12565	.40790	.25250	.33386	.67496	.41601
.12933	.40573	.25941	.32986	.69241	.41980
.13301	.40355	.26705	.32547	.71031	.42348
.13668	.40139	.27545	.32079	.72862	.42711
.14036	.39922	.28492	.31644	.74720	.43094
.14404	.39704	.29547	.31283	.76604	.43482
.14772	.39487	.30707	.31061	.78513	.43856
.15139	.39269	.31938	.30974	.80434	.44226
.15508	.39051	.33212	.31048	.82362	.44603
.15875	.38835	.34494	.31284		
.16243	.38618	.35753	.31660		
.16610	.38400	.36968	.32134		
.16978	.38183	.38136	.32650		
.17345	.37965	.39257	.33168		
.17714	.37748	.40337	.33637		
.18081	.37530	.41364	.34057		
.18585	.37230	.42326	.34435		
.18810	.37098	.43217	.34771		
.19262	.36830	.44035	.35068		
.19617	.36620	.44777	.35331		
.19893	.36458	.45442	.35565		
.20111	.36332	.46039	.35766		

Table 3. Internal Geometry of Short Unvented Shroud

x/d_{nc}	r/d_{nc}	x/d_{nc}	r/d_{nc}	x/d_{nc}	r/d_{nc}	x/d_{nc}	r/d_{nc}
0	0.44555	0.20278	0.36233	0.33070	0.32643	0.48255	0.41814
.00745	.44537	.20408	.36157	.33449	.32939	.48634	.41928
.01488	.44491	.20587	.36054	.33830	.33236	.49015	.42038
.02232	.44424	.20704	.35985	.34208	.33532	.49393	.42141
.02973	.44319	.20892	.35876	.34589	.33830	.49774	.42240
.03712	.44183	.21077	.35769	.34967	.34125	.50152	.42334
.04450	.44029	.21194	.35701	.35348	.34423	.50533	.42422
.05185	.43847	.21332	.35623	.35728	.34719	.50913	.42507
.05919	.43643	.21492	.35531	.36107	.35015	.51292	.42587
.06653	.43420	.21677	.35425	.36487	.35312	.51672	.42684
.07388	.43175	.21893	.35300	.36866	.35608	.52051	.42758
.08123	.42909	.22143	.35158	.37246	.35906	.52431	.42832
.08860	.42621	.22431	.34993	.37625	.36202	.52810	.42906
.09599	.42308	.22764	.34803	.38005	.36499	.53190	.42980
.10341	.41972	.23144	.34587	.38384	.36761	.53569	.43054
.11087	.41610	.23579	.34339	.38764	.37044	.53949	.43128
.11829	.41224	.23960	.34123	.39145	.37319	.54330	.43202
.12197	.41006	.24339	.33905	.39524	.37585	.54708	.43275
.12565	.40790	.24719	.33689	.39904	.37843	.55089	.43349
.12933	.40573	.25098	.33473	.40283	.38093	.55468	.43423
.13301	.40355	.25478	.33255	.40663	.38335	.55848	.43497
.13668	.40139	.25857	.33039	.41042	.38571	.56227	.43571
.14036	.39922	.26237	.32823	.41422	.38798	.56607	.43645
.14404	.39704	.26616	.32606	.41801	.39019	.56986	.43719
.14772	.39487	.26996	.32390	.42181	.39232	.57366	.43791
.15139	.39269	.27375	.32174	.42560	.39439	.57745	.43865
.15508	.39051	.27755	.31956	.42940	.39640	.58125	.43939
.15875	.38835	.28136	.31740	.43321	.39834	.58505	.44013
.16243	.38618	.28514	.31524	.43699	.40021	.58884	.44087
.16610	.38400	.28895	.31307	.44080	.40203	.59265	.44161
.16978	.38183	.29273	.31126	.44458	.40377	.59643	.44235
.17345	.37965	.29654	.31018	.44839	.40547	.60024	.44309
.17714	.37748	.30033	.30975	.45218	.40710	.60402	.44381
.18081	.37530	.30413	.30993	.45598	.40867	.60783	.44455
.18585	.37230	.30792	.31073	.45977	.41020	.61162	.44529
.18810	.37098	.31172	.31222	.46357	.41166	.61542	.44603
.19262	.36830	.31552	.31456	.46737	.41307		
.19617	.36620	.31931	.31753	.47116	.41441		
.19893	.36458	.32311	.32049	.47496	.41571		
.20111	.36332	.32690	.32345	.47875	.41696		

Table 4. Geometry of Annular Vented Shroud

(a) Forward component of shroud

Forward shroud internal flow path				Boattail and passage inner wall			
x/d_{nc}	r/d_{nc}	x/d_{nc}	r/d_{nc}	x/d_{nc}	r/d_{nc}	x/d_{nc}	r/d_{nc}
0	0.44555	0.21492	0.35531	0	0.50000	0.36240	0.39451
.00745	.44537	.21677	.35425	.00755	.49956	.36996	.39146
.01488	.44491	.21893	.35300	.01510	.49904	.37751	.38841
.02232	.44424	.22143	.35158	.02265	.49845	.38505	.38535
.02973	.44319	.22431	.34993	.03020	.49775	.39260	.38230
.03712	.44183	.22764	.34803	.03775	.49700	.40016	.37925
.04450	.44029	.23144	.34587	.04530	.49614	.40771	.37621
.05185	.43847	.23579	.34339	.05285	.49521	.41526	.37316
.05919	.43643	.24072	.34059	.06040	.49418	.42280	.37011
.06653	.43420	.24629	.33742	.06795	.49309	.43036	.36706
.07388	.43175	.25250	.33386	.07550	.49191	.43791	.36400
.08123	.42909	.25941	.32986	.08305	.49063	.44546	.36095
.08860	.42621	.26705	.32547	.09060	.48927	.45300	.35790
.09599	.42308	.27545	.32079	.09815	.48782		
.10341	.41972	.28492	.31644	.10570	.48630		
.11087	.41610	.29547	.31283	.11325	.48467		
.11829	.41224	.30707	.31061	.12080	.48297		
.12197	.41006	.31938	.30974	.12835	.48118		
.12565	.40790	.33212	.31048	.13590	.47930		
.12933	.40573	.34494	.31284	.14345	.47732		
.13301	.40355	.35753	.31660	.15101	.47526		
.13668	.40139	.36968	.32134	.15855	.47310		
.14036	.39922	.38136	.32650	.16610	.47085		
.14404	.39704	.39257	.33168	.17366	.46851		
.14772	.39487	.40337	.33637	.18121	.46607		
.15139	.39269	.41364	.34057	.18875	.46354		
.15508	.39051	.42326	.34435	.19630	.46092		
.15875	.38835	.43217	.34771	.20385	.45818		
.16243	.38618	.44035	.35068	.21141	.45537		
.16610	.38400	.44777	.35331	.21896	.45244		
.16978	.38183			.22650	.44942		
.17345	.37965			.23405	.44636		
.17714	.37748			.24161	.44331		
.18081	.37530			.24916	.44026		
.18585	.37230			.25670	.43722		
.18810	.37098			.26425	.43417		
.19262	.36830			.27181	.43112		
.19617	.36620			.27936	.42807		
.19893	.36458			.28690	.42501		
.20111	.36332			.29445	.42196		
.20278	.36233			.30201	.41891		
.20408	.36157			.30956	.41586		
.20587	.36054			.31711	.41281		
.20704	.35985			.32465	.40977		
.20892	.35876			.33221	.40670		
.21077	.35769			.33976	.40365		
.21194	.35701			.34731	.40061		
.21332	.35623			.35485	.39756		

Table 4. Concluded

(b) Aft component of shroud

Passage outer wall and shroud internal flow path				Aft shroud boattail			
x/d_{nc}	r/d_{nc}	x/d_{nc}	r/d_{nc}	x/d_{nc}	r/d_{nc}	x/d_{nc}	r/d_{nc}
0.18562	0.48735	0.52345	0.38933	0.18613	0.49025	0.71737	0.46240
.19256	.48516	.52946	.39096	.19676	.48969	.72800	.46185
.19951	.48289	.53545	.39256	.20738	.48914	.73862	.46129
.20645	.48056	.54146	.39411	.21801	.48858	.74925	.46073
.21339	.47814	.54747	.39563	.22863	.48801	.75987	.46018
.22035	.47566	.55346	.39711	.23926	.48747	.77049	.45962
.22729	.47308	.55947	.39854	.24988	.48690	.78112	.45907
.23423	.47045	.56548	.39991	.26051	.48634	.79174	.45851
.24118	.46779	.57147	.40126	.27113	.48579	.80237	.45795
.24812	.46512	.57748	.40260	.28175	.48523	.81299	.45740
.25506	.46246	.58349	.40391	.29238	.48467	.82362	.45684
.26202	.45981	.58949	.40513	.30300	.48412		
.26896	.45715	.59549	.40633	.31363	.48356		
.27590	.45450	.60149	.40750	.32425	.48301		
.28285	.45185	.60750	.40867	.33488	.48245		
.28979	.44920	.61350	.40984	.34550	.48189		
.29673	.44655	.61950	.41101	.35613	.48134		
.30368	.44390	.62551	.41218	.36675	.48078		
.31062	.44125	.63150	.41335	.37737	.48022		
.31756	.43862	.63751	.41450	.38800	.47967		
.32452	.43597	.64352	.41563	.39862	.47911		
.33146	.43334	.64953	.41675	.40925	.47856		
.33841	.43070	.65552	.41786	.41987	.47800		
.34535	.42807	.66153	.41897	.43050	.47743		
.35229	.42544	.66753	.42008	.44112	.47689		
.35925	.42282	.67353	.42117	.45175	.47632		
.36619	.42018	.67954	.42224	.46237	.47576		
.37313	.41756	.68554	.42329	.47299	.47521		
.38008	.41493	.69155	.42434	.48362	.47465		
.38702	.41231	.69754	.42538	.49424	.47410		
.39396	.40969	.70355	.42643	.50487	.47354		
.40092	.40709	.70956	.42752	.51549	.47298		
.40786	.40447	.71555	.42860	.52612	.47243		
.41480	.40186	.72156	.42961	.53674	.47187		
.42175	.39926	.72757	.43056	.54737	.47131		
.42869	.39664	.73356	.43152	.55799	.47076		
.43563	.39405	.74558	.43254	.56861	.47020		
.44259	.39145	.75158	.43452	.57925	.46964		
.44953	.38884	.75758	.43550	.58988	.46909		
.45647	.38625	.76358	.43648	.60050	.46853		
.46342	.38366	.76959	.43742	.61113	.46798		
.46941	.38177	.77558	.43838	.62175	.46742		
.47542	.38048	.78159	.43936	.63238	.46685		
.48143	.37986	.78760	.44035	.64300	.46631		
.48744	.37989	.79359	.44134	.65363	.46574		
.49343	.38053	.79960	.44235	.66425	.46518		
.49944	.38214	.80561	.44334	.67487	.46463		
.50545	.38402	.81162	.44429	.68550	.46407		
.51144	.38588	.81761	.44518	.69612	.46352		
.51745	.38764	.82362	.44603	.70675	.46296		

Table 5. Centerbody Coordinates

x/d_{nc}	r/r_{\max}	x/d_{nc}	r/r_{\max}	x/d_{nc}	r/r_{\max}
Centerbody					
0	1.0	0.04439	0.97321	0.08878	0.89859
.00370	.99955	.04809	.96839	.09248	.89201
.00740	.99905	.05179	.96308	.09618	.88547
.01110	.99818	.05549	.95731	.09988	.87893
.01480	.99691	.05919	.95100	.10358	.87234
.01850	.99532	.06289	.94446	.10728	.86580
.02220	.99332	.06659	.93792	.11098	.85926
.02590	.99096	.07029	.93134	.11468	.85268
.02959	.98824	.07399	.92480	.11838	.84614
.03329	.98510	.07769	.91826	.12208	.83960
.03699	.98156	.08139	.91167	.12726	.83043
.04069	.97761	.08508	.90513		
Concave base					
0.09037	0	0.08374	0.61285	0.11880	0.79905
.08227	.05604	.08779	.63951	.12012	.80418
.07507	.11257	.09158	.66344	.12129	.80863
.06874	.16886	.09514	.68483	.12232	.81258
.06435	.22512	.09846	.70386	.12324	.81599
.06155	.28025	.10157	.72066	.12405	.81894
.06046	.33350	.10445	.73551	.12477	.82157
.06106	.38411	.10712	.74859	.12540	.82384
.06351	.43128	.10957	.76004	.12596	.82584
.06668	.47493	.11181	.77003	.12645	.82757
.07043	.51490	.11385	.77879	.12688	.82911
.07472	.55109	.11568	.78647	.12726	.83043
.07934	.58347	.11733	.79319		
Convex base					
0.12726	0.83043	0.19236	0.67443	0.25747	0.42206
.13022	.82539	.19532	.66521	.26043	.40850
.13318	.81998	.19828	.65577	.26339	.39469
.13613	.81421	.20124	.64605	.26635	.38056
.13909	.80831	.20420	.63610	.26931	.36609
.14205	.80223	.20716	.62589	.27227	.35127
.14501	.79600	.21012	.61535	.27523	.33611
.14797	.78969	.21308	.60459	.27819	.32059
.15093	.78338	.21604	.59360	.28115	.30473
.15389	.77698	.21900	.58243	.28411	.28867
.15685	.77044	.22196	.57112	.28707	.27235
.15981	.76371	.22492	.55967	.29003	.25545
.16277	.75663	.22788	.54805	.29299	.23765
.16573	.74923	.23084	.53629	.29595	.21863
.16869	.74151	.23380	.52434	.29891	.19815
.17165	.73356	.23676	.51222	.30186	.17525
.17461	.72543	.23972	.49986	.30482	.14857
.17757	.71721	.24268	.48733	.30778	.12008
.18053	.70895	.24563	.47457	.31074	.07454
.18349	.70059	.24859	.46167	.31225	0
.18645	.69210	.25155	.44861		
.18941	.68338	.25451	.43541		

Table 6. Long and Short Shroud Pressure
Orifice Locations

ϕ , deg	Long shroud x/d_{nc}	Short shroud x/d_{nc}
Internal pressure orifice locations		
55	0	0
76	.0923	.0923
84	.1848	.1848
96	.2307	.2307
104	.2773	.2773
125	.3192	.3001
129	.3579	.3244
141	.3967	.3486
170	.4355	.3727
186	.4744	.3970
190	.5132	.4213
215	.5519	.4455
219	.5907	.4698
231	.6295	.4941
235	.6682	.5183
256	.7070	.5425
264	.7459	.5667
276	.7847	.5910
284	.8087	.6005
174	.8235 TE	.6153 TE
354	.8235 TE	.6153 TE
External pressure orifice locations		
305	0.0087	0.0087
309	.0923	.0923
321	.1848	.1848
325	.3579	.3232
346	.5907	.4617
350	.8087	.6005

Table 7. Annular Vented Shroud Pressure Orifice Locations

ϕ , deg	x/d_{nc}	Surface
14	0.18645	Inner, forward shroud
35	.23084	
39	.27523	
84	.31933	
96	.36372	
141	.40811	
170	.44407	
215	0	Outer, forward shroud
219	.09086	
264	.18112	
276	.27168	
321	.36224	
6	0.23650	Inner, aft shroud
10	.32021	
51	.41048	
55	.48935	
76	.52131	
104	.55460	
125	.59692	
129	.64220	
186	.68955	
190	.73247	
231	.78100	
235	.81651	
256	0.81651	Outer, aft shroud
284	.51228	
305	.29195	
309	.20154	
174	0.82376	Trailing edge, aft shroud
354	.82376	

Table 8. Centerbody Pressure Orifice
Radial Locations

ϕ , deg	r/r_{\max}
0	0
	.2398
	.4155
	.5363
	.6344
	.7193
352	0.7952
20	.8760
340	.9605
8	1.0

Table 9. Accuracy of Pressure Transducers Connected to Model Orifices

Pressure transducer accuracy, psi, atN		
Orifice	$M = 0$ (at low nozzle pressure ratios) and 0.60 to 1.25	$M = 0$ (at high nozzle pressure ratios) and 2.16 to 2.86
1,2	-0.263	-0.175
3,4	-0.175	-0.175
5	-0.175	-0.088
6 to 27	-0.018	-0.018
28 to 31	-0.175	-0.018
32	-0.018	-0.088
33	-0.263	-0.175
34 to 37	-0.350	-0.175
38 to 43	-0.018	
44,45	-0.263	-0.175
46	-0.350	-0.088
47,48	-0.263	-0.175
49 to 58	-0.018	-0.018
59	-0.350	-0.175
60	-0.263	-0.175
61	-0.263	-0.088
62 to 73	-0.018	-0.018

Table 10. Force Balance Accuracy and Tunnel
Parameter Uncertainties

(a) Accuracy

Balance component	Accuracy
NF	± 2.46 lb
AF	± 3.12 lb
PM	± 25.1 in-lb
YM	± 18.1 in-lb
SF	± 2.46 lb

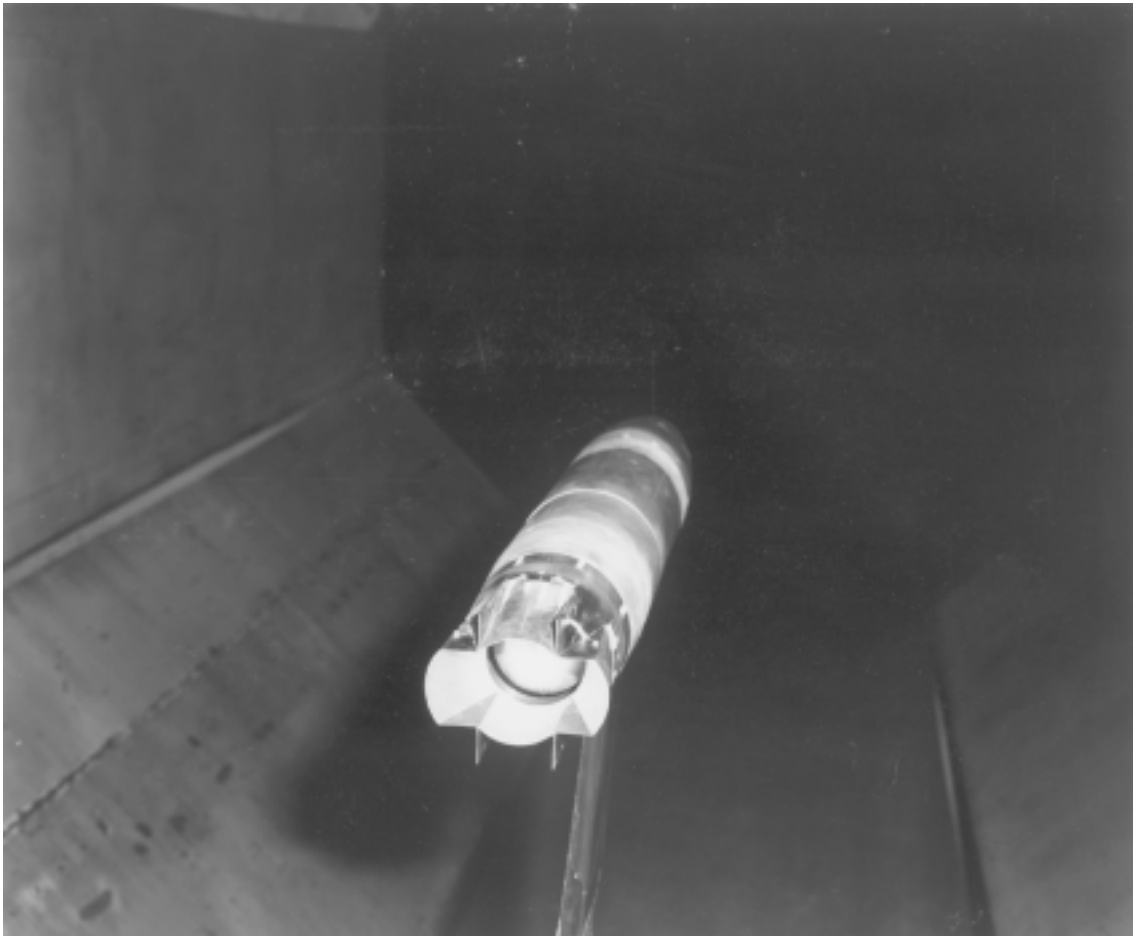
(b) Uncertainties

Facility	$(p_{t,j})_{\text{un}}, \text{psi}$	$(p_{\infty})_{\text{un}}, \text{psi}$	$(p_{\infty})_{\text{un}}, \text{psi}$	$(w_p/w_i)_{\text{un}}$	$(F/F_i)_{\text{un}}$
16FT TT	± 0.253	± 0.005	± 0.005	± 0.003	± 0.006
UPWT	± 0.131	± 0.009	± 0.009	± 0.003	± 0.006



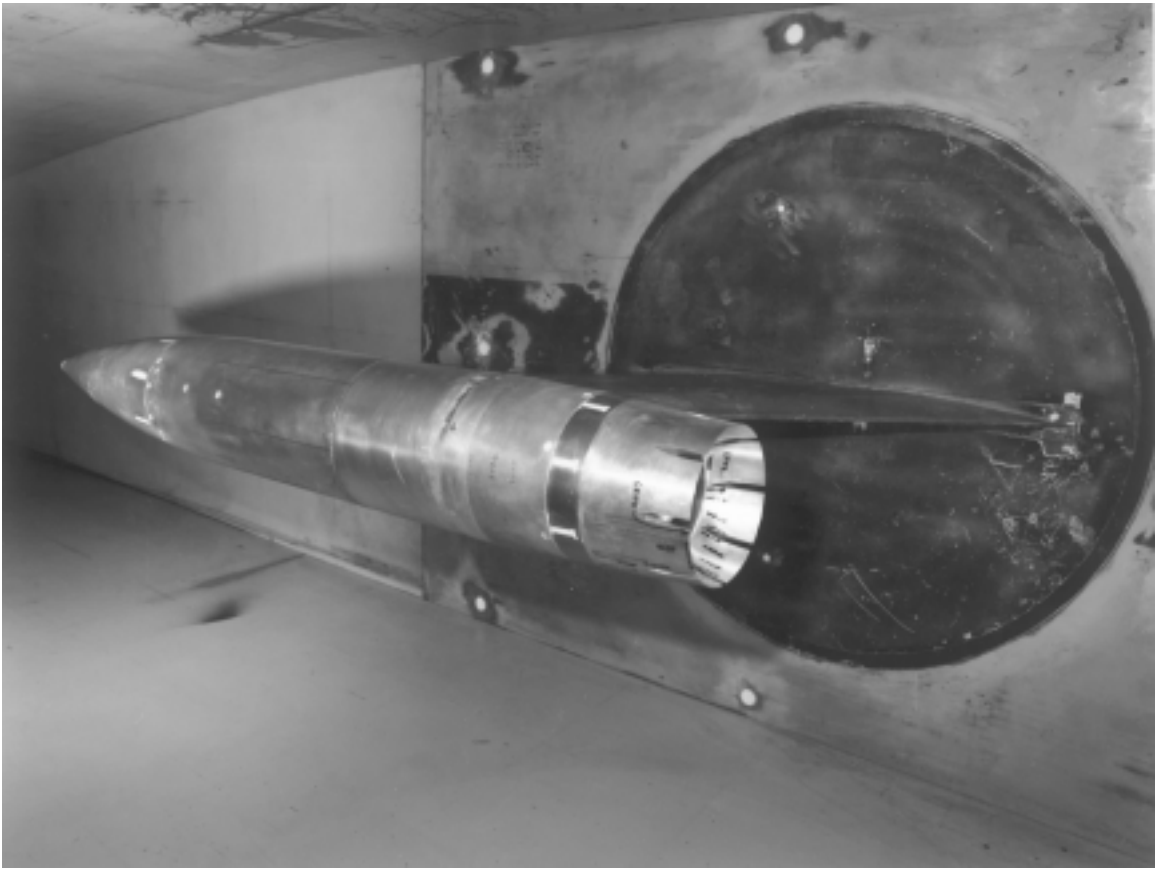
(a) View of model with cruciform shroud installed in 16-Foot Transonic Tunnel test section (top removed).

Figure 1. Photographs showing model installations in Langley 16-Foot Transonic Tunnel and Langley Unitary Plan Wind Tunnel.



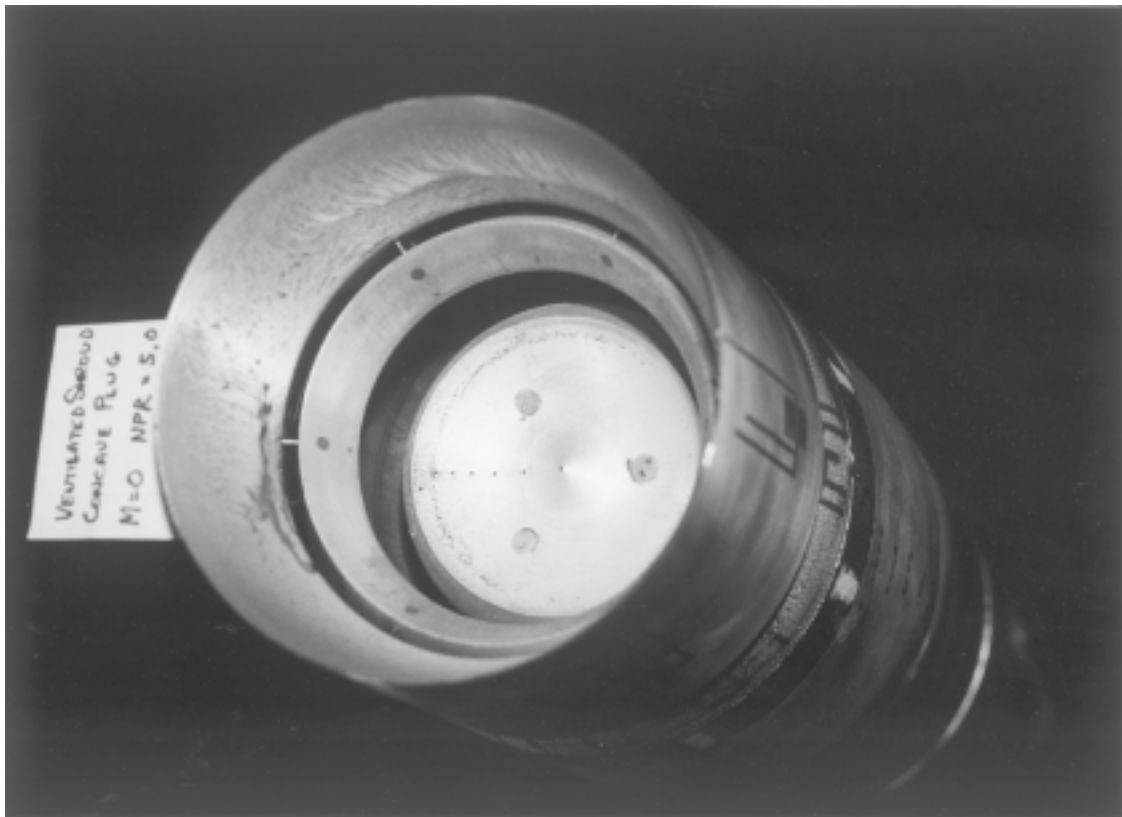
(b) Closeup of cruciform nozzle with one pair of opposite flaps in position a and other pair of opposite flaps in position d.

Figure 1. Continued.



(c) Model with long axially vented shroud mounted from test section sidewall of Unitary Plan Wind Tunnel.

Figure 1. Continued



(d) Closeup of annularly vented nozzle mounted on test pod.

Figure 1. Concluded.

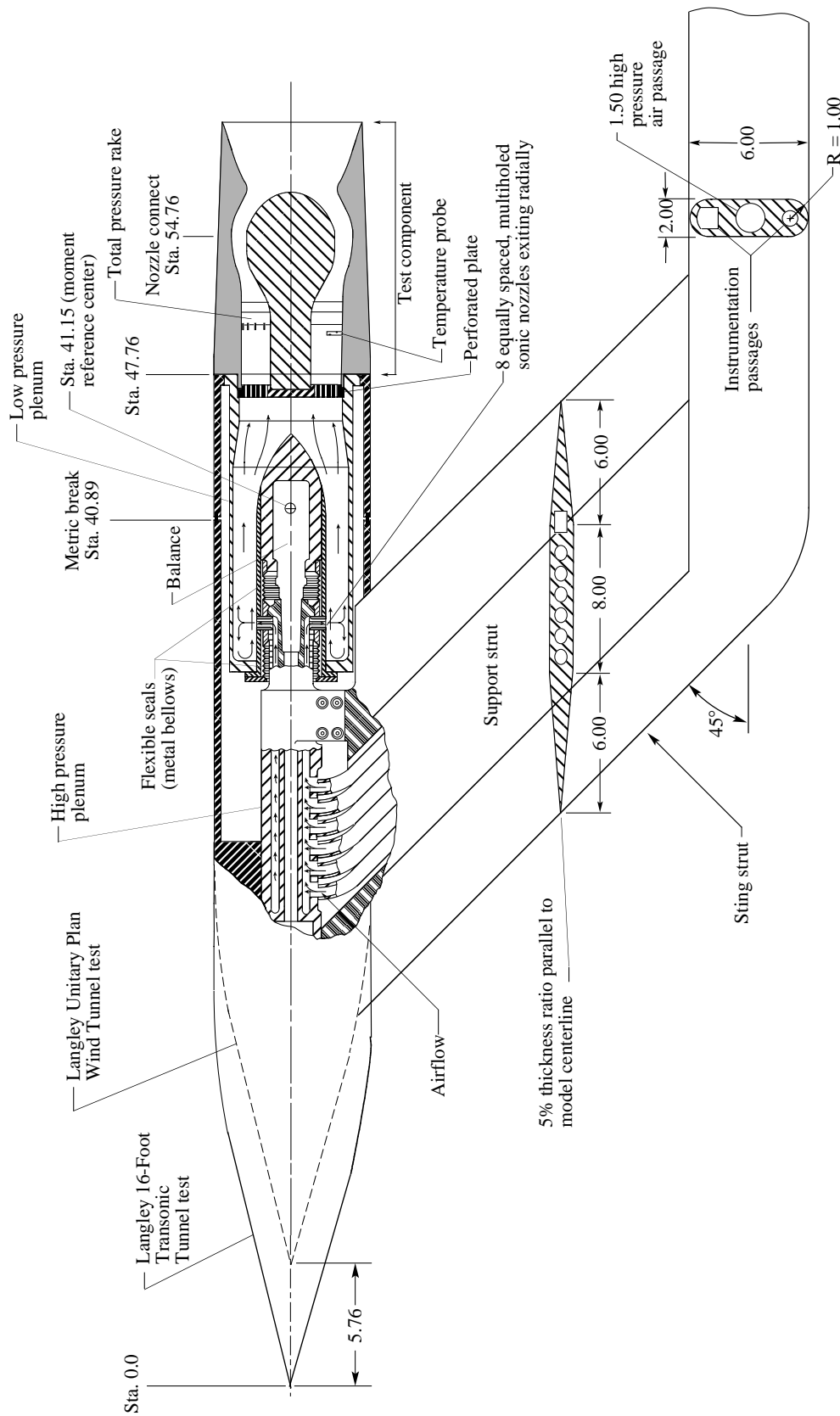


Figure 2. Sketch showing typical test nozzle mounted on single-engine propulsion simulator. All dimensions are referenced to nose used during 16-Foot Transonic Tunnel tests (long nose) and are in inches unless otherwise noted.

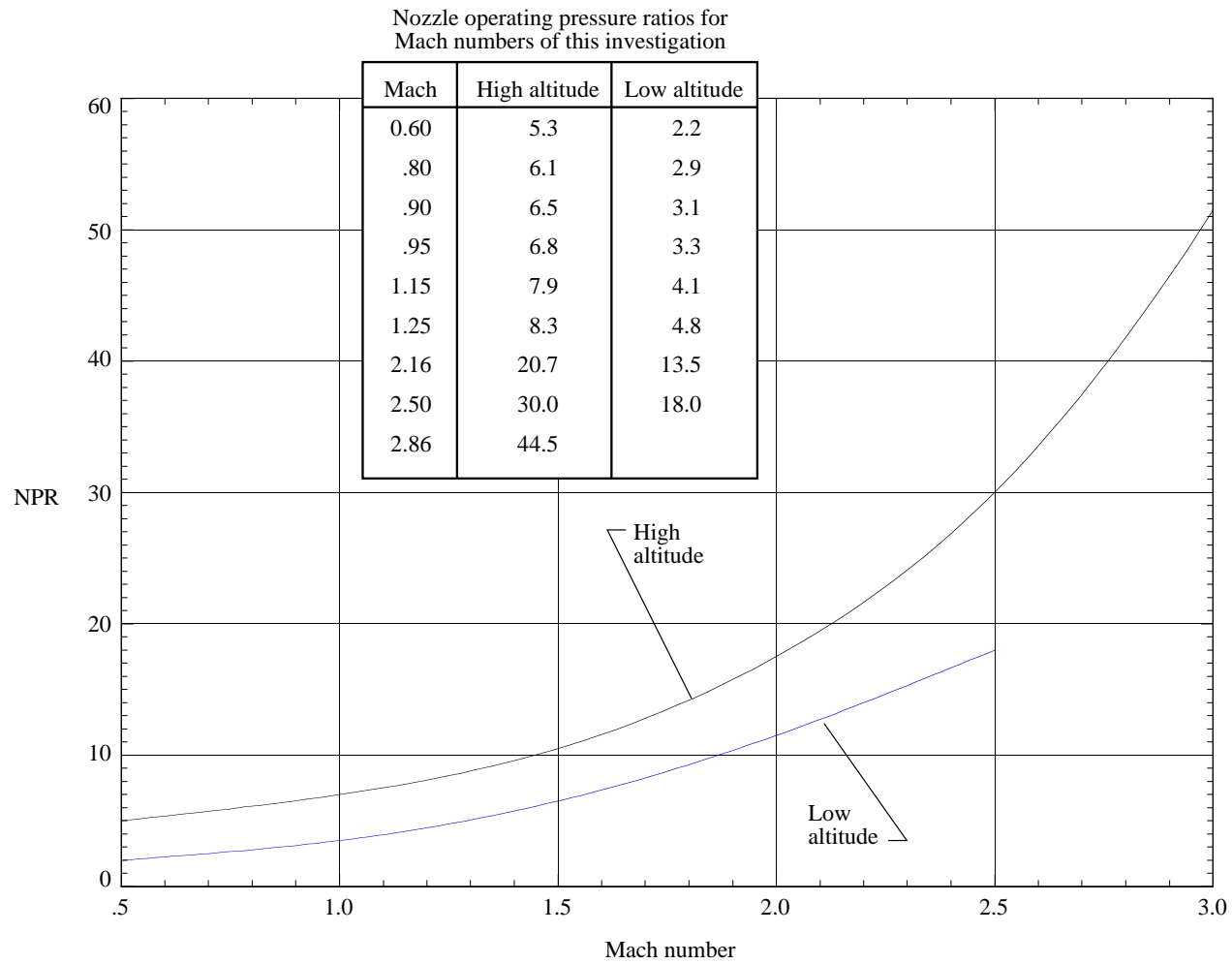
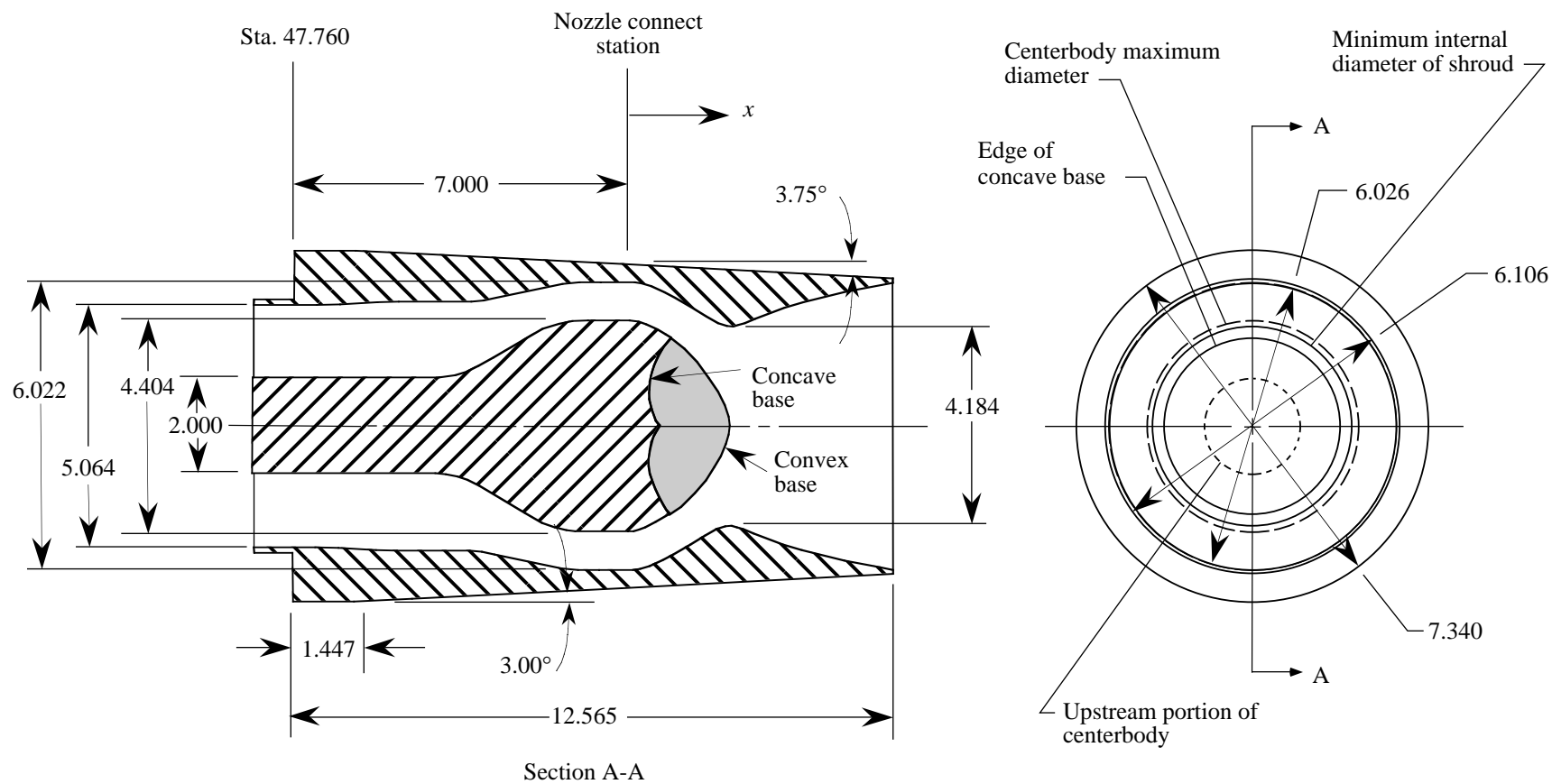
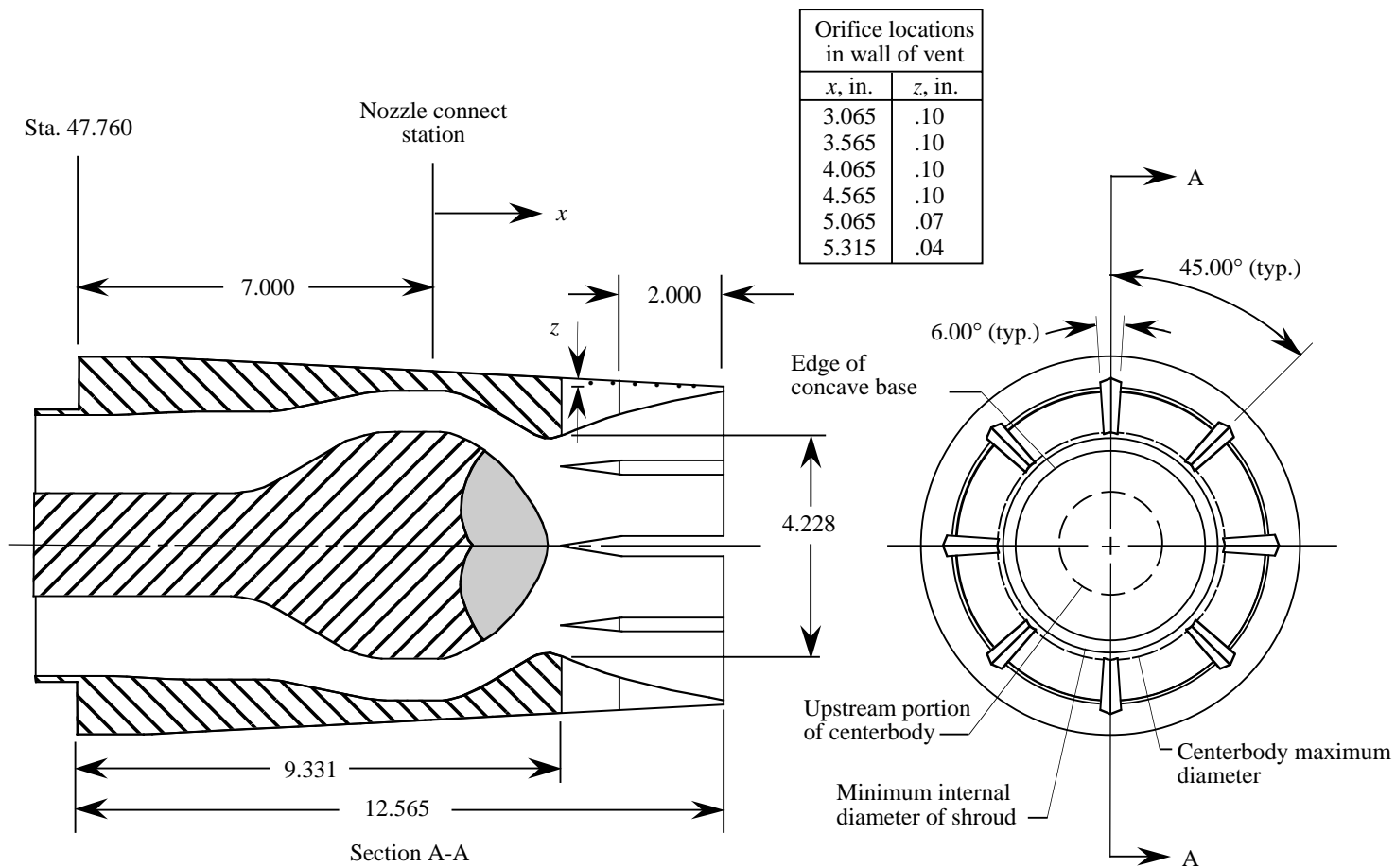


Figure 3. Nozzle operating pressure ratios over range of Mach numbers for high and low altitudes.



(a) Unvented long shroud nozzle.

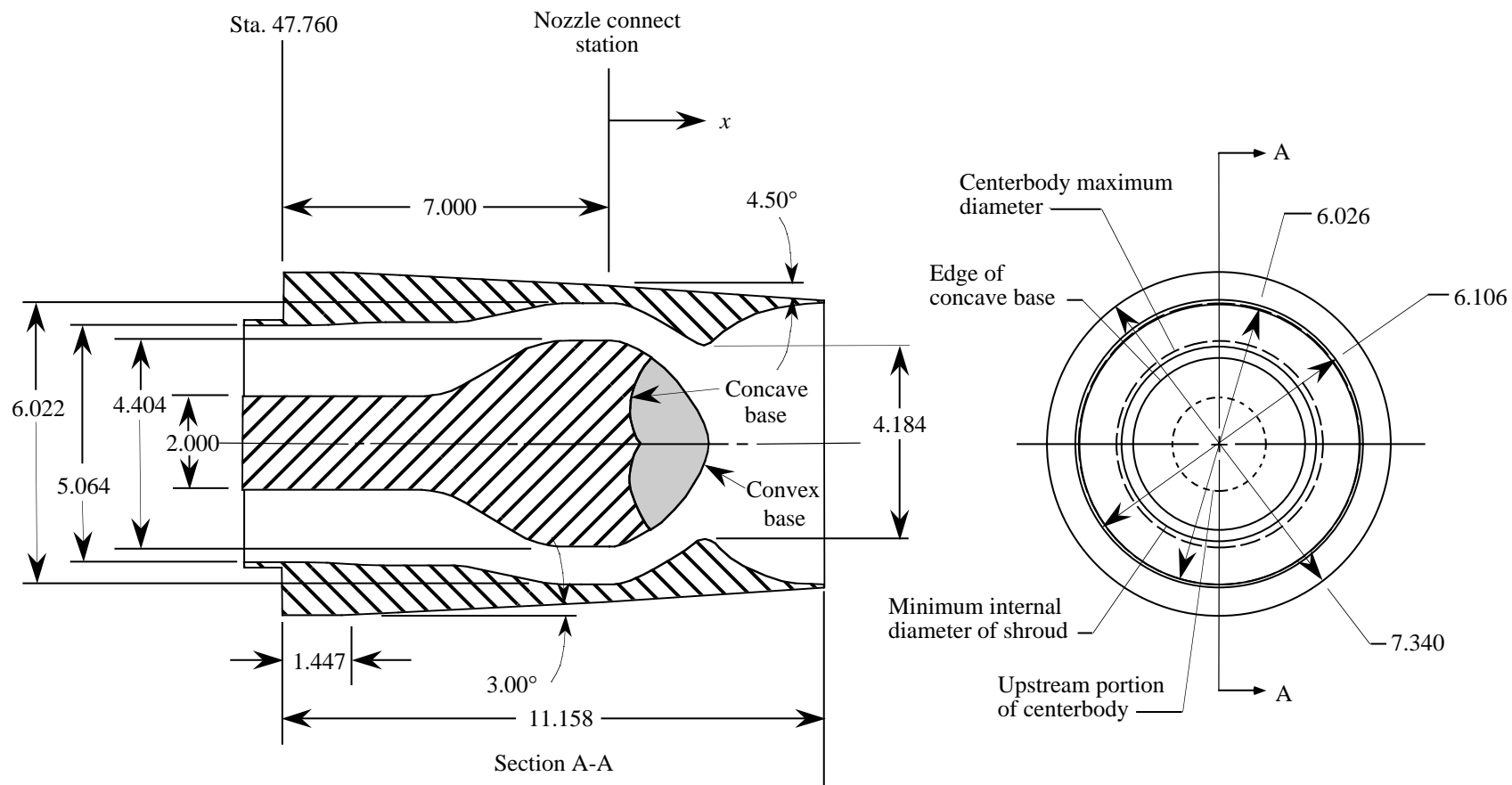
Figure 4. Sketches showing nozzle geometries with centerbody support struts and mass flow instrumentation omitted. All dimensions are in inches unless otherwise indicated.



Note: All other dimensions identical to long shroud nozzle shown in figure 4(a).

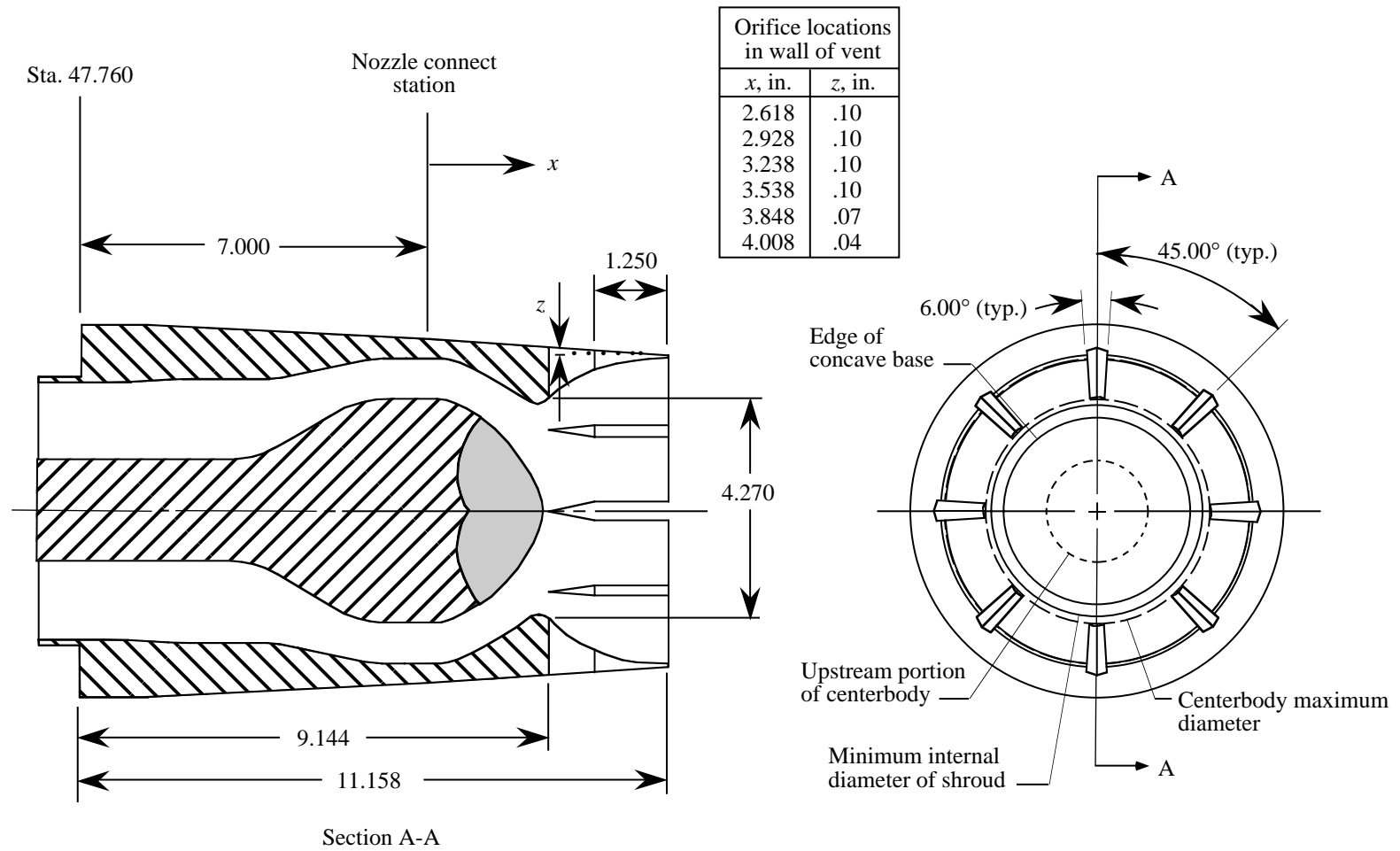
(b) Axially vented long shroud nozzle.

Figure 4. Continued.



(c) Unvented short shroud nozzle.

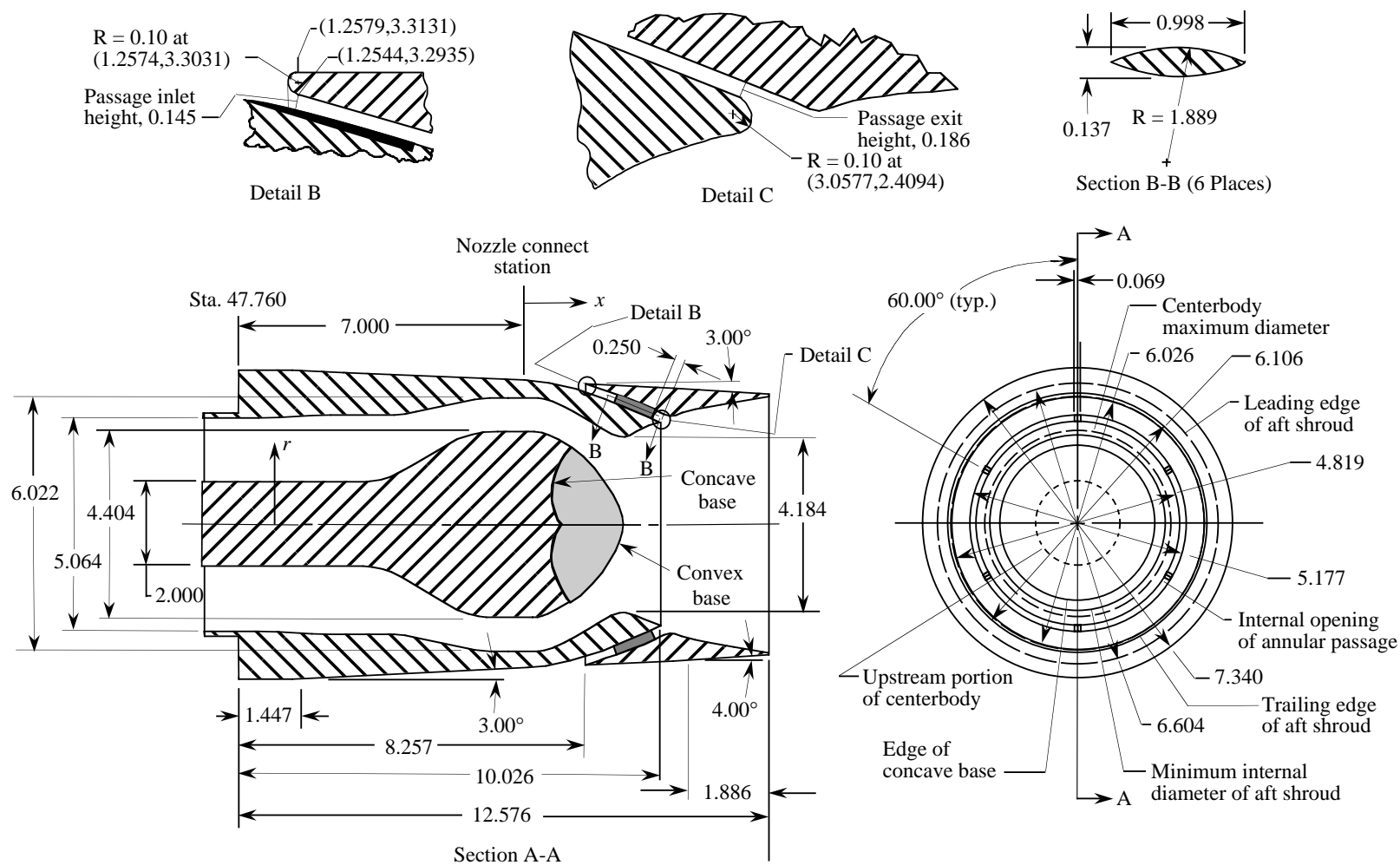
Figure 4. Continued.



Note: All other dimensions are identical to short shroud nozzle shown in figure 4(c).

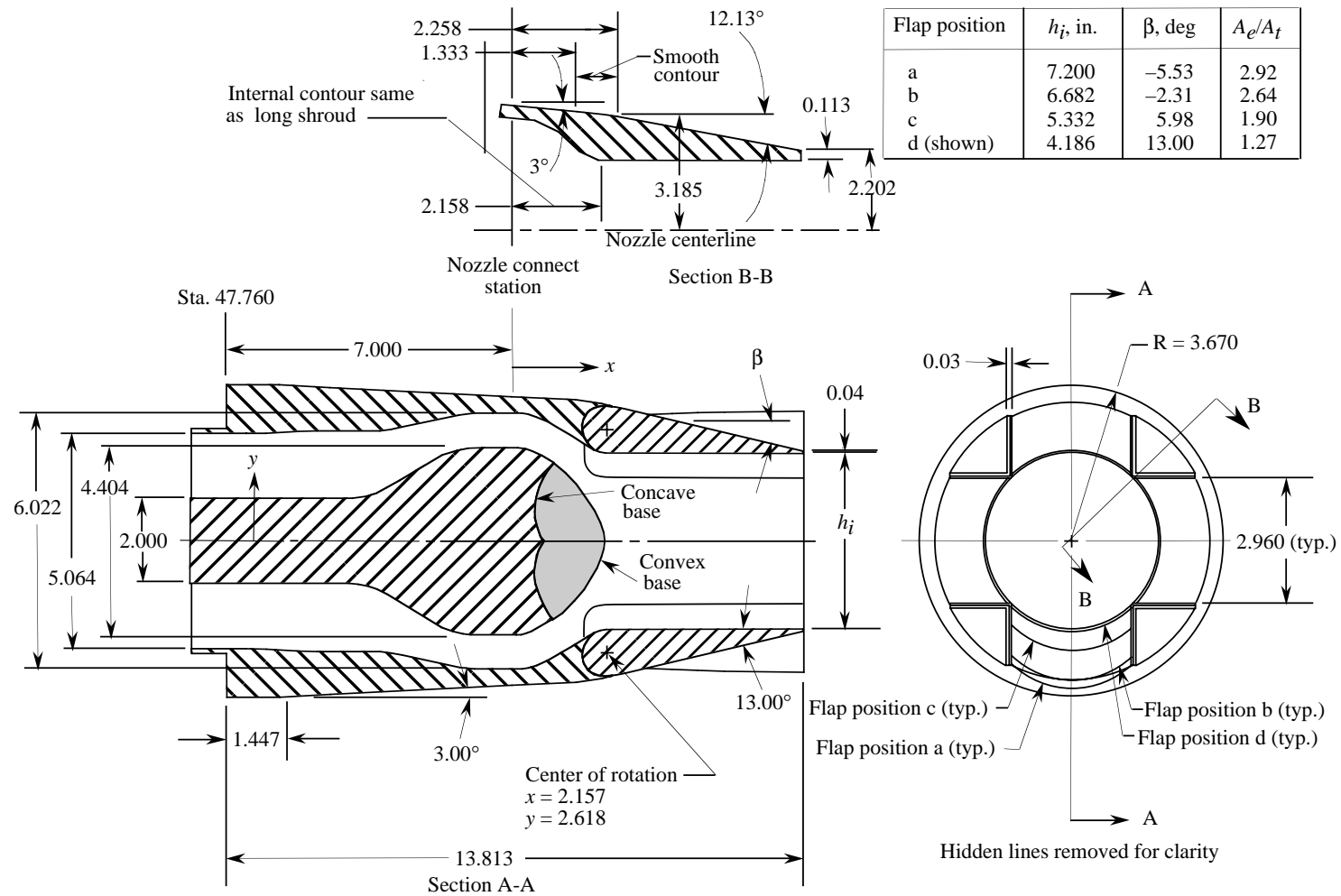
(d) Axially vented short shroud nozzle.

Figure 4. Continued



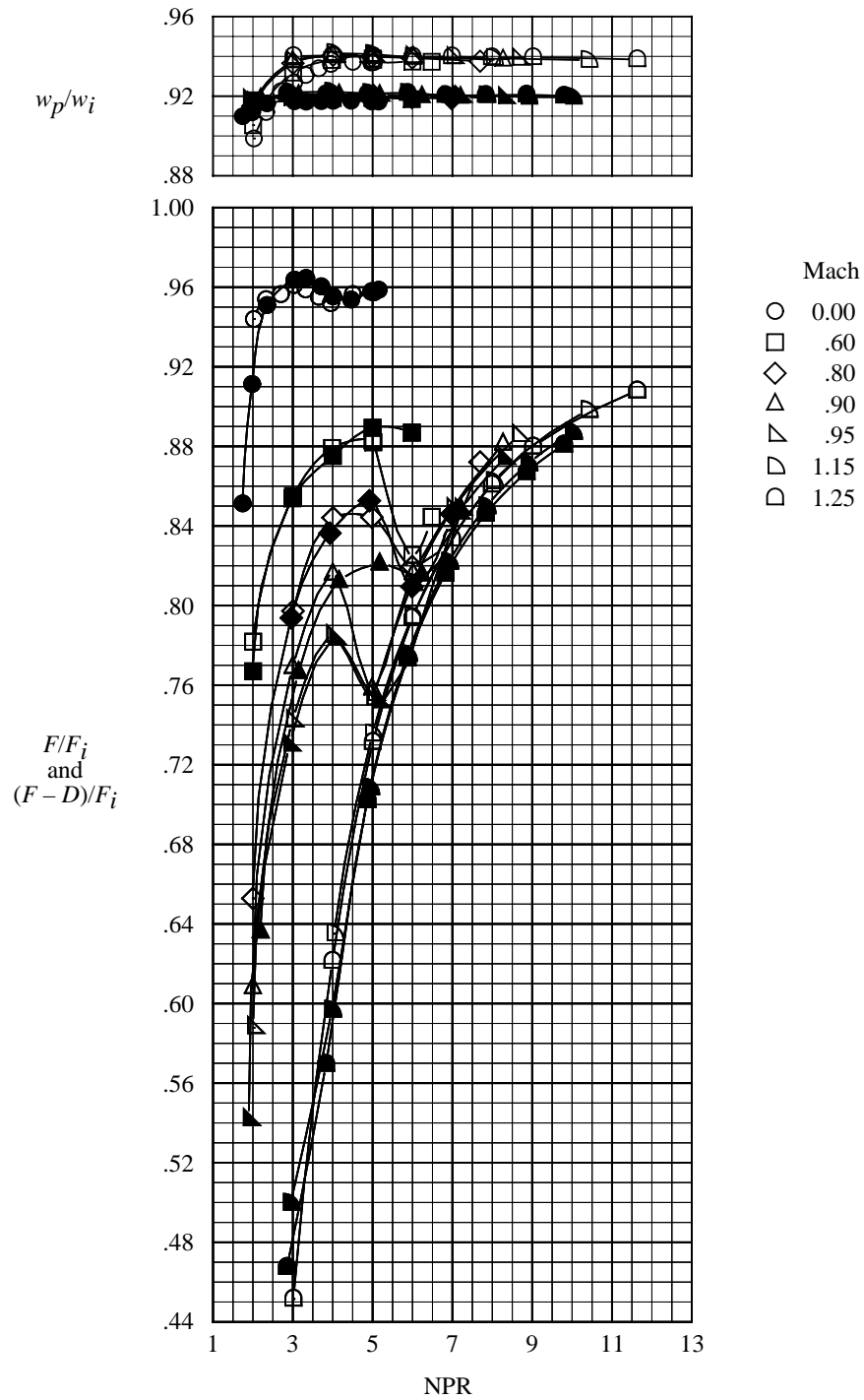
(e) Annularly vented long shroud nozzle.

Figure 4. Continued.



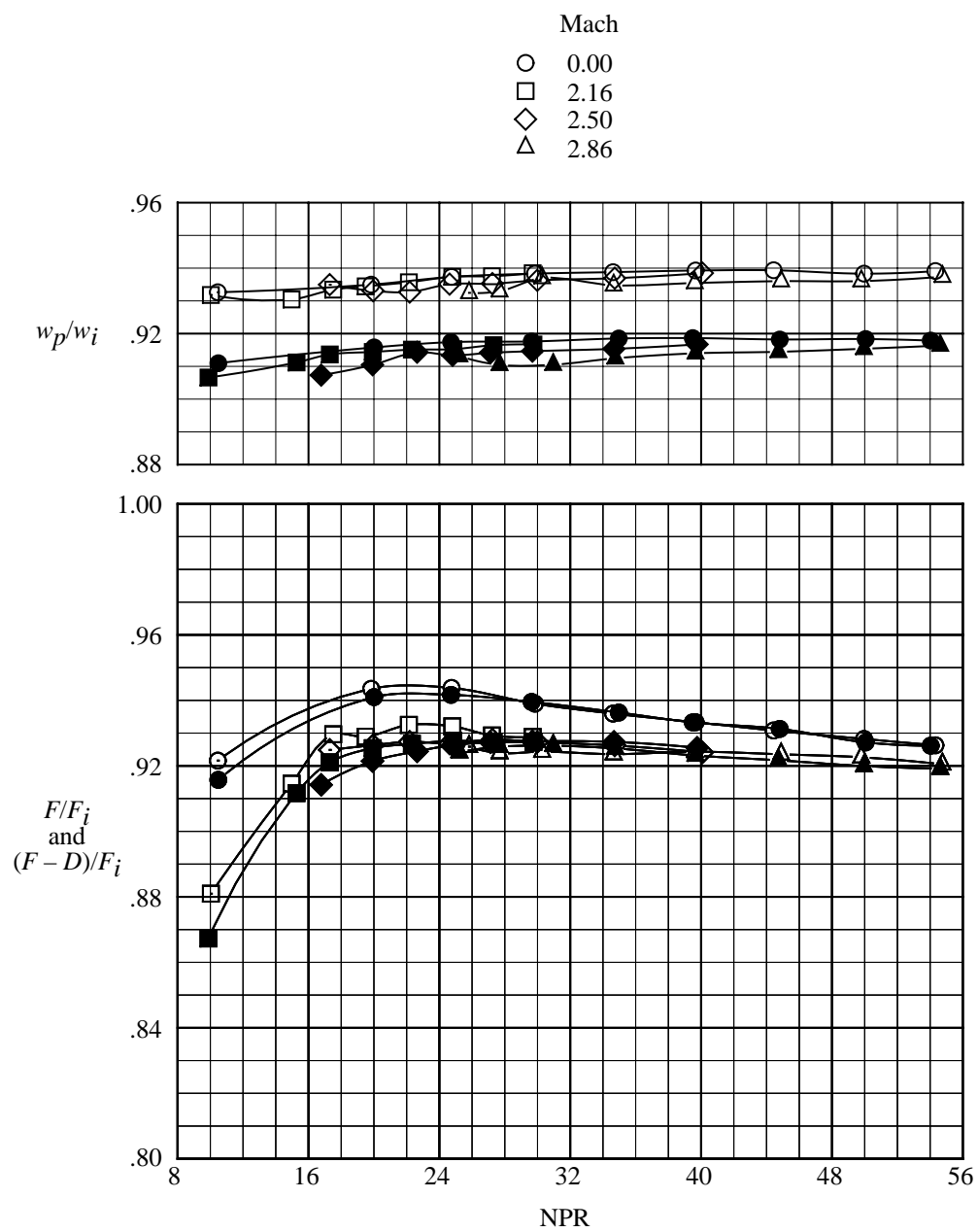
(f) Cruciform nozzle.

Figure 4. Concluded.



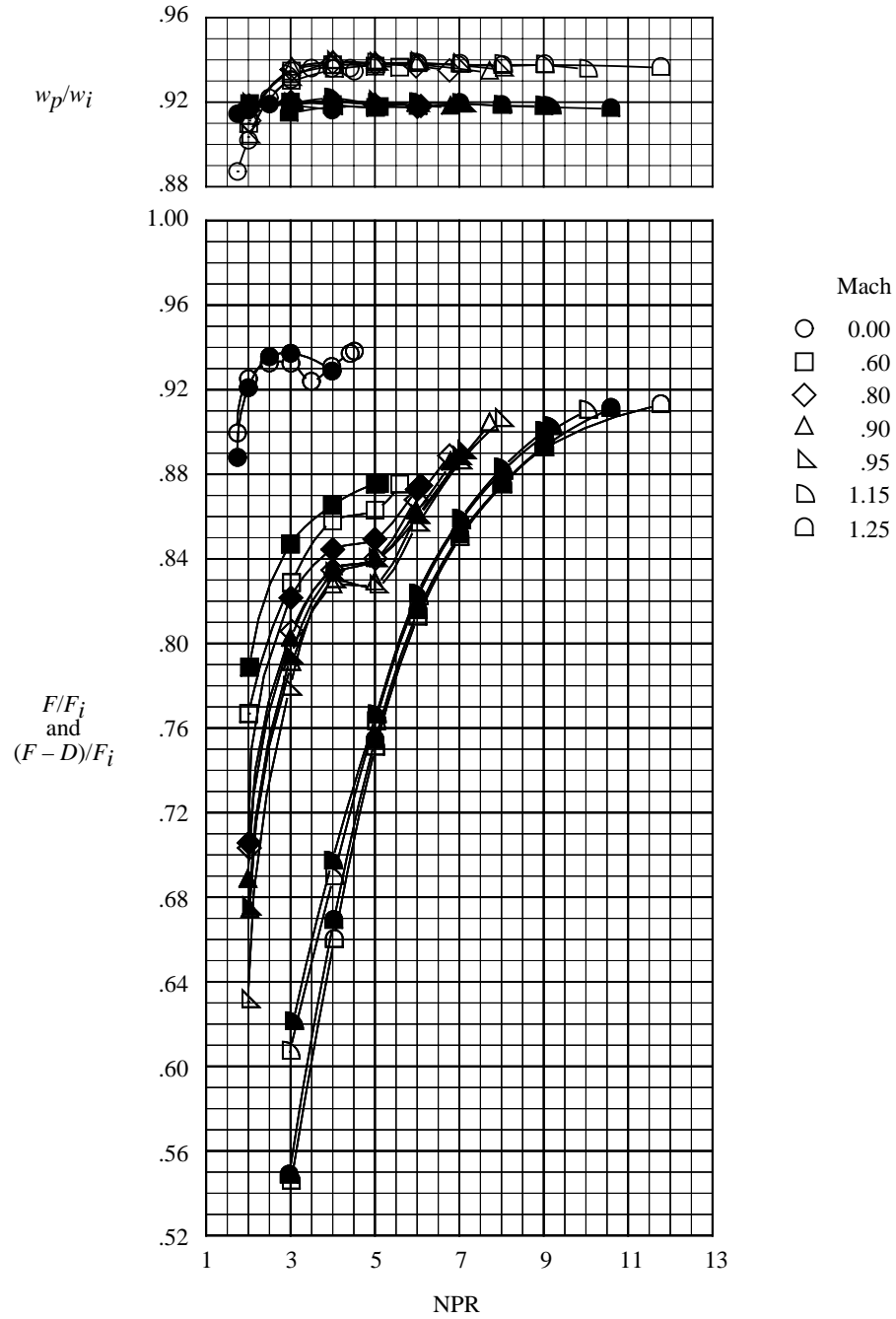
(a) Subsonic and transonic speeds.

Figure 5. Thrust ratio, thrust-minus-drag ratio, and discharge coefficient for long unvented nozzles. Open symbols indicate concave centerbody base and solid symbols indicate convex centerbody base.



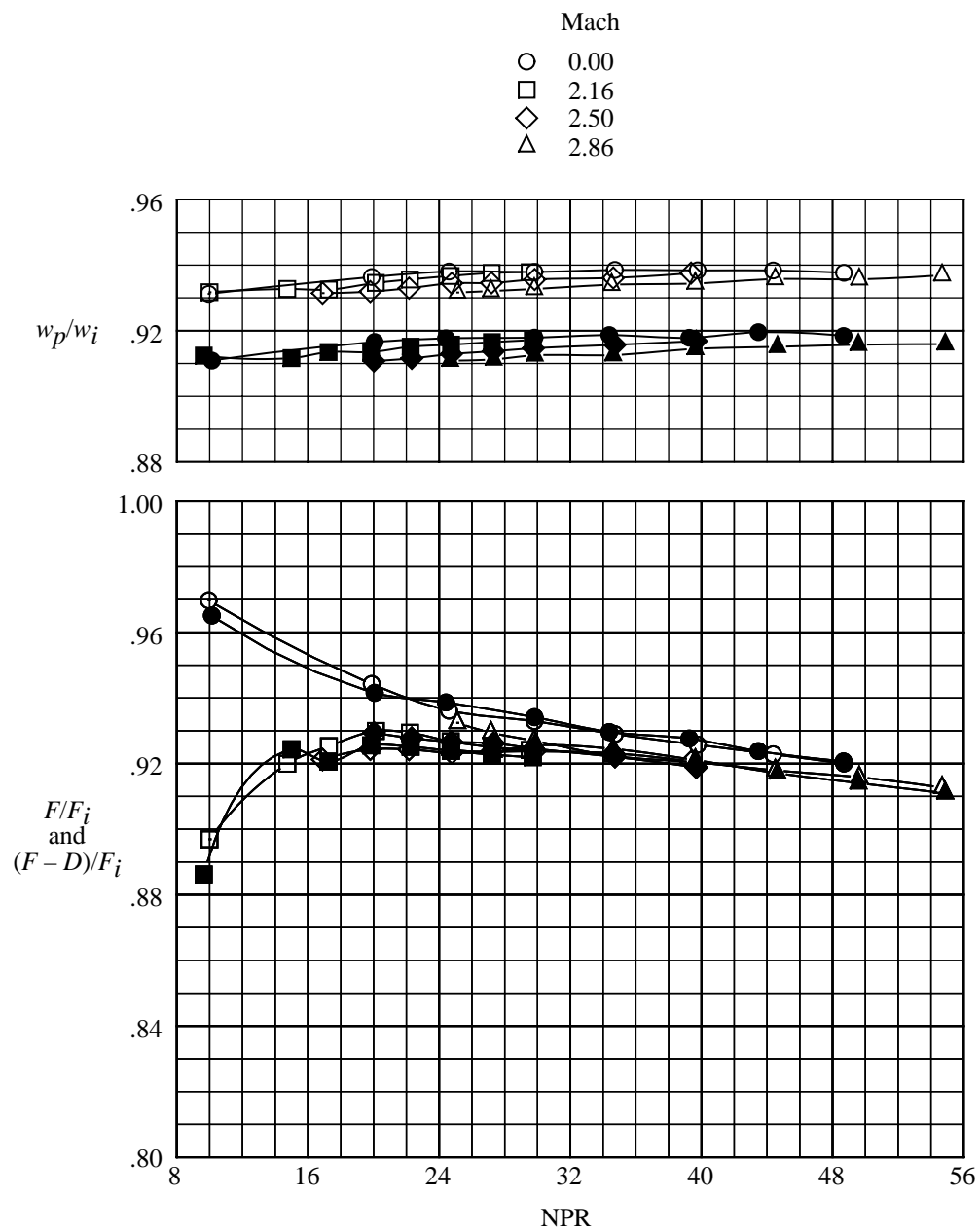
(b) Supersonic speeds.

Figure 5. Concluded.



(a) Subsonic and transonic speeds.

Figure 6. Thrust ratio, thrust-minus-drag ratio, and discharge coefficient for long axially vented nozzles. Open symbols indicate concave centerbody base and solid symbols indicate convex centerbody base.



(b) Supersonic speeds.

Figure 6. Concluded.

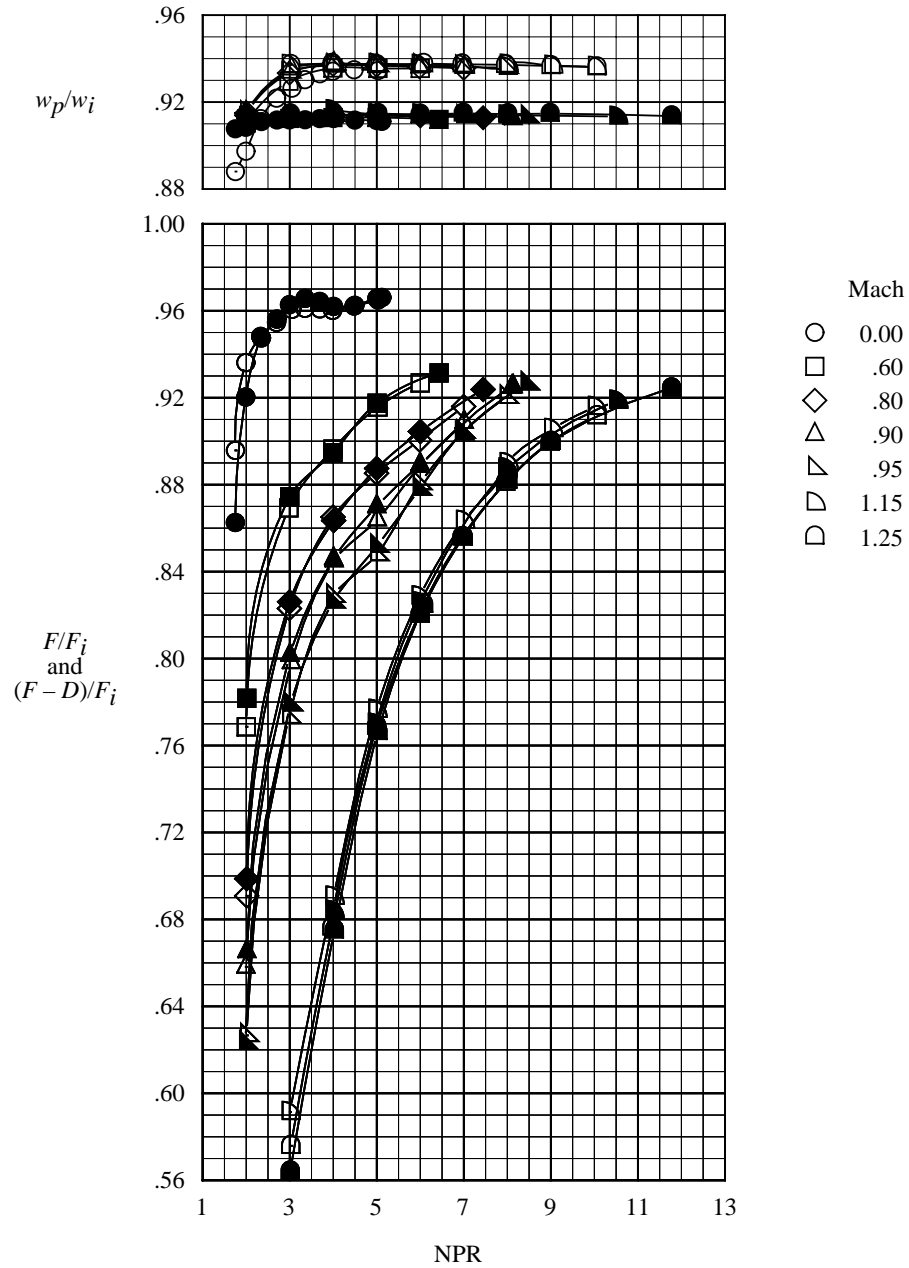
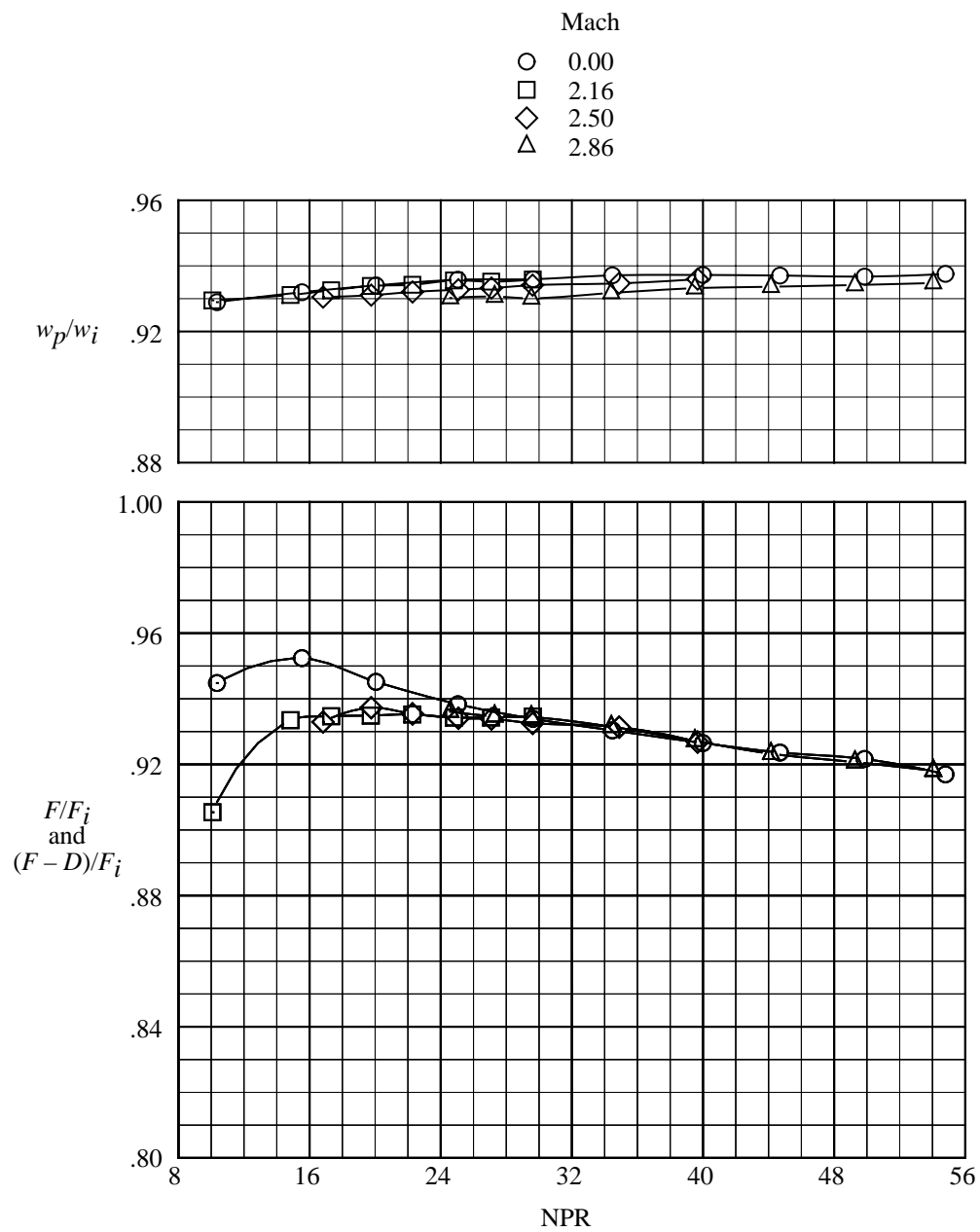
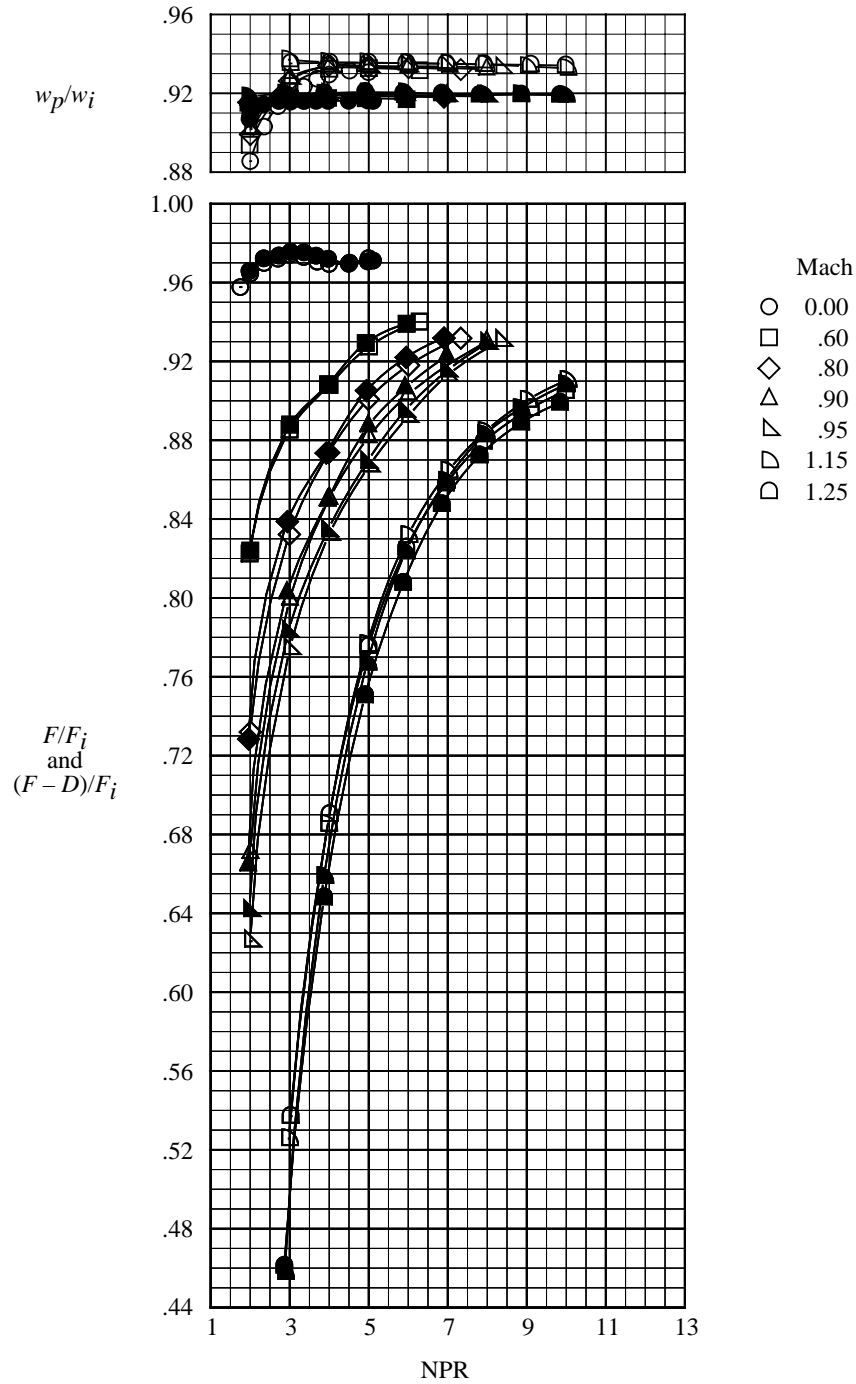


Figure 7. Thrust ratio, thrust-minus-drag ratio, and discharge coefficient for long annularly vented nozzles. Open symbols indicate concave centerbody base and solid symbols indicate convex centerbody base.



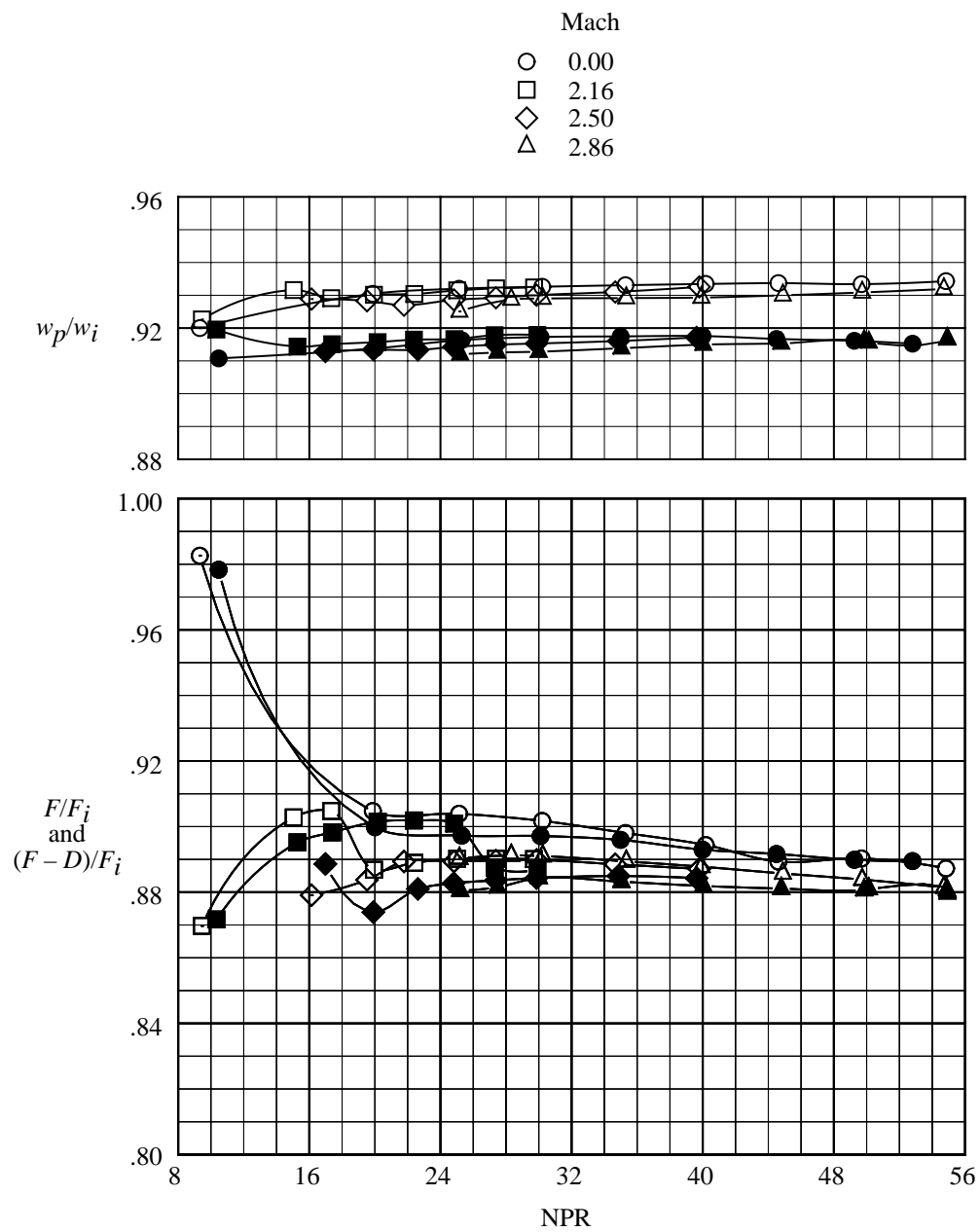
(b) Supersonic speeds.

Figure 7. Concluded.



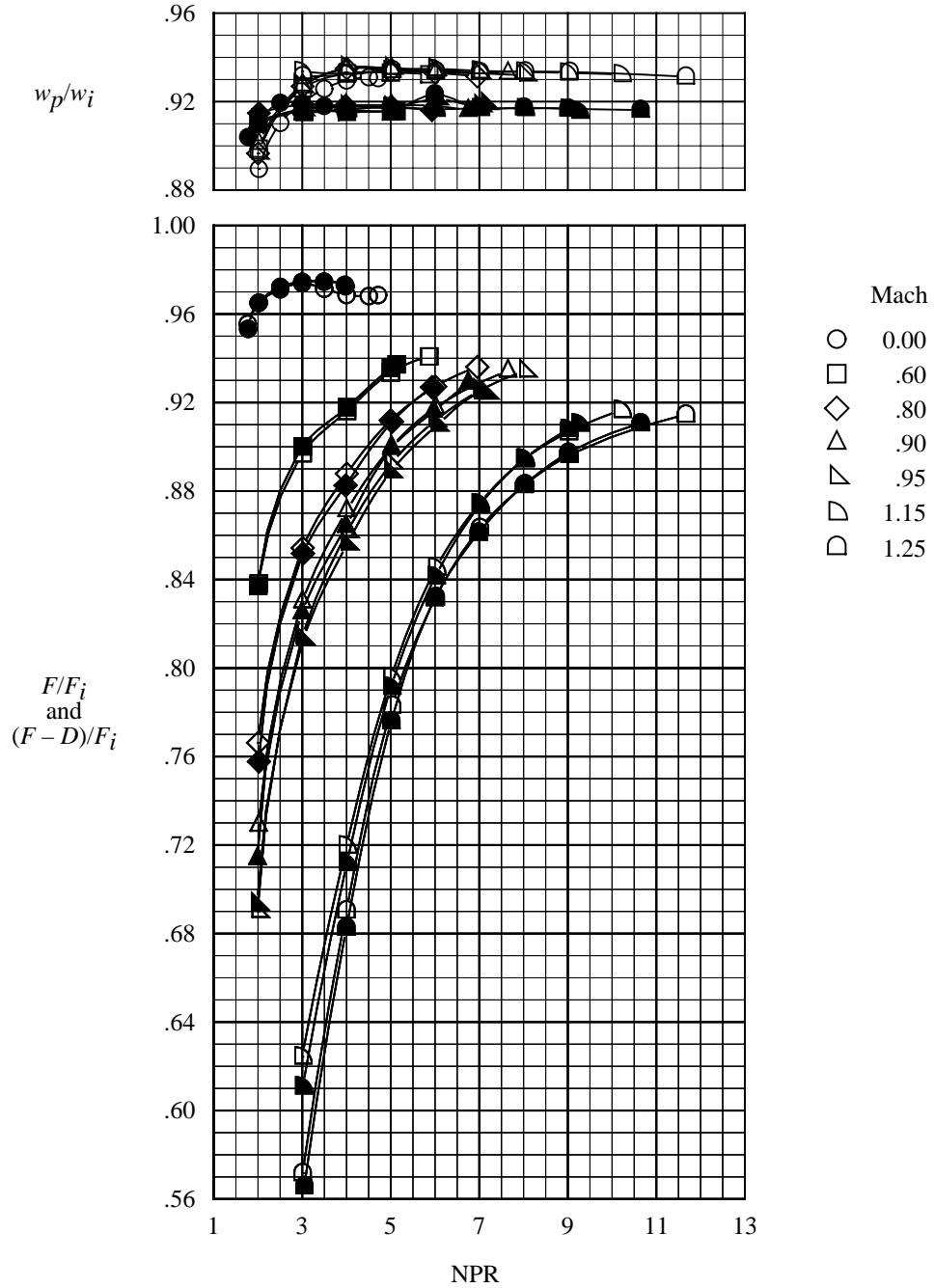
(a) Subsonic and transonic speeds.

Figure 8. Thrust ratio, thrust-minus-drag ratio, and discharge coefficient for short unvented nozzles. Open symbols indicate concave centerbody base and solid symbols indicate convex centerbody base.



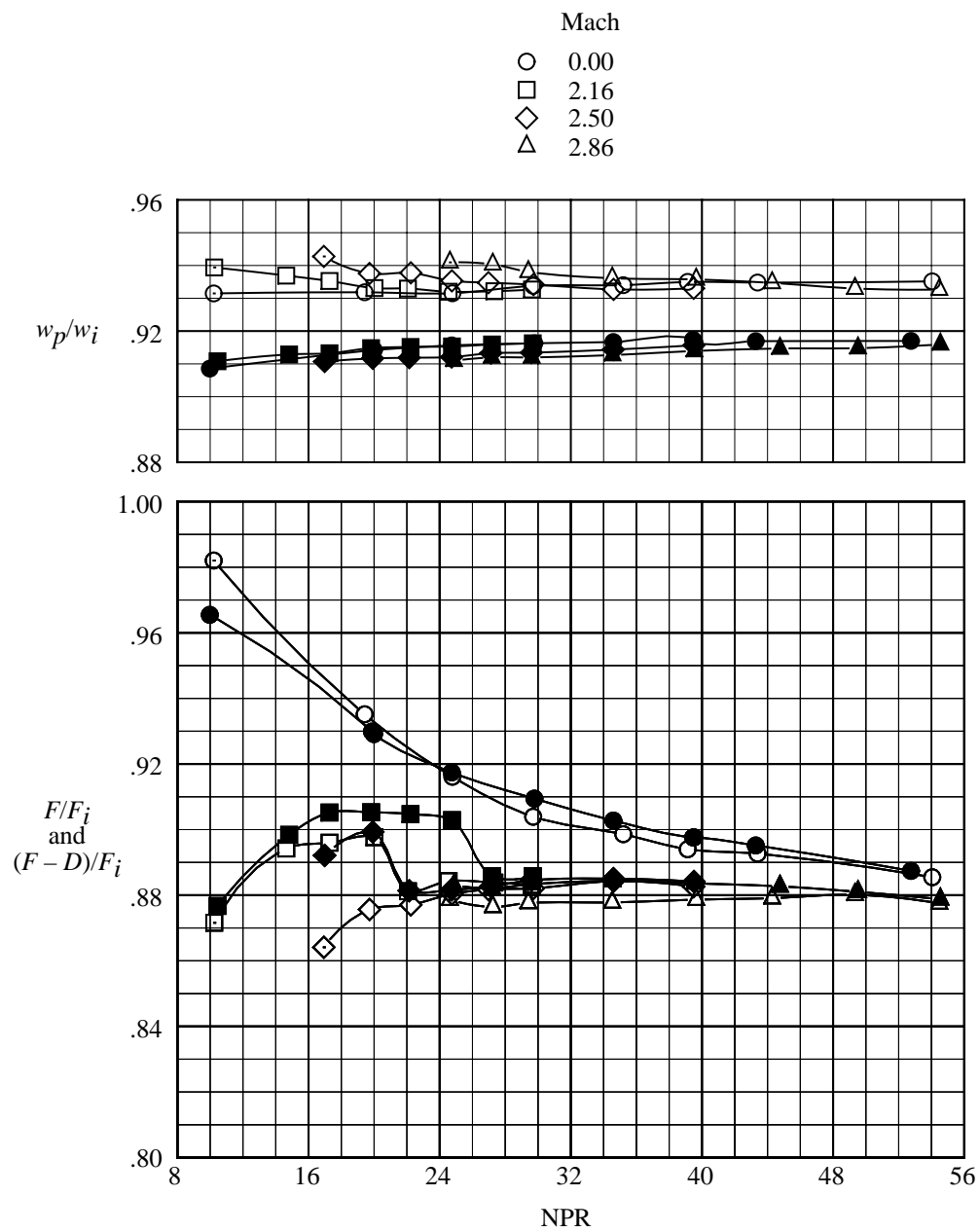
(b) Supersonic speeds.

Figure 8. Concluded.



(a) Subsonic and transonic speeds.

Figure 9. Thrust ratio, thrust-minus-drag ratio, and discharge coefficient for short axially nozzles. Open symbols indicate concave centerbody base and solid symbols indicate convex centerbody base.



(b) Supersonic speeds.

Figure 9. Concluded.

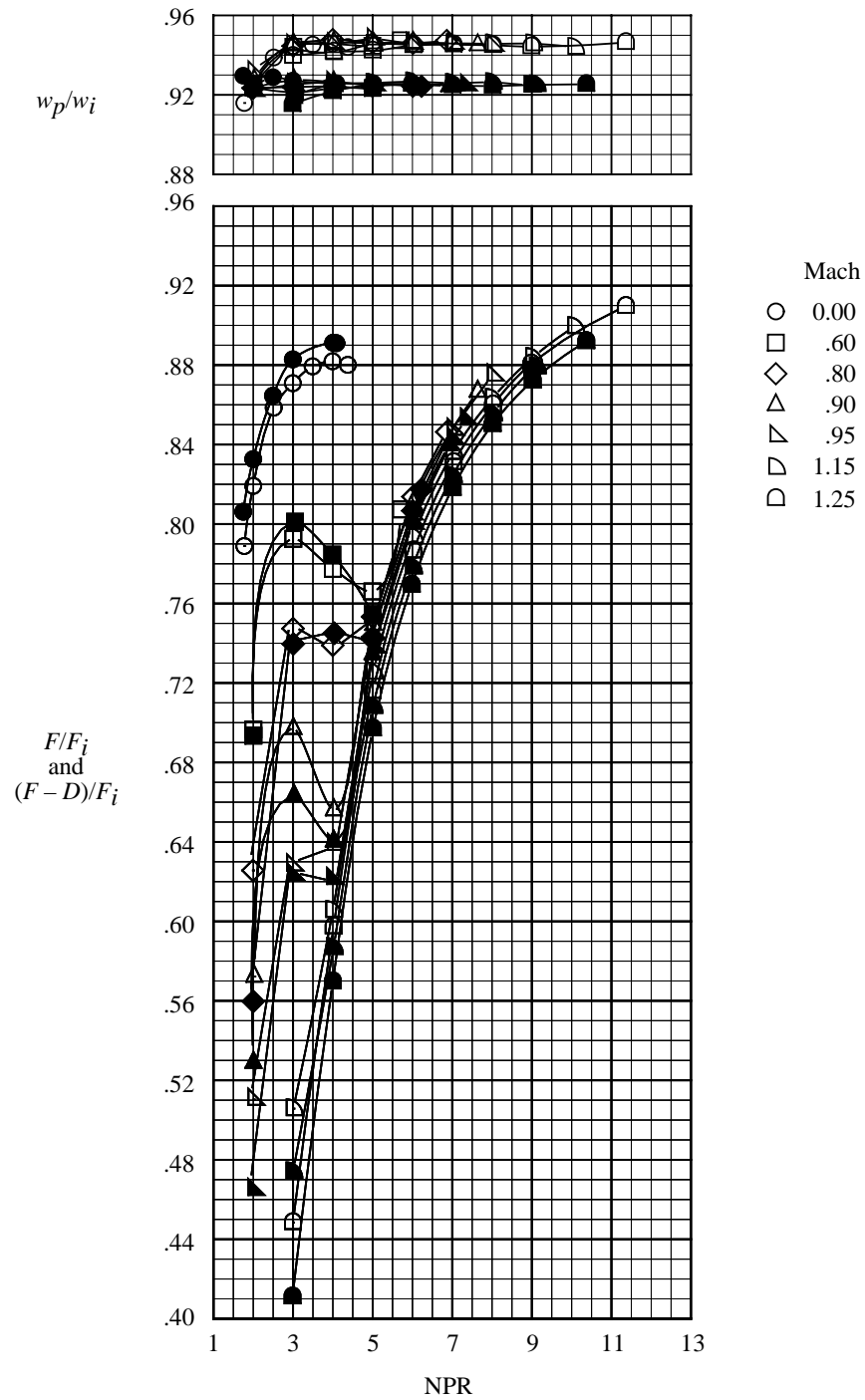
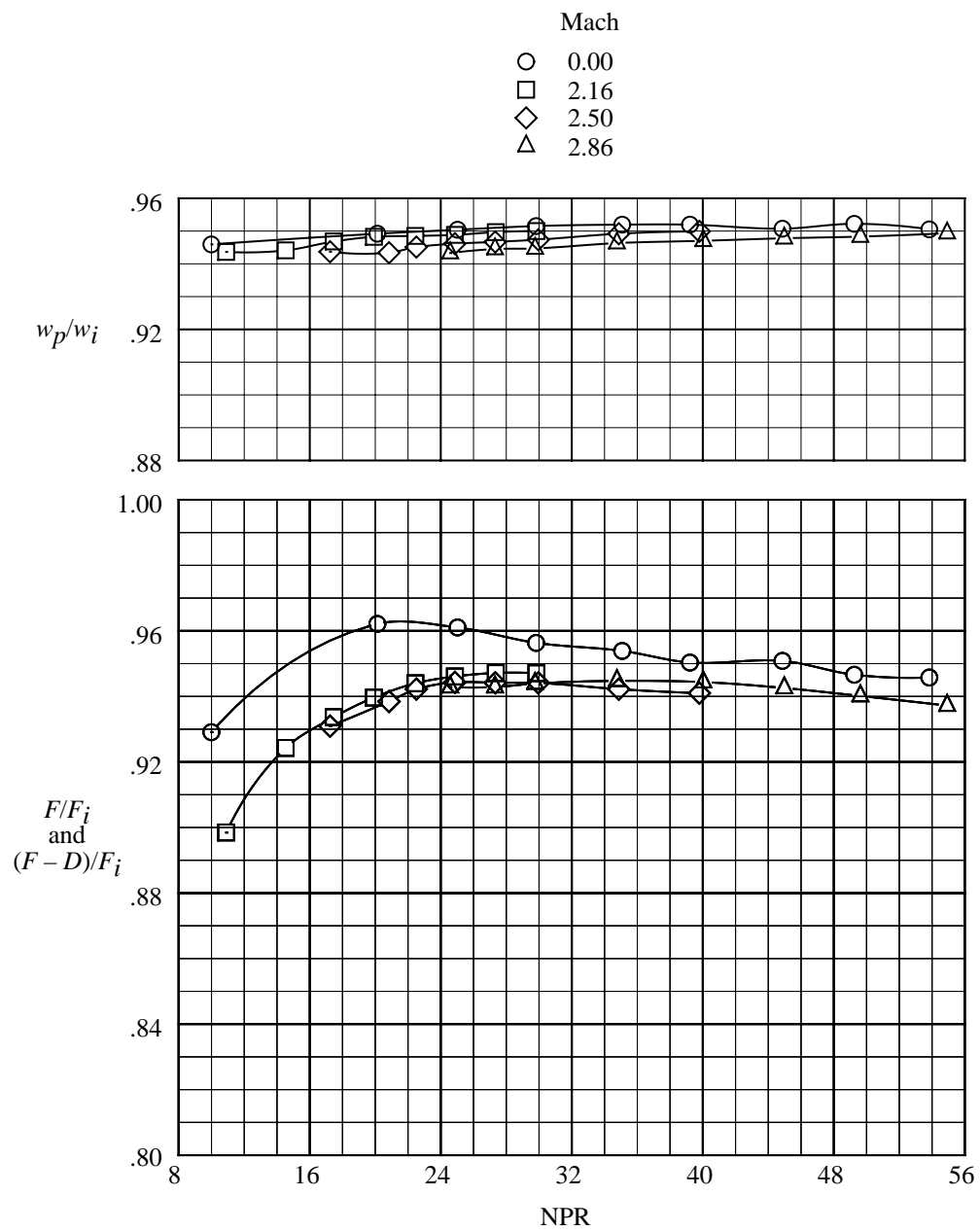
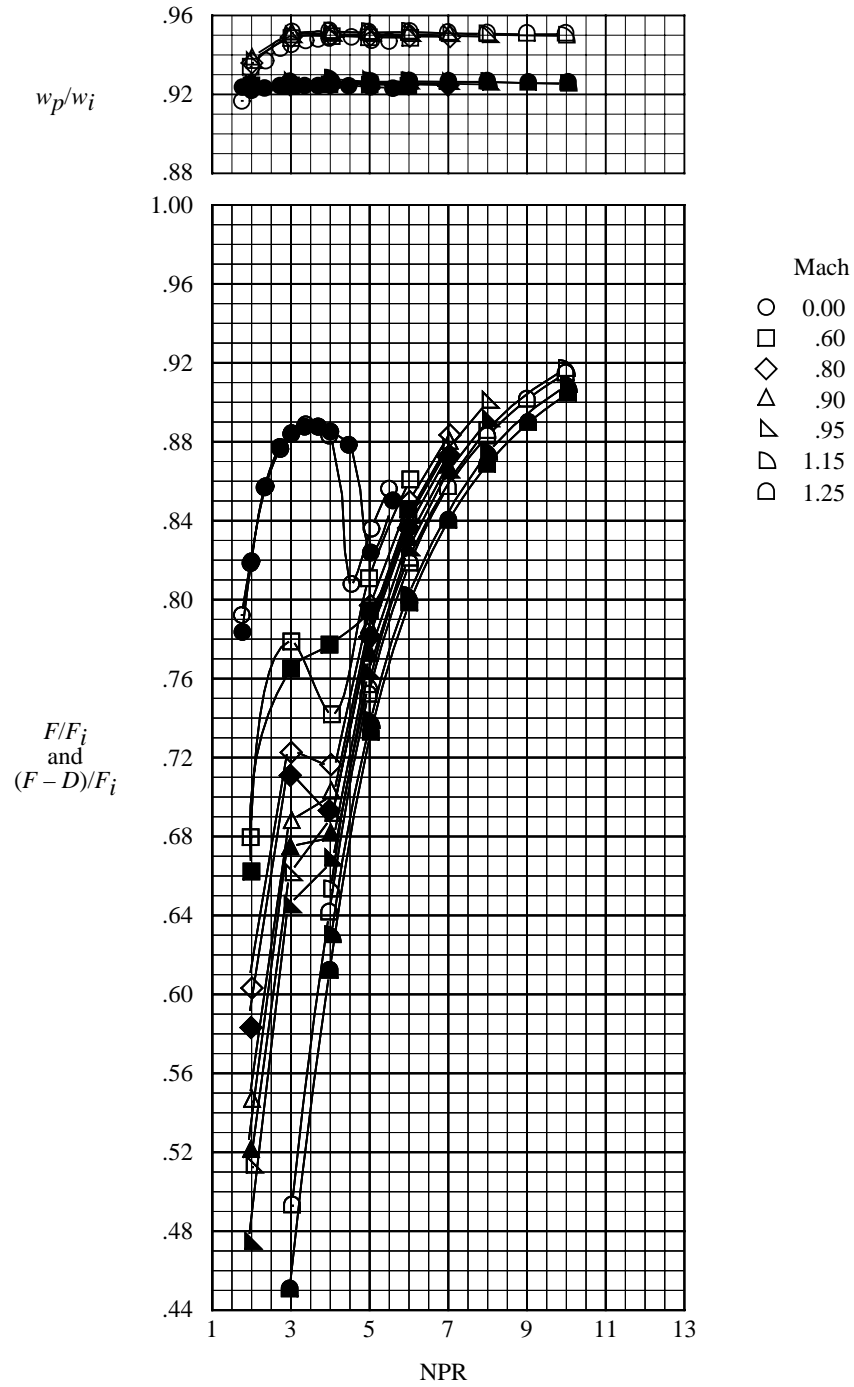


Figure 10. Thrust ratio, thrust-minus-drag ratio, and discharge coefficient for cruciform nozzle with all flaps in position a. Open symbols indicate concave centerbody base and solid symbols indicate convex centerbody base.



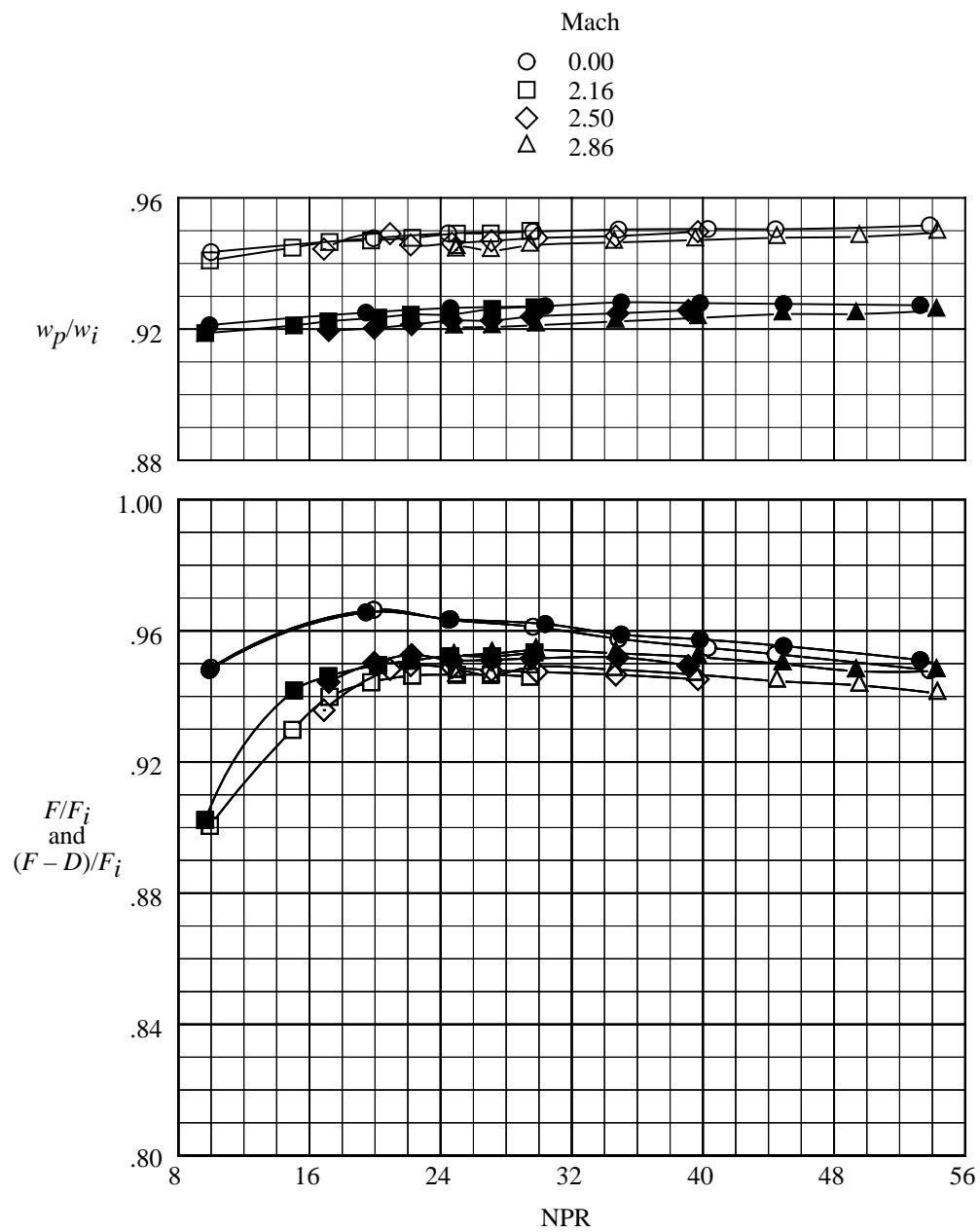
(b) Supersonic speeds.

Figure 10. Concluded.



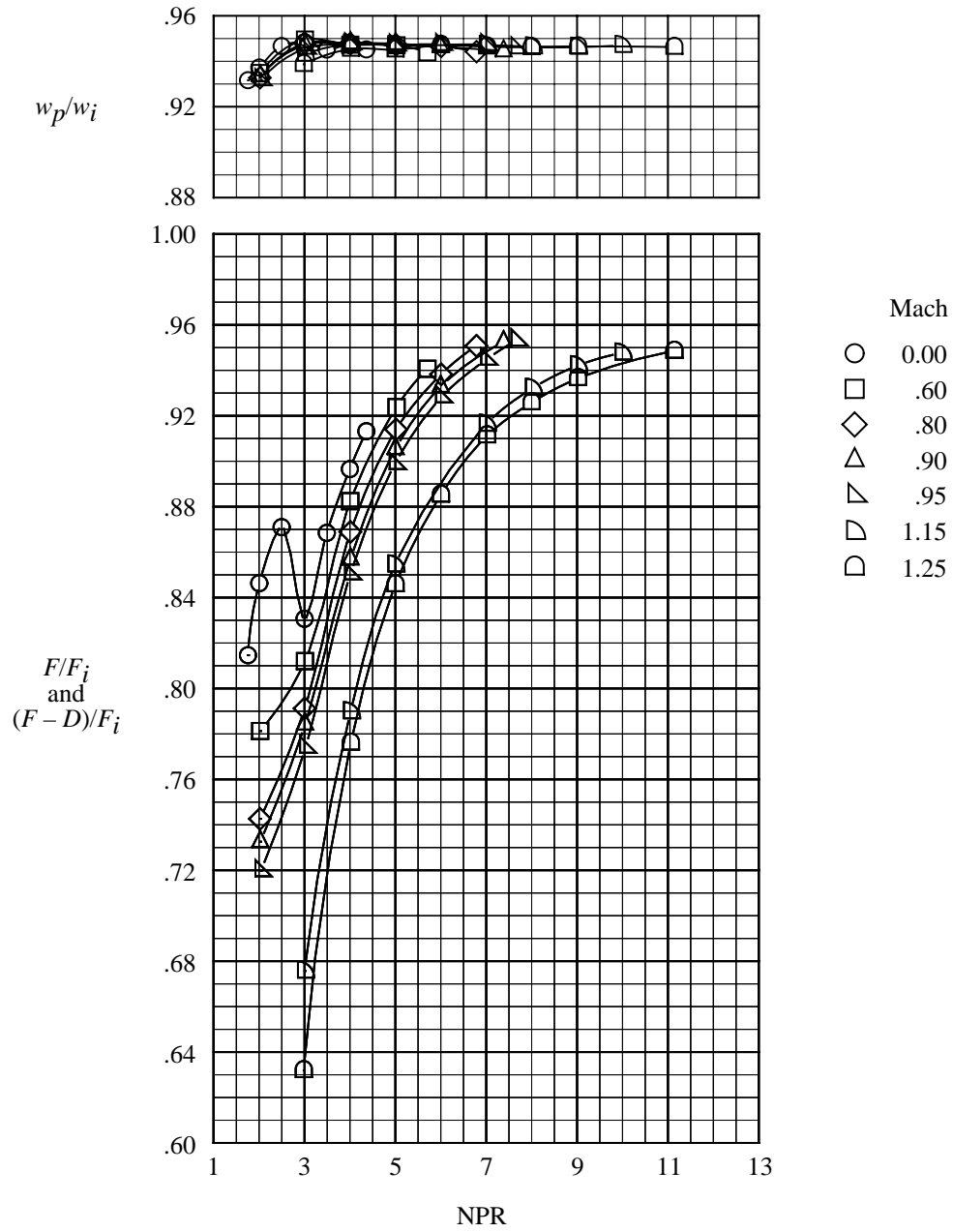
(a) Subsonic and transonic speeds.

Figure 11. Thrust ratio, thrust-minus-drag ratio, and discharge coefficient for cruciform nozzle with all flaps in position b. Open symbols indicate concave centerbody base and solid symbols indicate convex centerbody base.



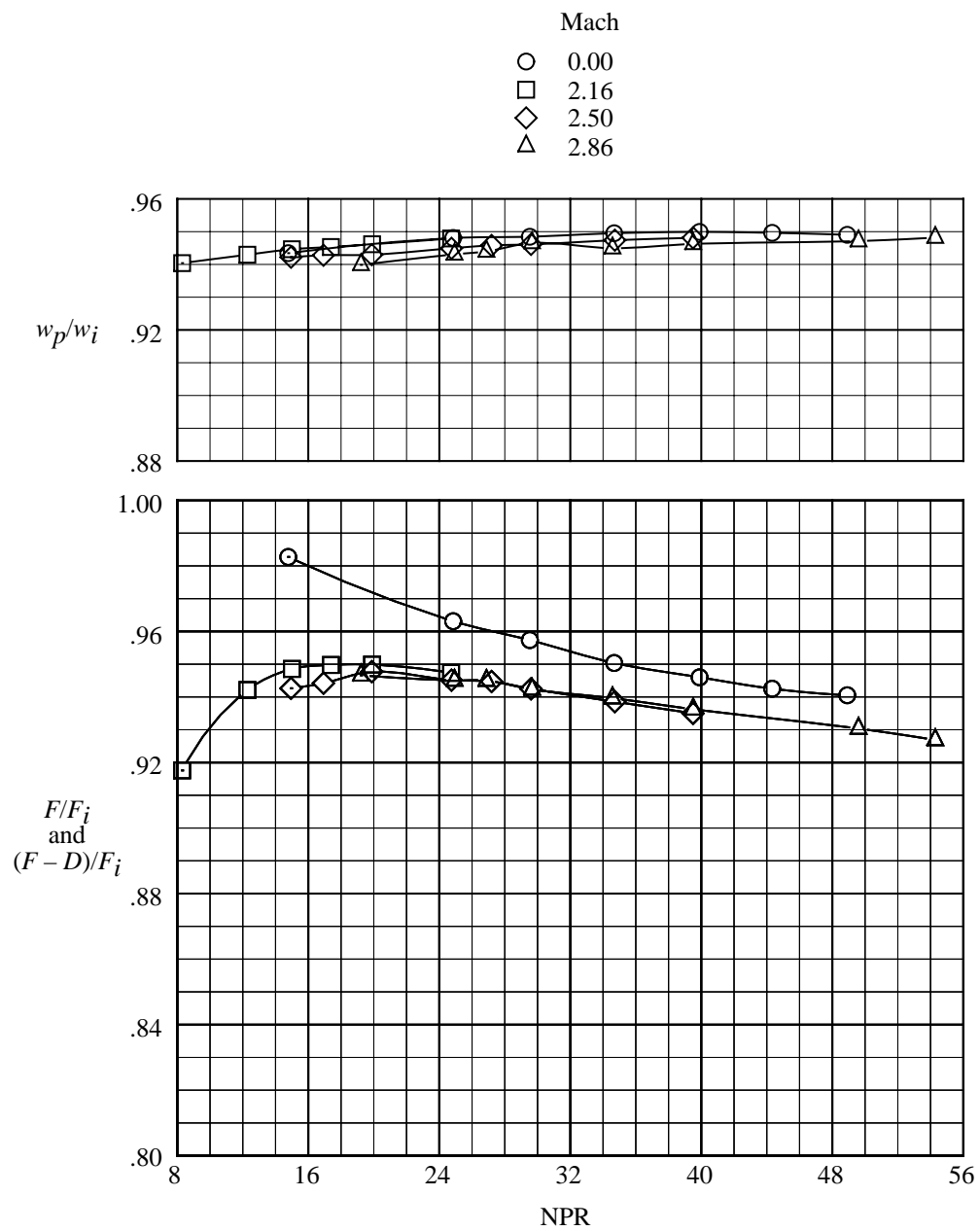
(b) Supersonic speeds.

Figure 11. Concluded.



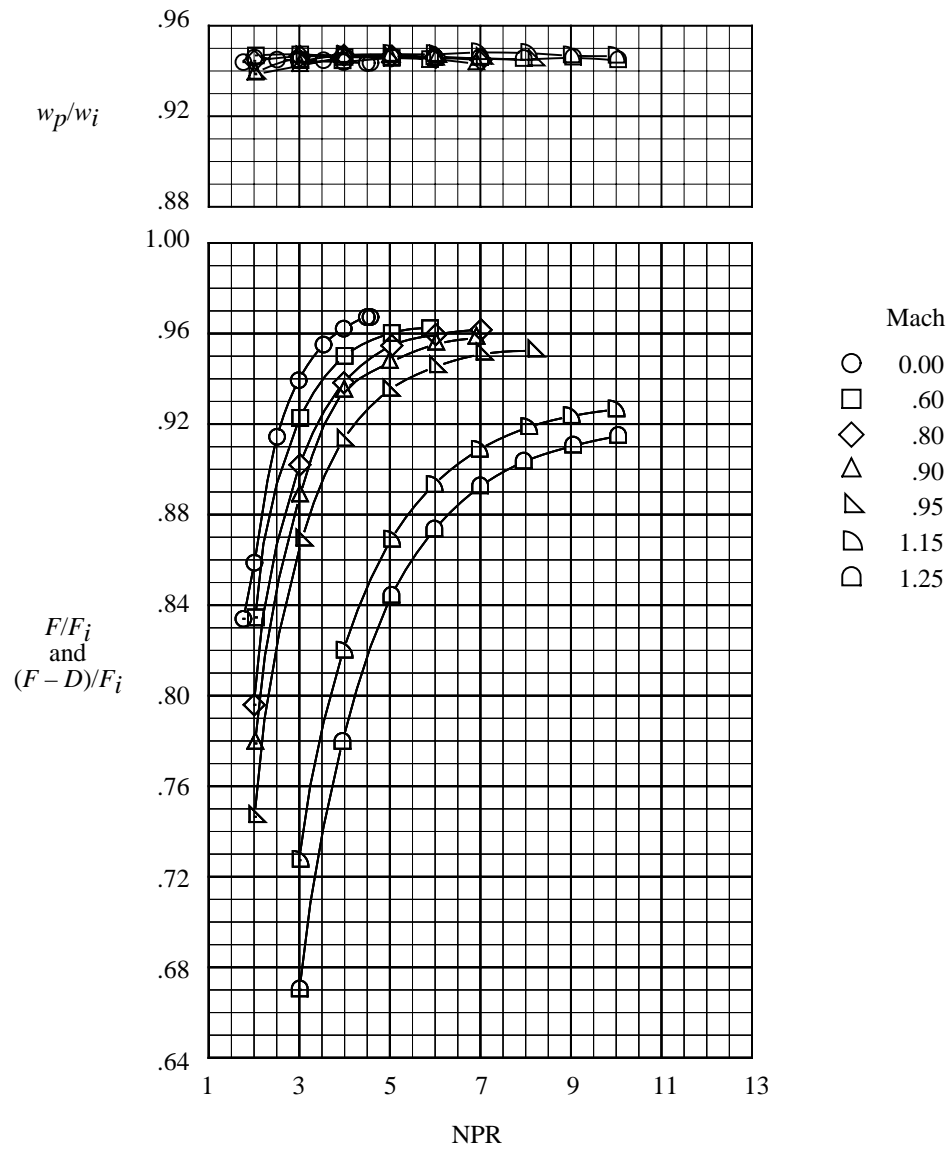
(a) Subsonic and transonic speeds.

Figure 12. Thrust ratio, thrust-minus-drag ratio, and discharge coefficient for cruciform nozzle with all flaps in position c with concave centerbody base.



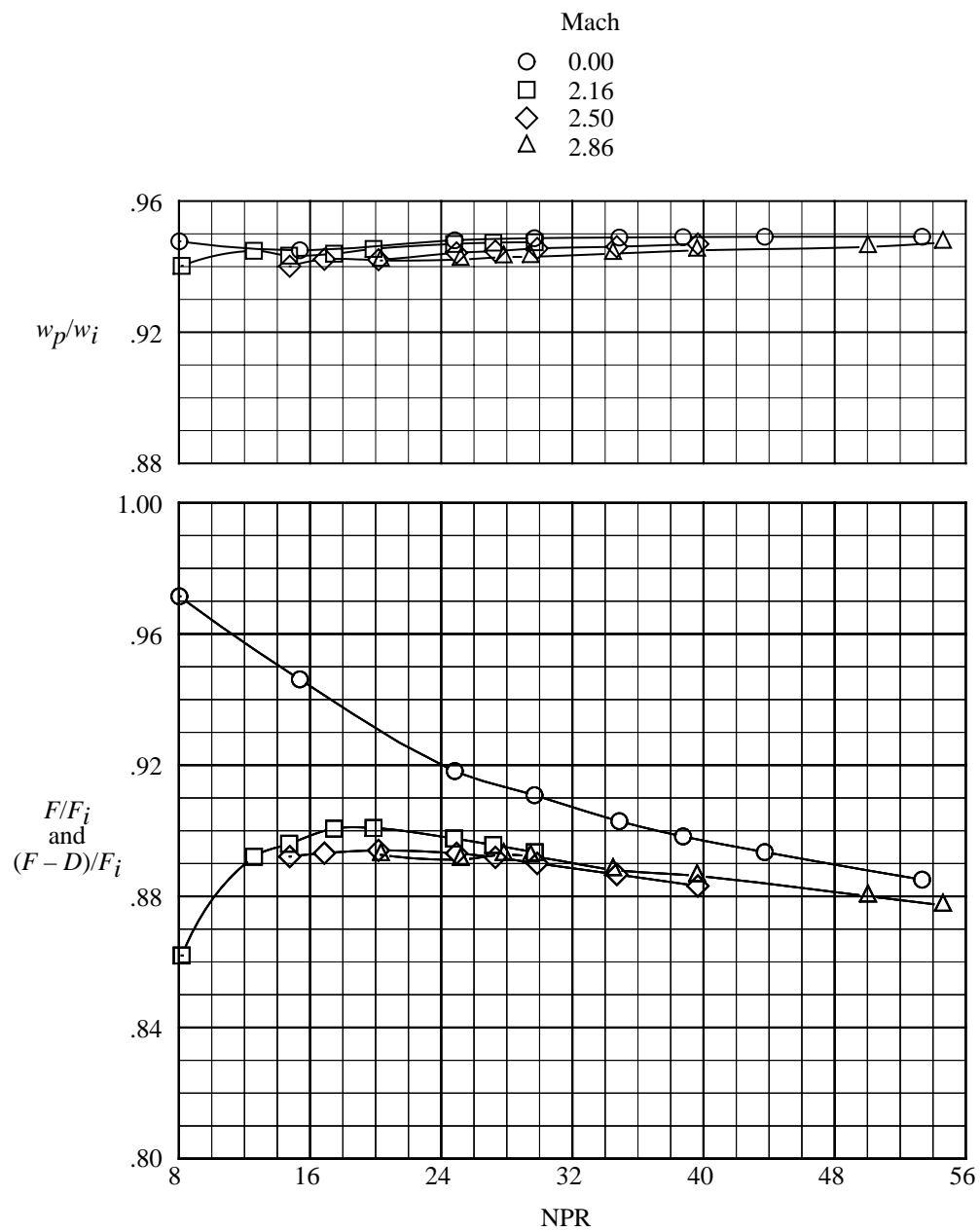
(b) Supersonic speeds.

Figure 12. Concluded.



(a) Subsonic and transonic speeds.

Figure 13. Thrust ratio, thrust-minus-drag ratio, and discharge coefficient for cruciform nozzle with all flaps in position d with concave centerbody base.



(b) Supersonic speeds.

Figure 13. Concluded.

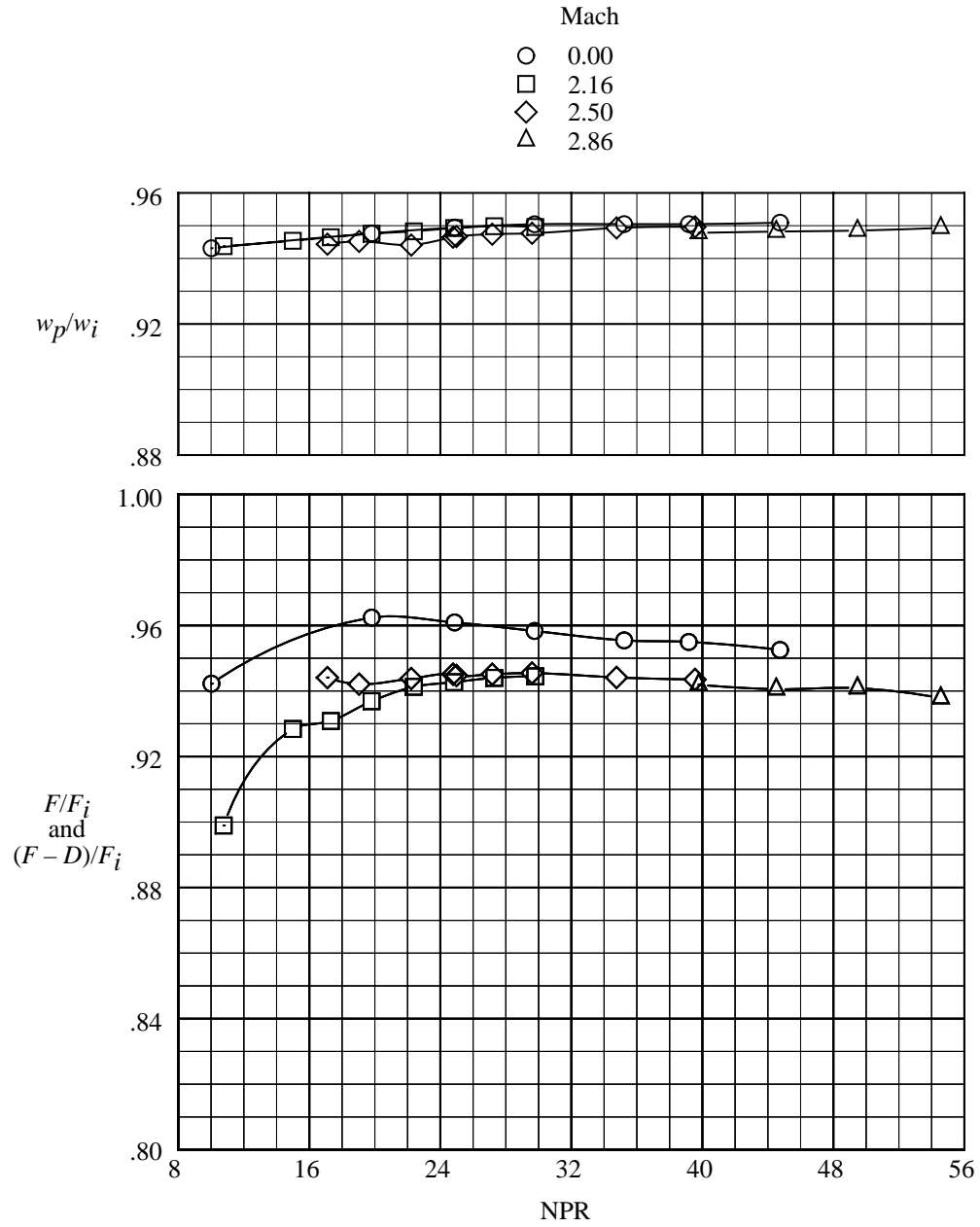


Figure 14. Thrust ratio, thrust-minus-drag ratio, and discharge coefficient for cruciform nozzle with two flaps in position a and two flaps in position b with concave centerbody base at supersonic speeds.

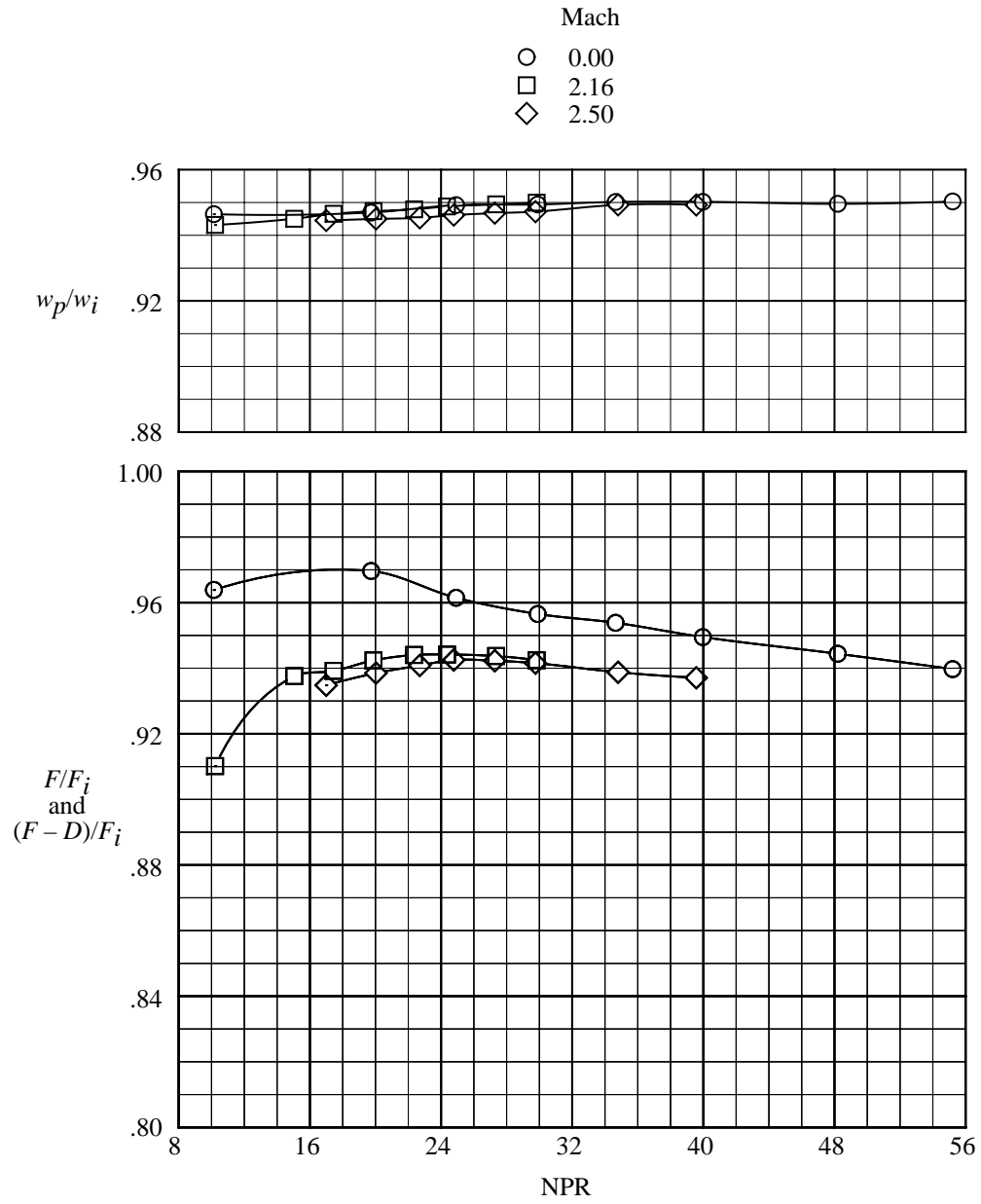


Figure 15. Thrust ratio, thrust-minus-drag ratio, and discharge coefficient for cruciform nozzle with two flaps in position a and two flaps in position c with concave centerbody base at supersonic speeds.

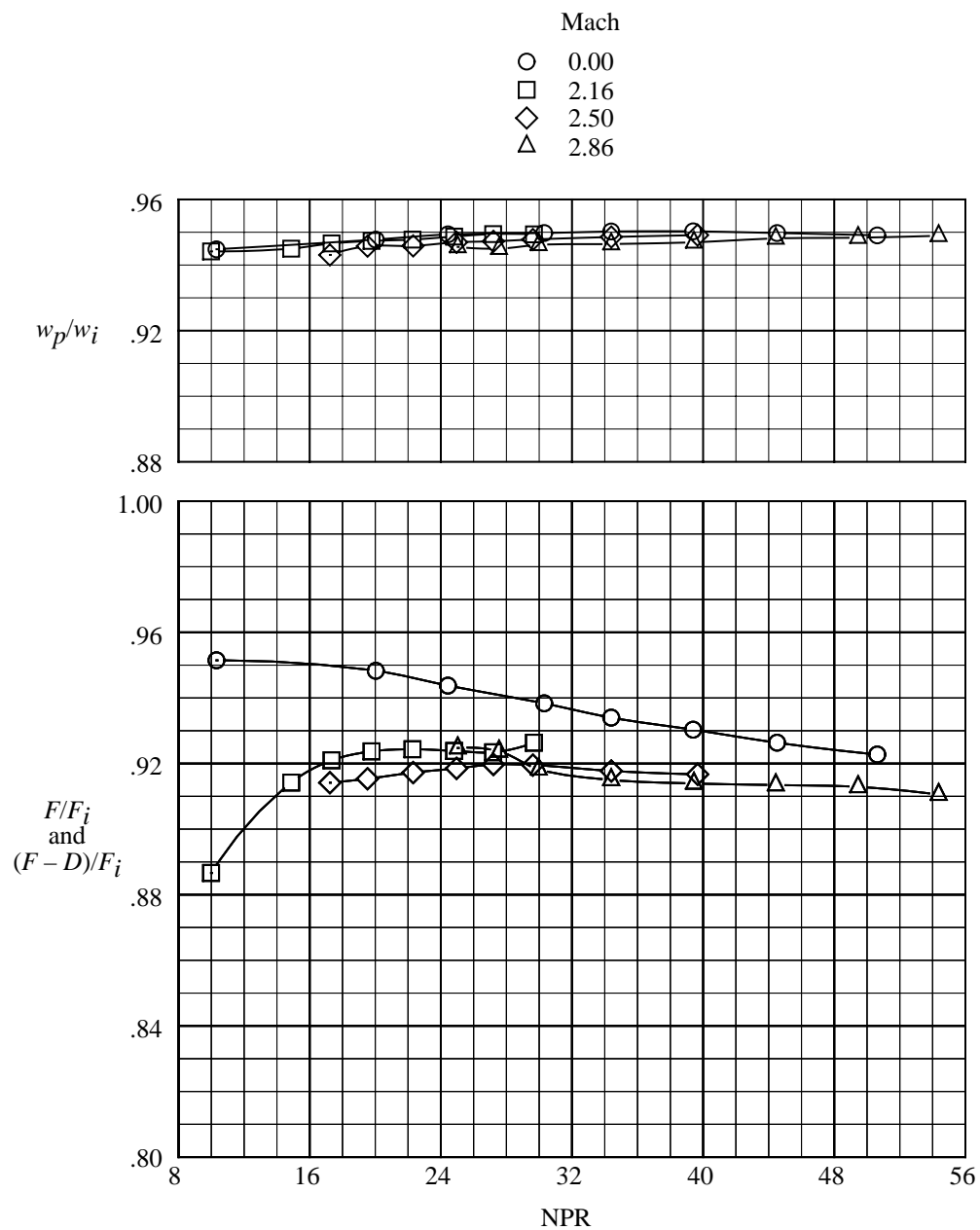
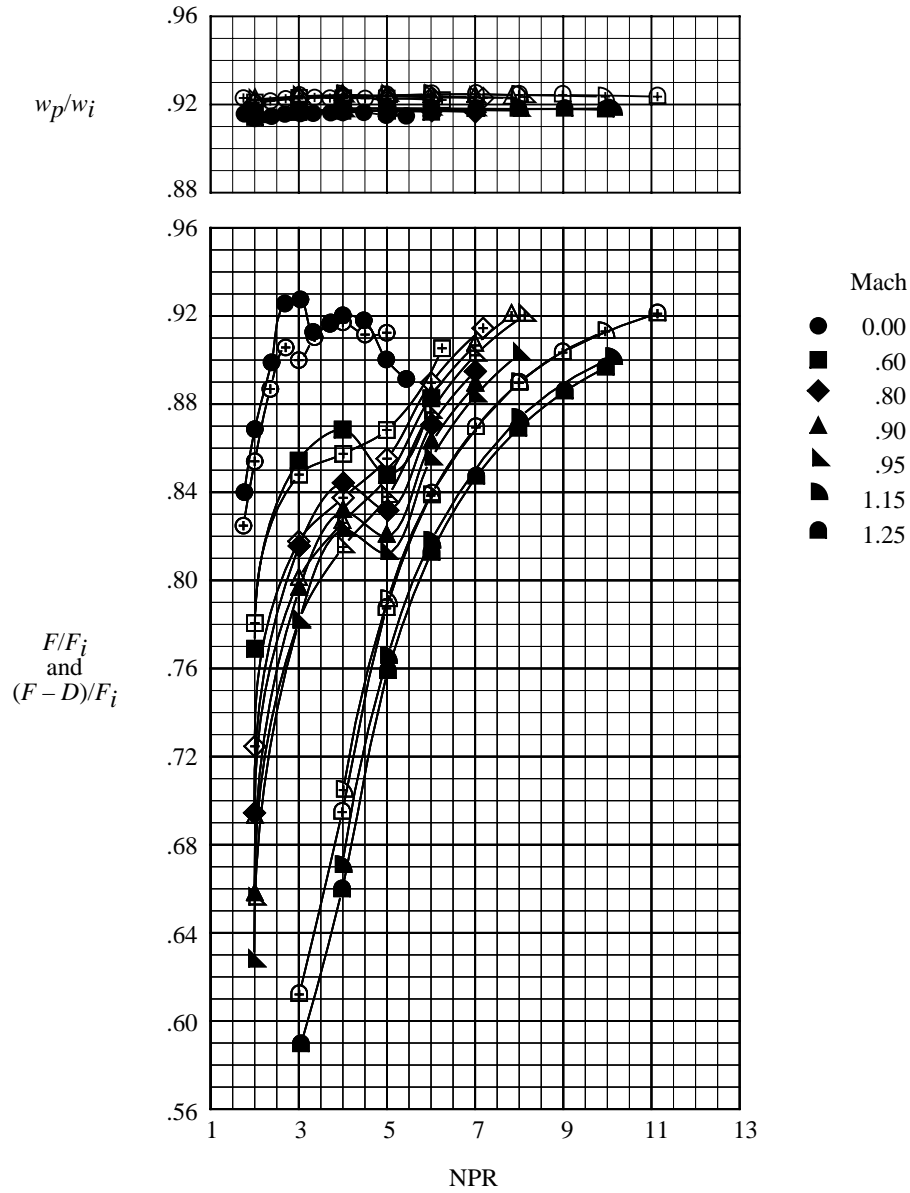


Figure 16. Thrust ratio, thrust-minus-drag ratio, and discharge coefficient for cruciform nozzle with two flaps in position a and two flaps in position d with concave centerbody base at supersonic speeds.



(a) Thrust ratio, thrust-minus-drag ratio, and discharge coefficient.

Figure 17. Thrust ratio, thrust-minus-drag ratio, discharge coefficient, thrust vector angles, and force and moment ratios for cruciform nozzle with two flaps in position a and two flaps in position d with convex centerbody base at subsonic and transonic speeds. Solid symbols indicate flaps not deflected for vectoring and symbols with plus signs indicate flaps deflected for vectoring.

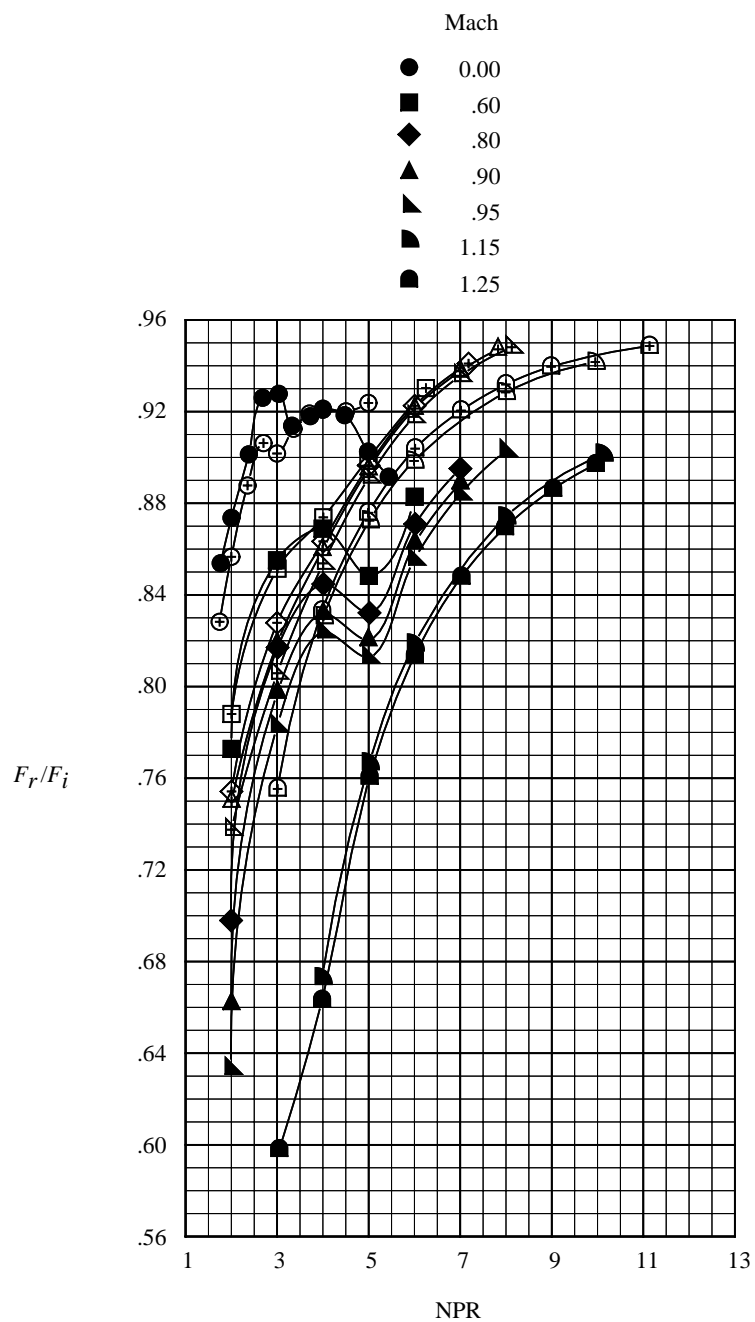
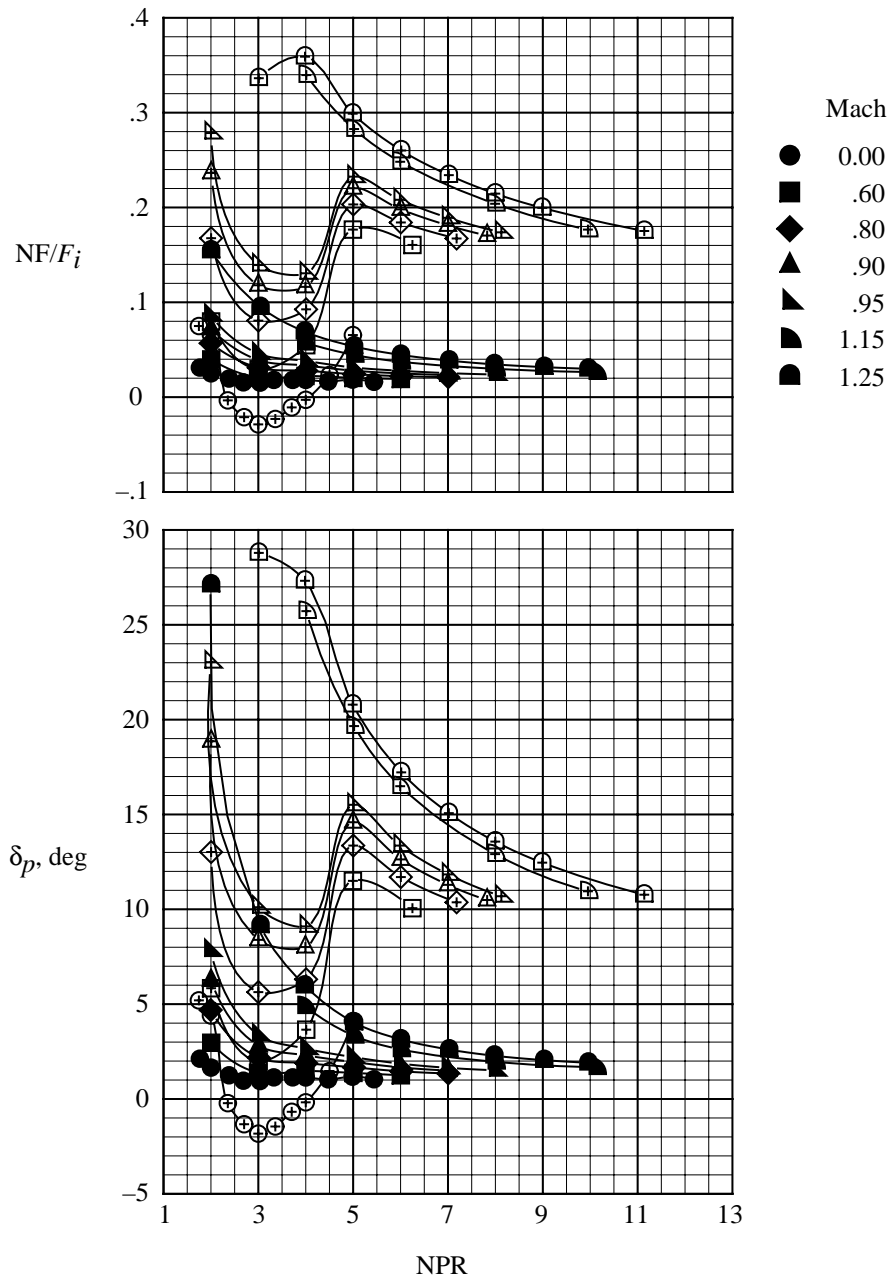
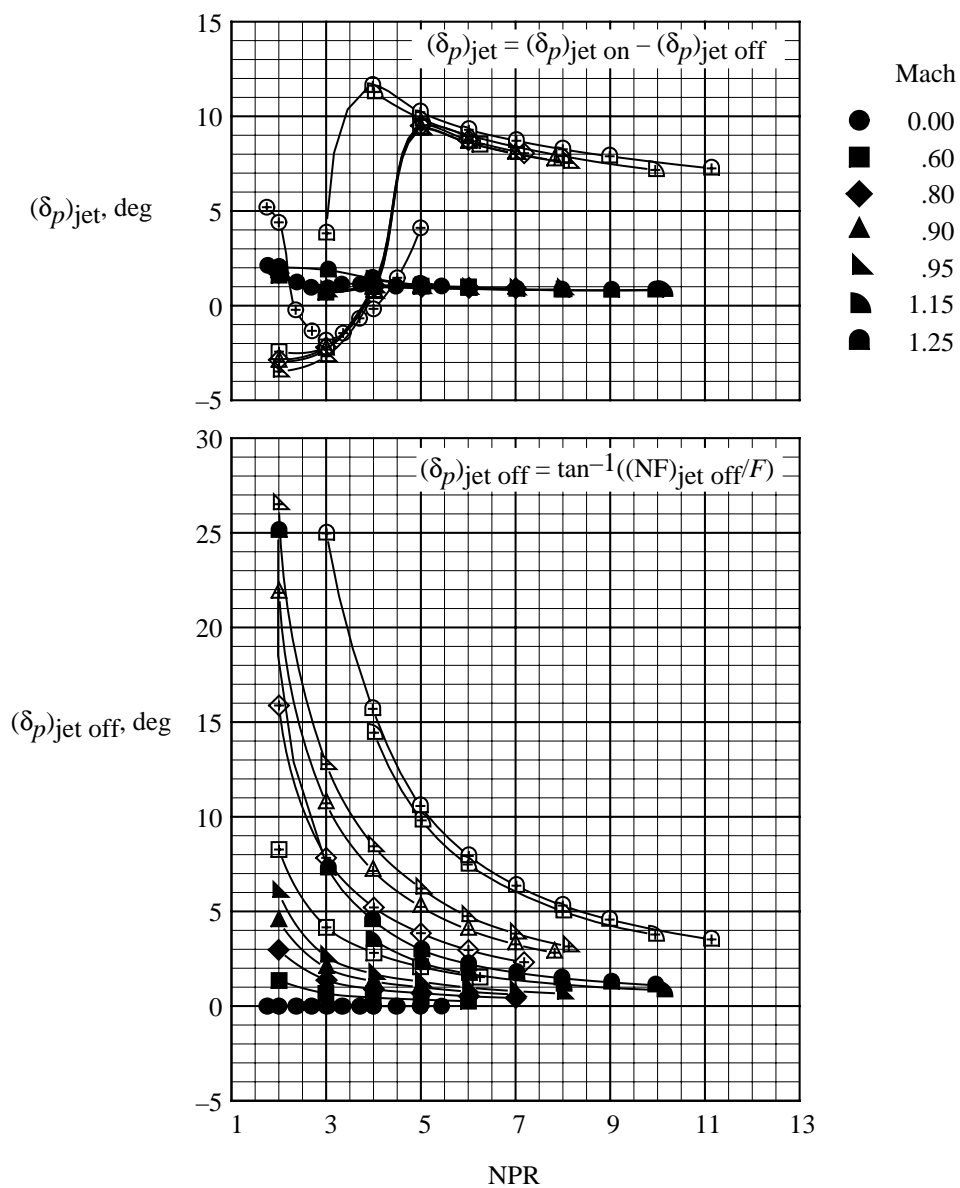


Figure 17. Continued.



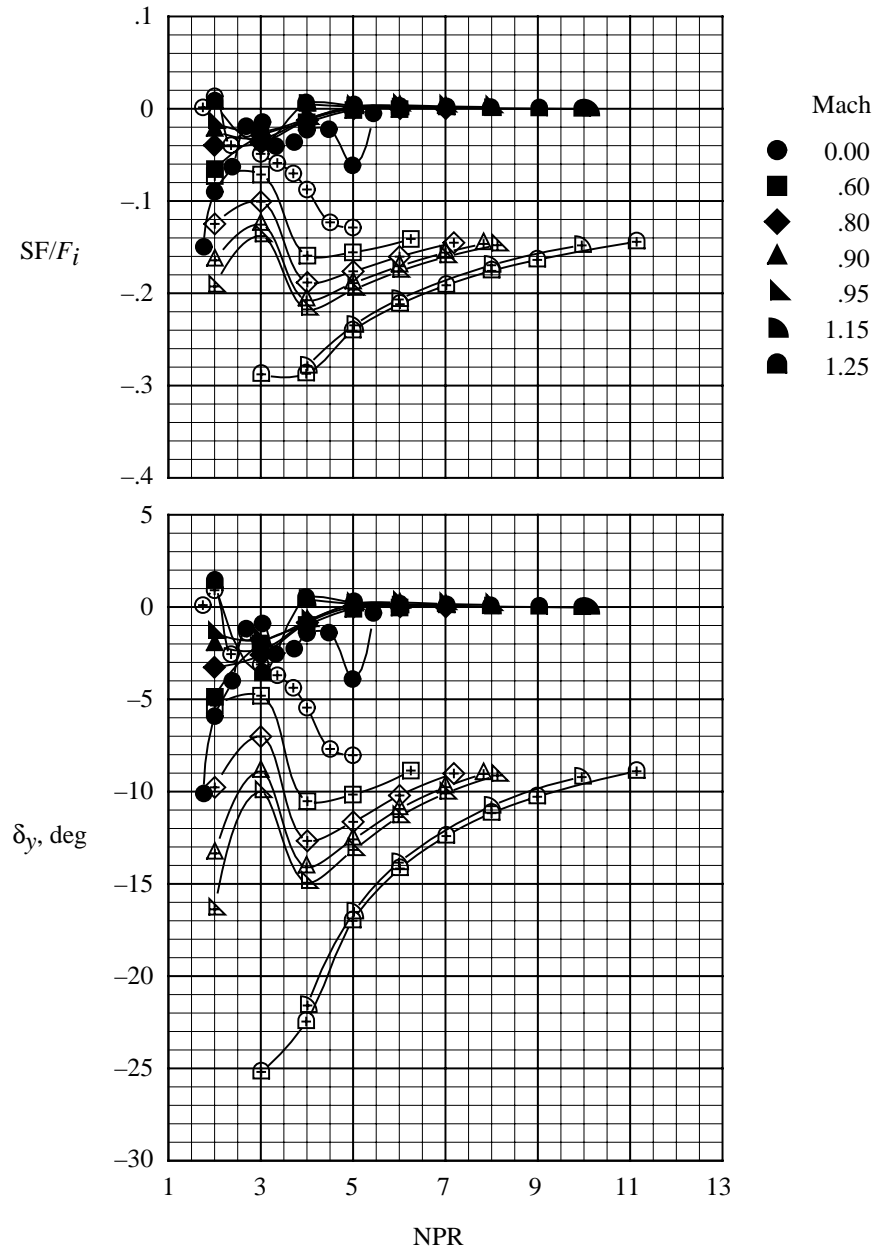
(c) Pitch vector angle and normal force ratio.

Figure 17. Continued.



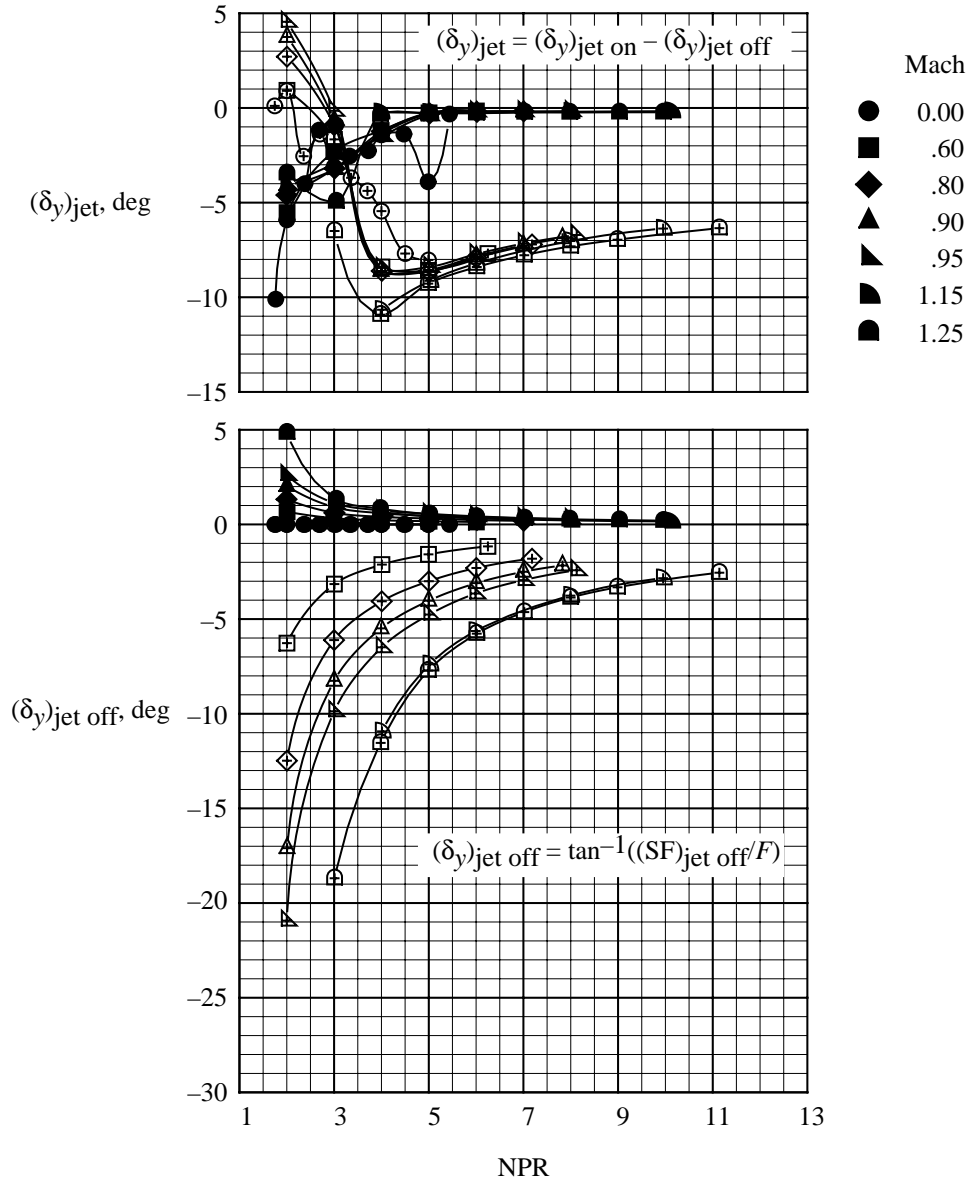
(d) Jet-on and jet-off pitch vector angles.

Figure 17. Continued.



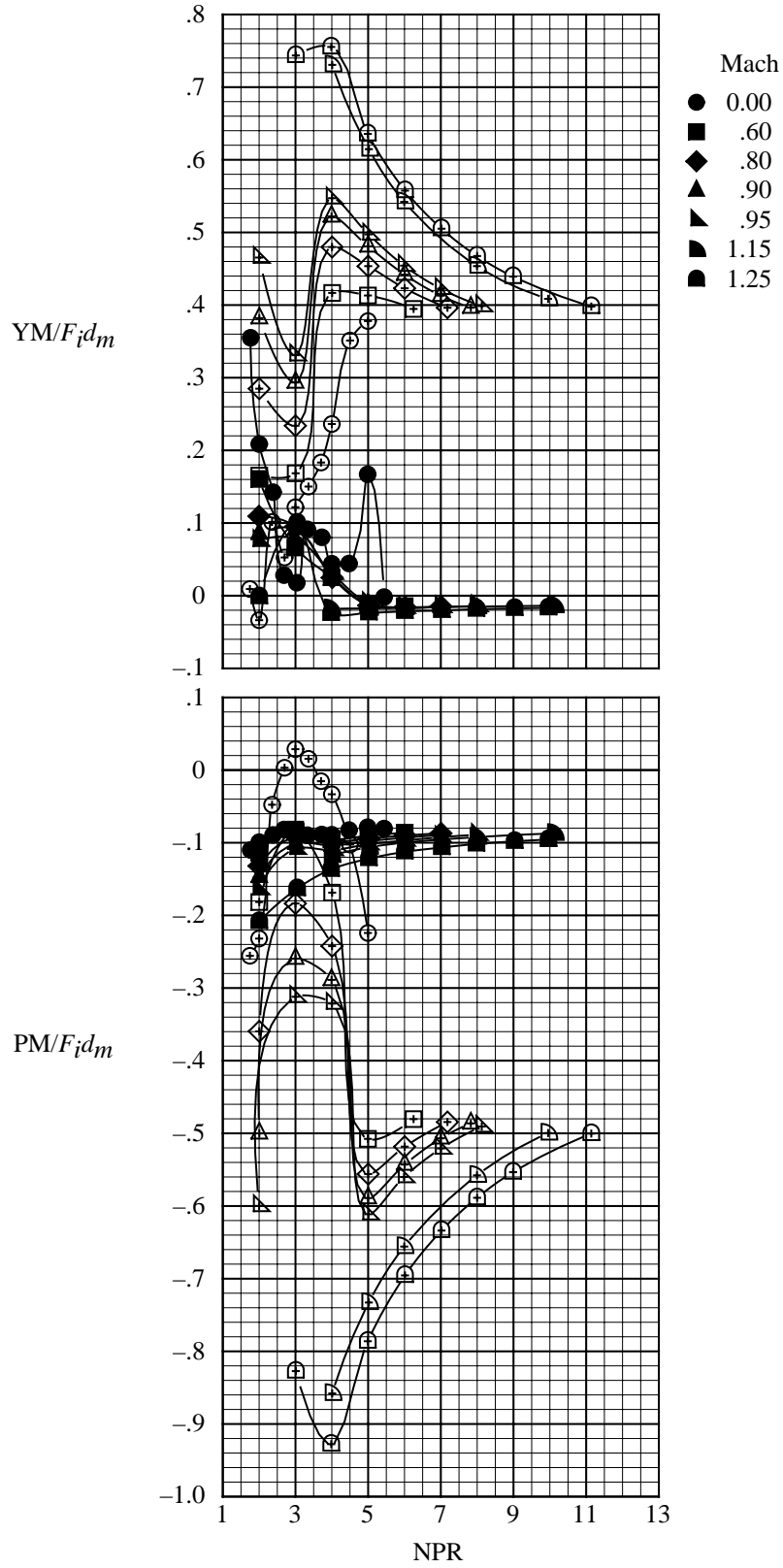
(e) Yaw vector angle and side force ratio.

Figure 17. Continued.



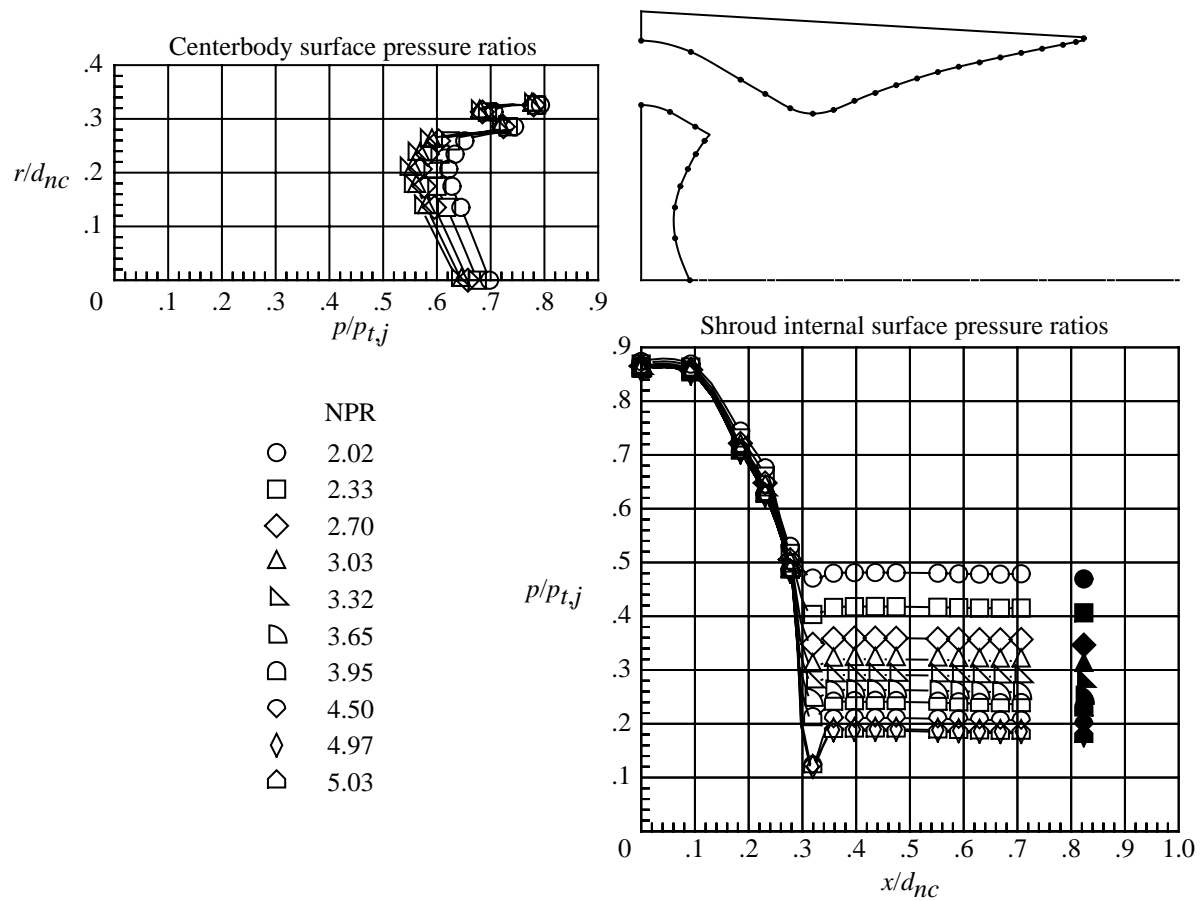
(f) Jet-on and jet-off yaw vector angles.

Figure 17. Continued.



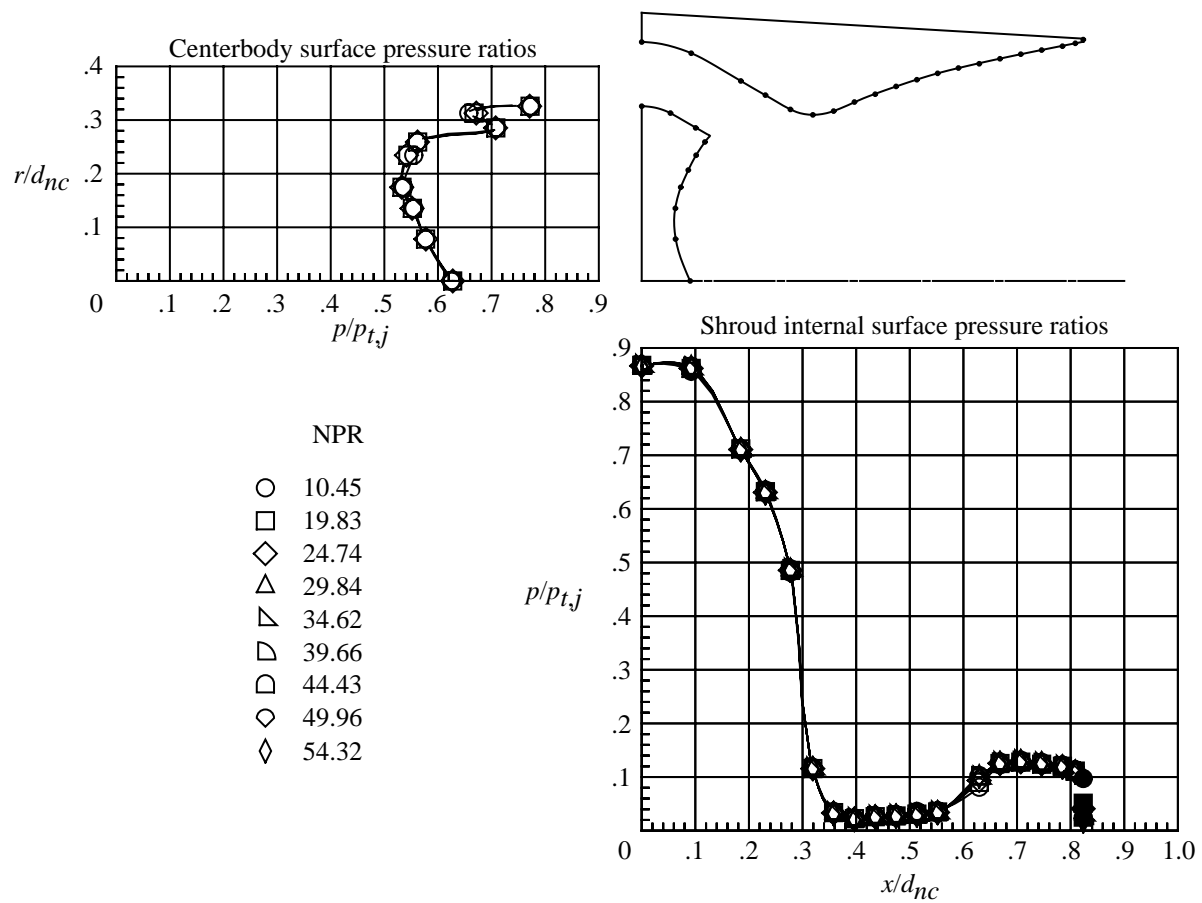
(g) Pitching and yawing moment ratios.

Figure 17. Concluded.



(a) $M = 0$; low nozzle pressure ratios.

Figure 18. Internal and external pressures on nozzle with long unvented shroud and concave centerbody. Solid symbols indicate data at shroud base. Dots on nozzle sketch indicate pressure orifice locations.



(b) $M = 0$; high nozzle pressure ratios.

Figure 18. Continued.

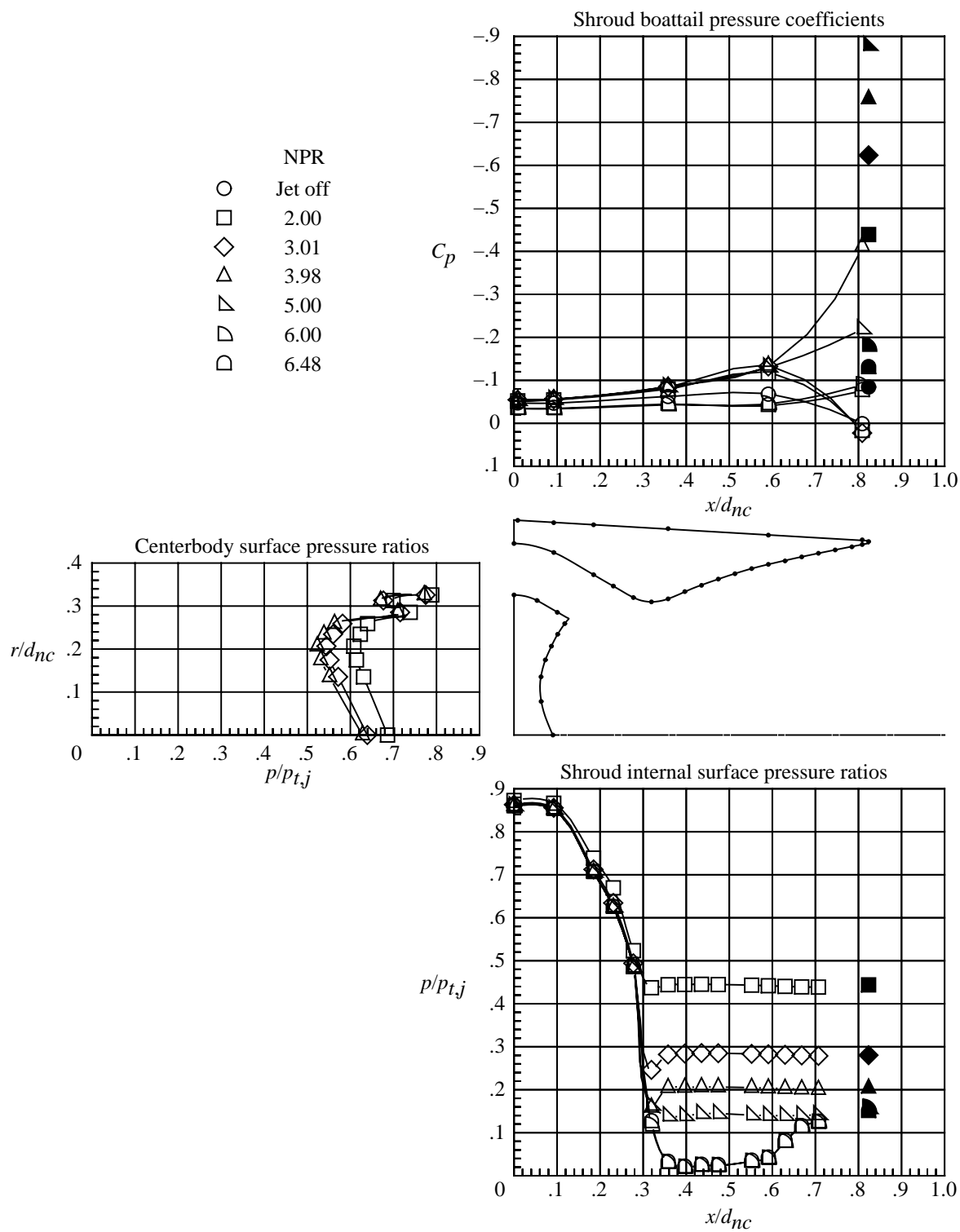
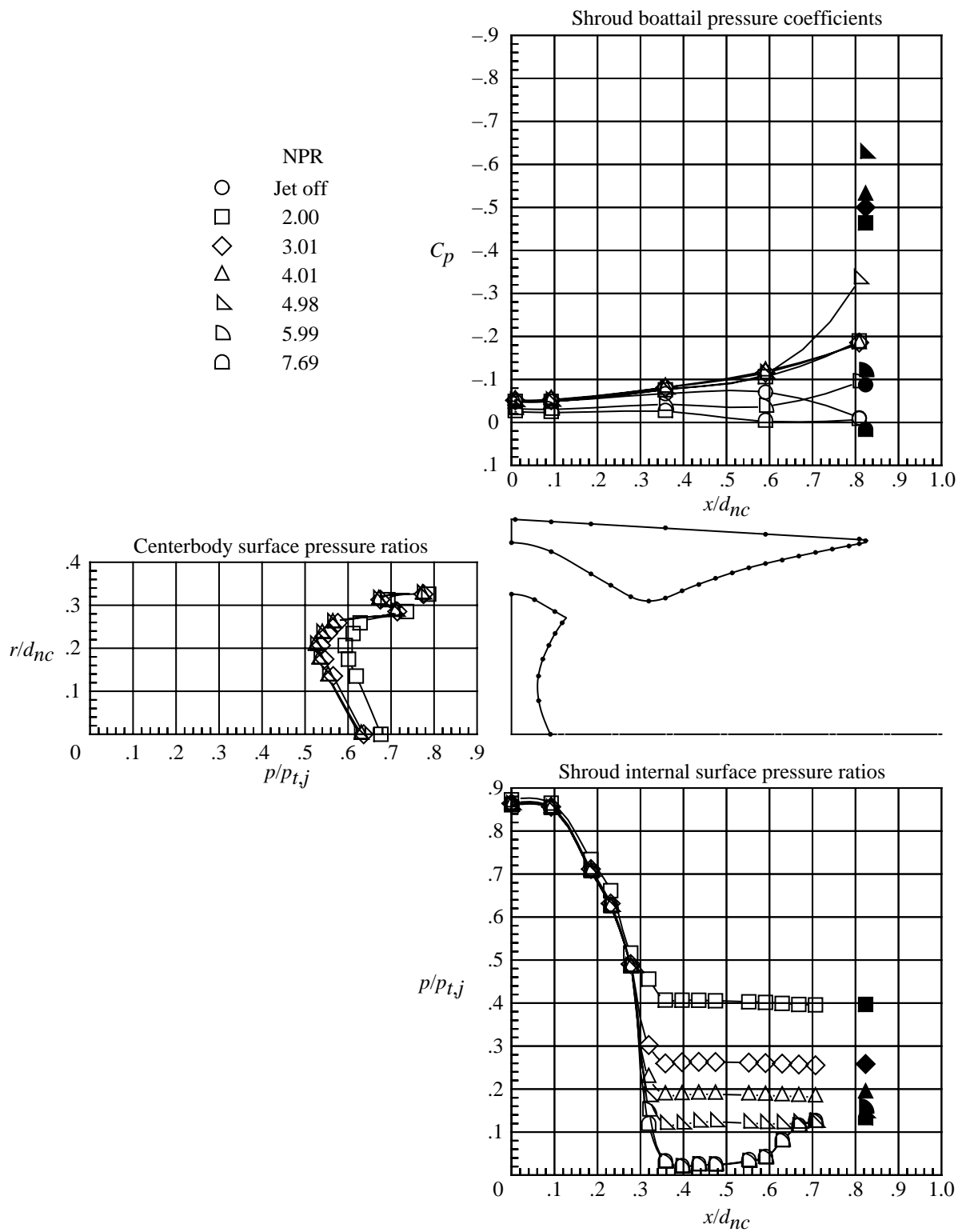
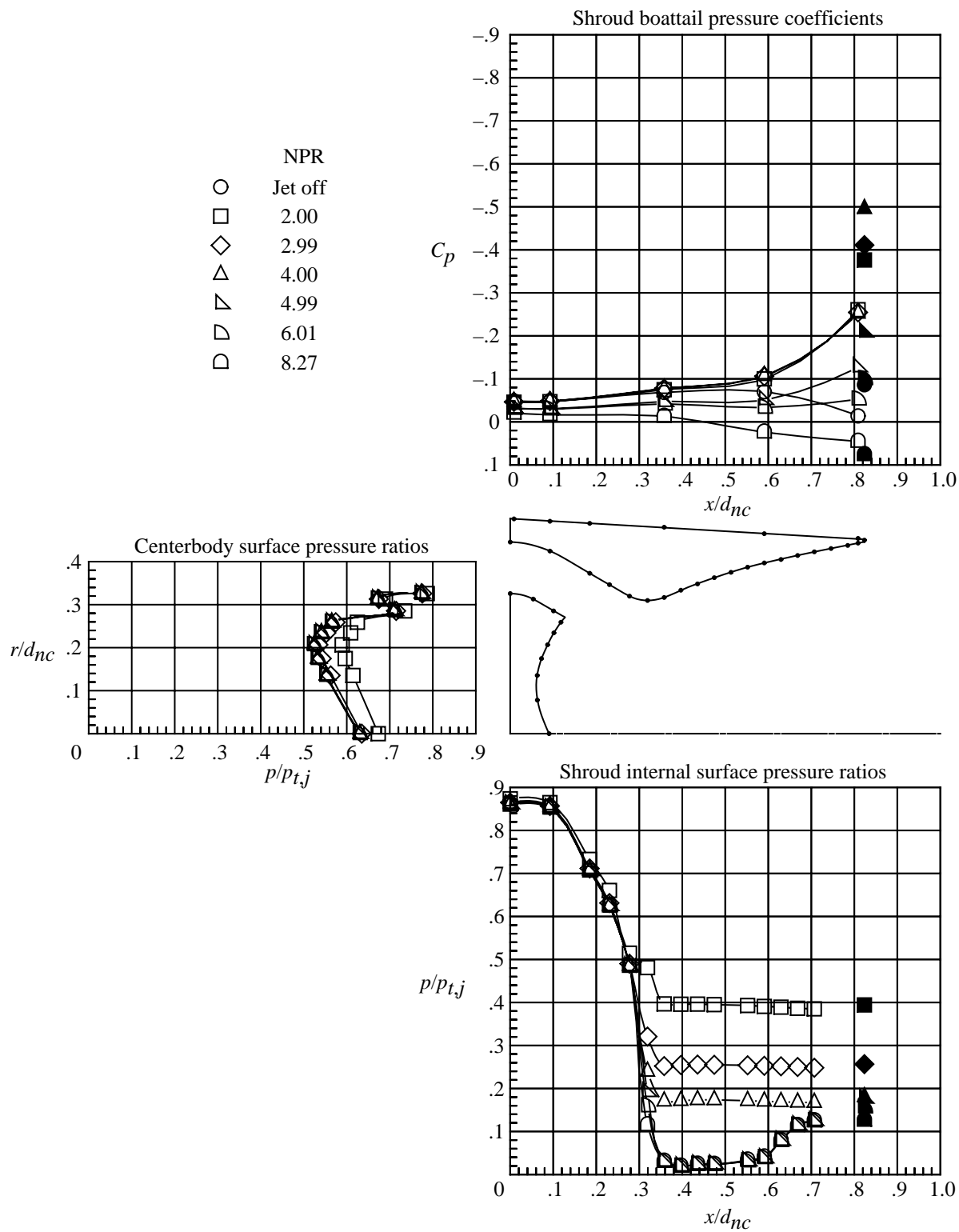


Figure 18. Continued.



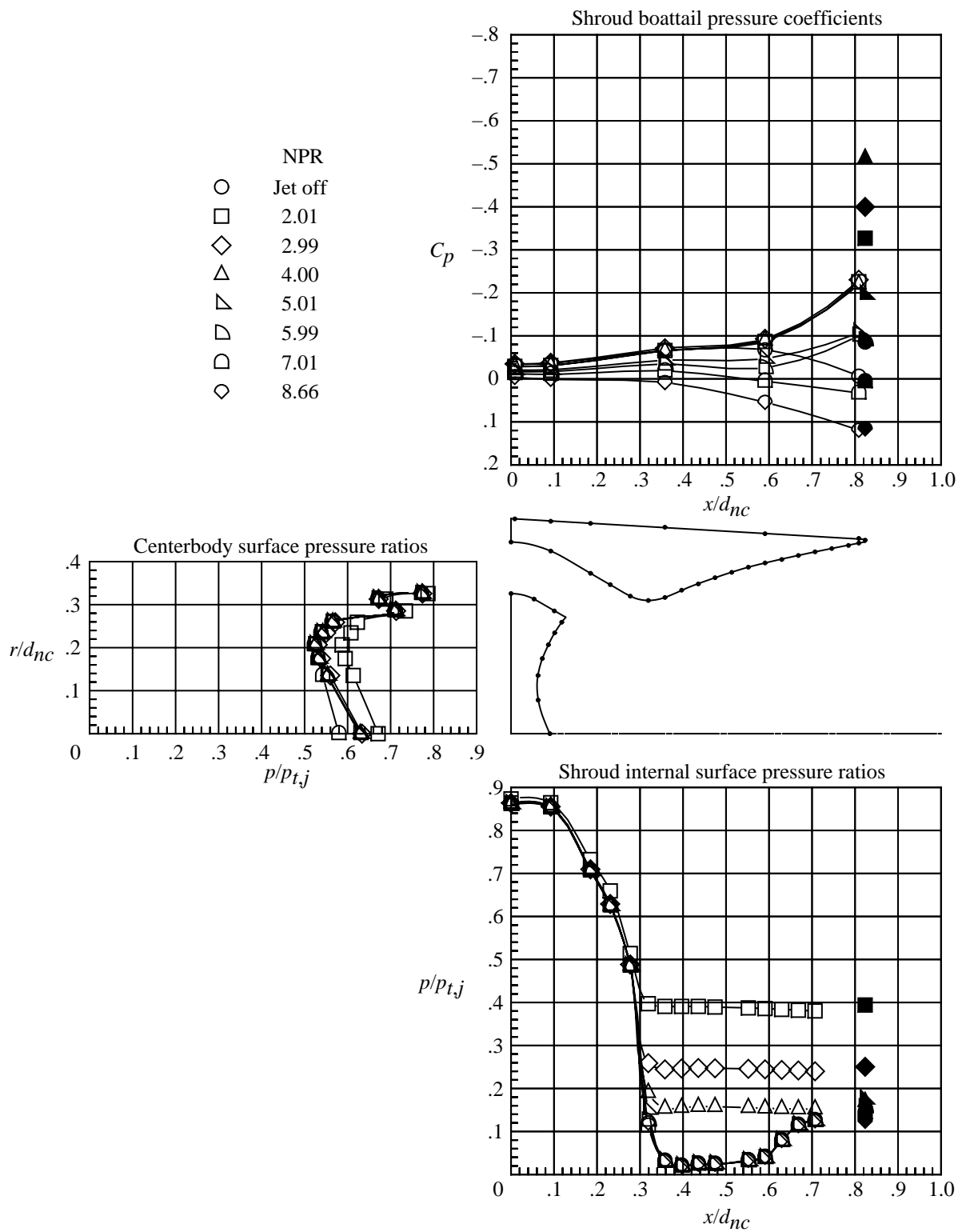
(d) $M = 0.80$.

Figure 18. Continued.



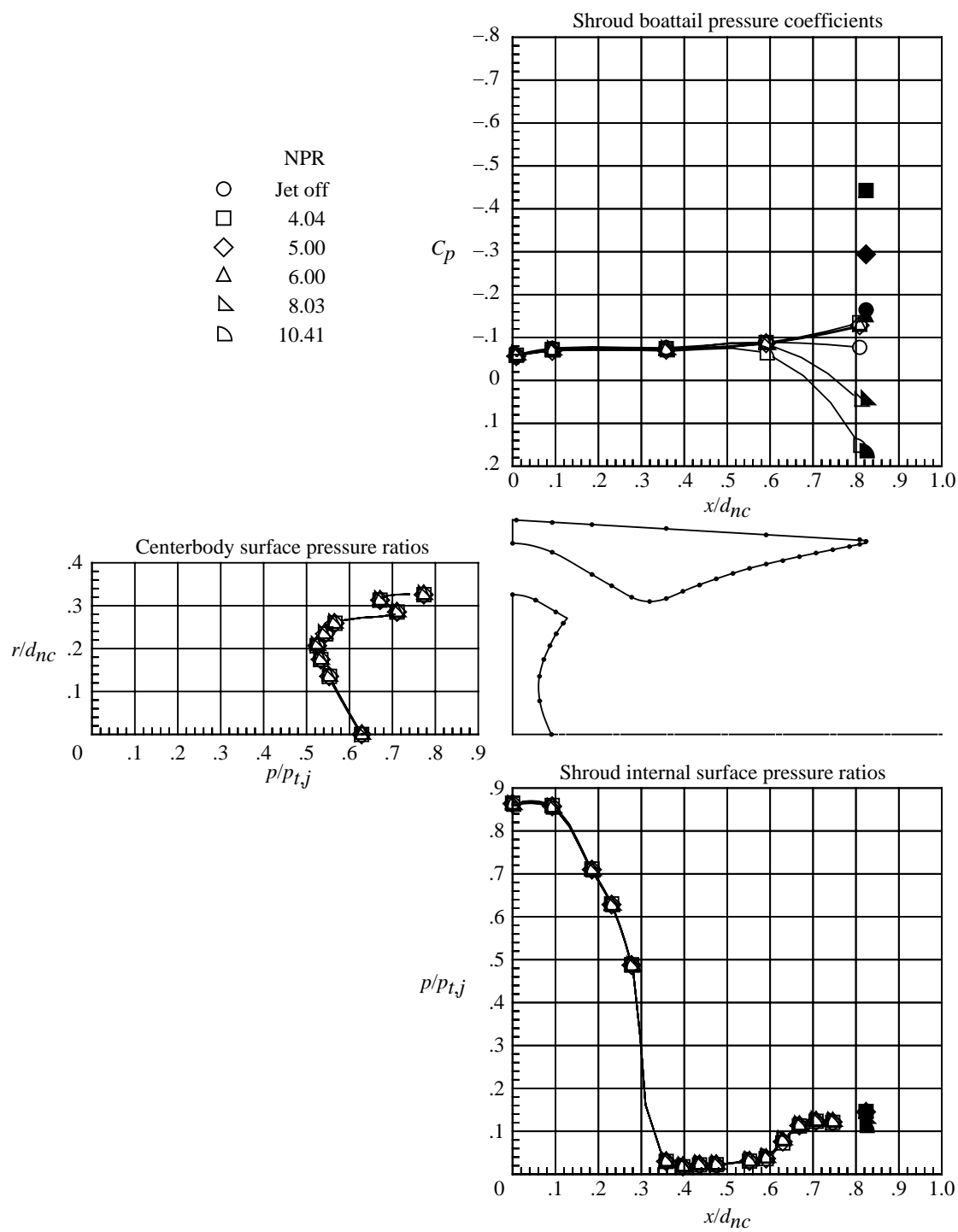
(e) $M = 0.90$.

Figure 18. Continued.



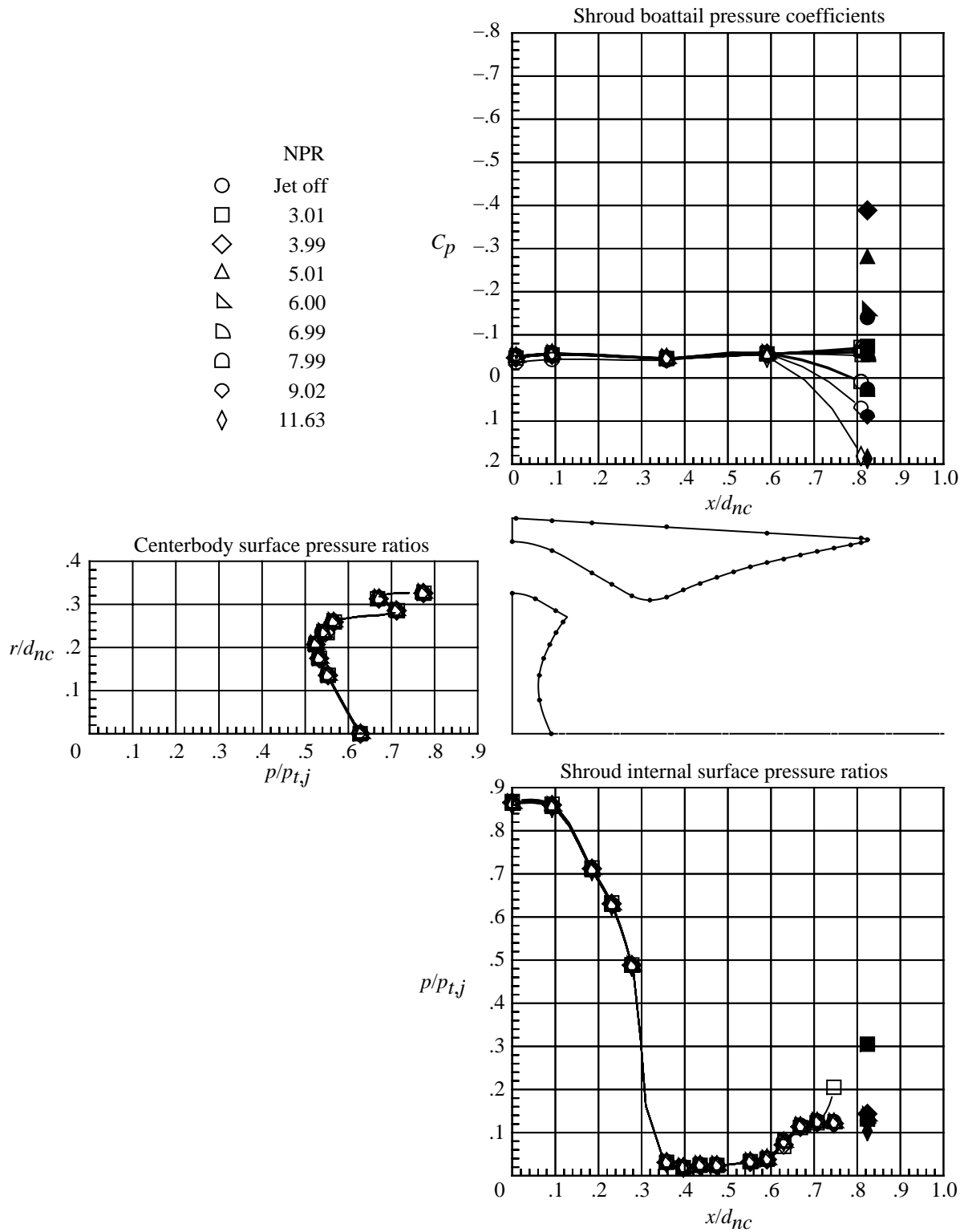
(f) $M = 0.95$.

Figure 18. Continued.



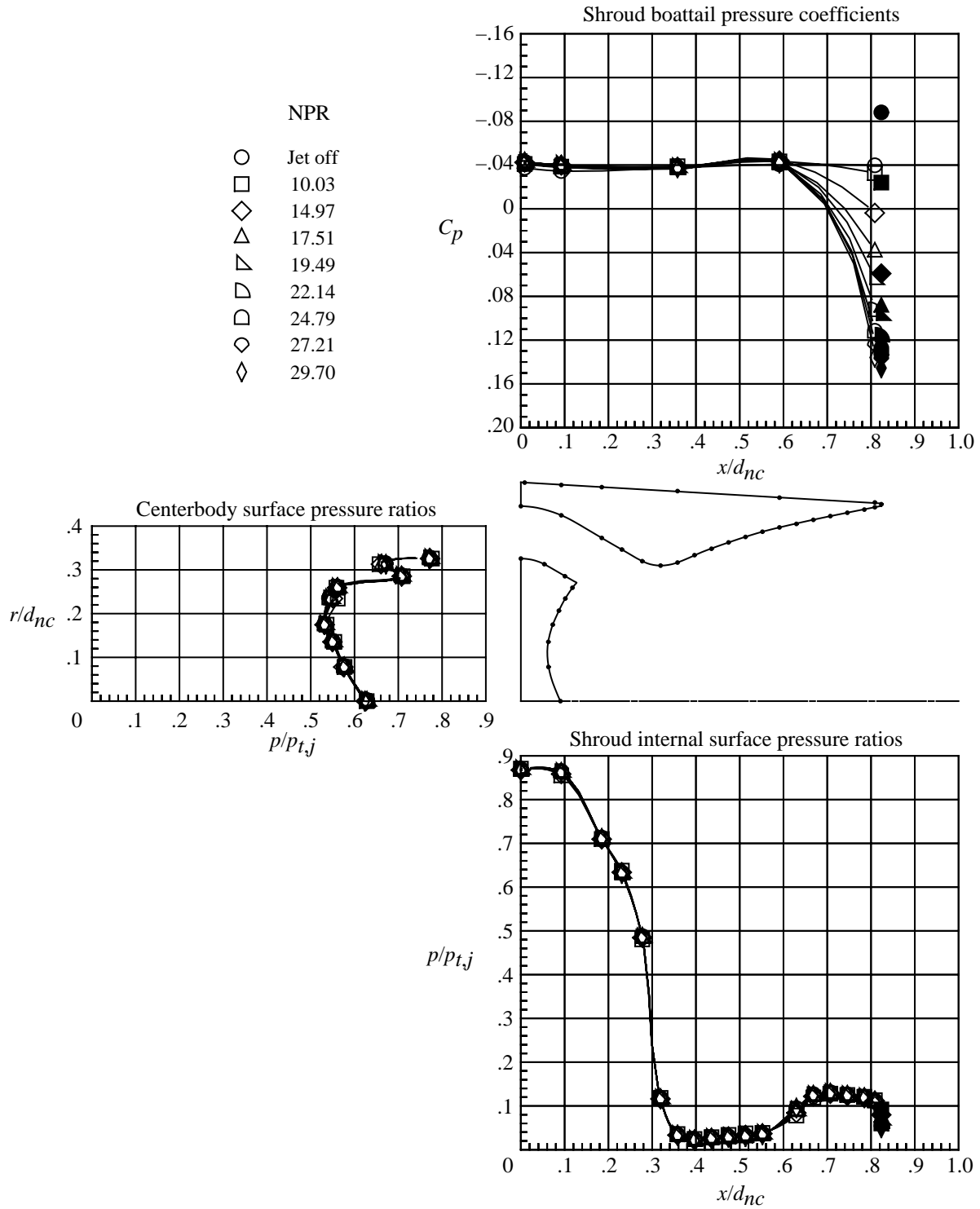
(g) $M = 1.15$.

Figure 18. Continued.



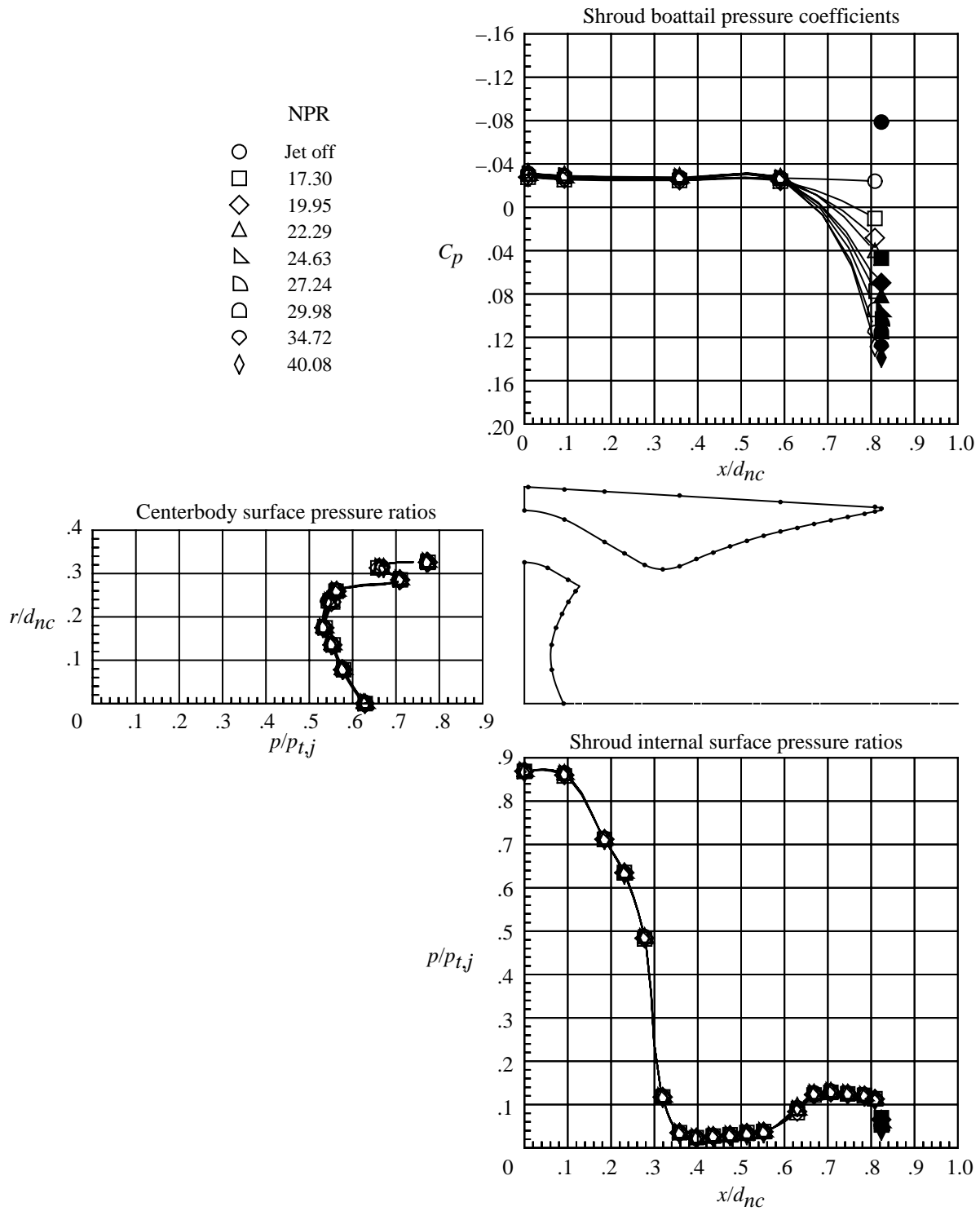
(h) $M = 1.25$.

Figure 18. Continued.



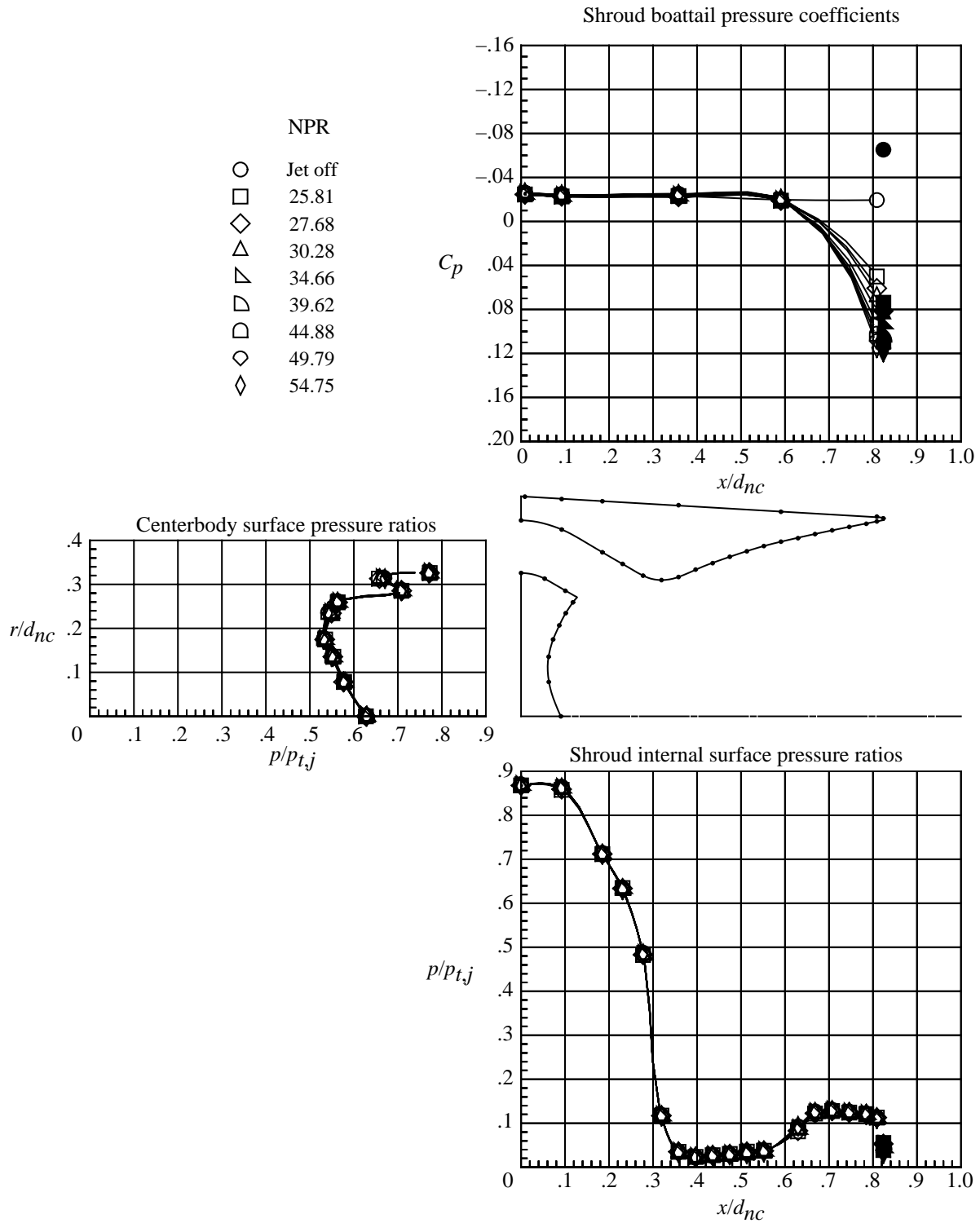
(i) $M = 2.16$.

Figure 18. Continued.



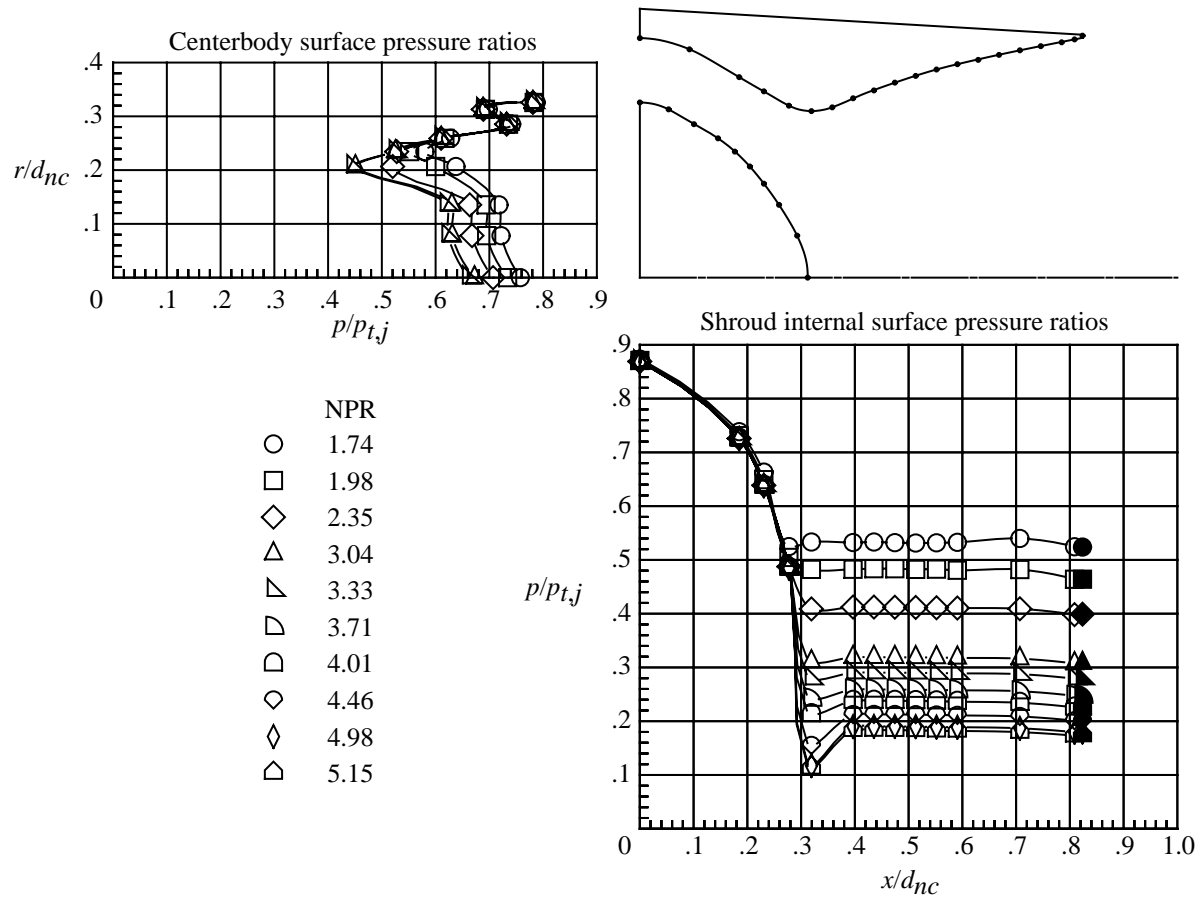
(j) $M = 2.50$.

Figure 18. Continued.



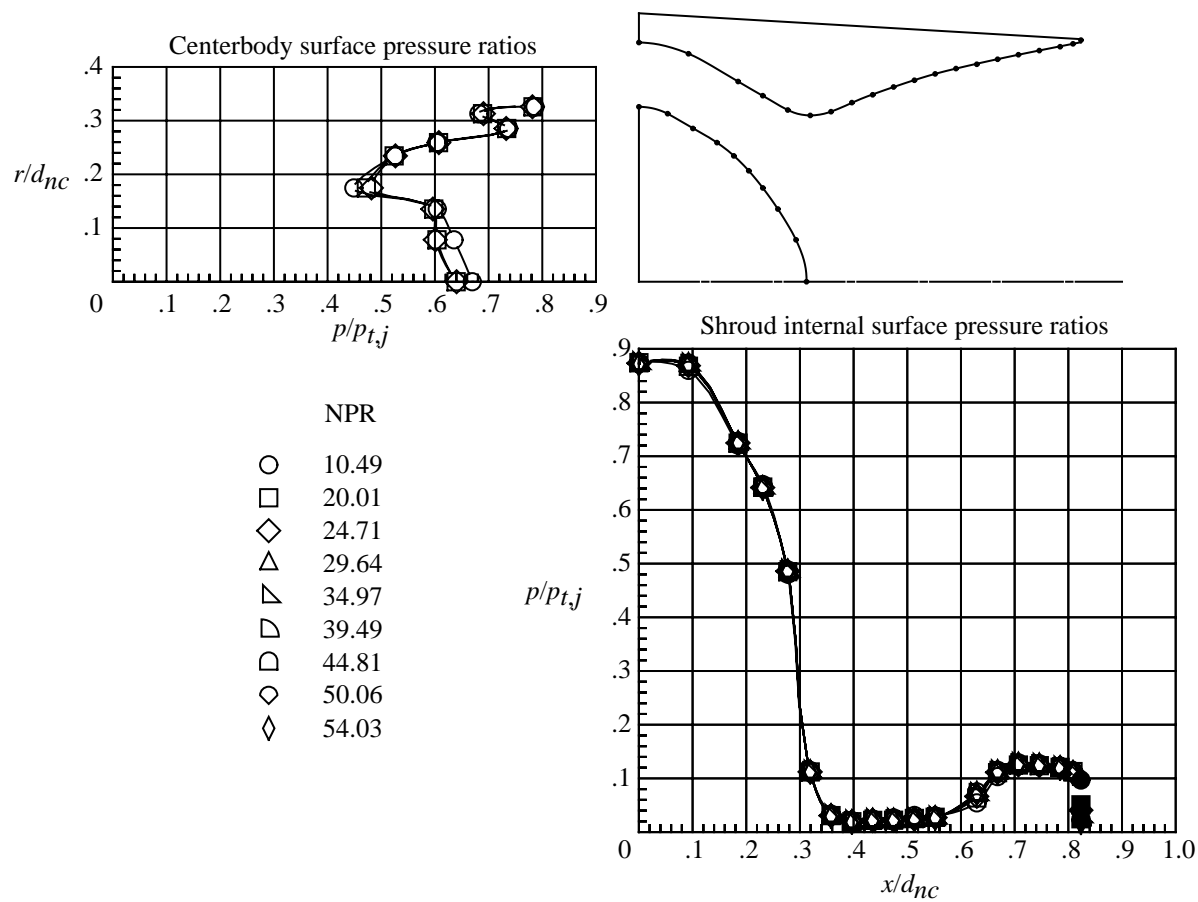
(k) $M = 2.86$.

Figure 18. Concluded.



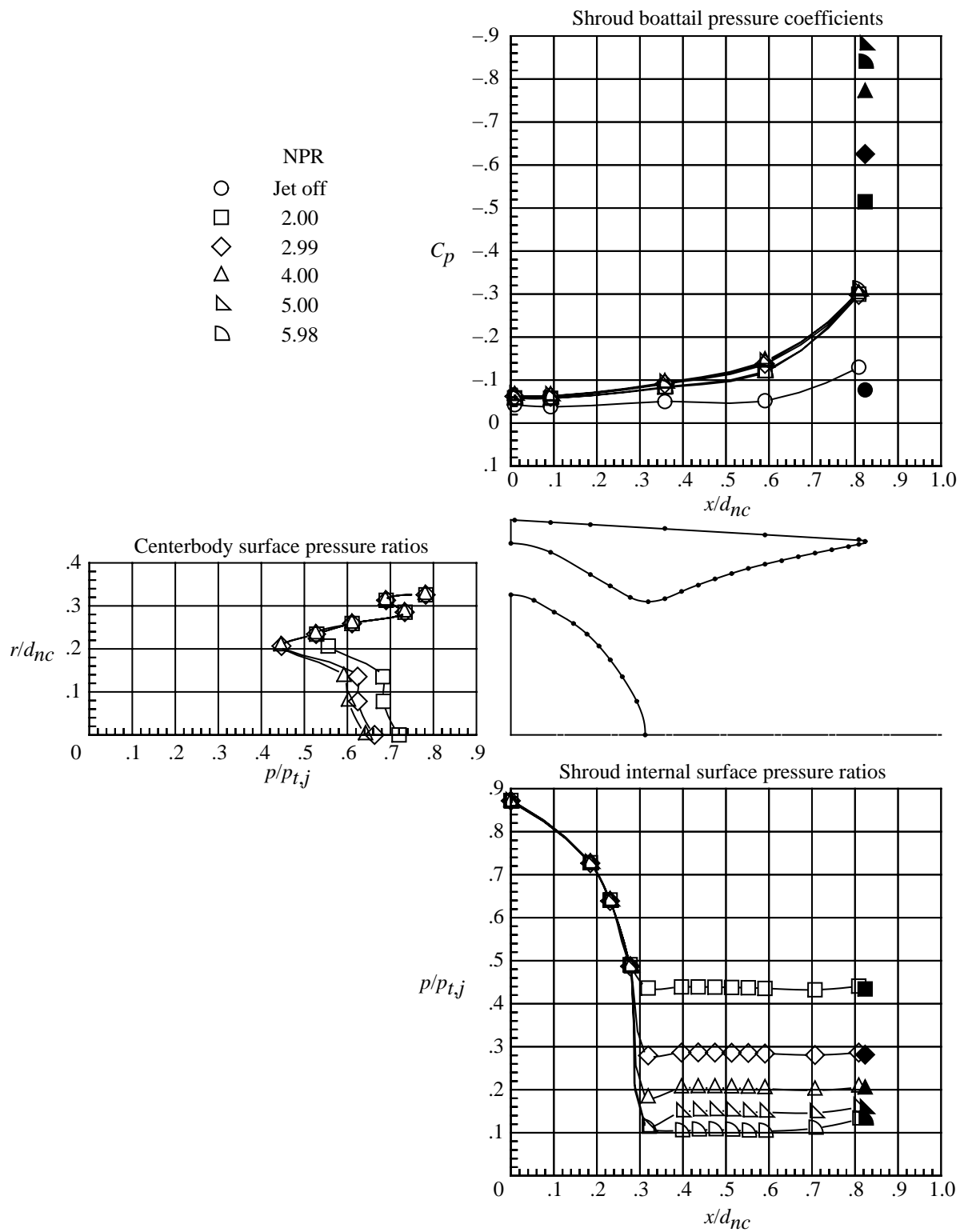
(a) $M = 0$; low nozzle pressure ratios.

Figure 19. Internal and external pressures on nozzle with long unvented shroud and convex centerbody. Solid symbols indicate data at shroud base. Dots on nozzle sketch indicate pressure orifice locations.



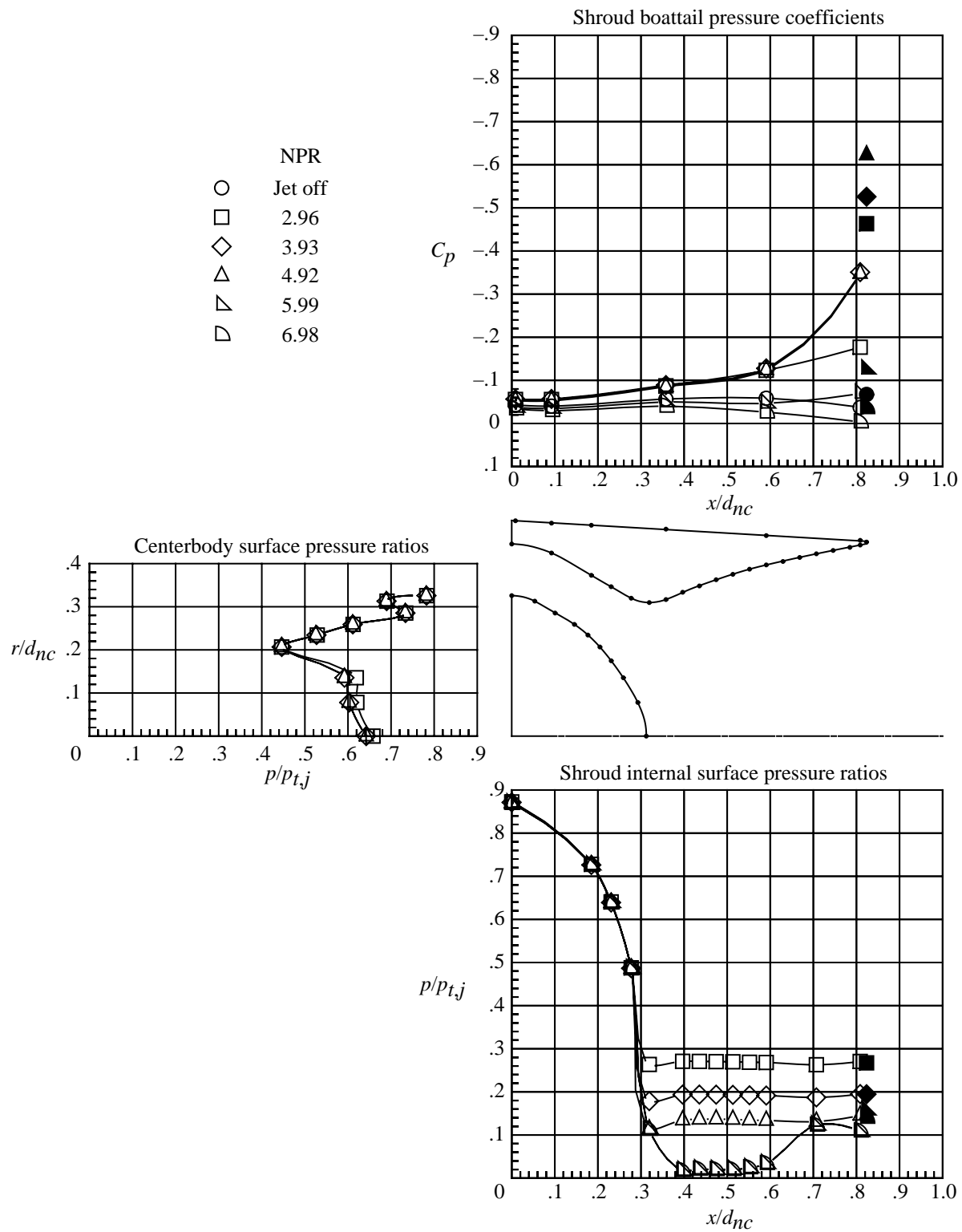
(b) $M = 0$; high nozzle pressure ratios.

Figure 19. Continued.



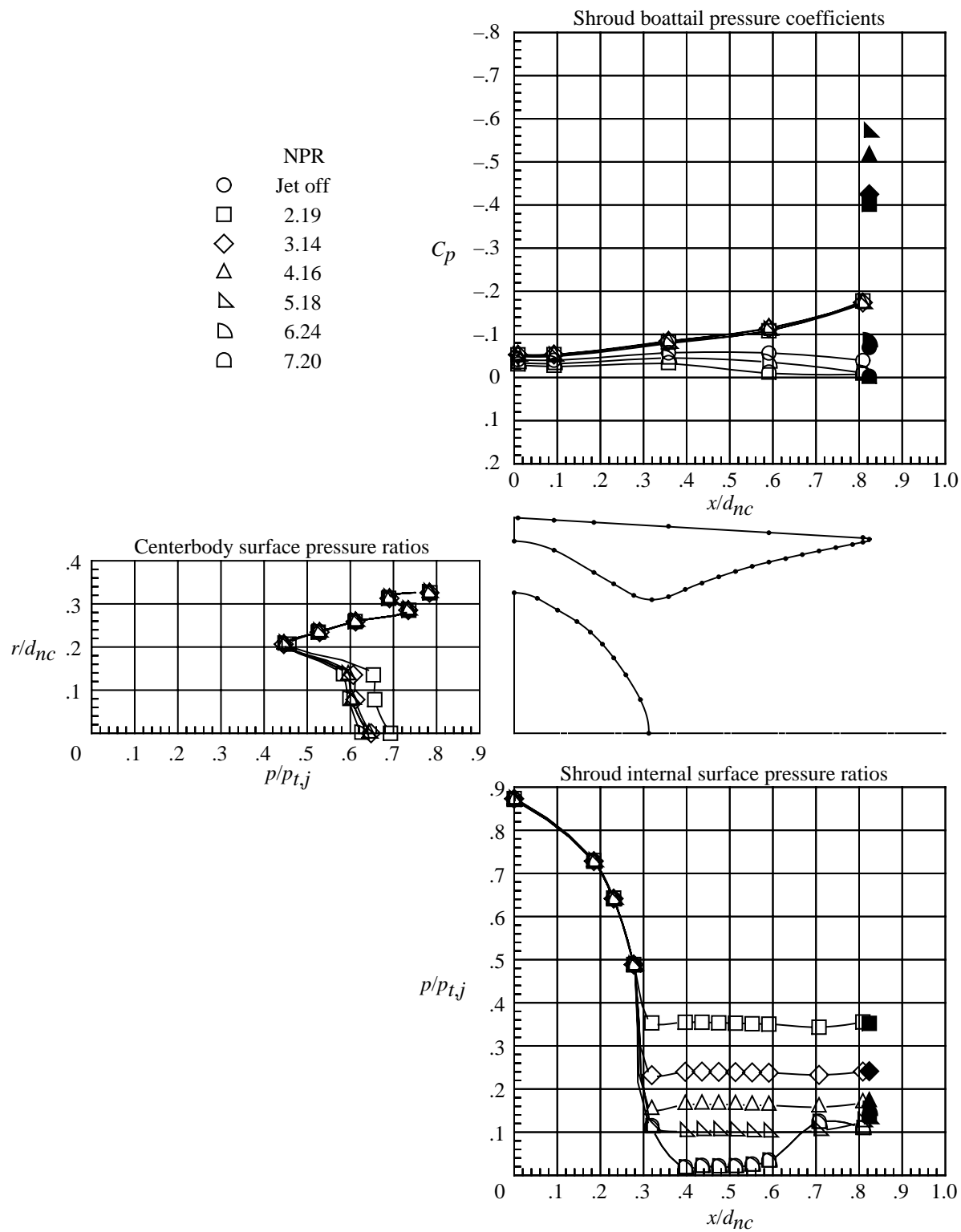
(c) $M = 0.60$.

Figure 19. Continued.



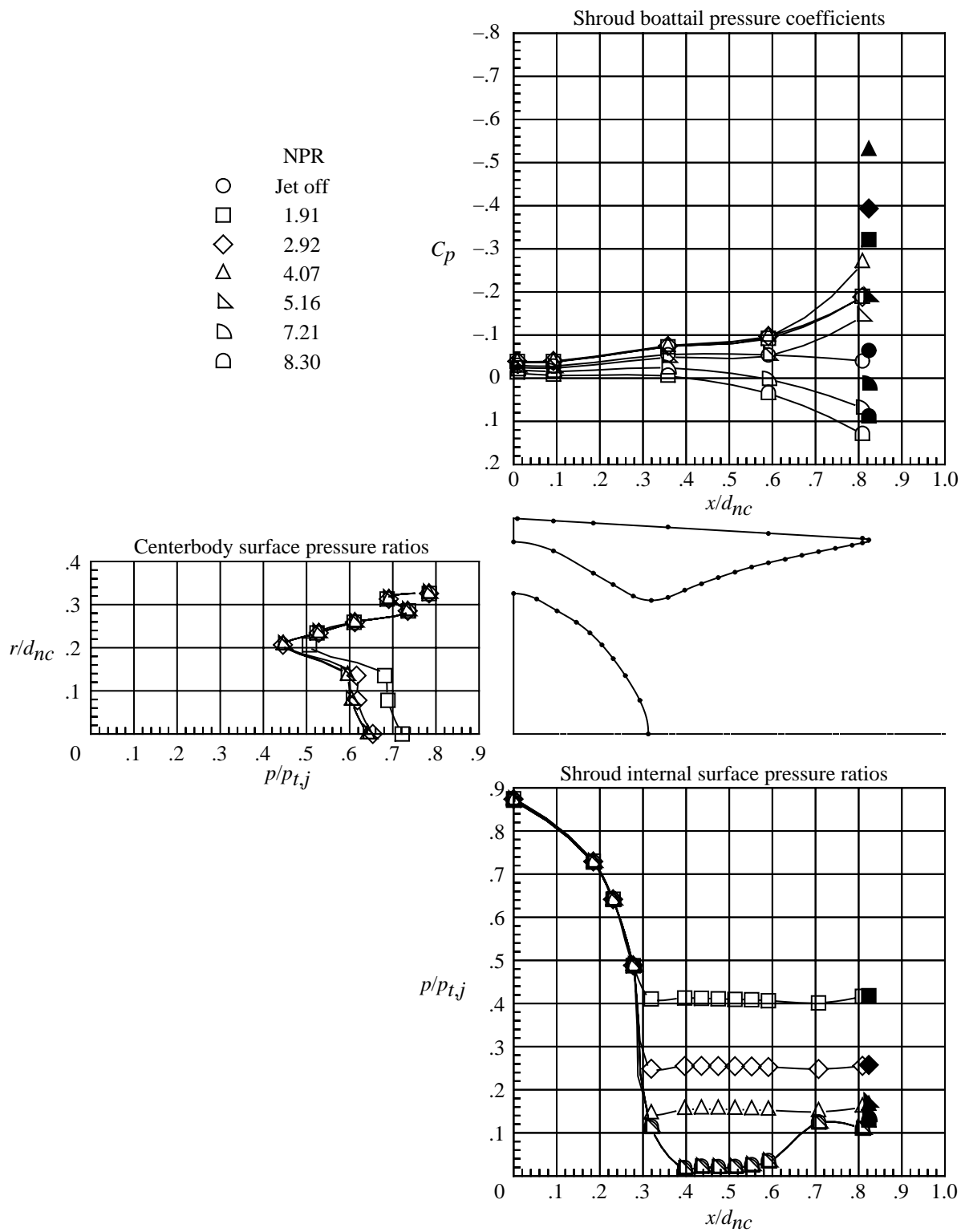
(d) $M = 0.80$.

Figure 19. Continued.



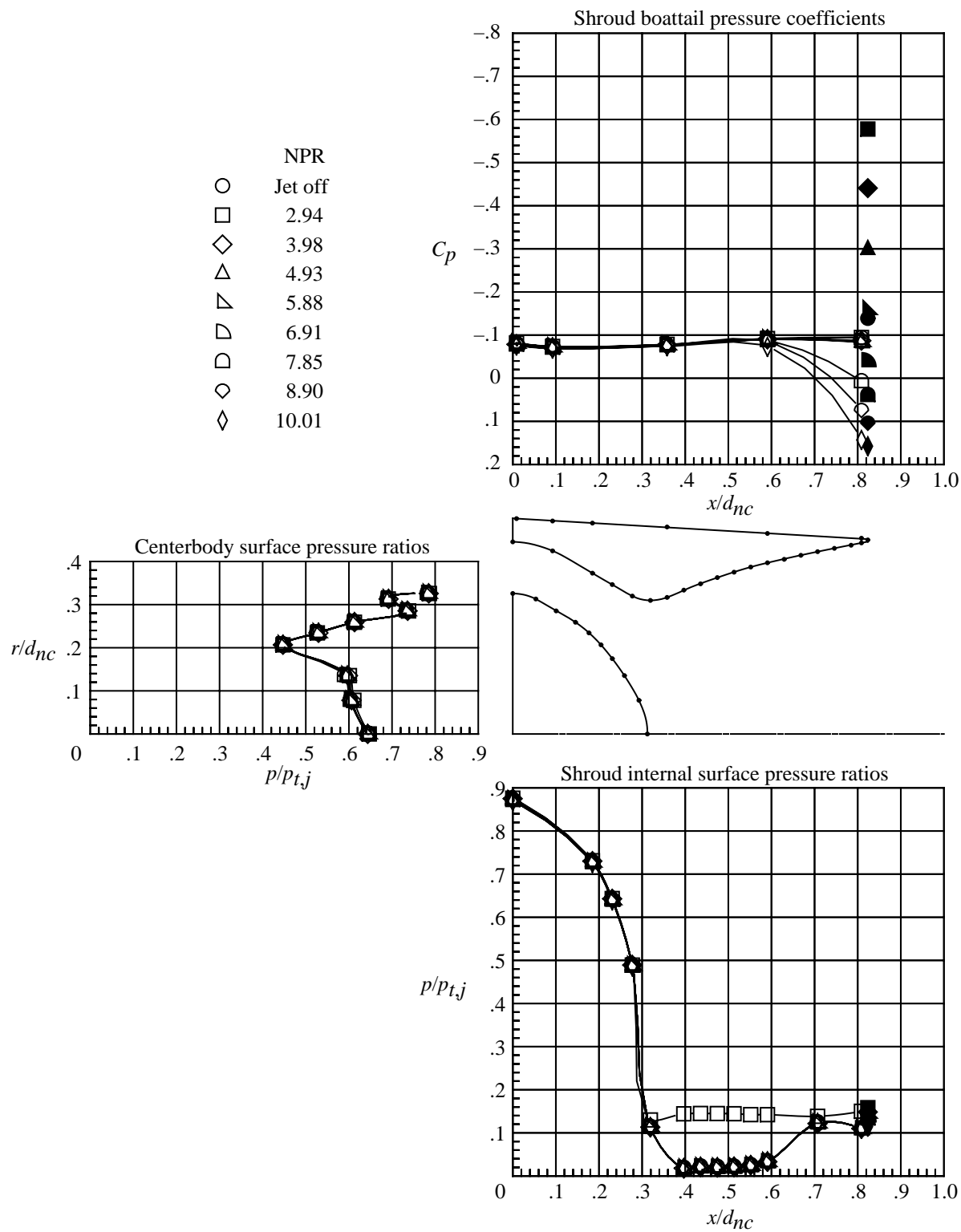
(e) $M = 0.90$.

Figure 19. Continued.



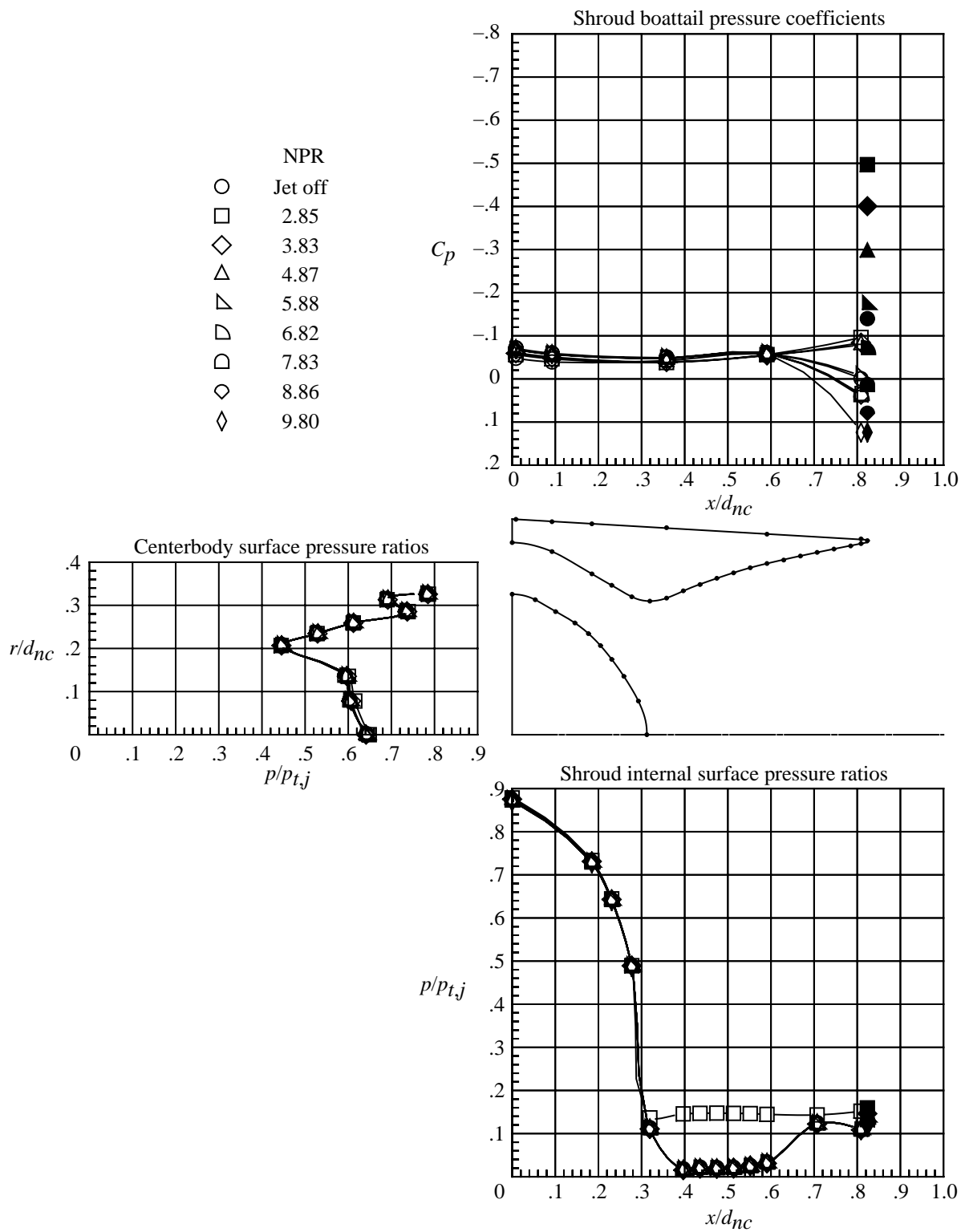
(f) $M = 0.95$.

Figure 19. Continued.



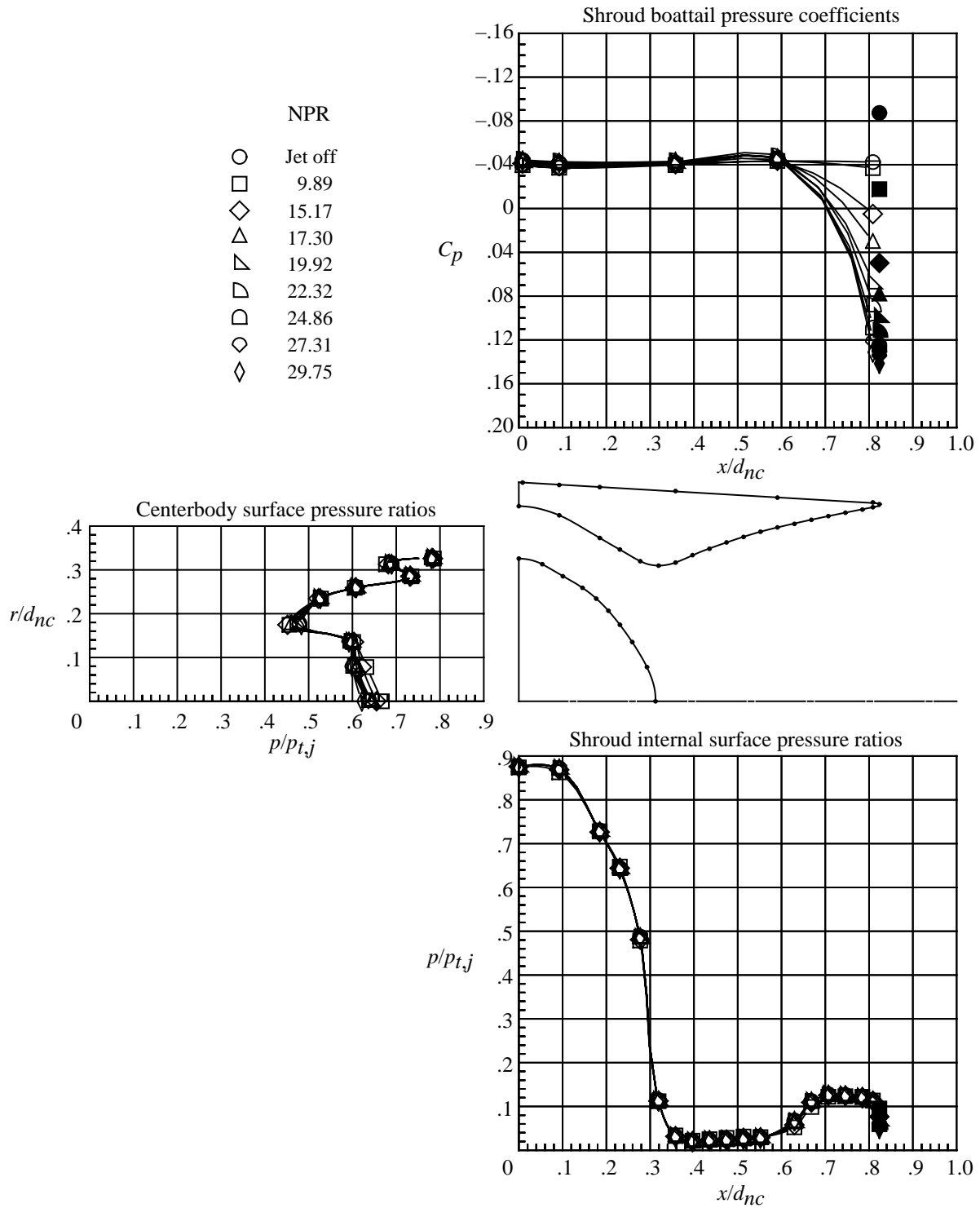
(g) $M = 1.15$.

Figure 19. Continued.



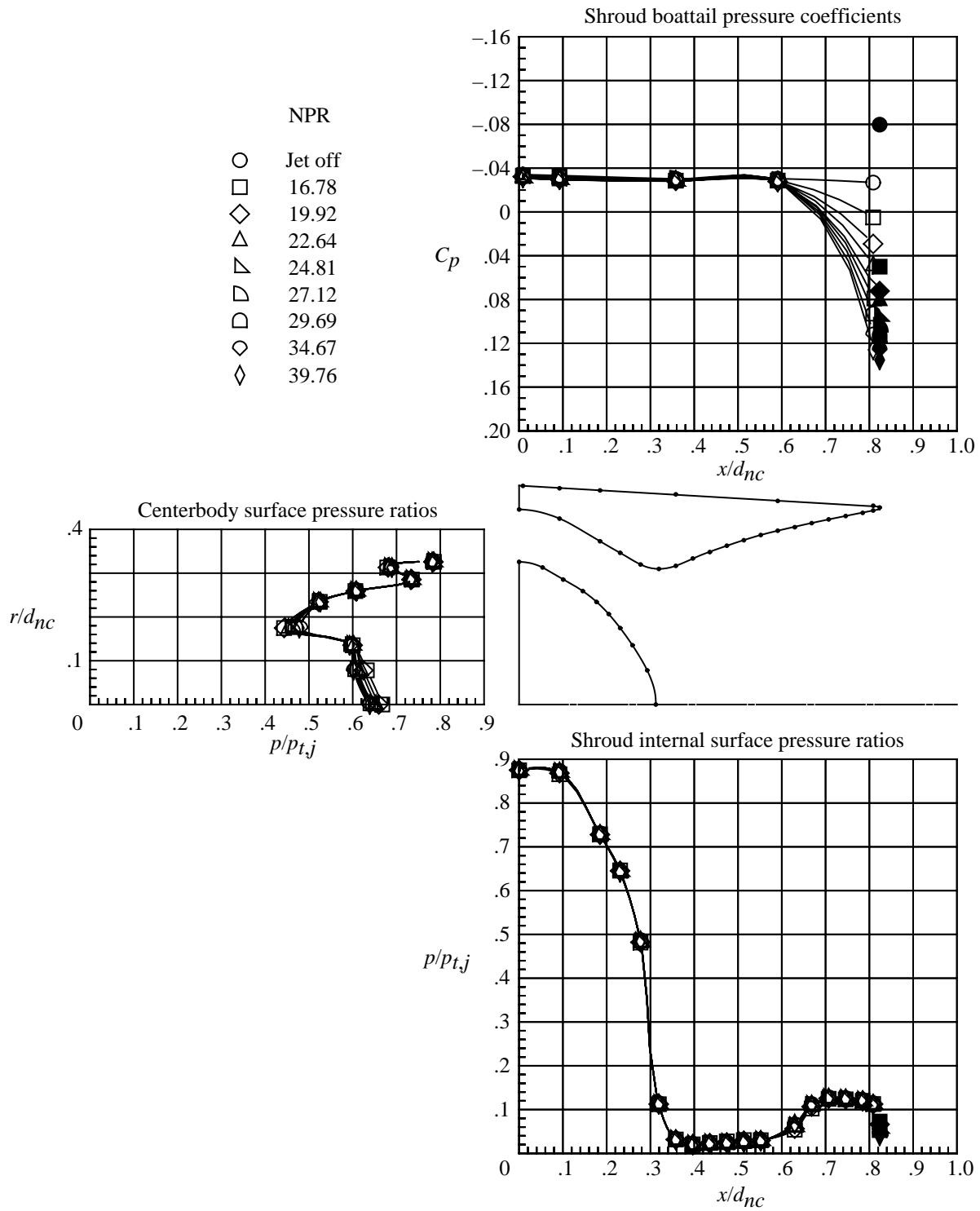
(h) $M = 1.25$.

Figure 19. Continued.



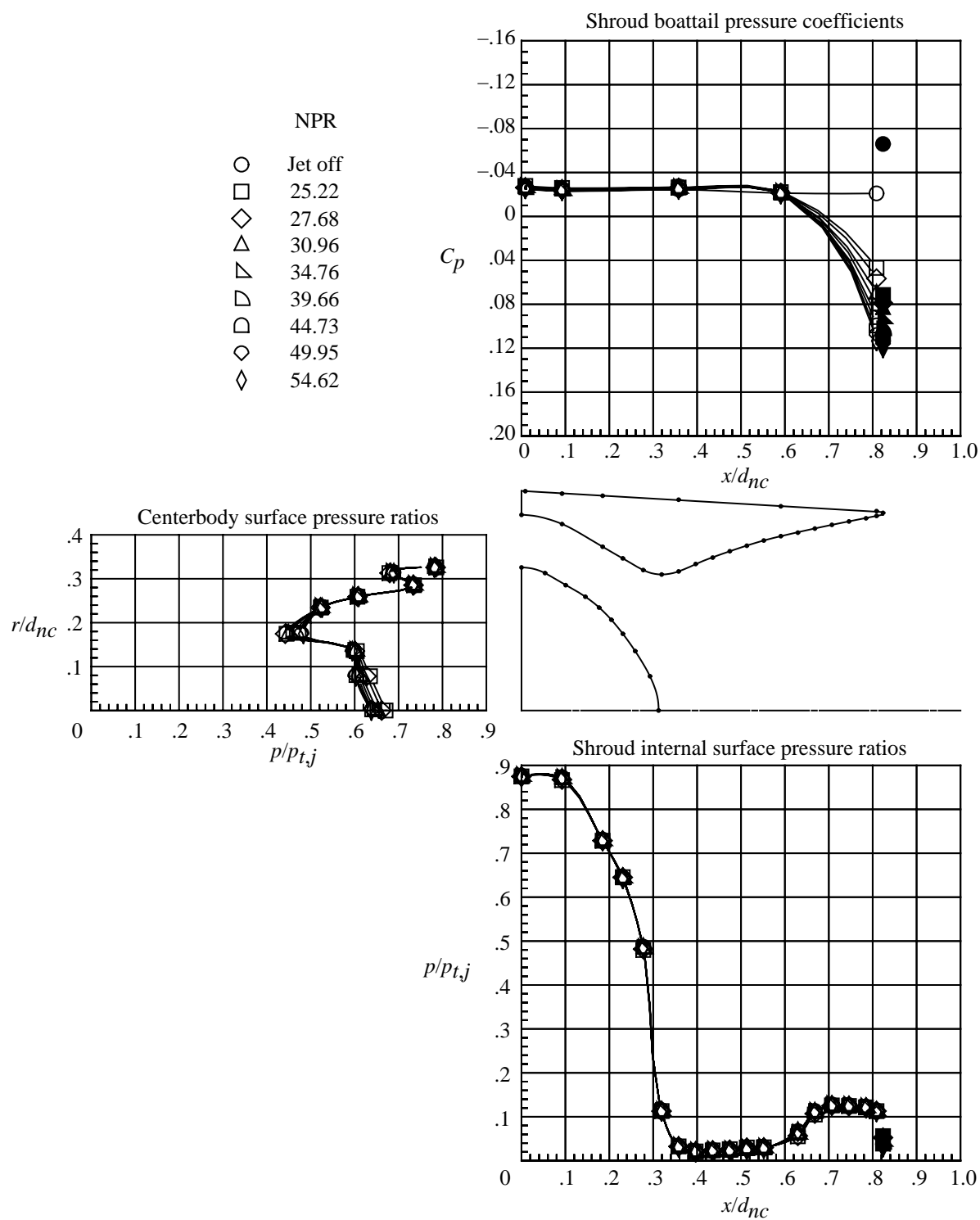
(i) $M = 2.16$.

Figure 19. Continued.



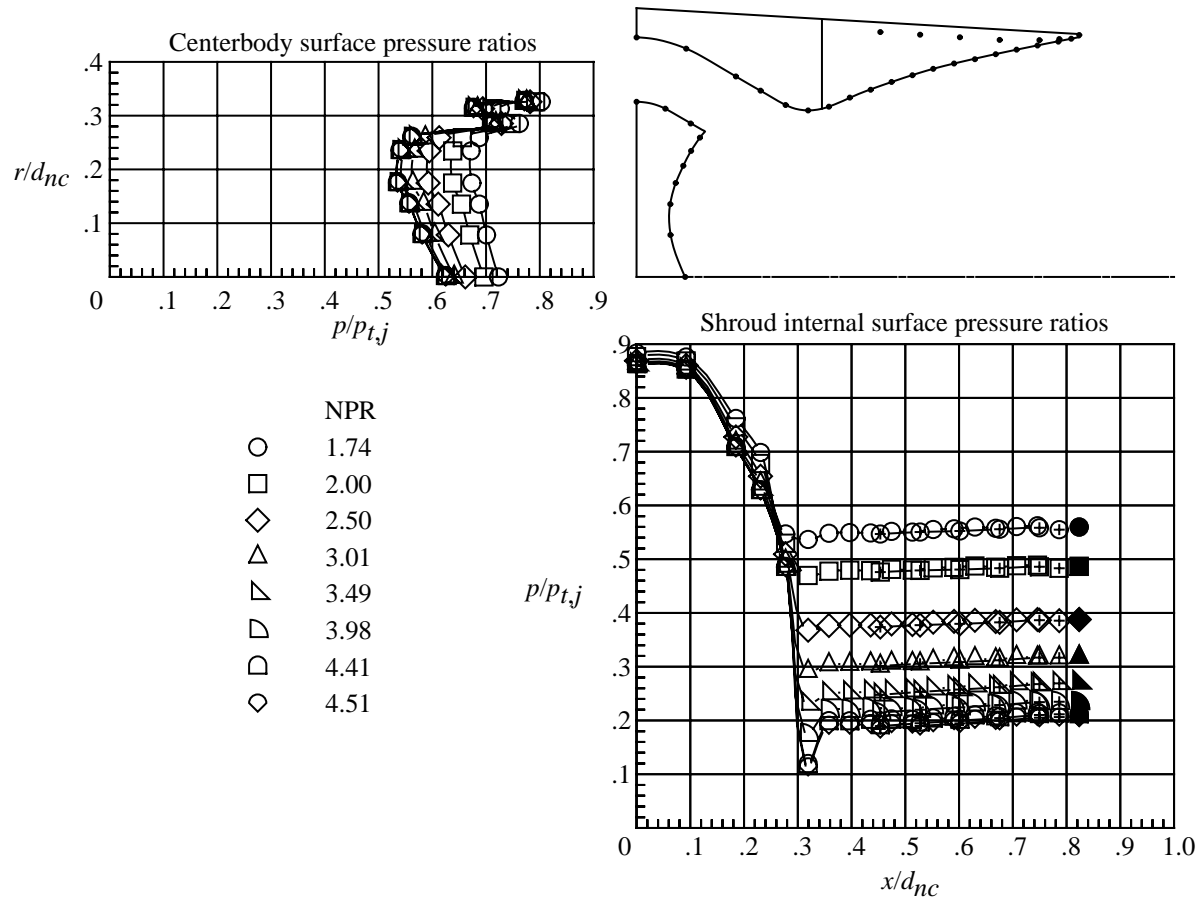
(j) $M = 2.50$.

Figure 19. Continued.



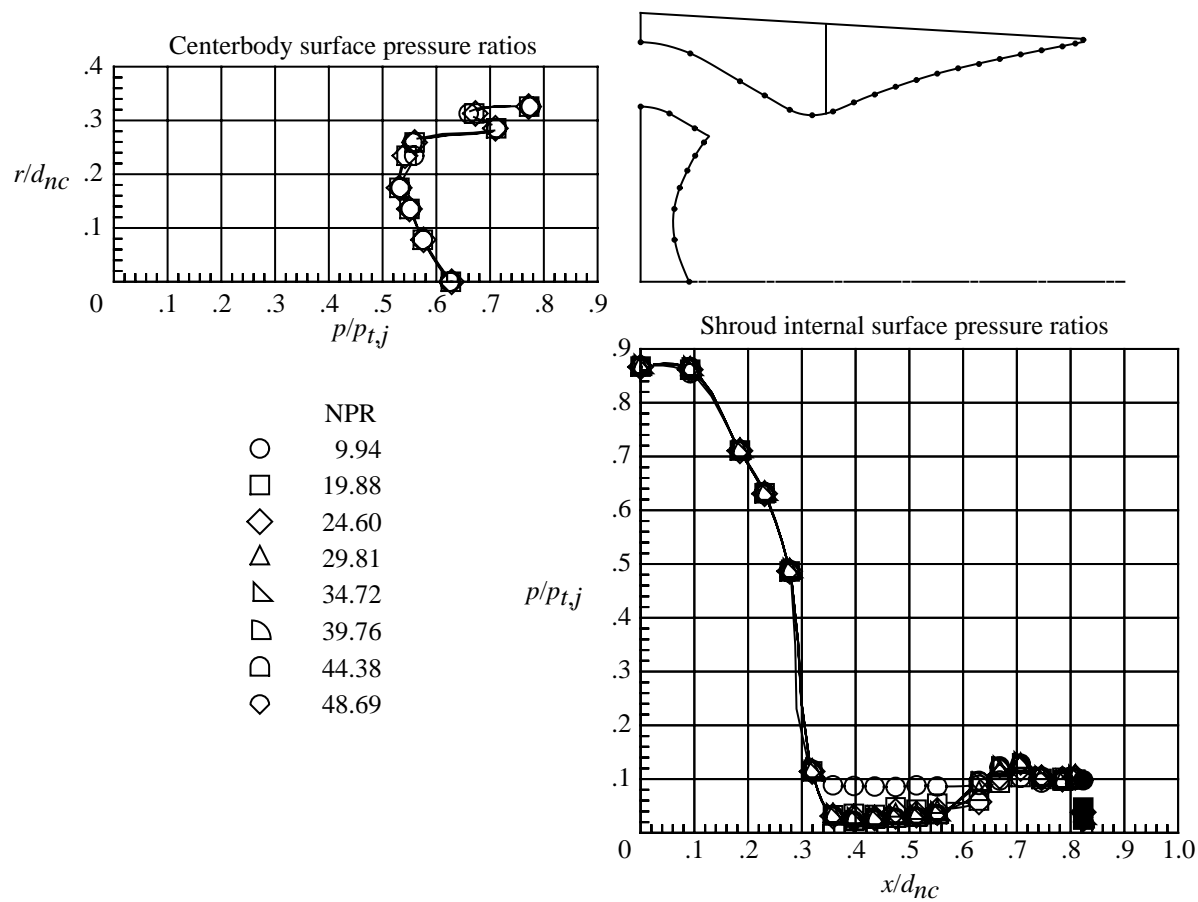
(k) $M = 2.86$.

Figure 19. Concluded.



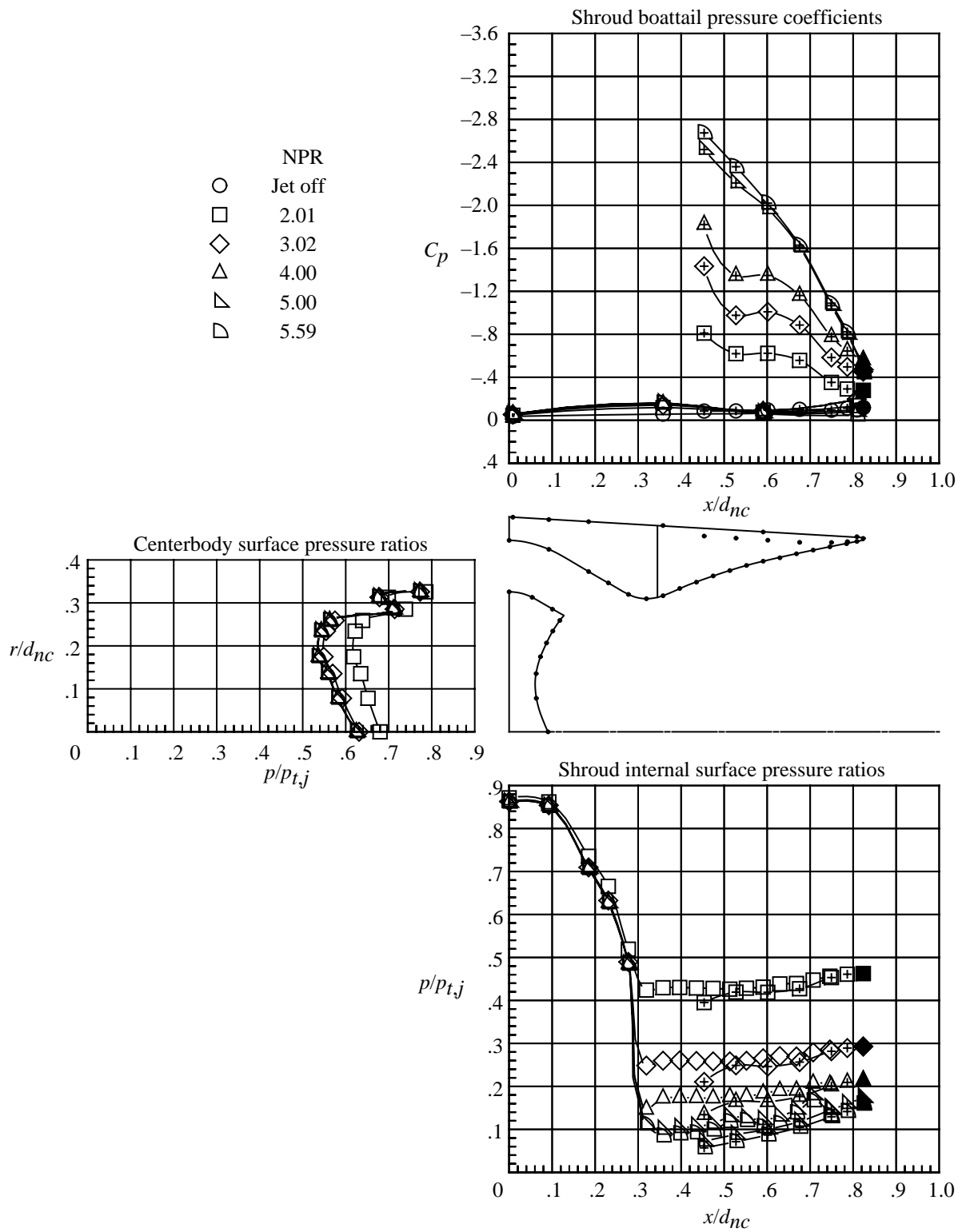
(a) $M = 0$; low nozzle pressure ratios.

Figure 20. Internal and external pressures on nozzle with long axially vented shroud and concave centerbody. Solid symbols indicate data at shroud base and plus signs in symbols indicate data on walls of vent. Dots on nozzle sketch indicate pressure orifice locations.



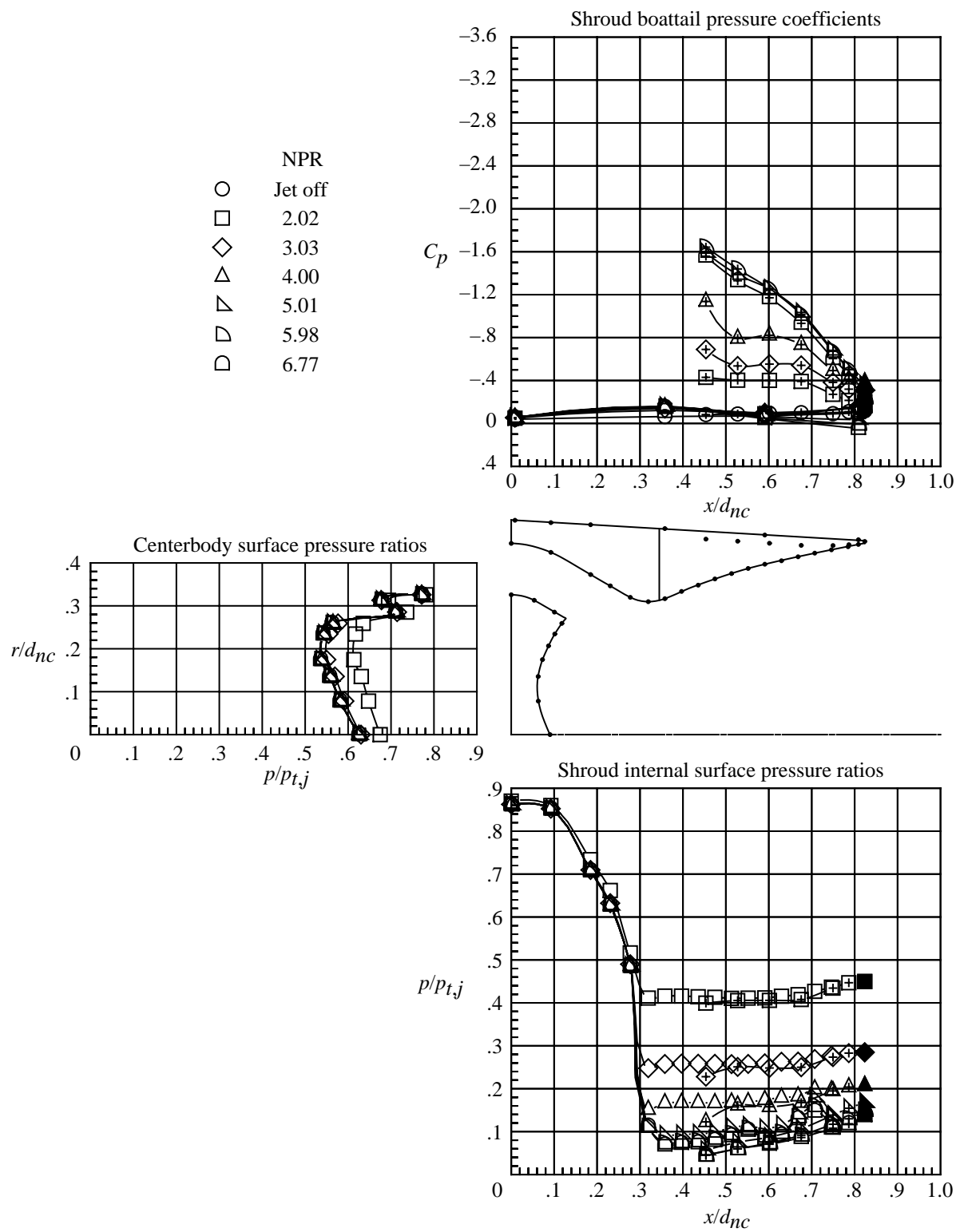
(b) $M = 0$; high nozzle pressure ratios.

Figure 20. Continued.



(c) $M = 0.60$.

Figure 20. Continued.



(d) $M = 0.80$.

Figure 20. Continued.

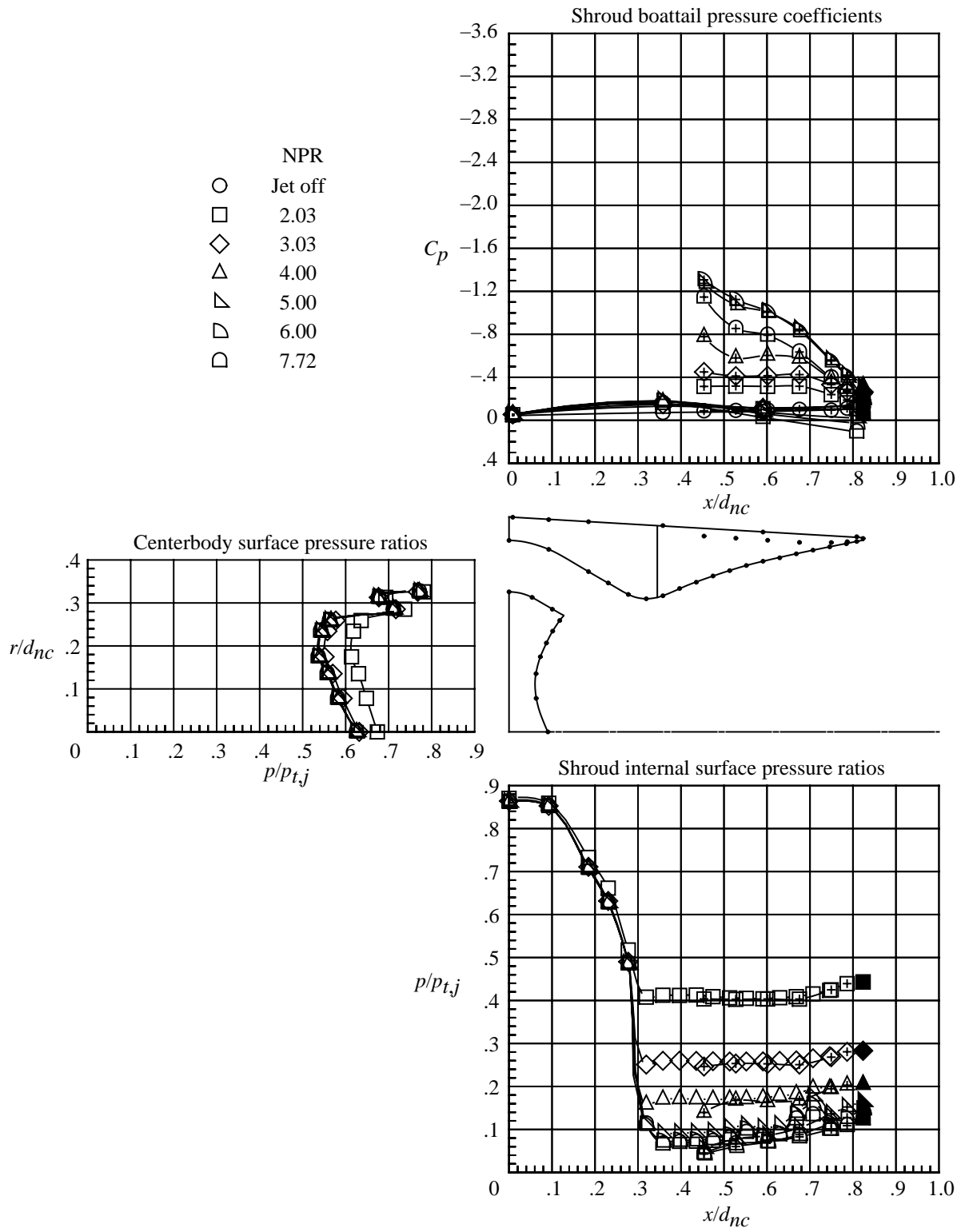
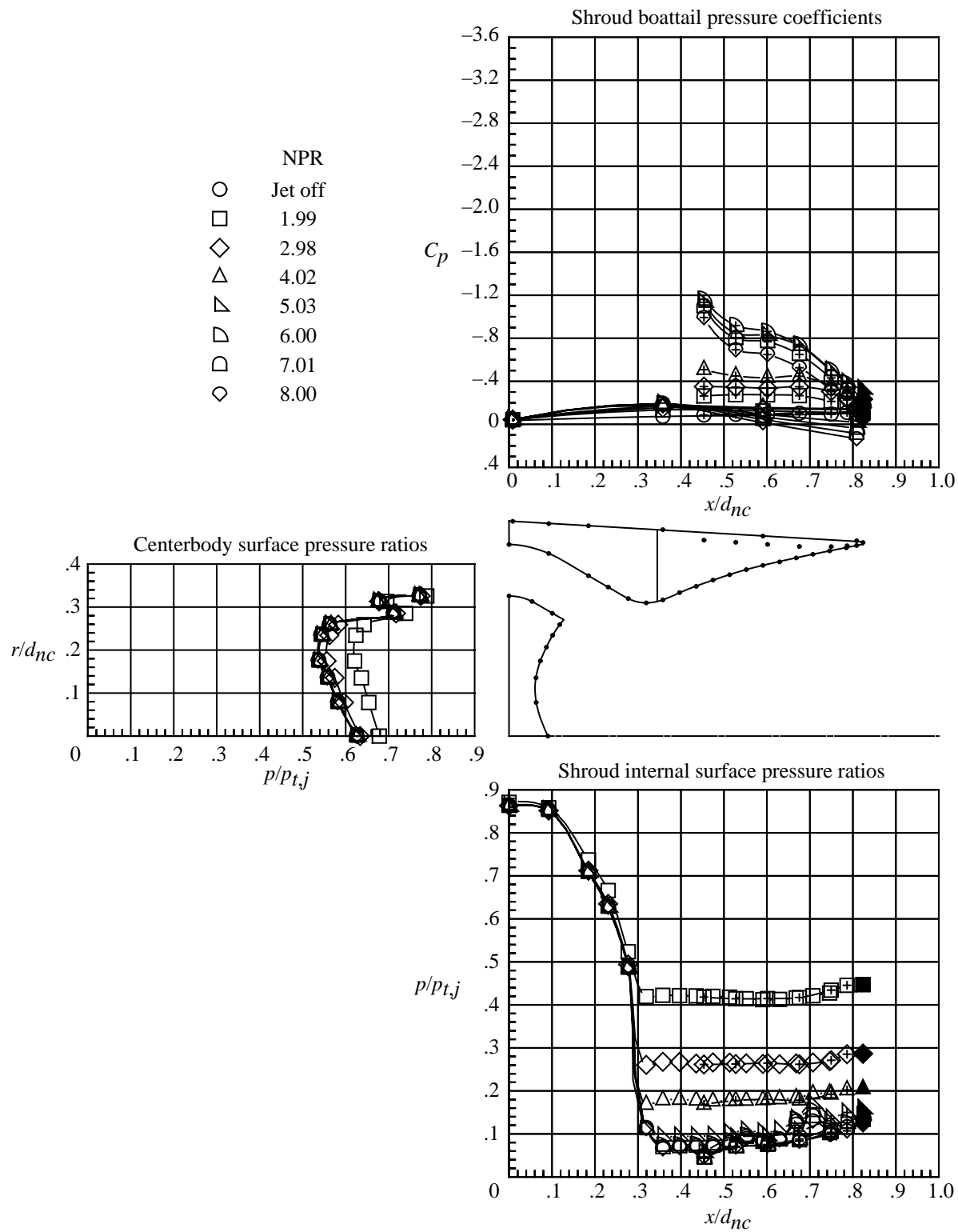
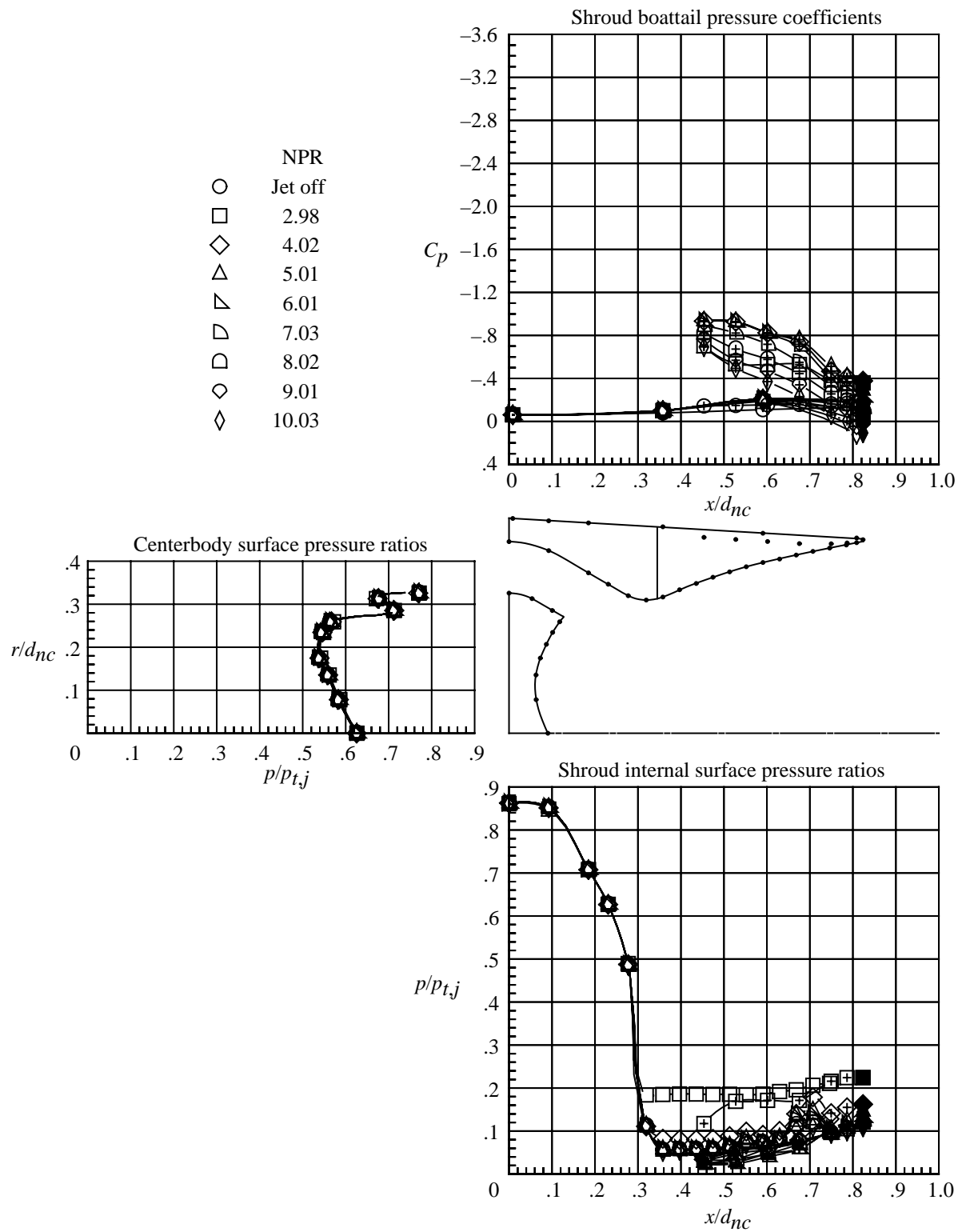


Figure 20. Continued.



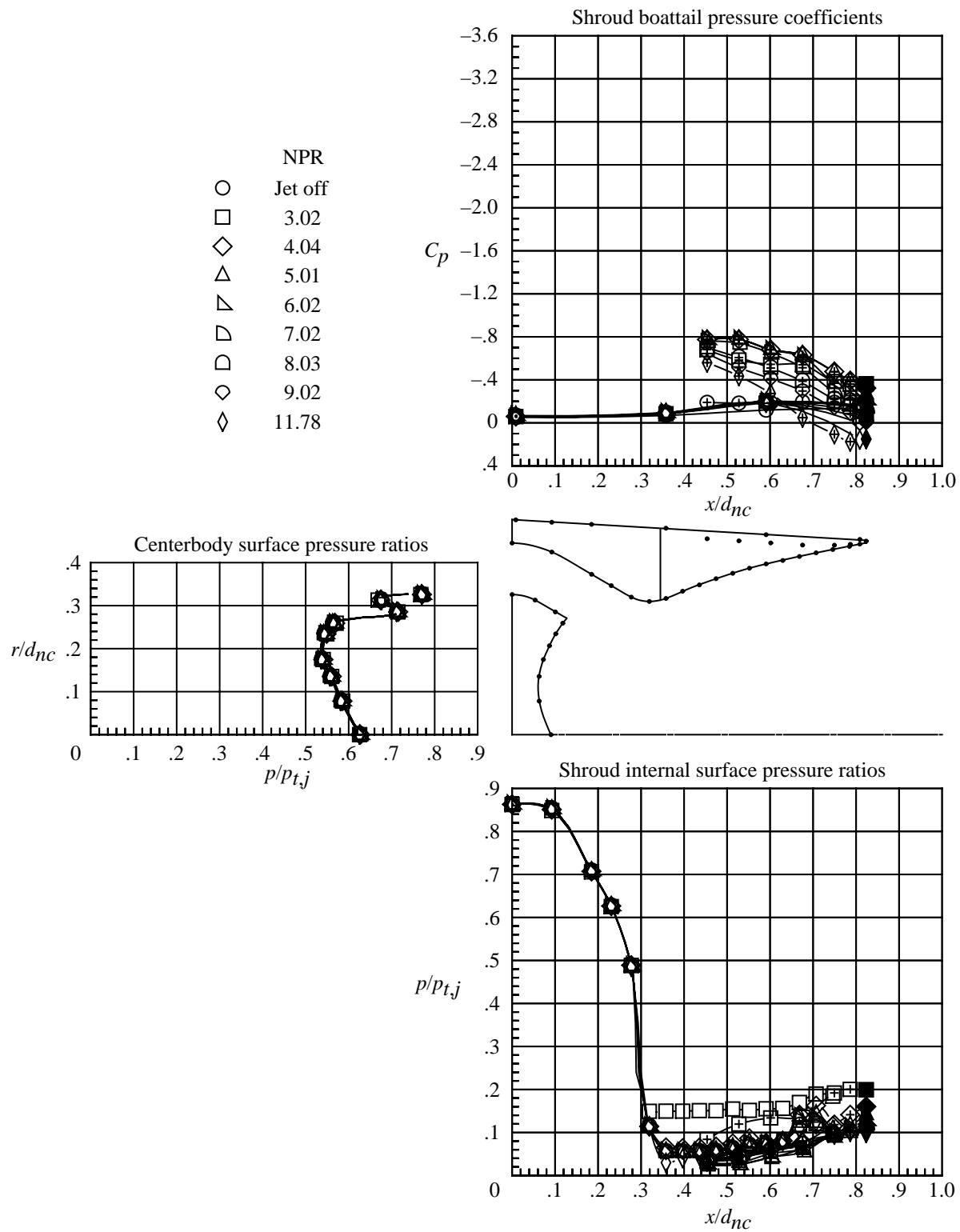
(f) $M = 0.95$.

Figure 20. Continued.



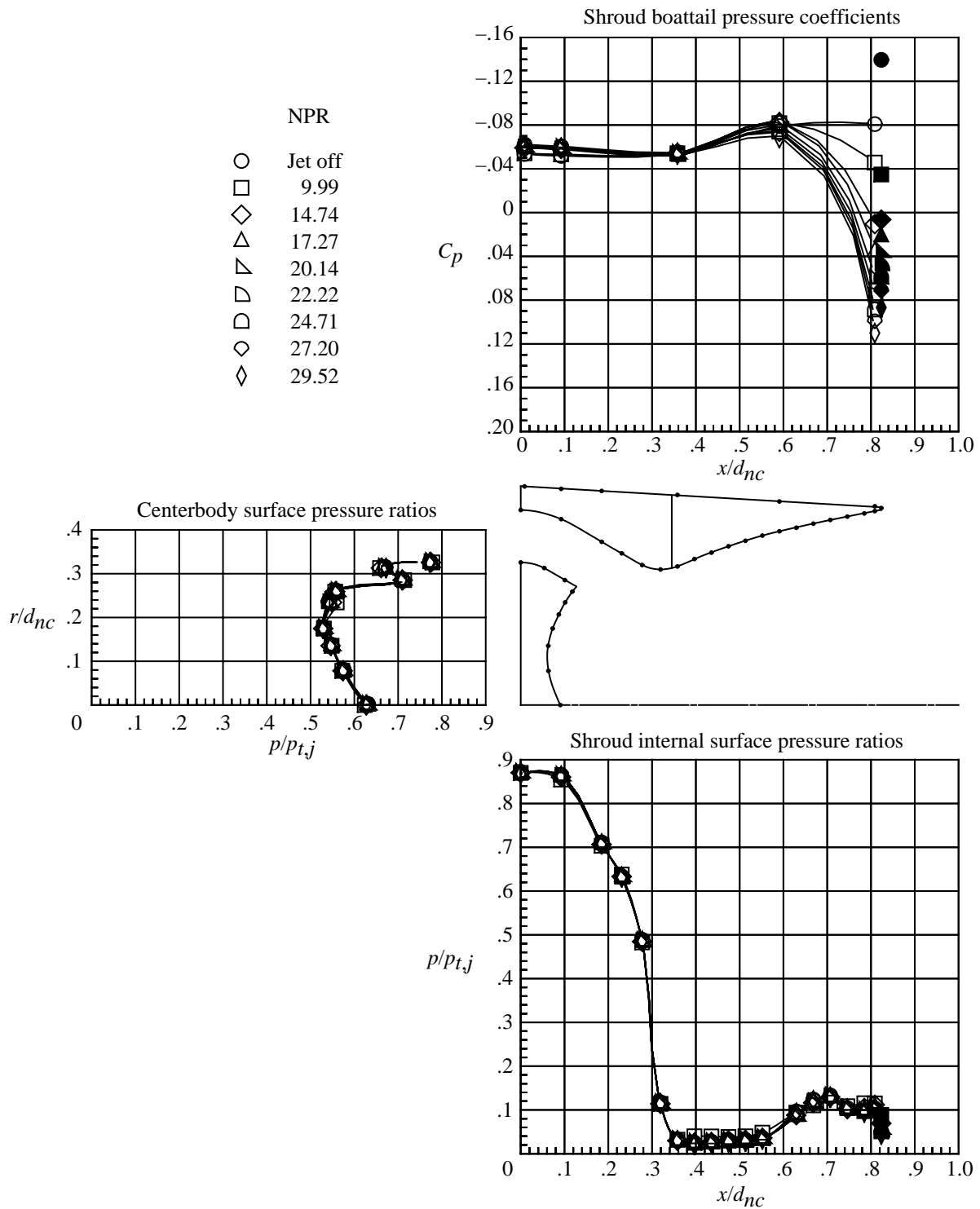
(g) $M = 1.15$.

Figure 20. Continued.



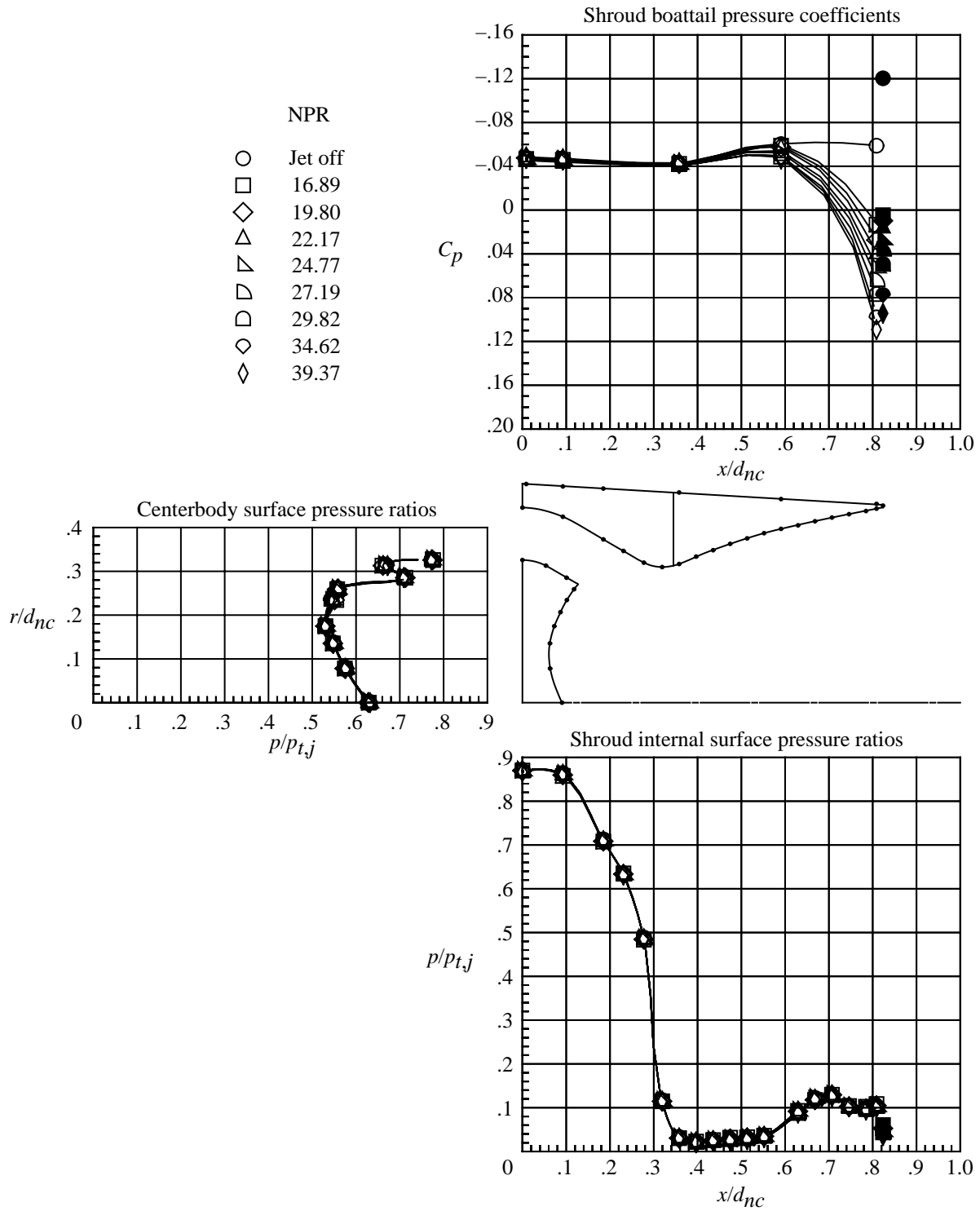
(h) $M = 1.25$.

Figure 20. Continued.



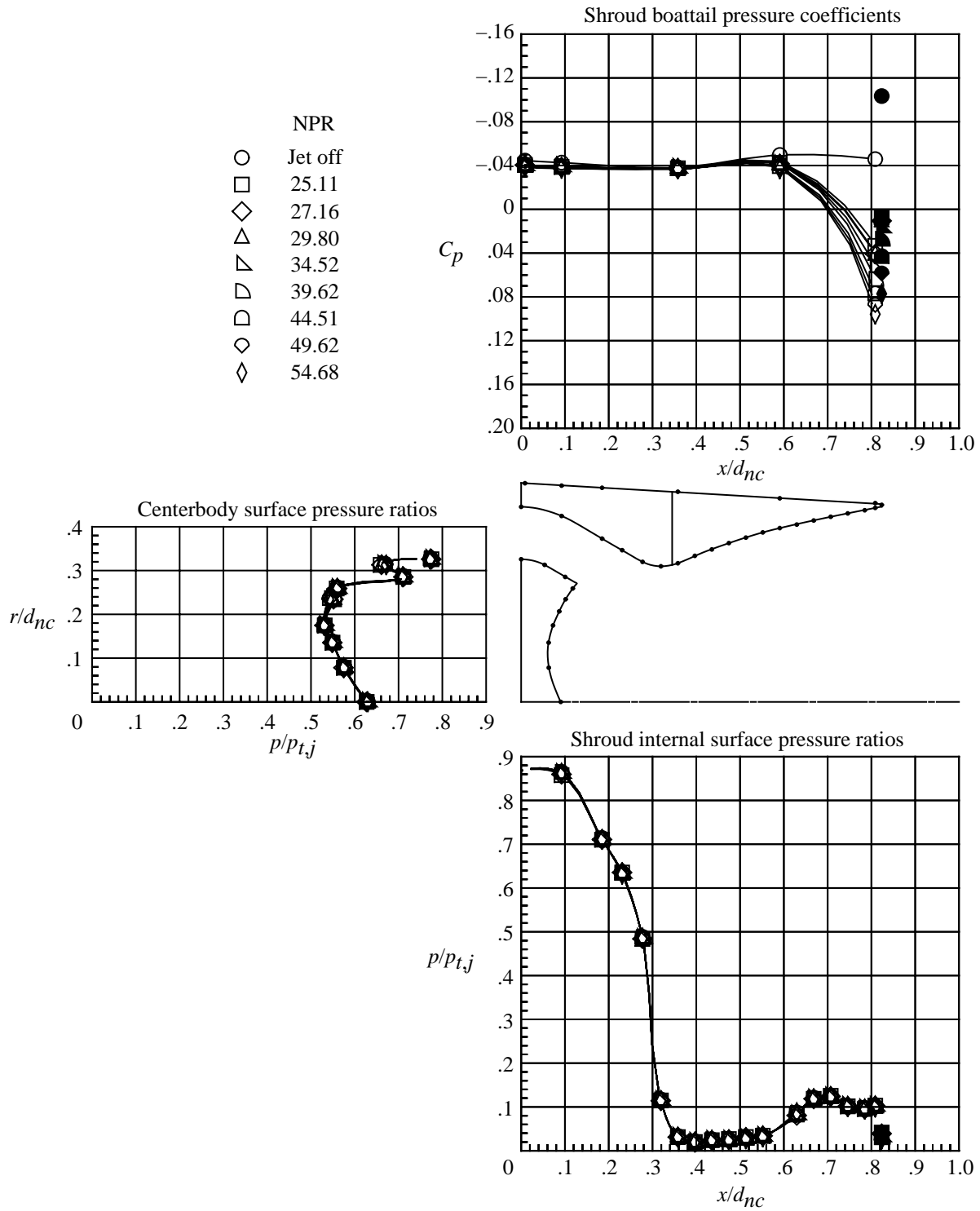
(i) $M = 2.16$.

Figure 20. Continued.



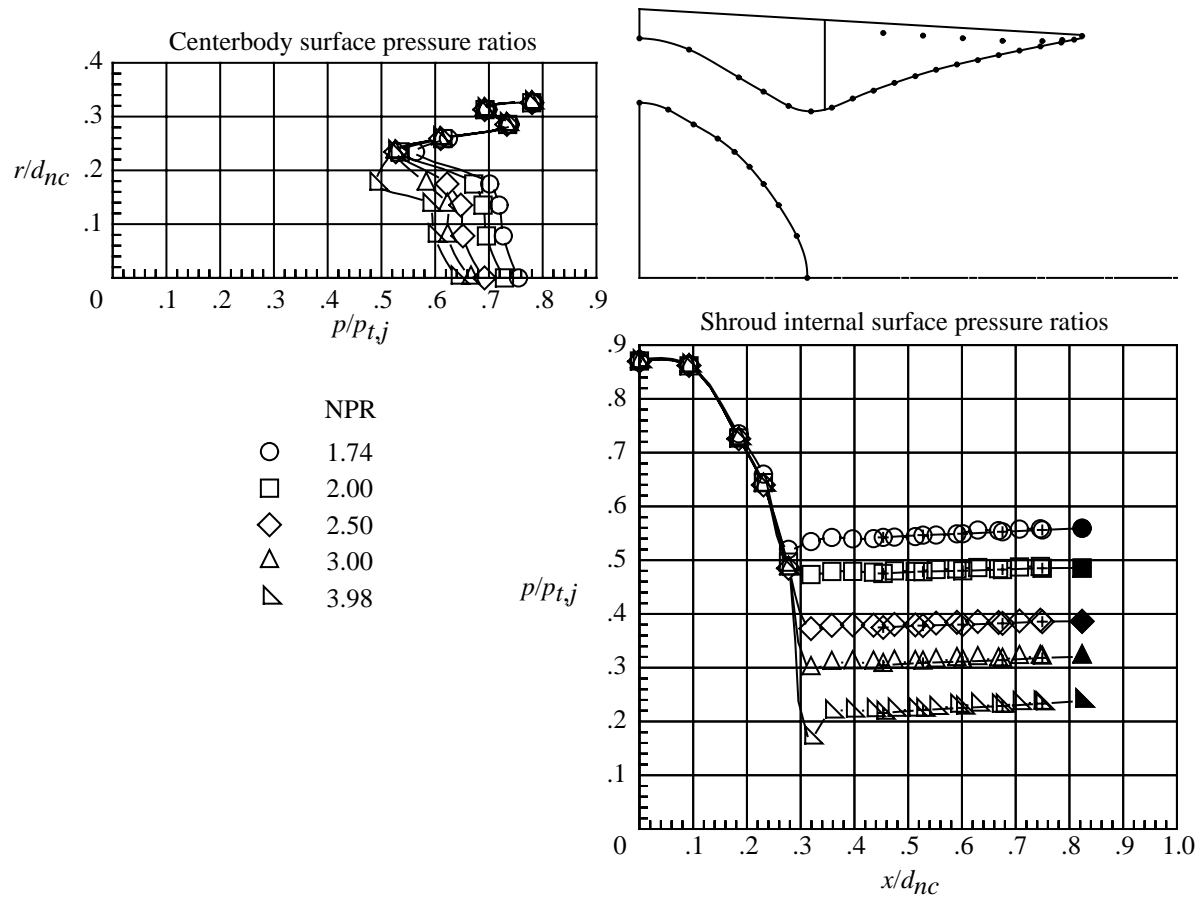
(j) $M = 2.50$.

Figure 20. Continued.



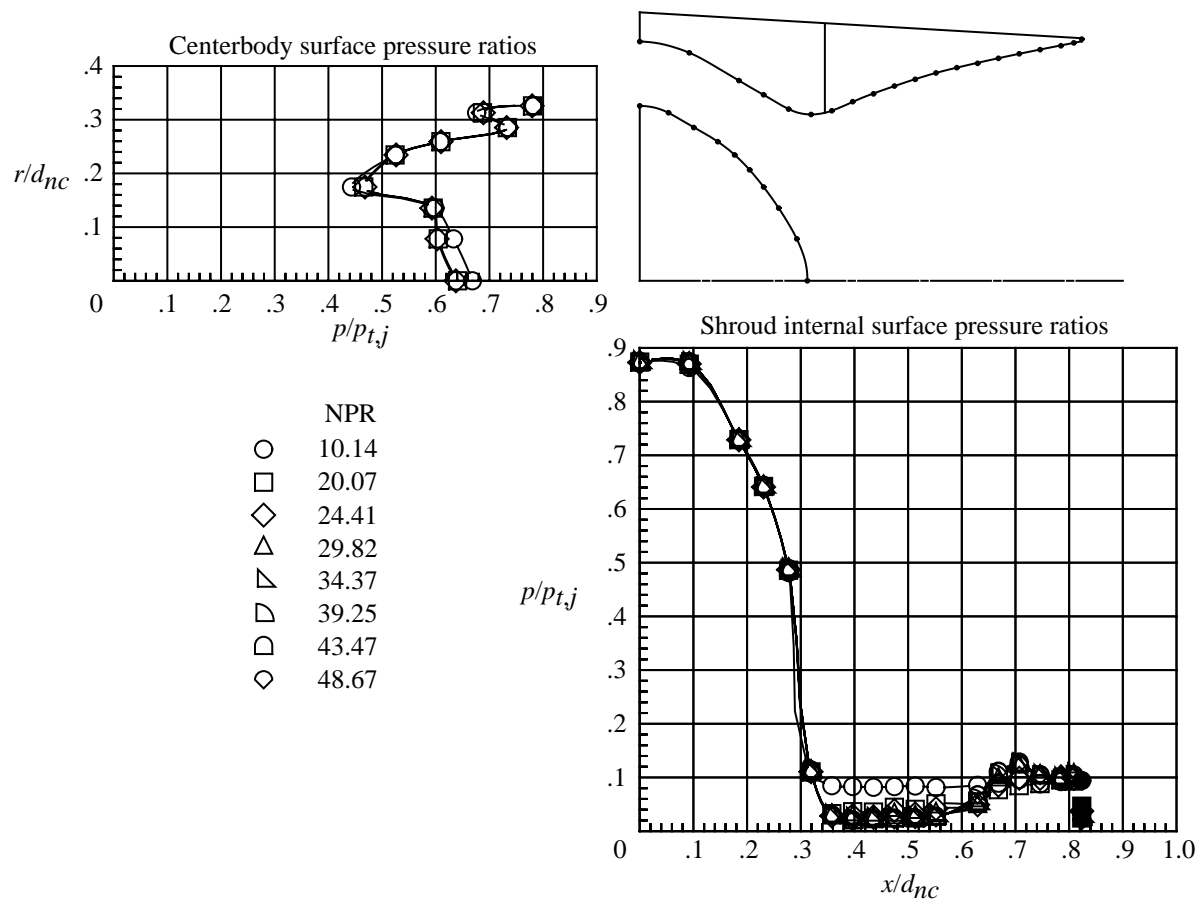
(k) $M = 2.86$.

Figure 20. Concluded.



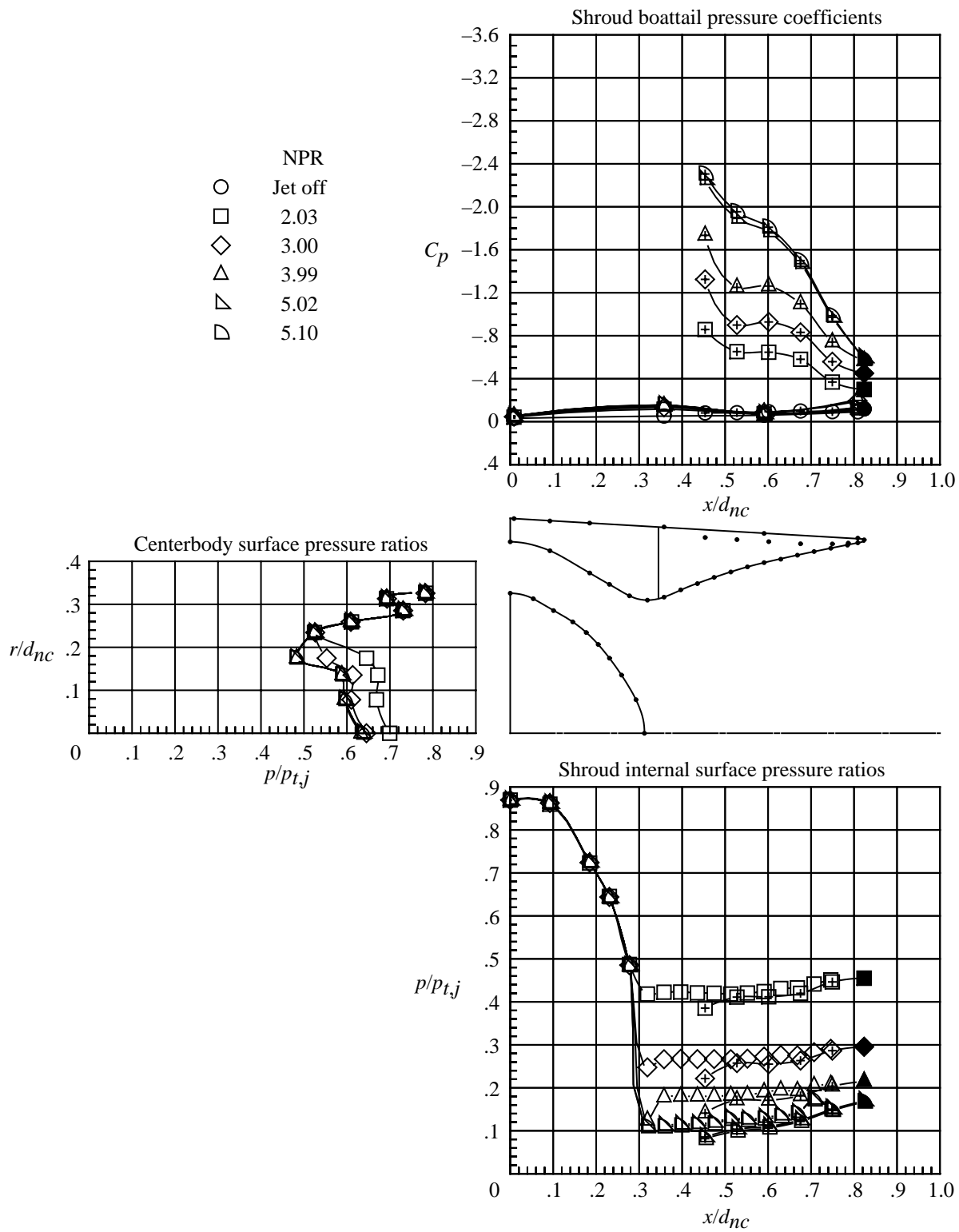
(a) $M = 0$; low nozzle pressure ratios.

Figure 21. Internal and external pressures on nozzle with long axially vented shroud and convex centerbody. Solid symbols indicate data at shroud base and plus signs in symbols indicate data on walls of vent. Dots on nozzle sketch indicate pressure orifice locations.



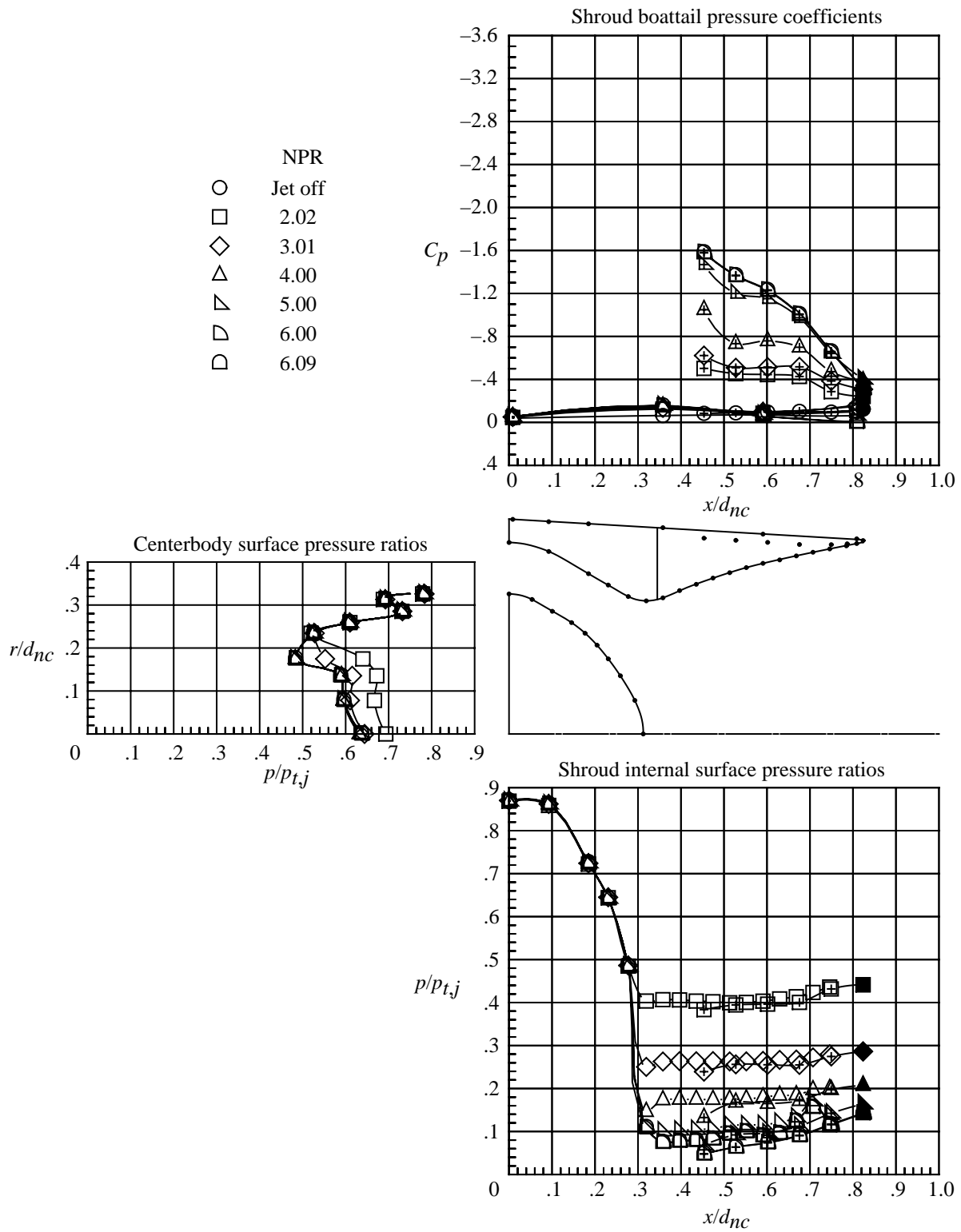
(b) $M = 0$; high nozzle pressure ratios.

Figure 21. Continued.



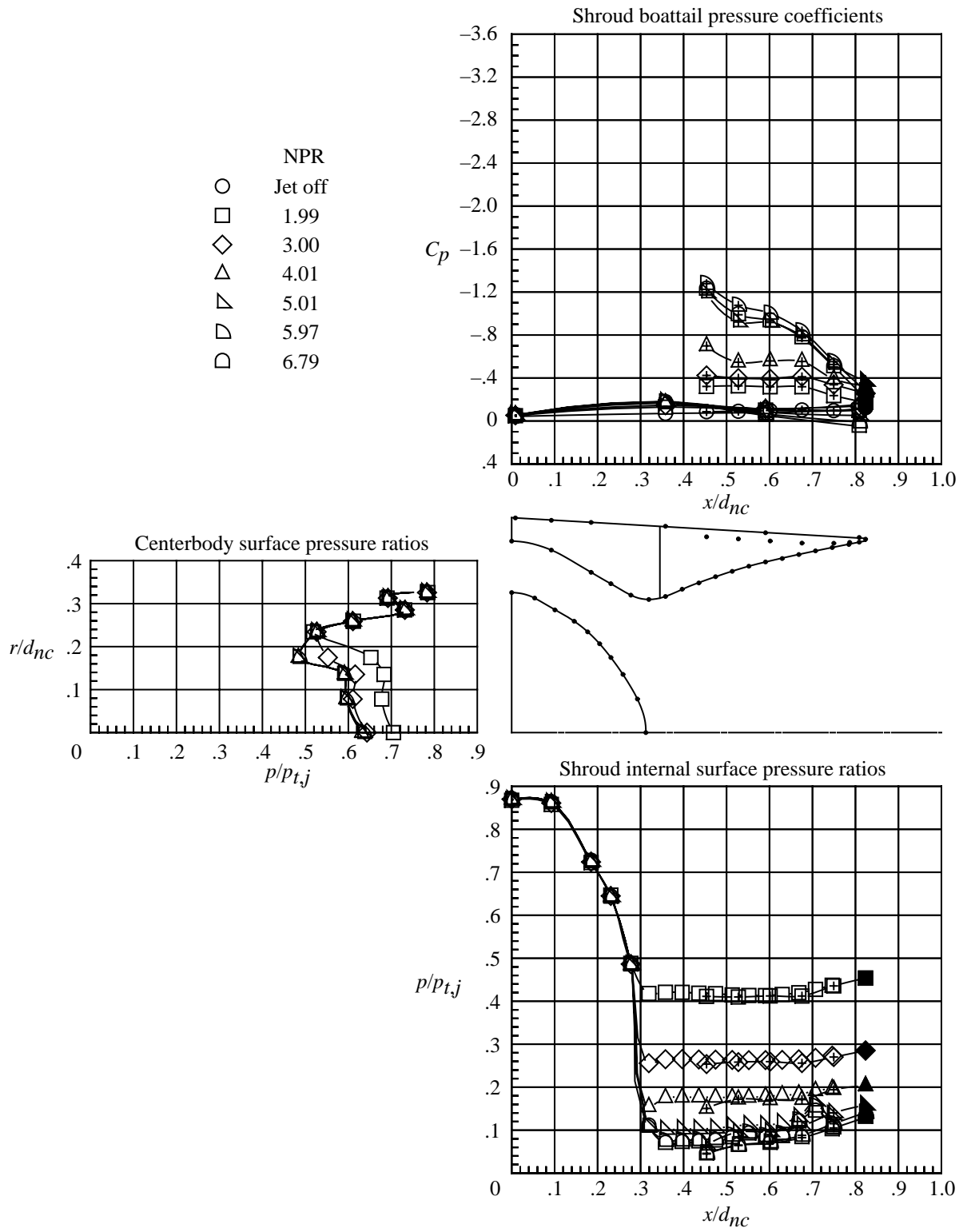
(c) $M = 0.60$.

Figure 21. Continued.



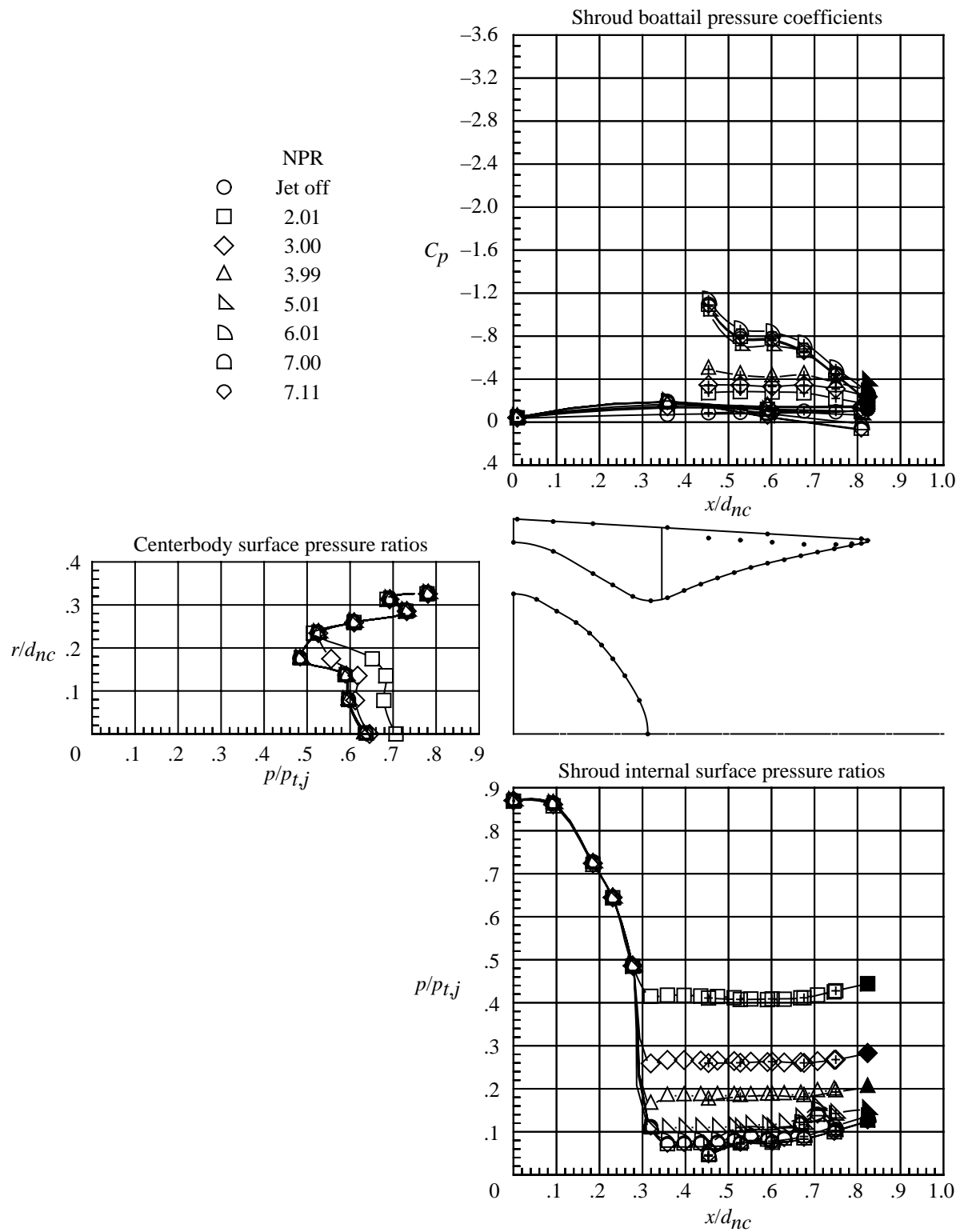
(d) $M = 0.80$.

Figure 21. Continued.



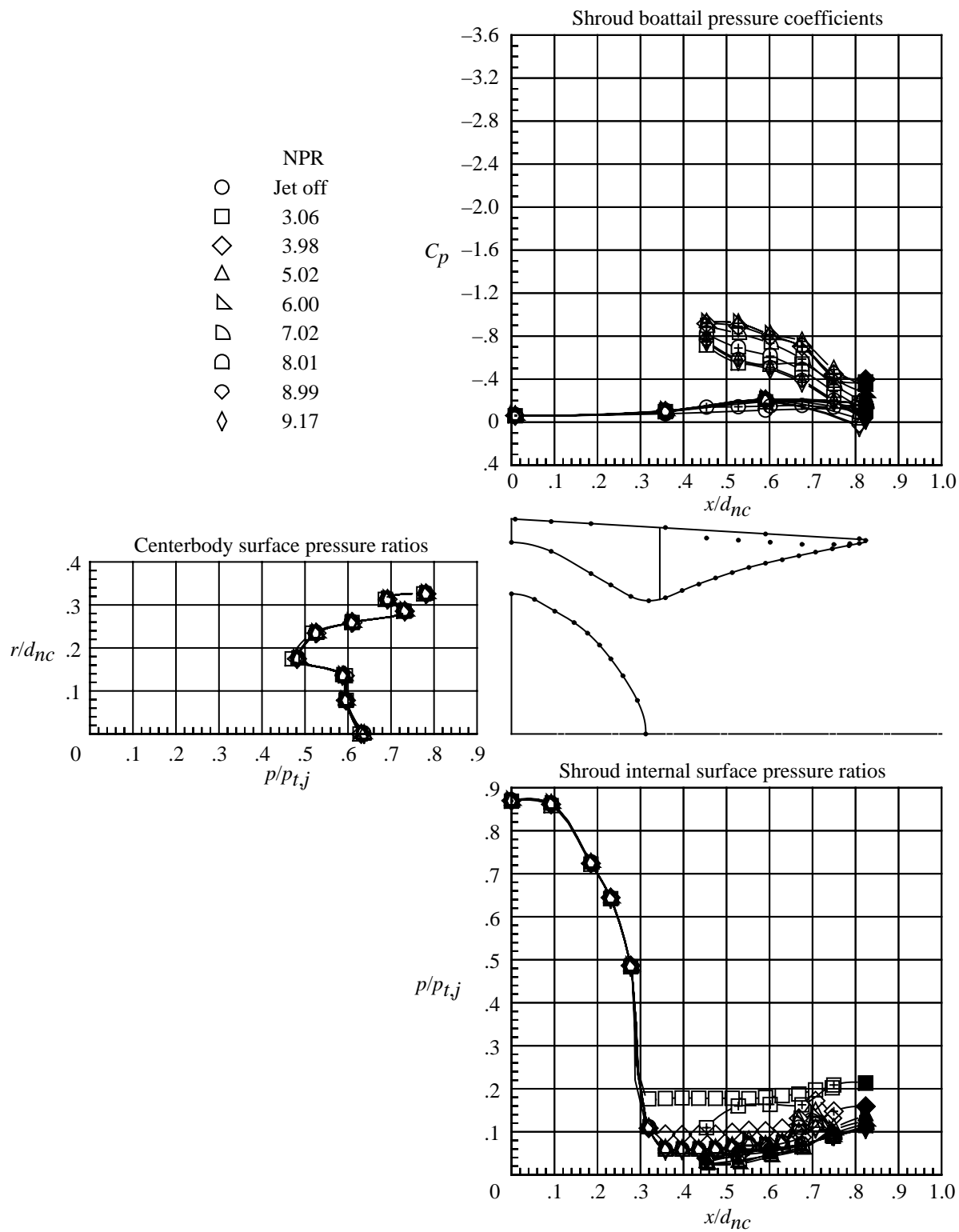
(e) $M = 0.90$.

Figure 21. Continued.



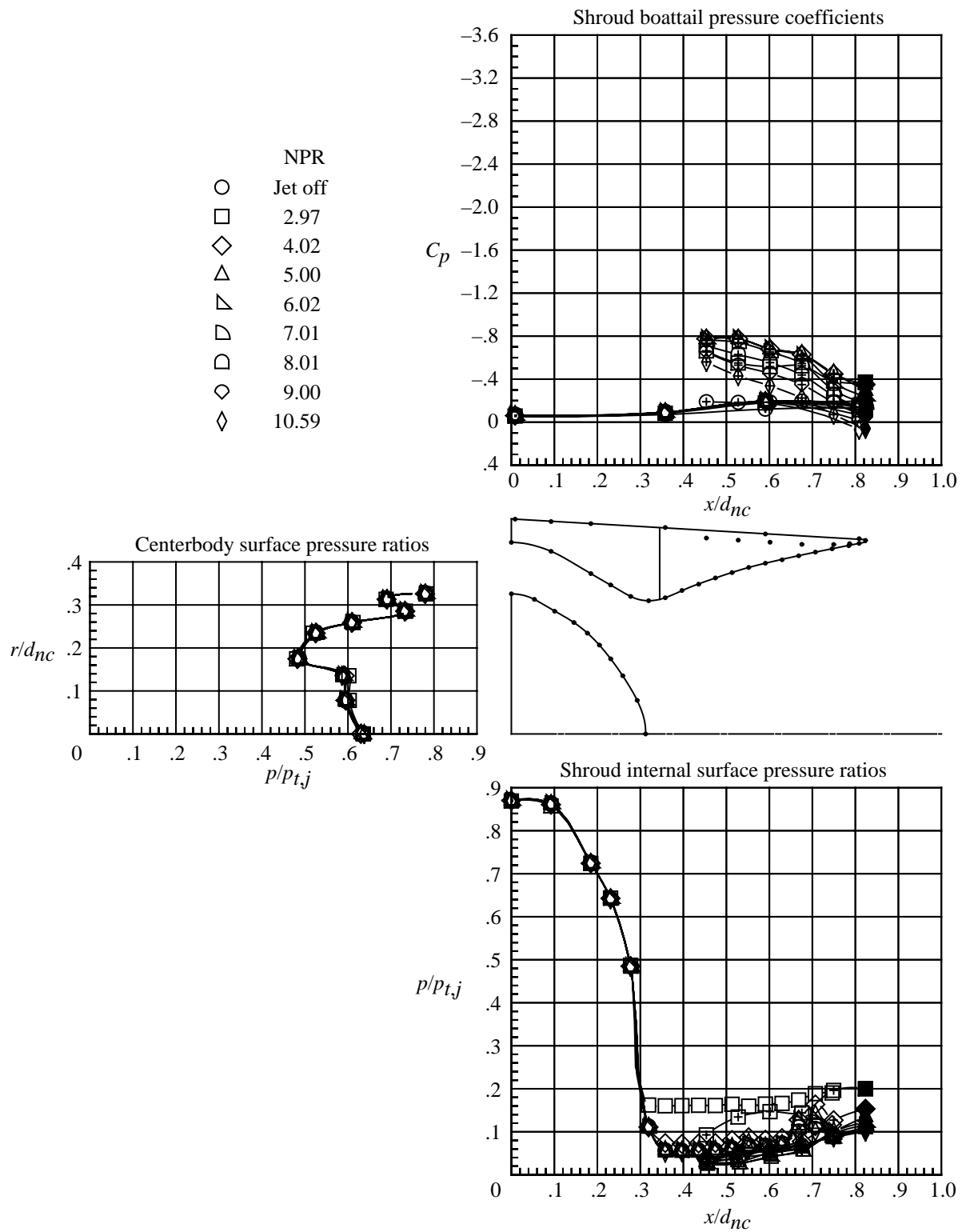
(f) $M = 0.95$.

Figure 21. Continued.



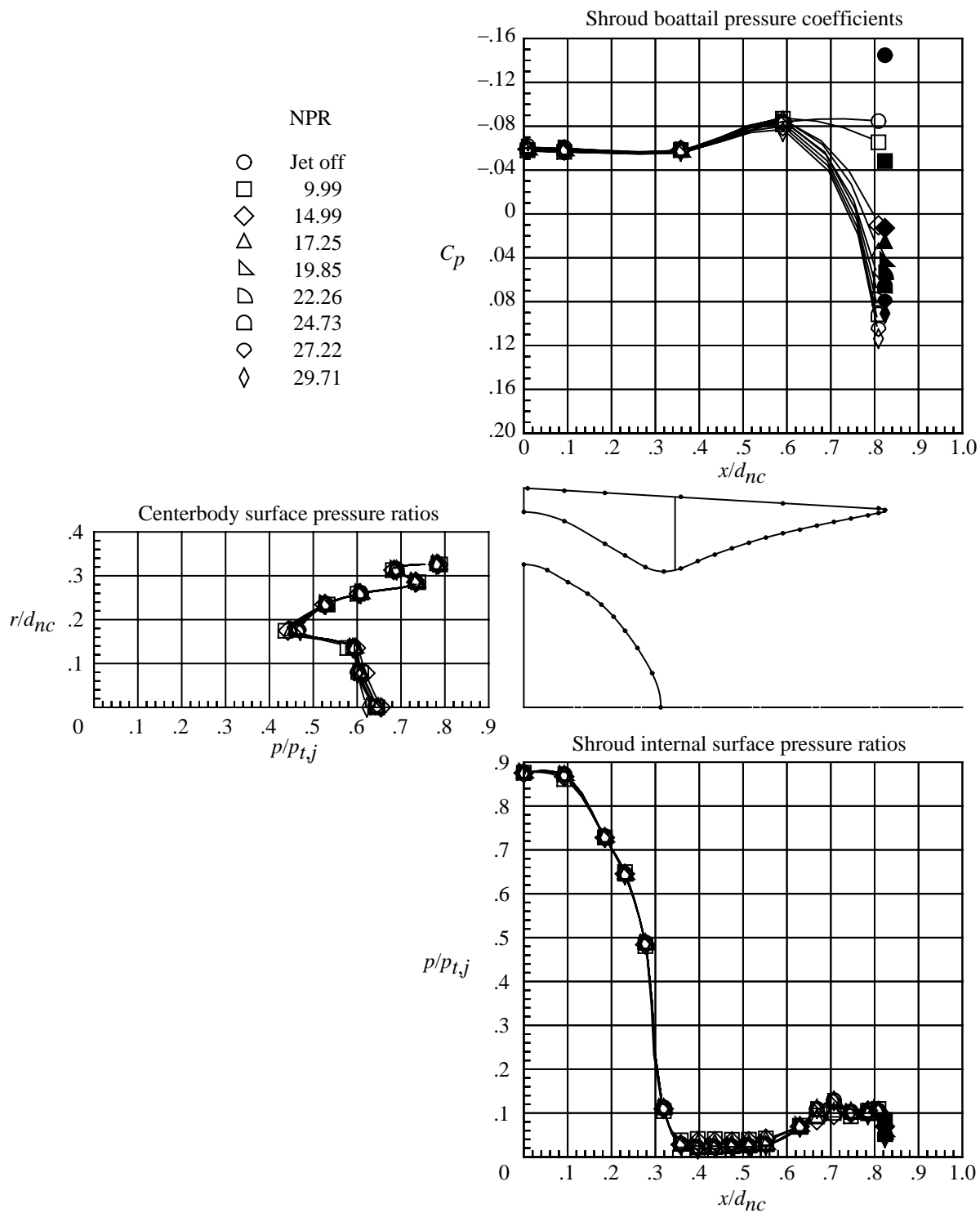
(g) $M = 1.15$.

Figure 21. Continued.



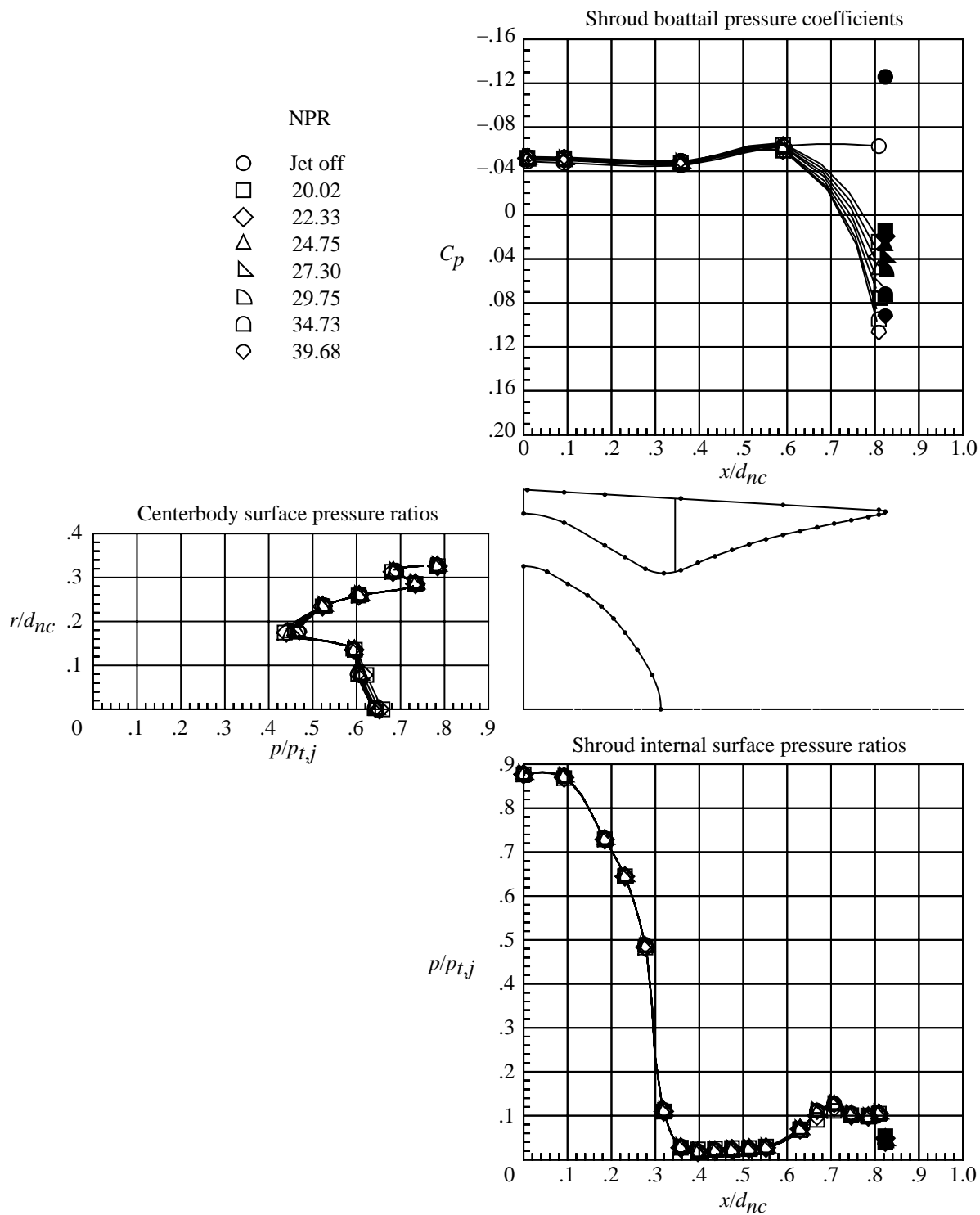
(h) $M = 1.25$.

Figure 21. Continued.



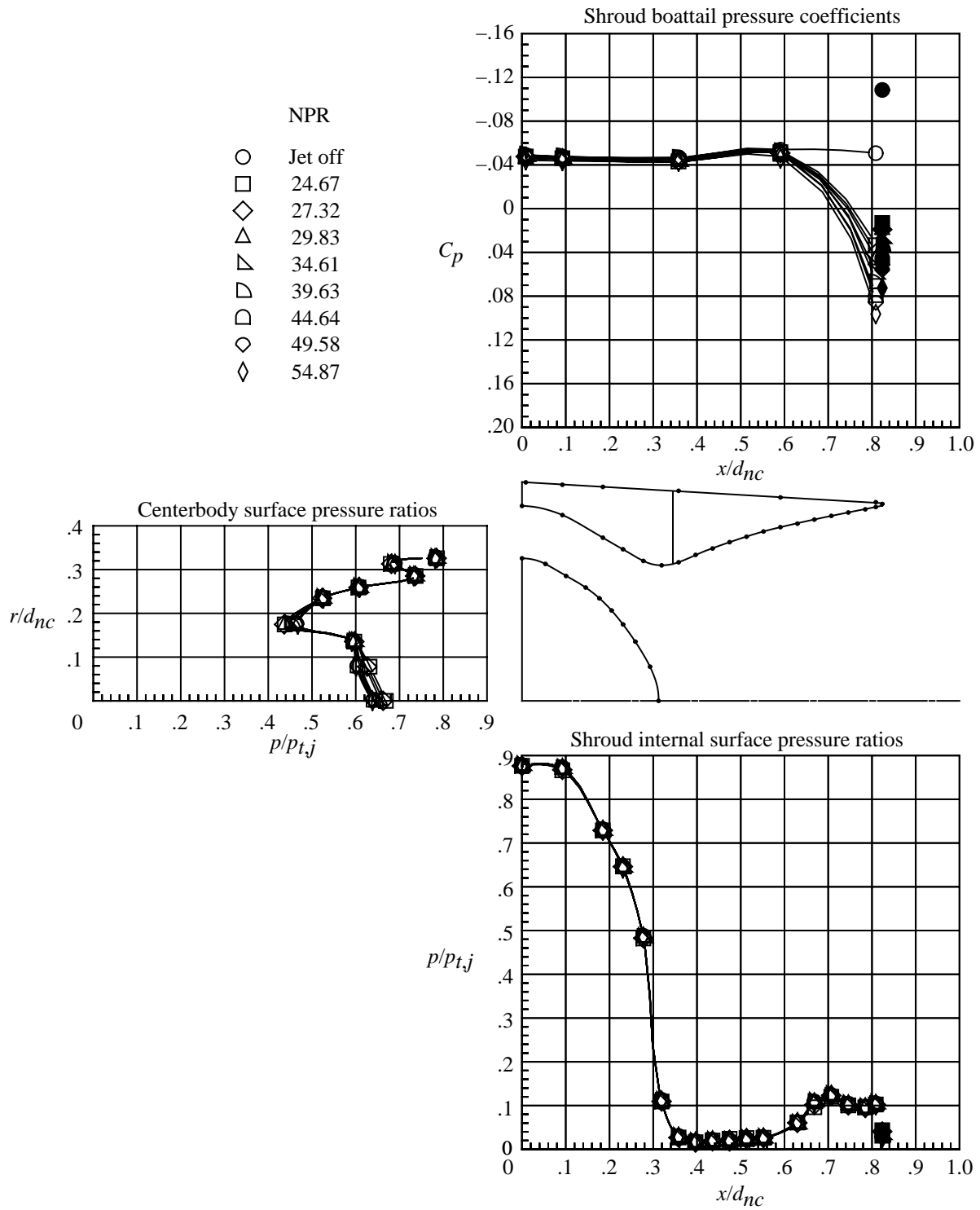
(i) $M = 2.16$.

Figure 21. Continued.



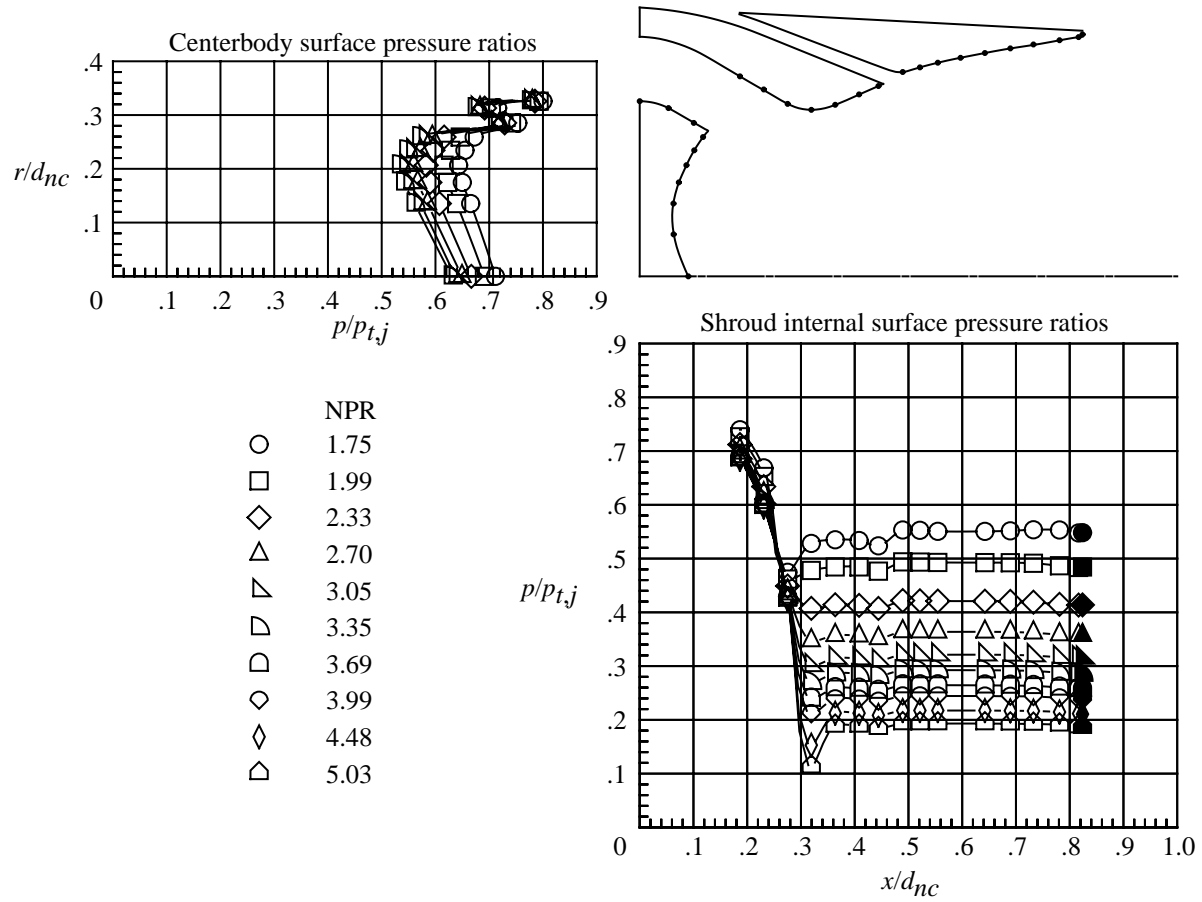
(j) $M = 2.50$.

Figure 21. Continued.



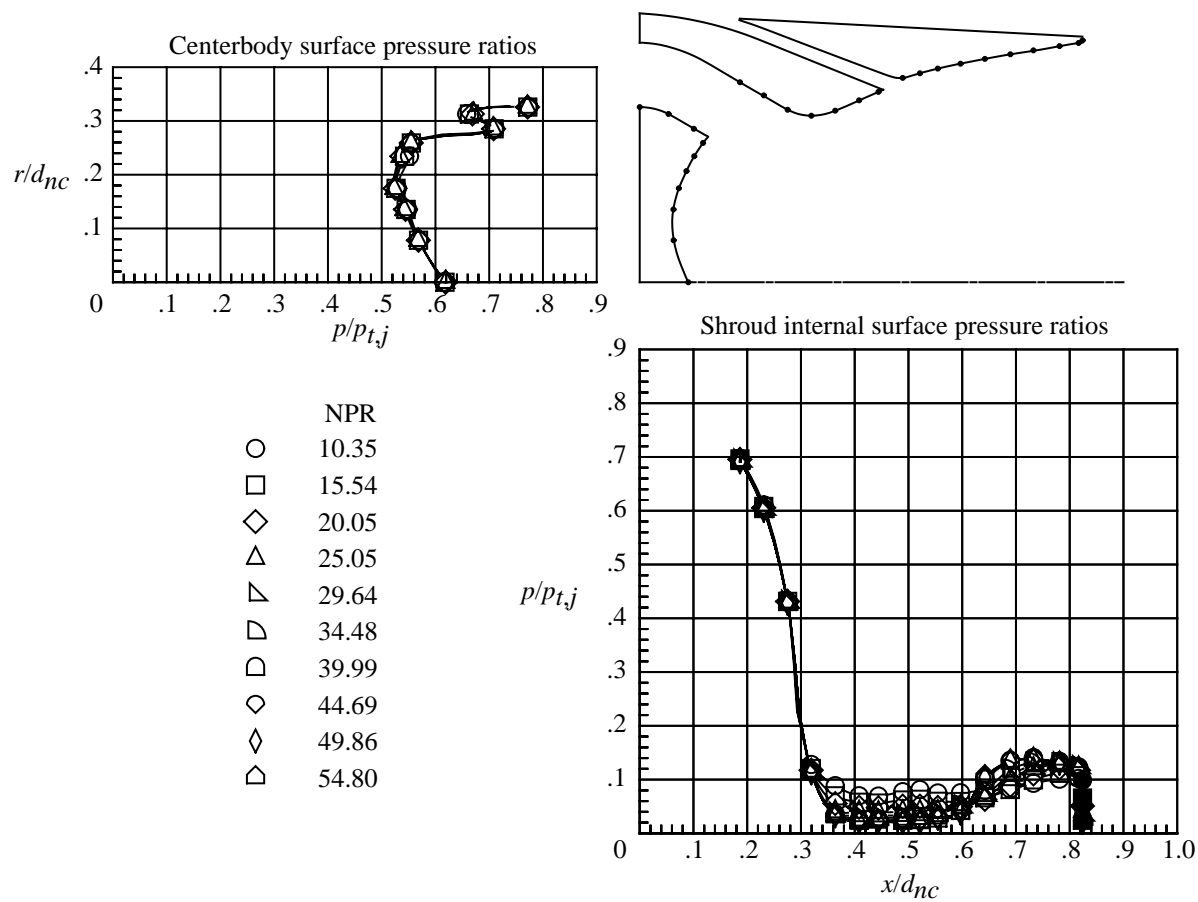
(k) $M = 2.86$.

Figure 21. Concluded.



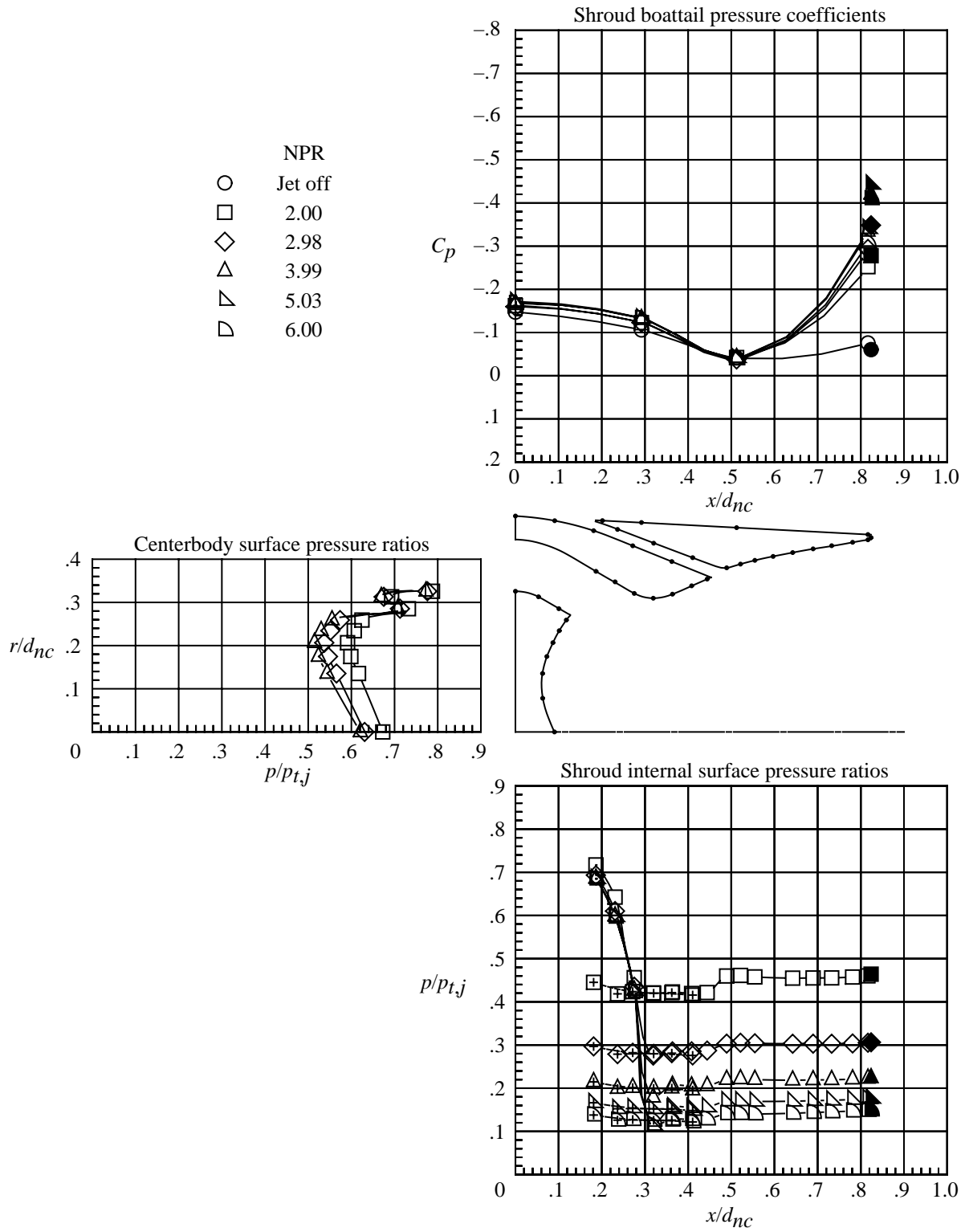
(a) $M = 0$; low nozzle pressure ratios.

Figure 22. Internal and external pressures on nozzle with long annularly vented shroud and concave centerbody. Solid symbols indicate data at shroud base and plus signs in symbols indicate wall pressures in annular slot. Dots on nozzle sketch indicate pressure orifice locations.



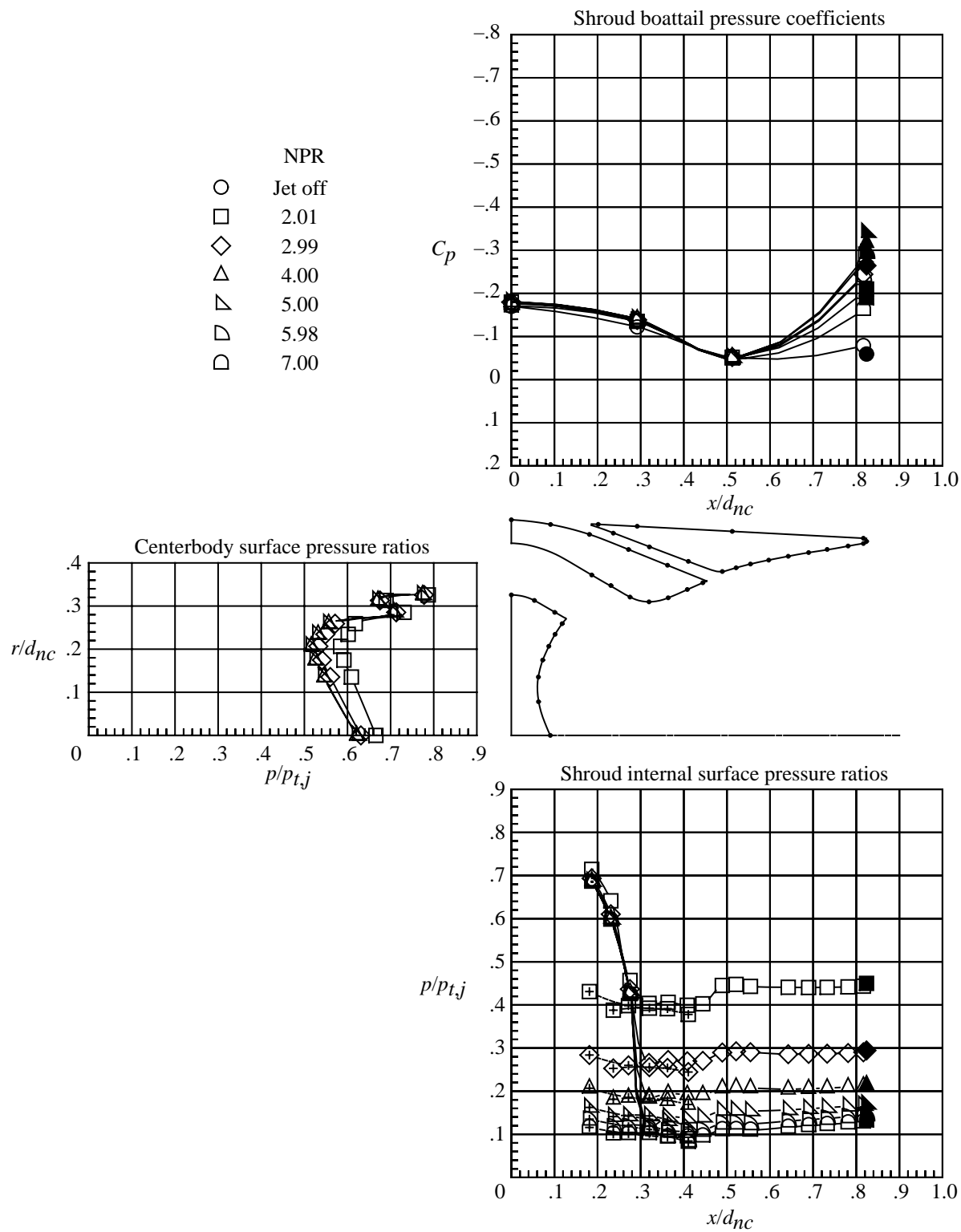
(b) $M = 0$; high nozzle pressure ratios.

Figure 22. Continued.



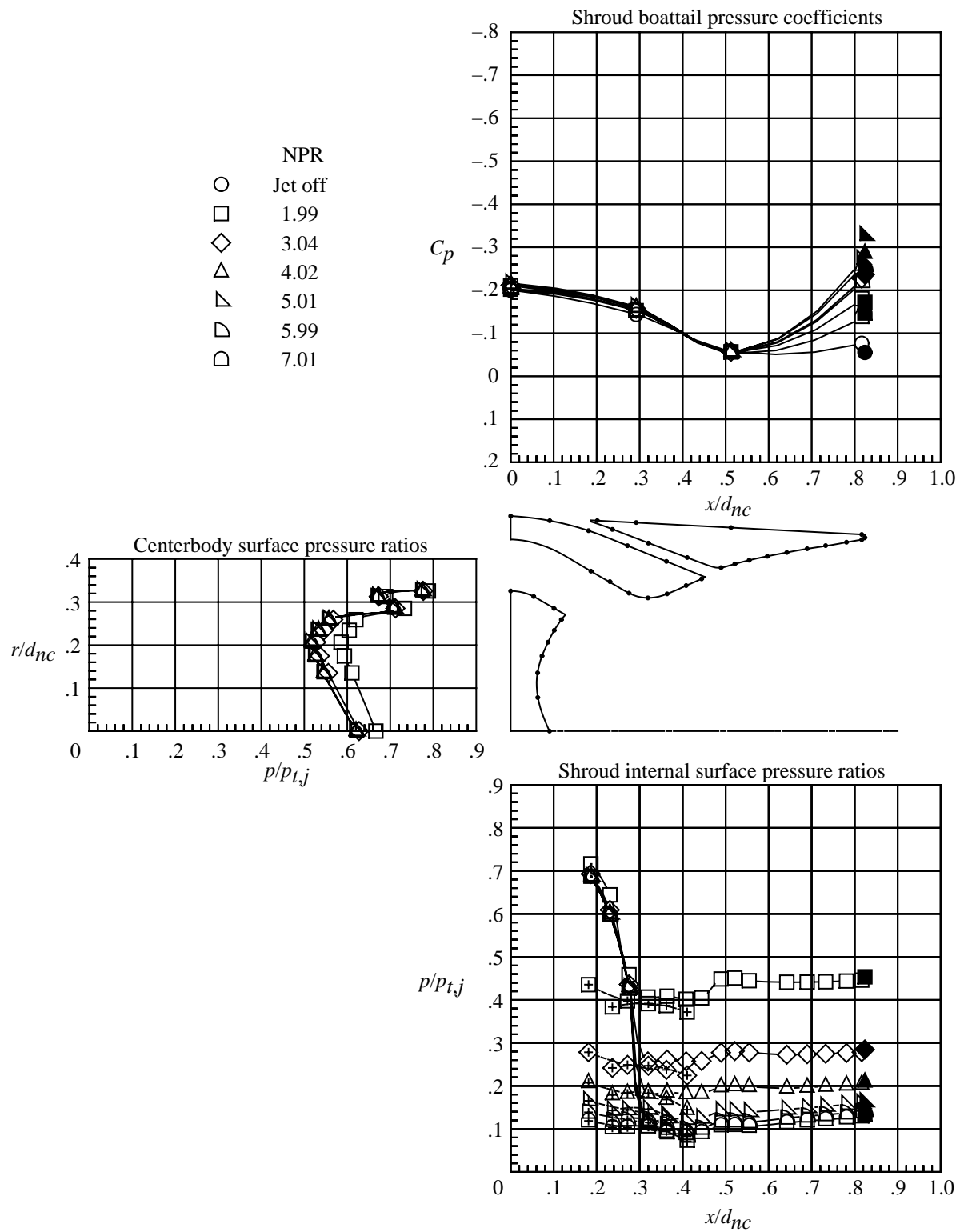
(c) $M = 0.60$.

Figure 22. Continued.



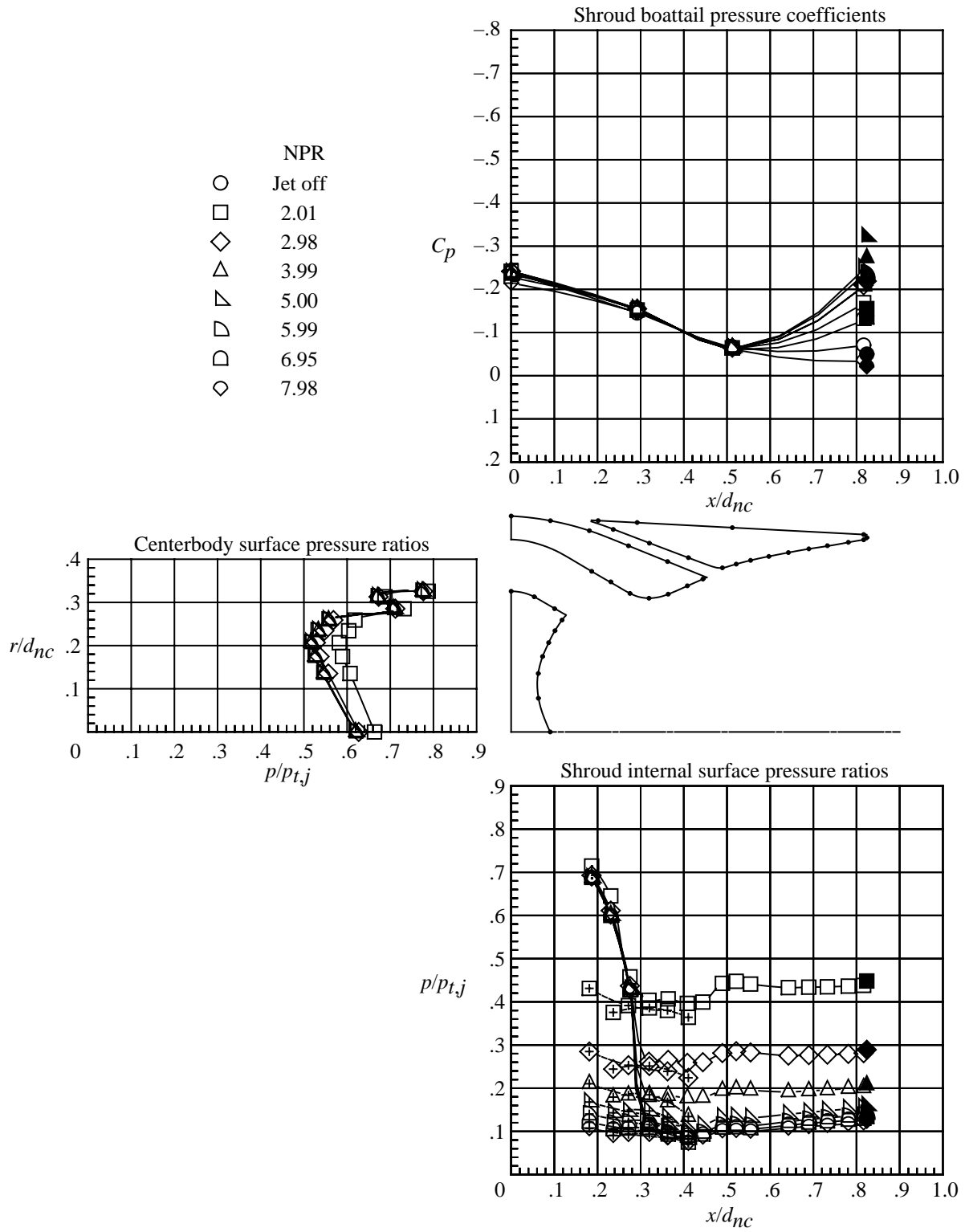
(d) $M = 0.80$.

Figure 22. Continued.



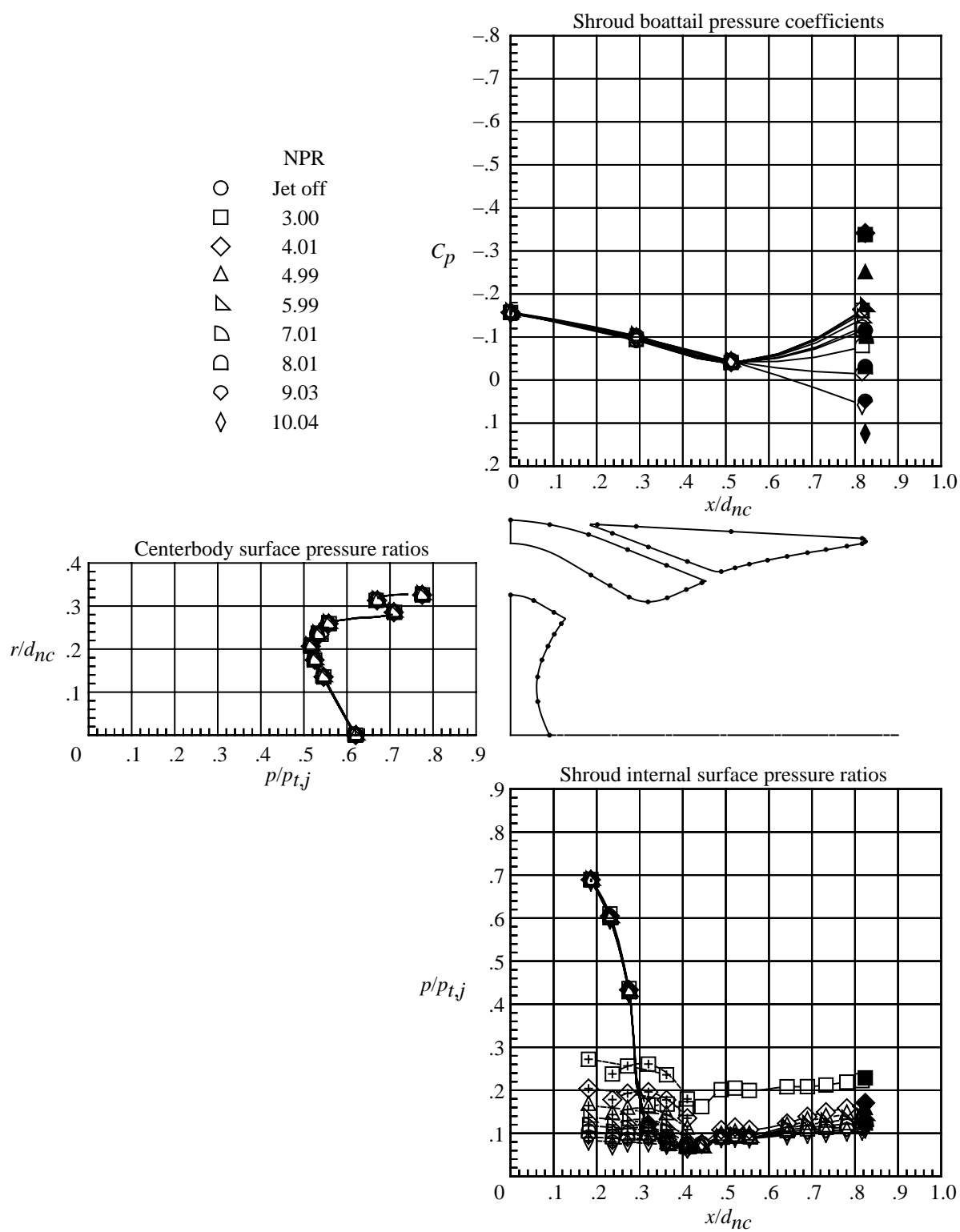
(e) $M = 0.90$.

Figure 22. Continued.



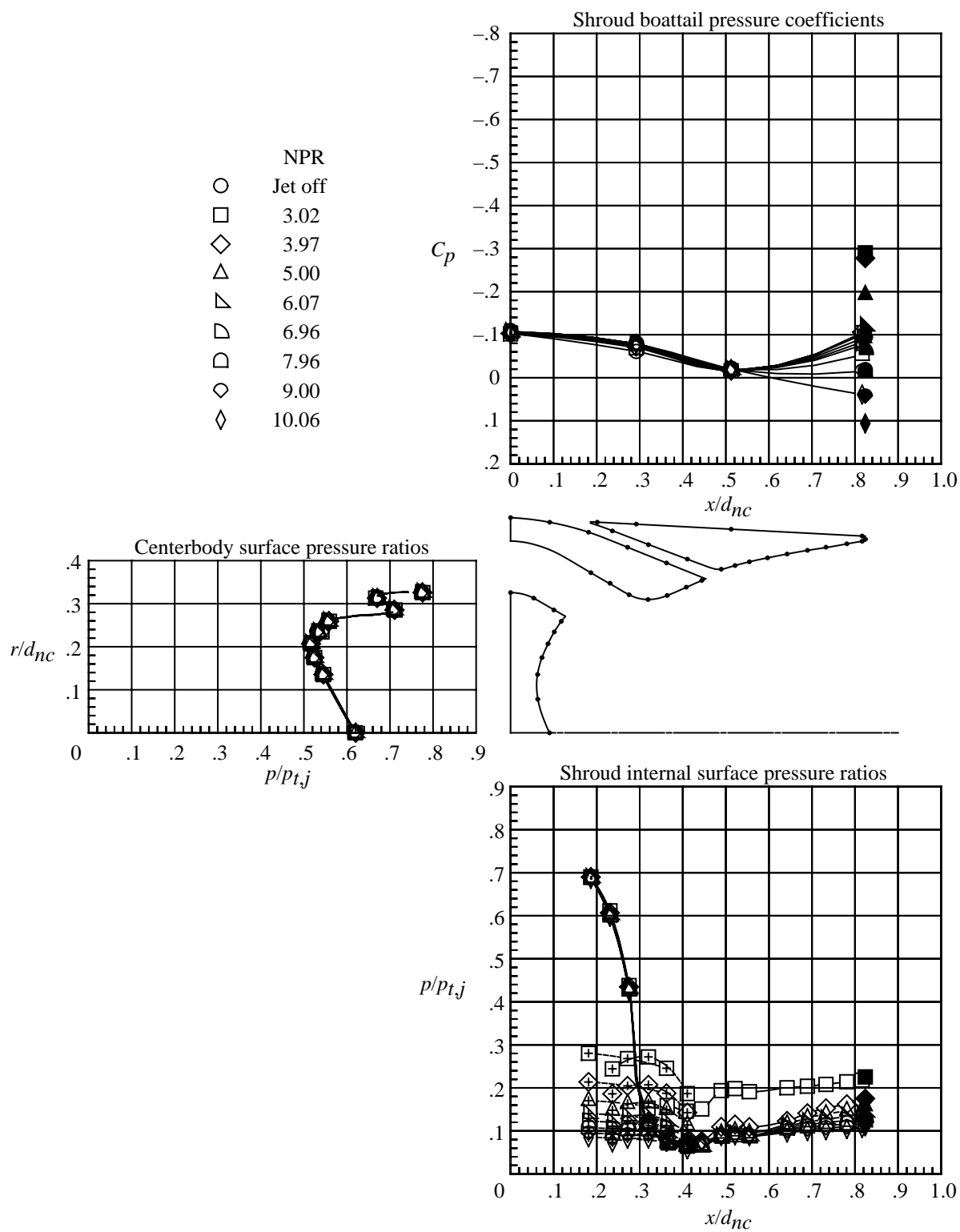
(f) $M = 0.95$.

Figure 22. Continued.



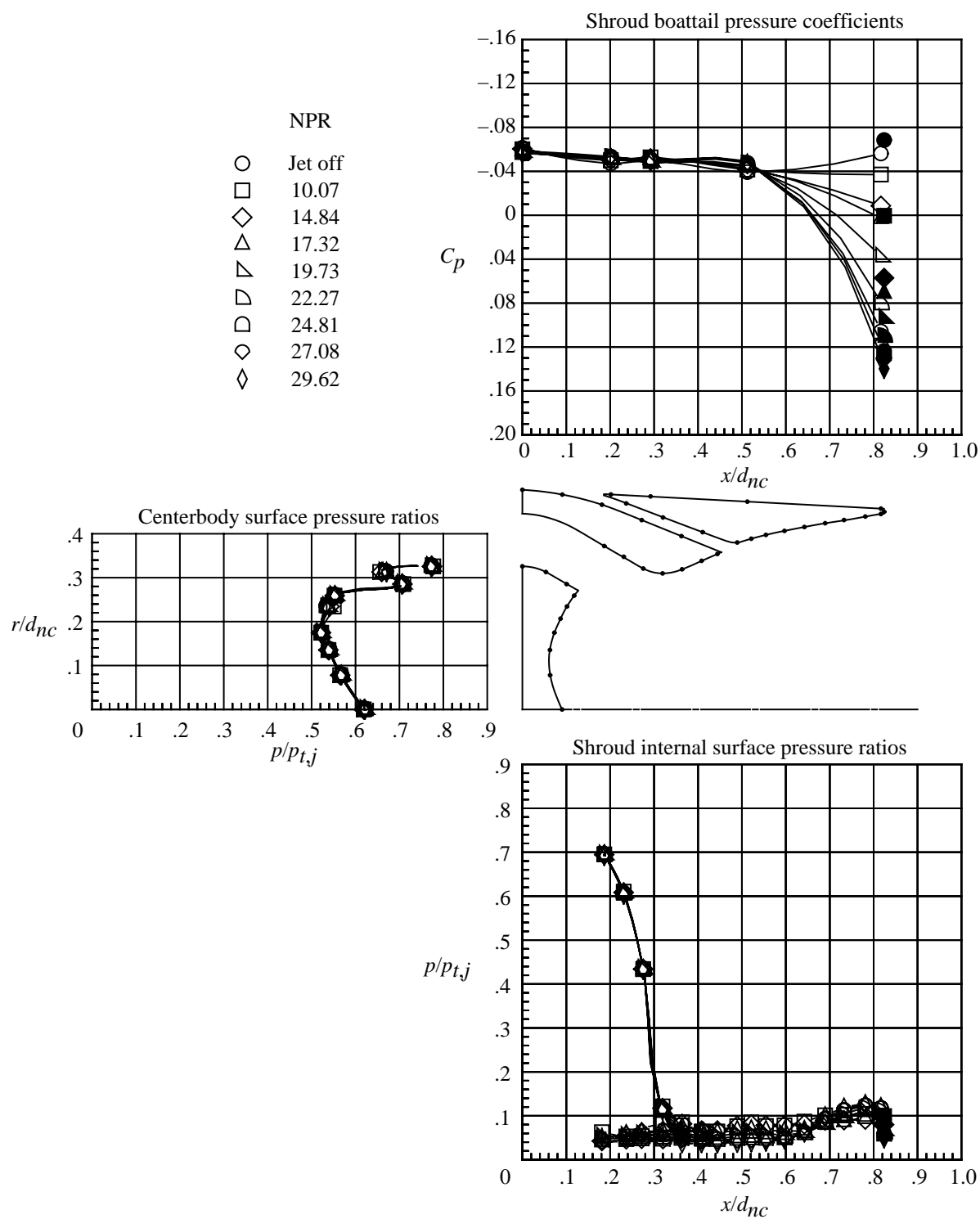
(g) $M = 1.15$.

Figure 22. Continued.



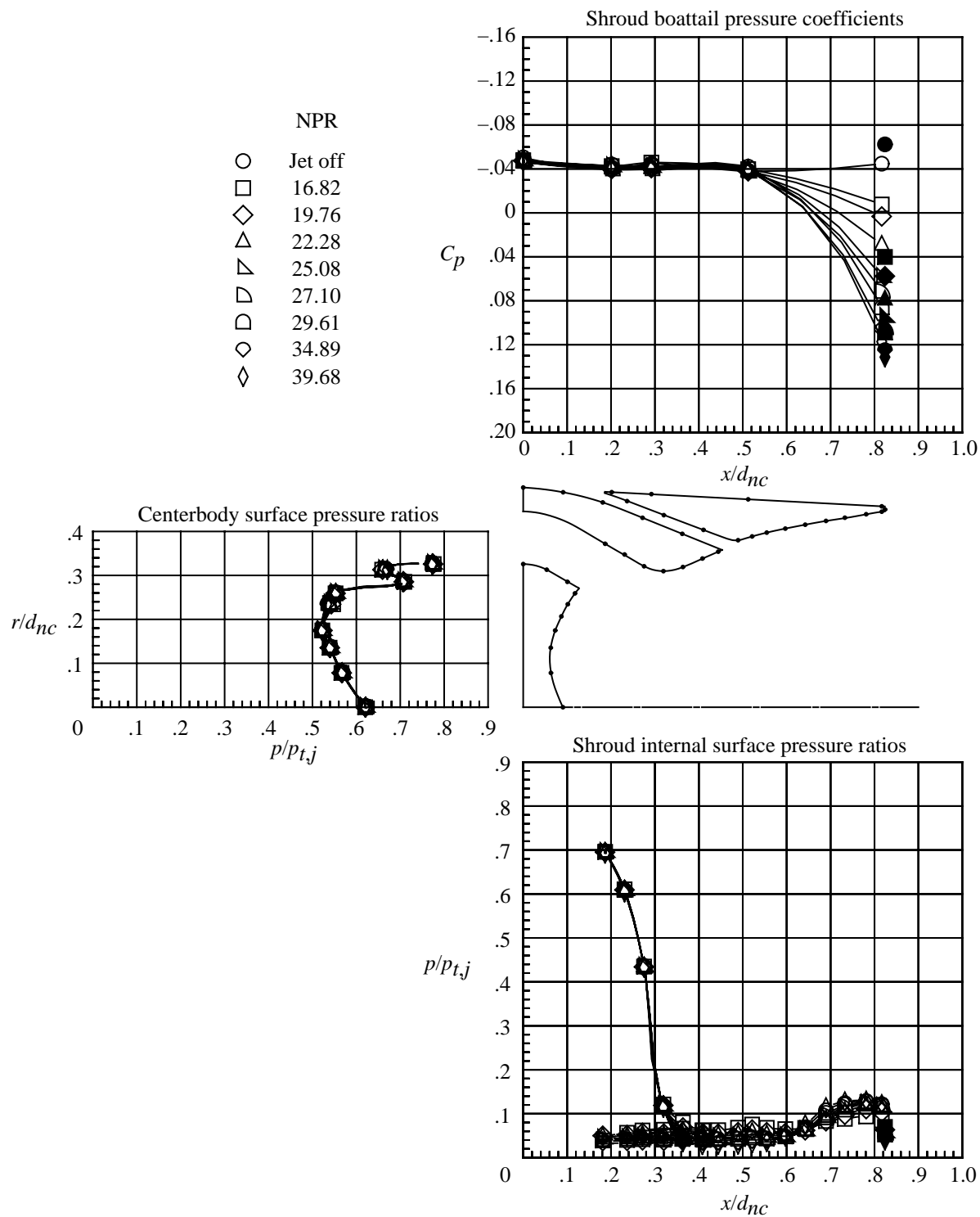
(h) $M = 1.25$.

Figure 22. Continued.



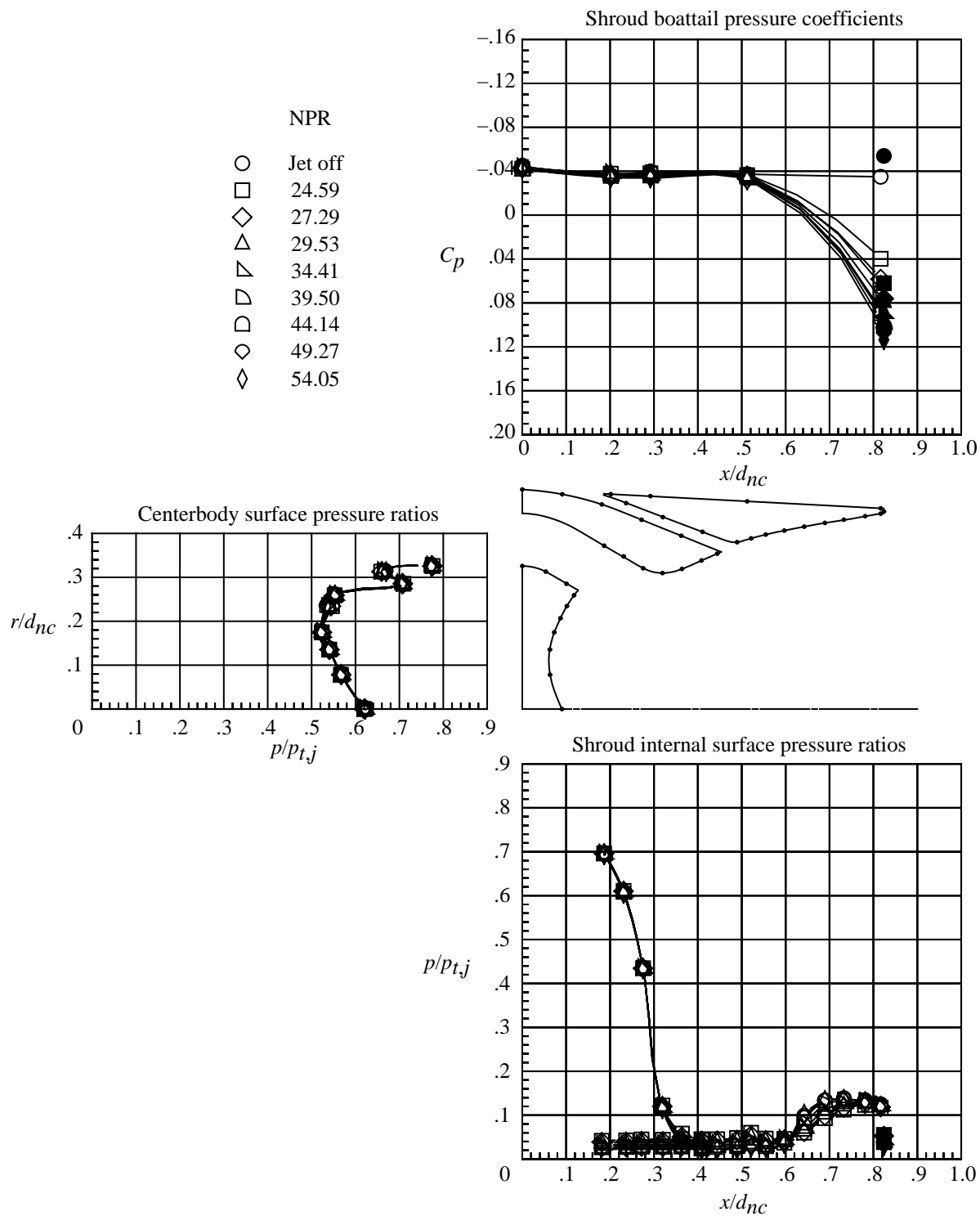
(i) $M = 2.16$.

Figure 22. Continued.



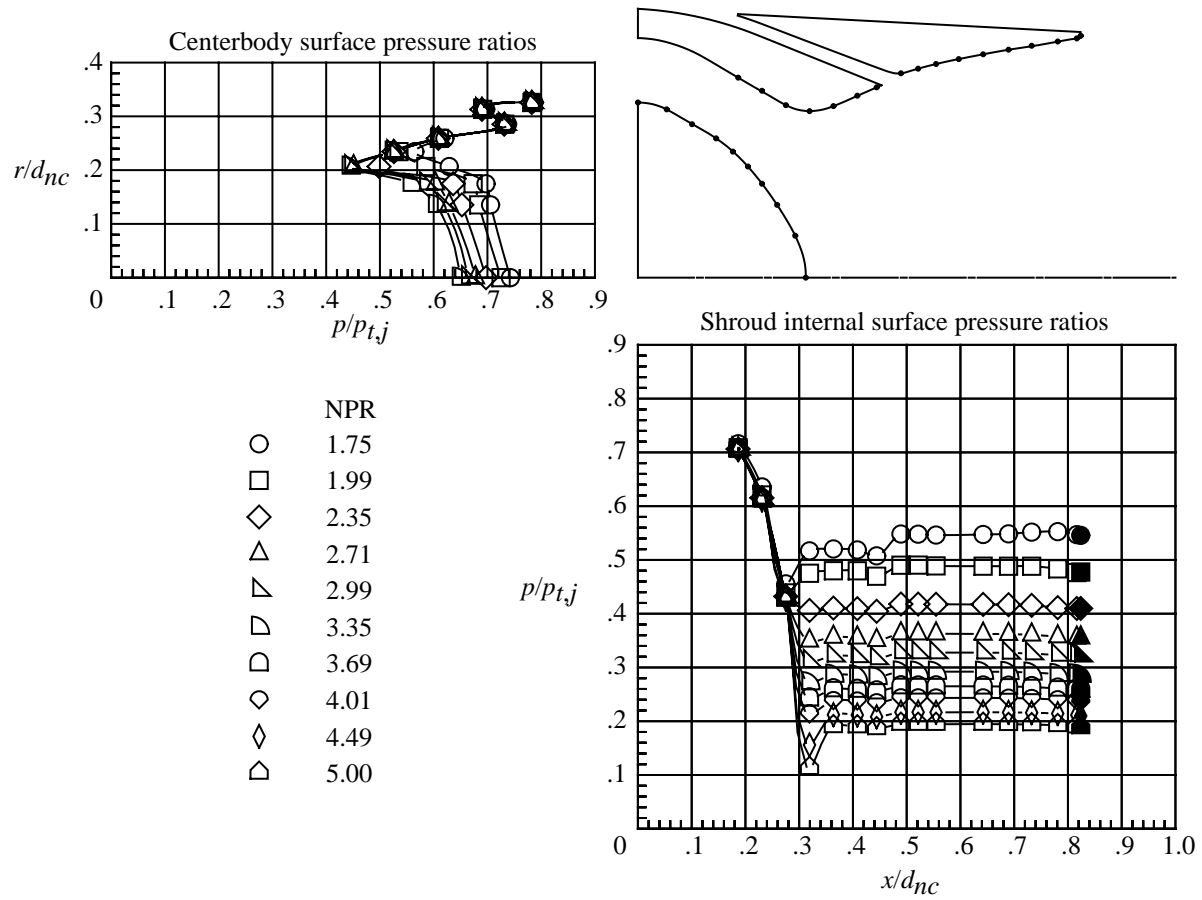
(j) $M = 2.50$.

Figure 22. Continued.



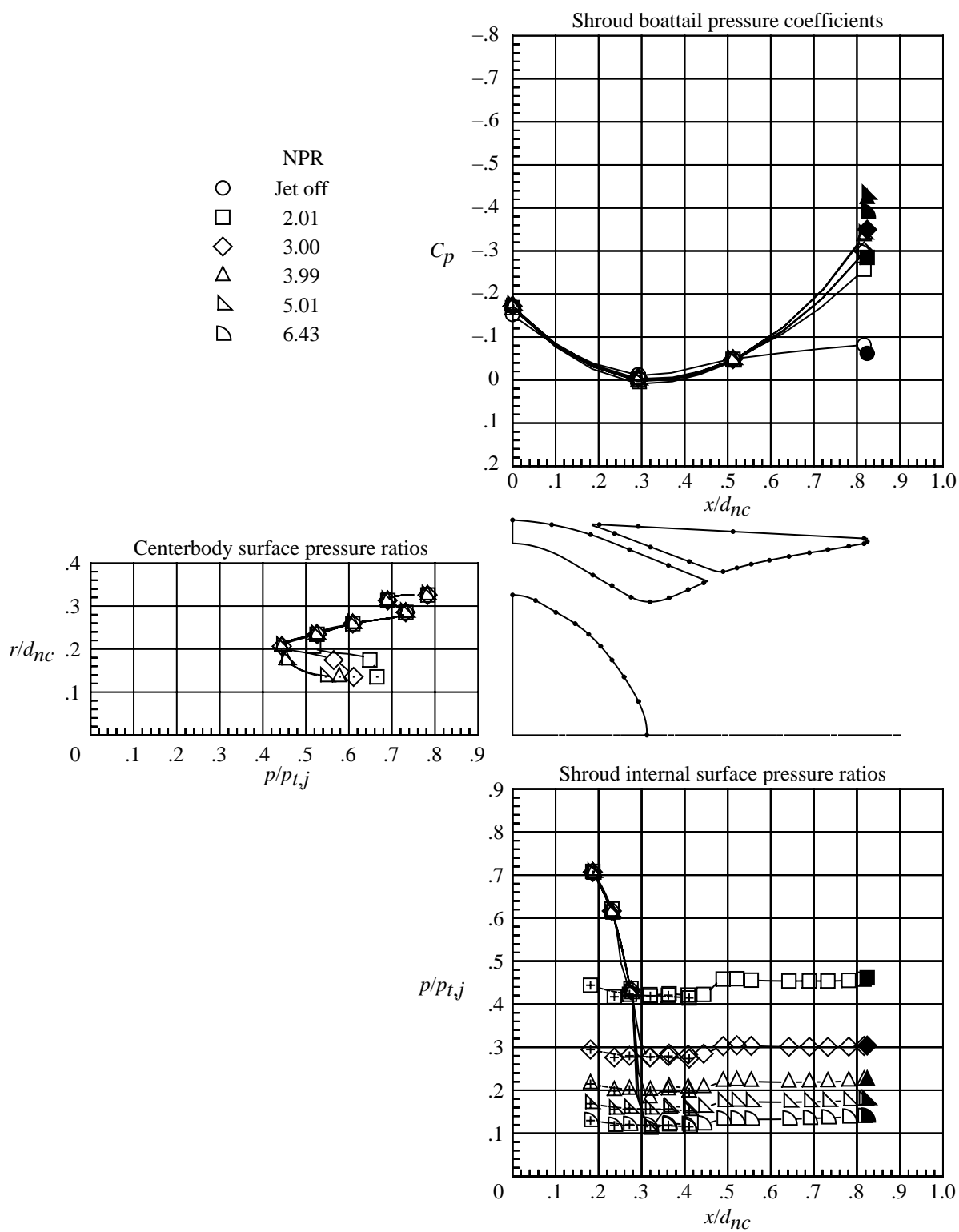
(k) $M = 2.86$.

Figure 22. Concluded.



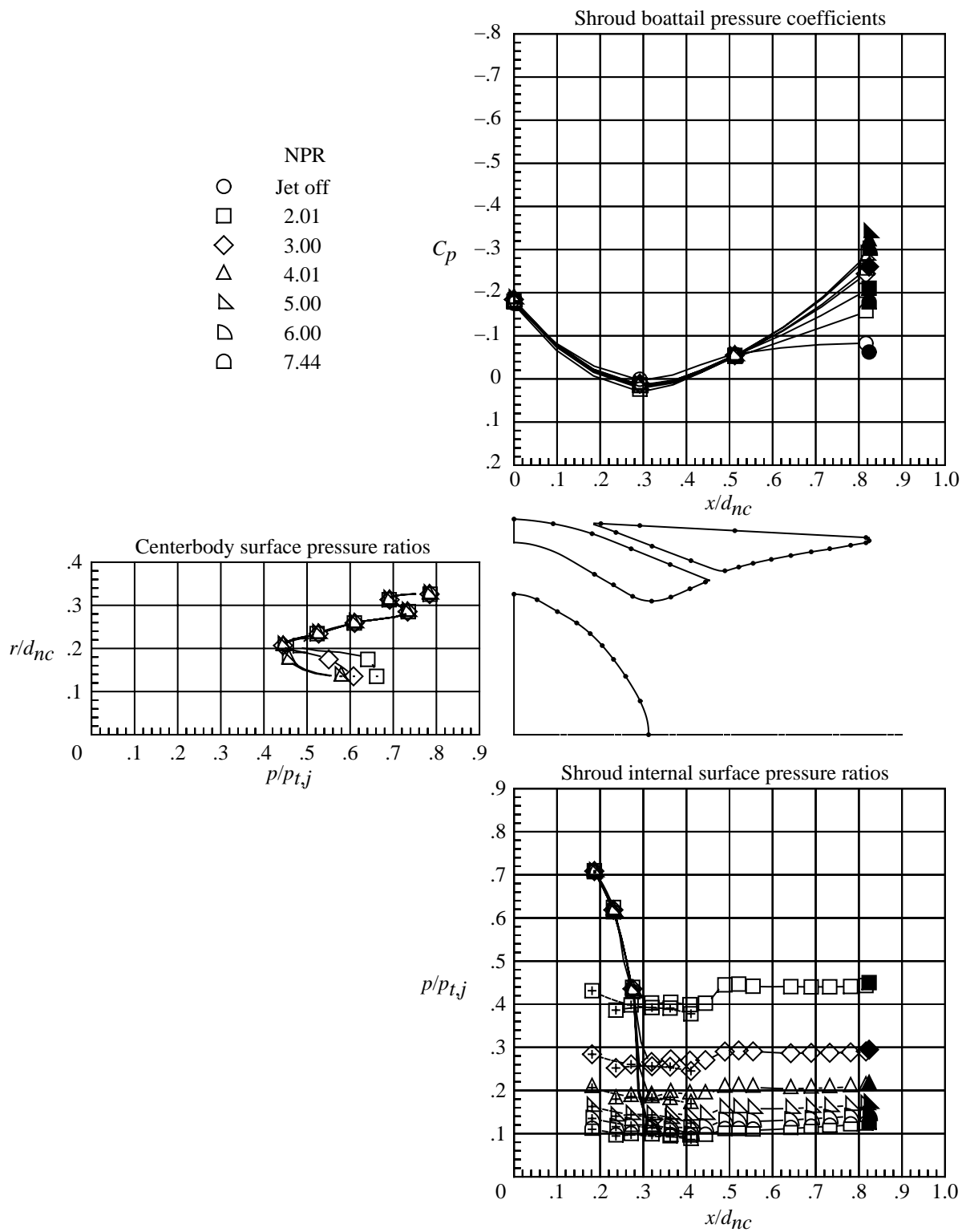
(a) $M = 0$; low nozzle pressure ratios.

Figure 23. Internal and external pressures on nozzle with long annularly vented shroud and convex centerbody. Solid symbols indicate data at shroud base and plus signs in symbols indicate wall pressures in annular slot. Dots on nozzle sketch indicate pressure orifice locations.



(b) $M = 0.60$.

Figure 23. Continued.



(c) $M = 0.80$.

Figure 23. Continued.

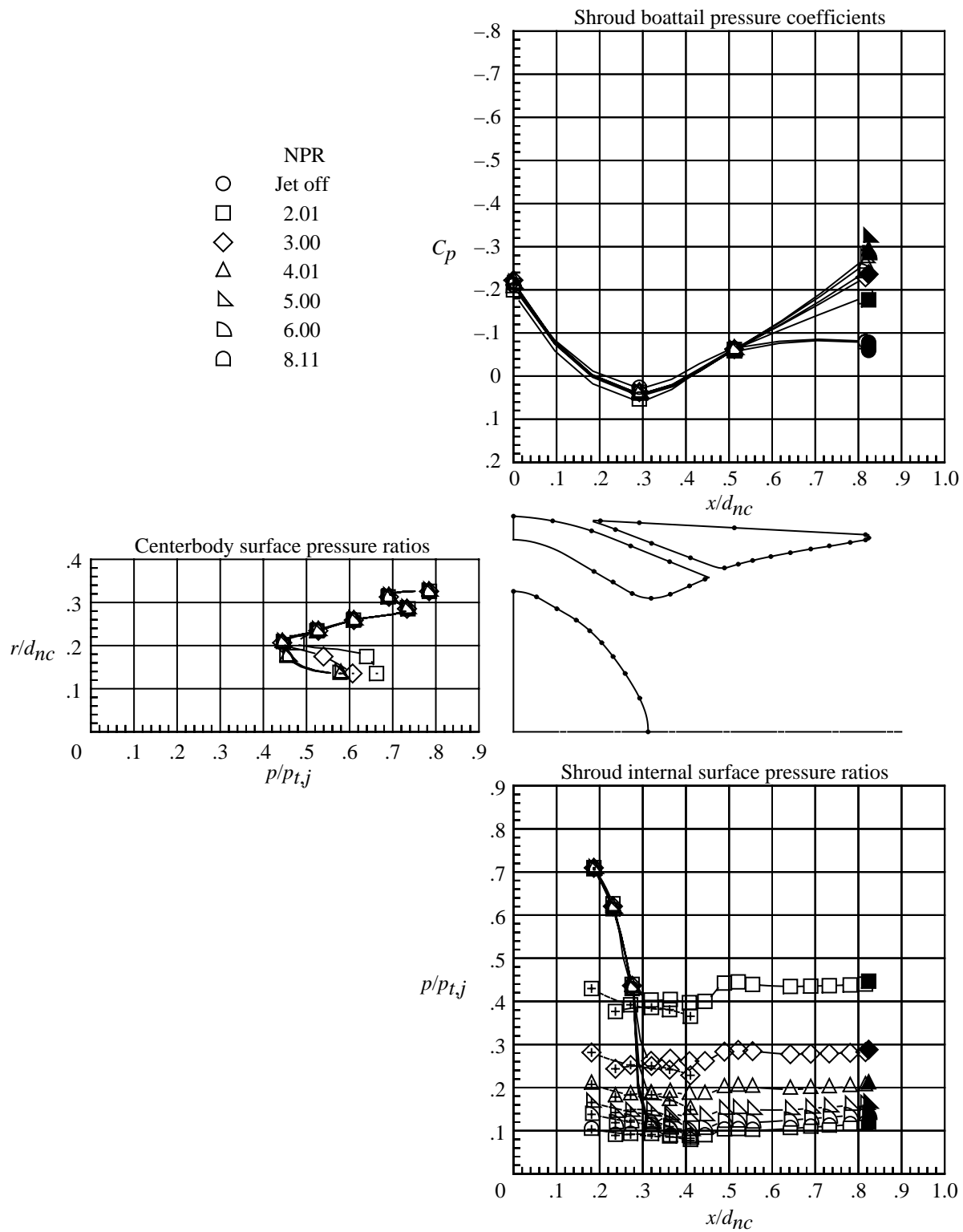
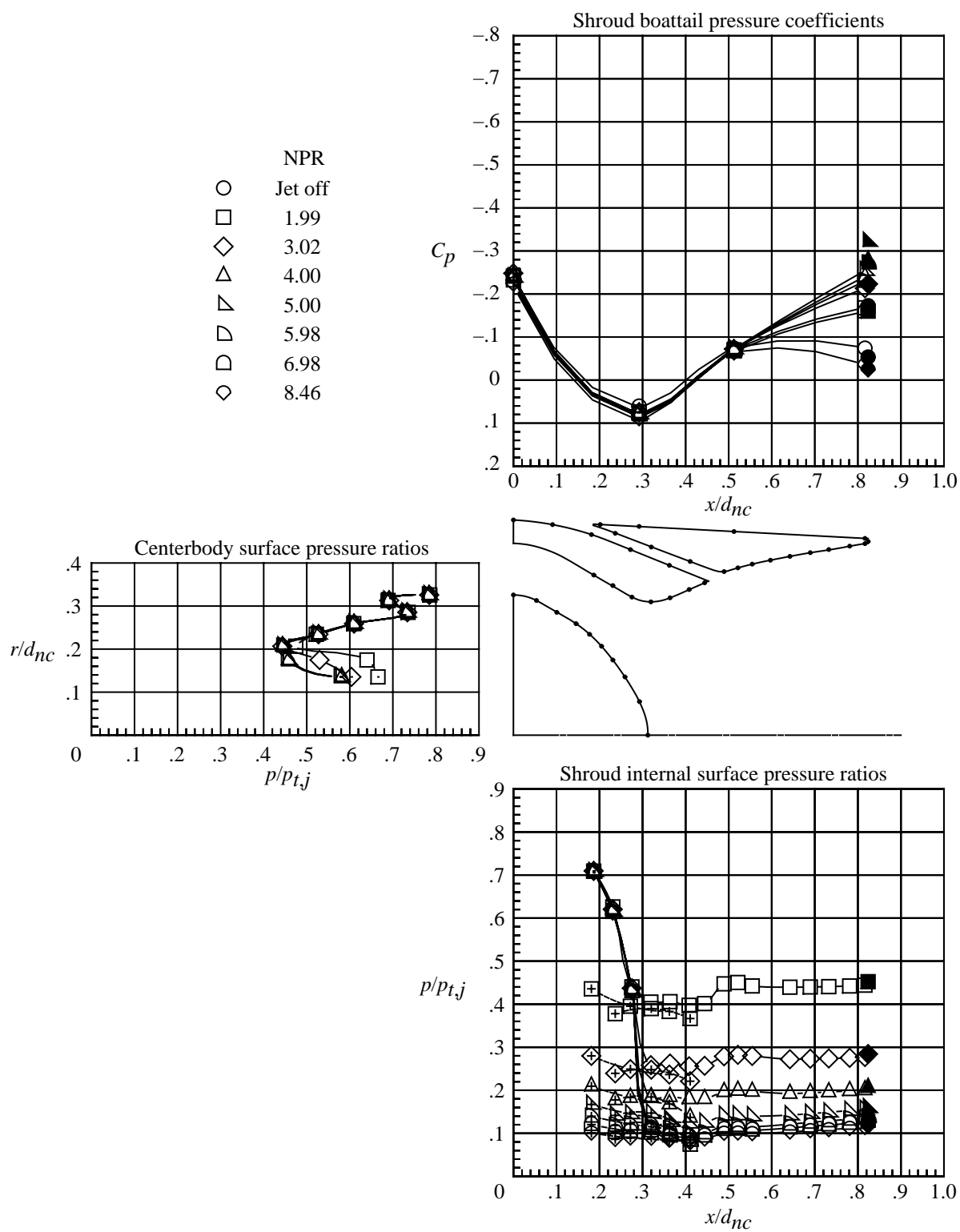
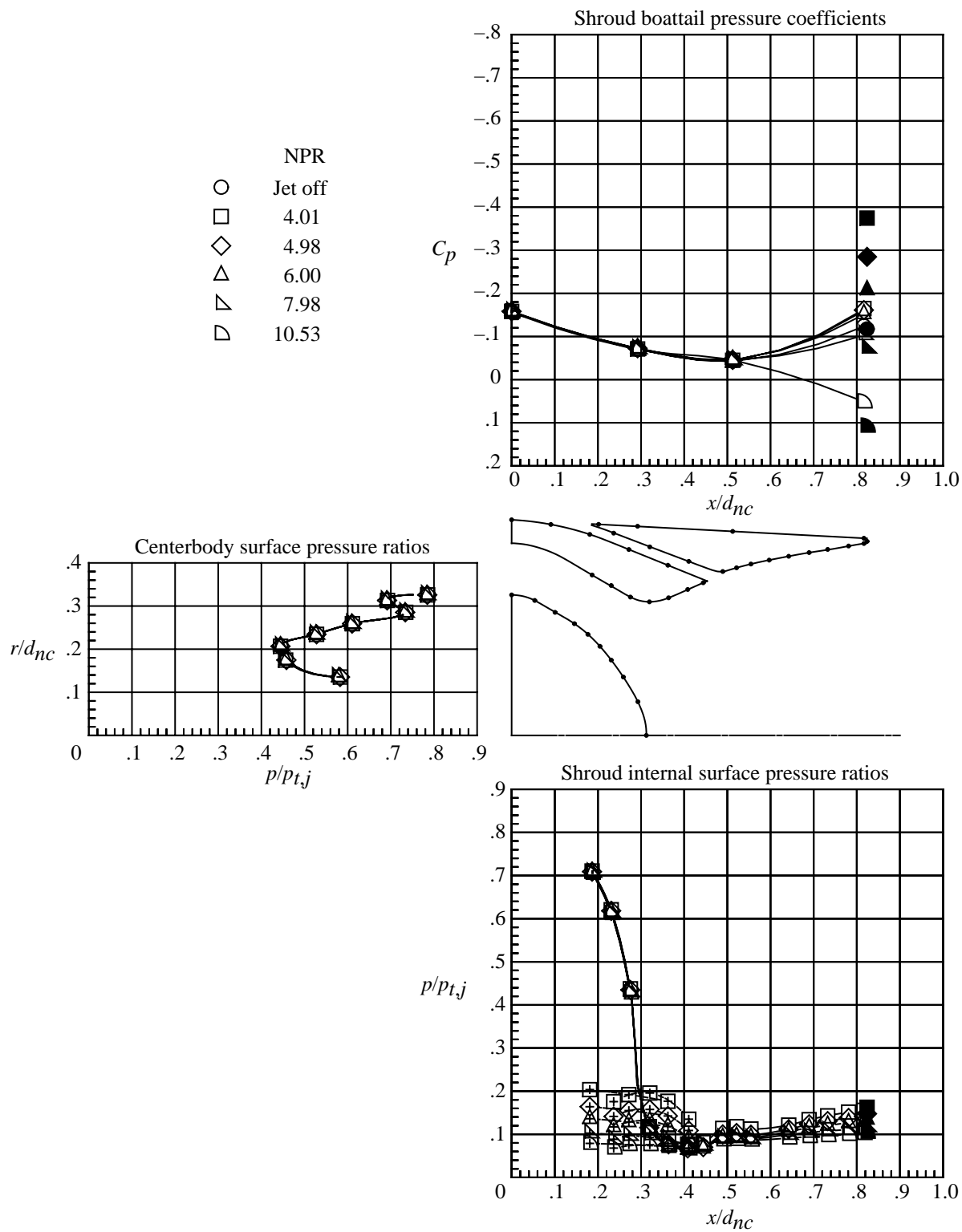


Figure 23. Continued.



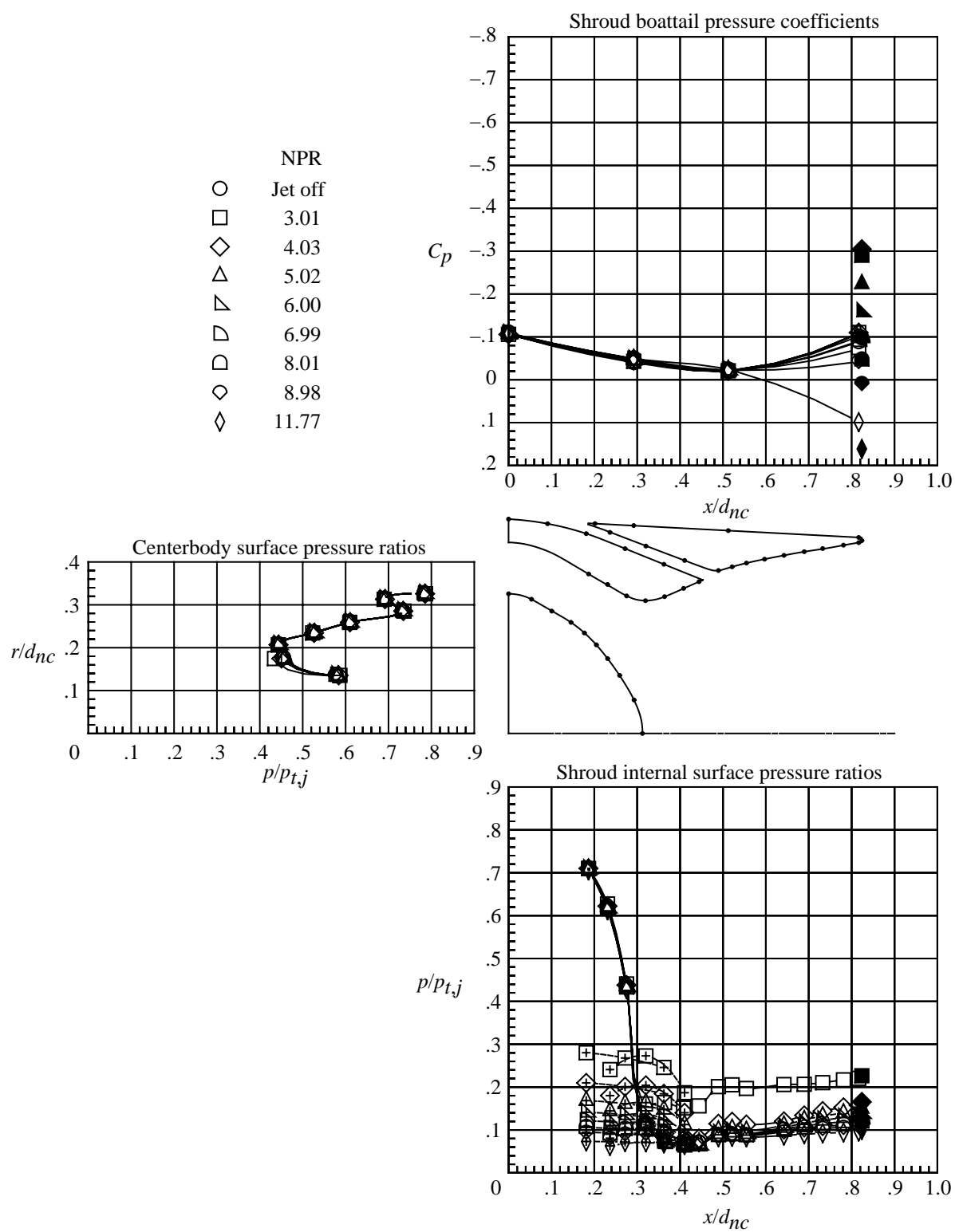
(e) $M = 0.95$.

Figure 23. Continued.



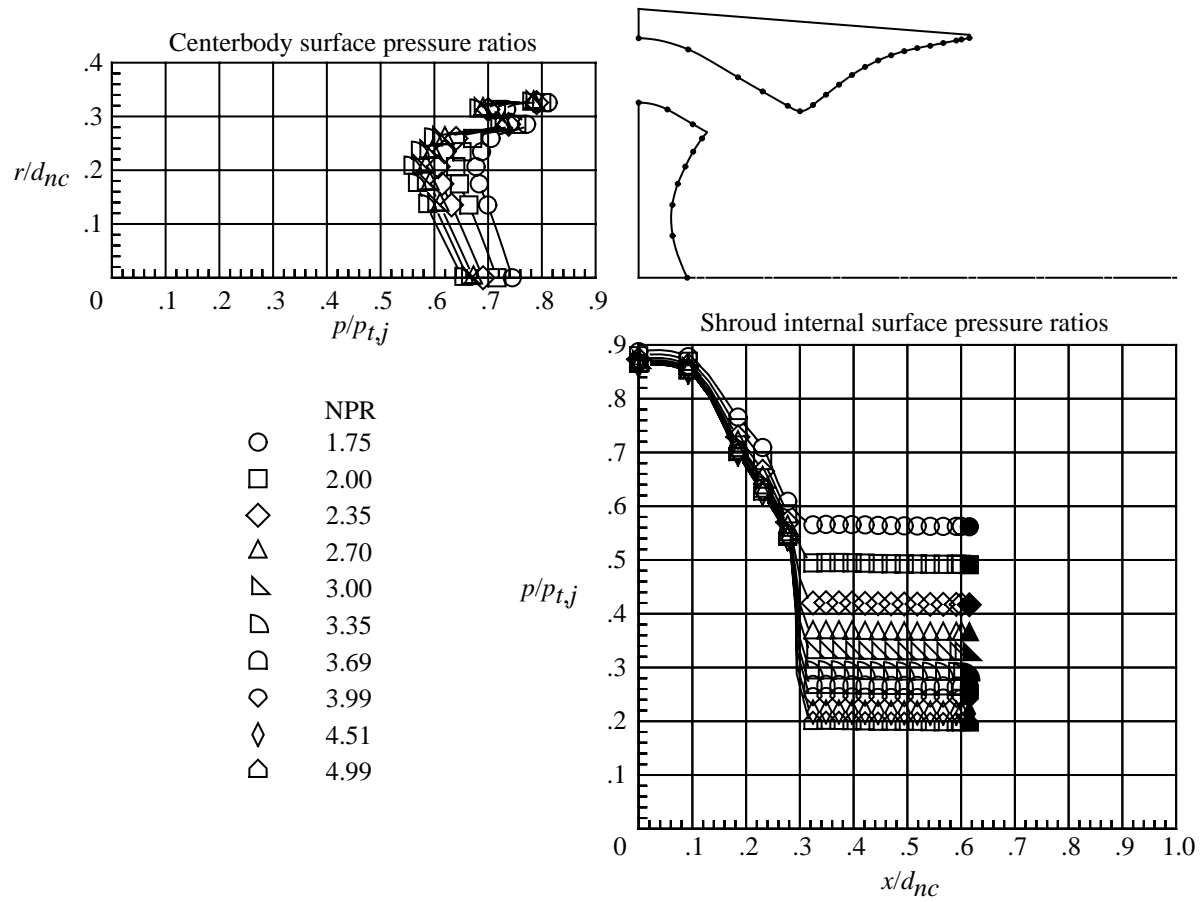
(f) $M = 1.15$.

Figure 23. Continued.



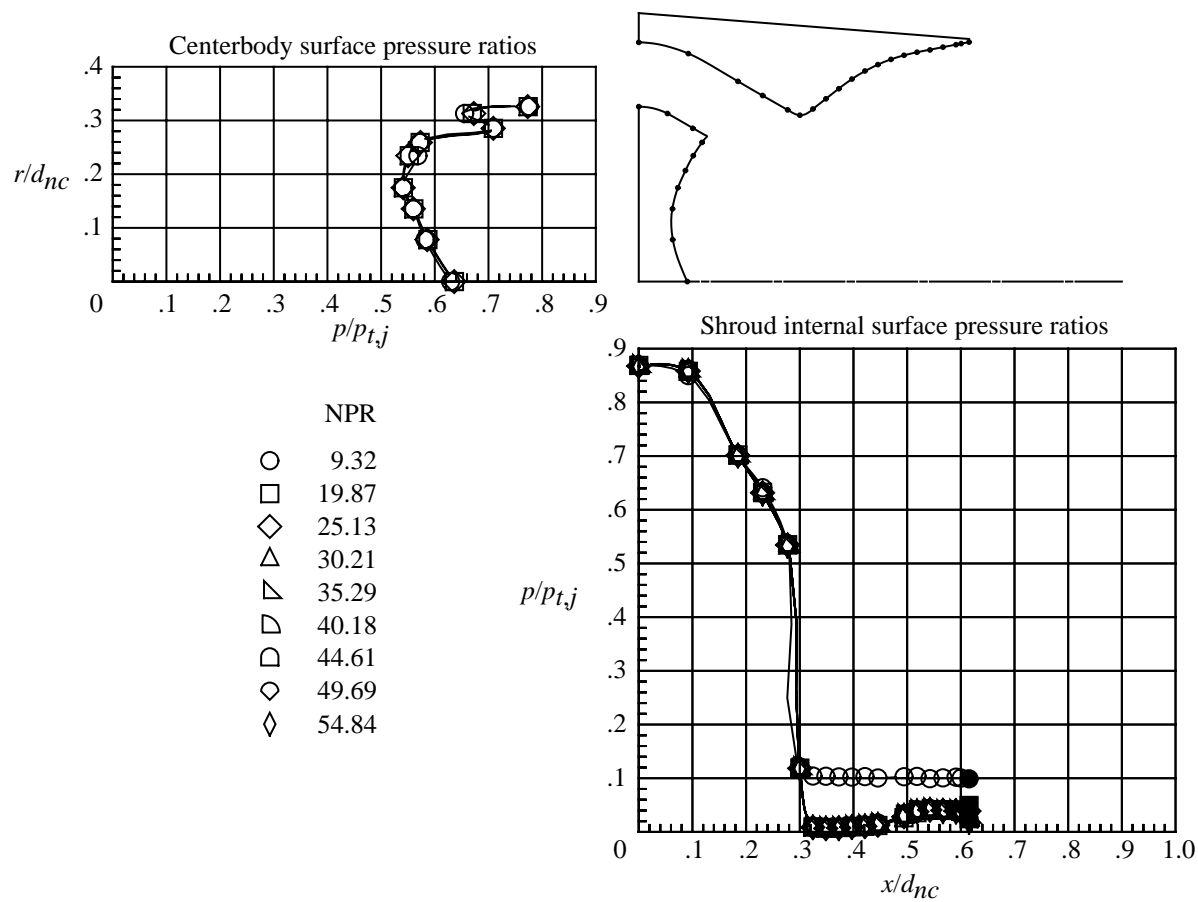
(g) $M = 1.25$.

Figure 23. Concluded.



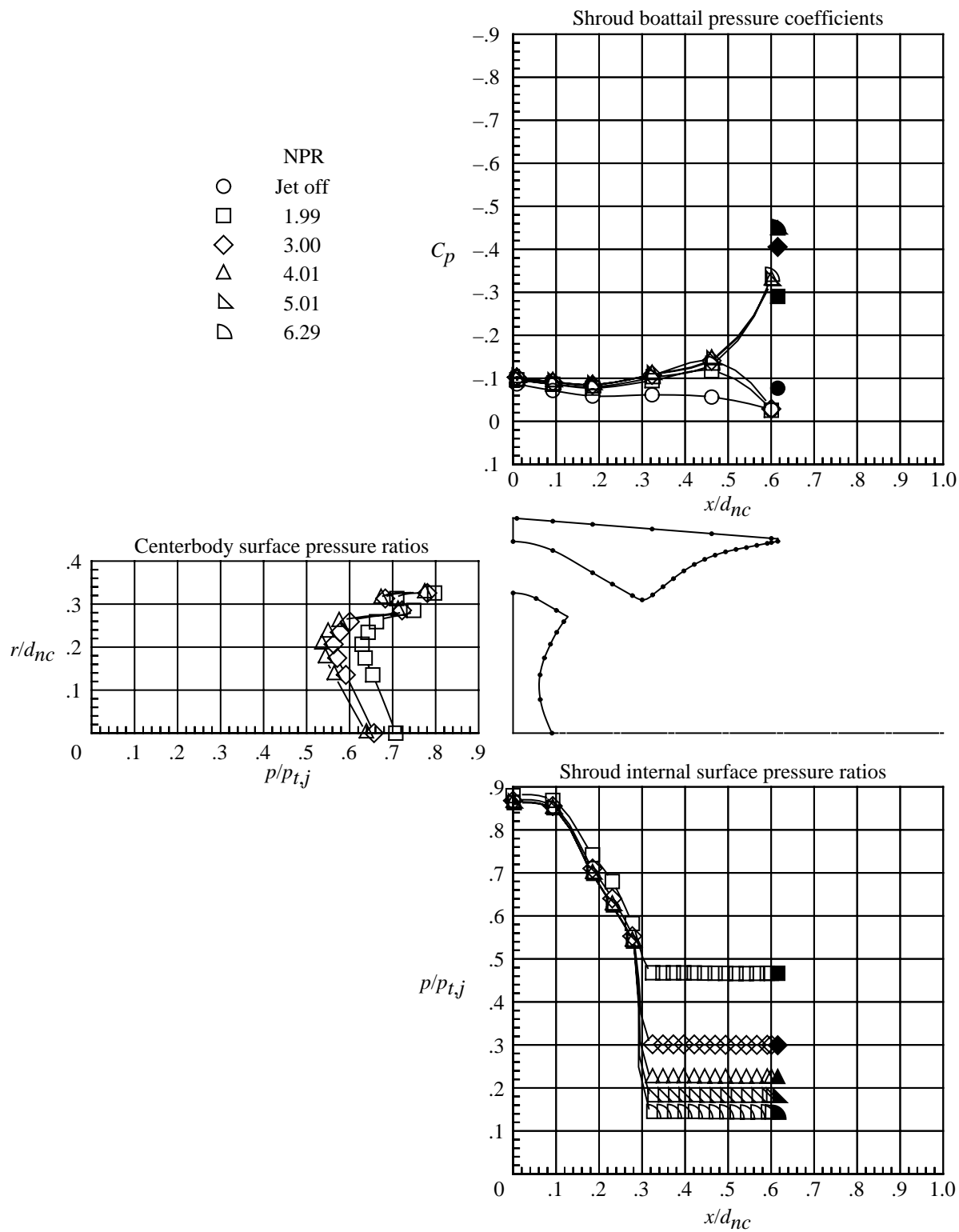
(a) $M = 0$; low nozzle pressure ratios.

Figure 24. Internal and external pressures on nozzle with short unvented shroud and concave centerbody. Solid symbols indicate data at shroud base. Dots on nozzle sketch indicate pressure orifice locations.



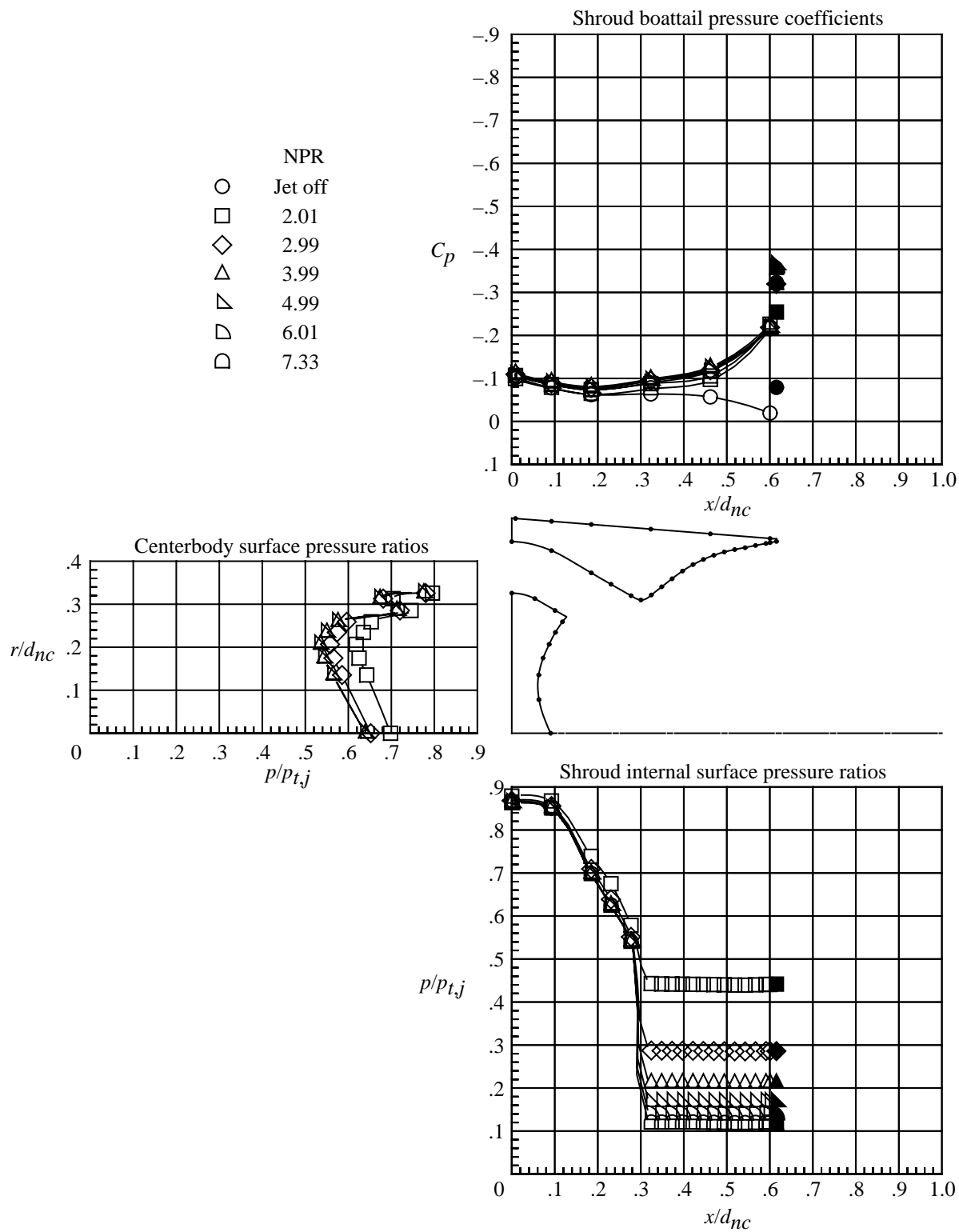
(b) $M = 0$; high nozzle pressure ratios.

Figure 24. Continued.



(c) $M = 0.60$.

Figure 24. Continued.



(d) $M = 0.80$.

Figure 24. Continued.

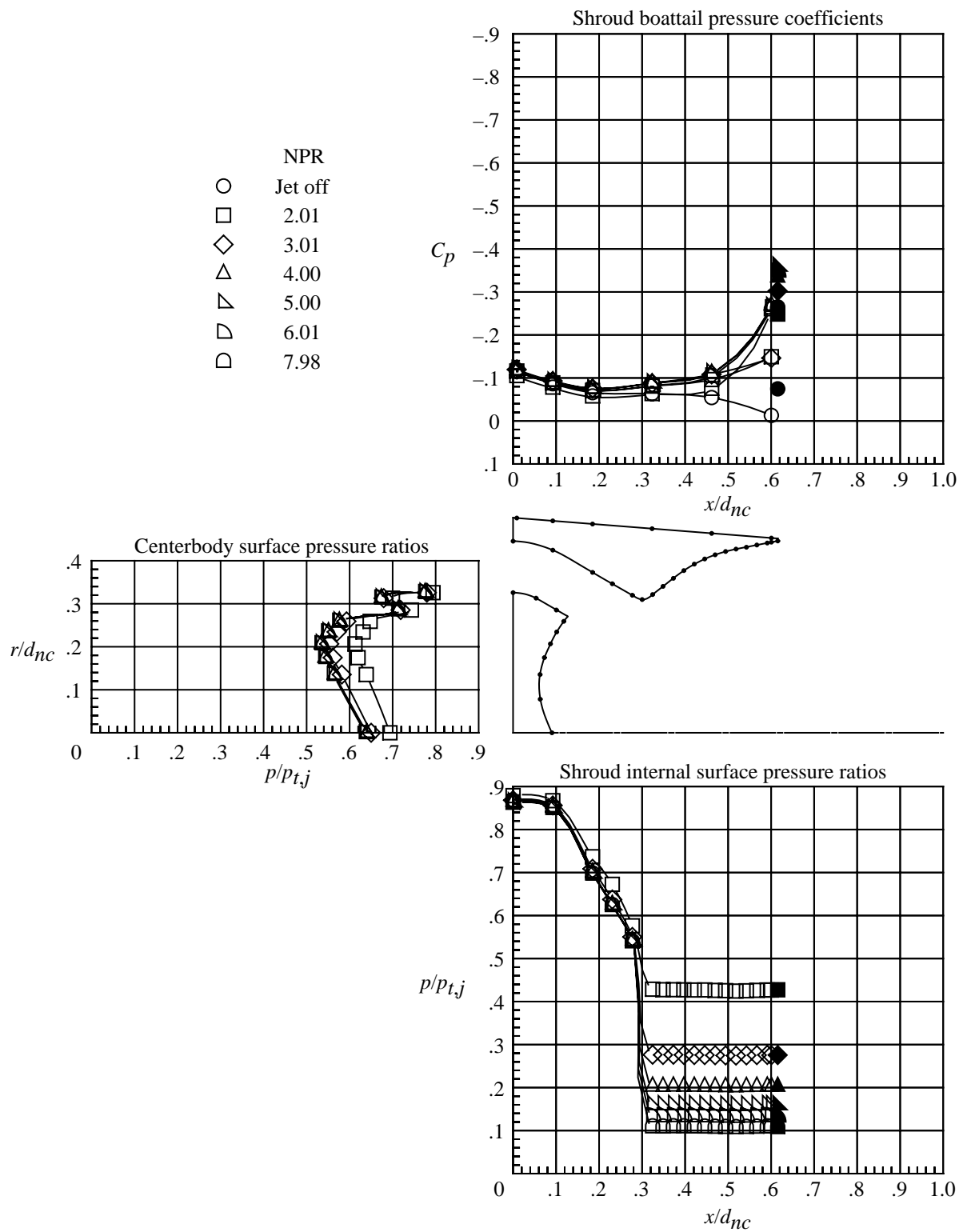


Figure 24. Continued.

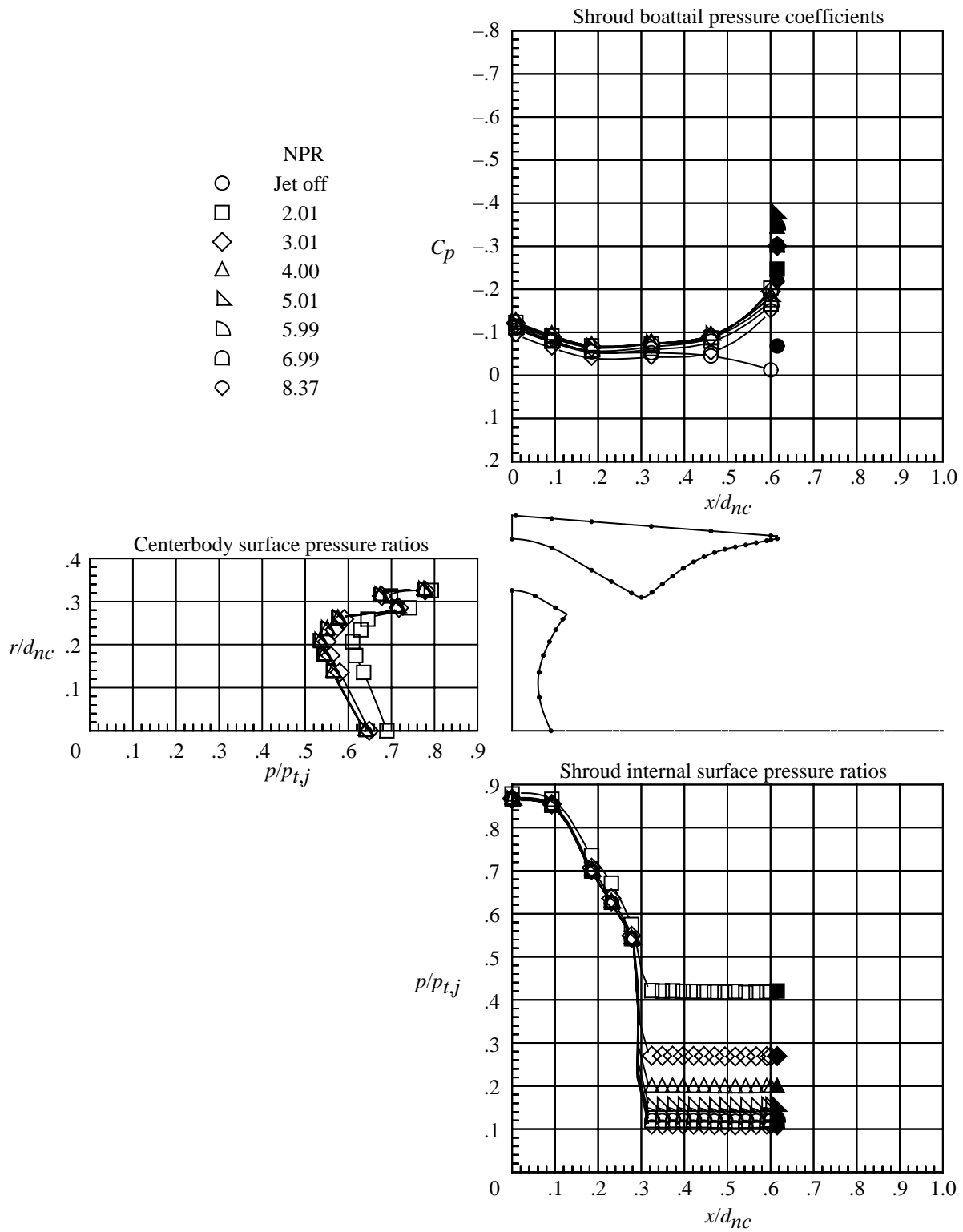
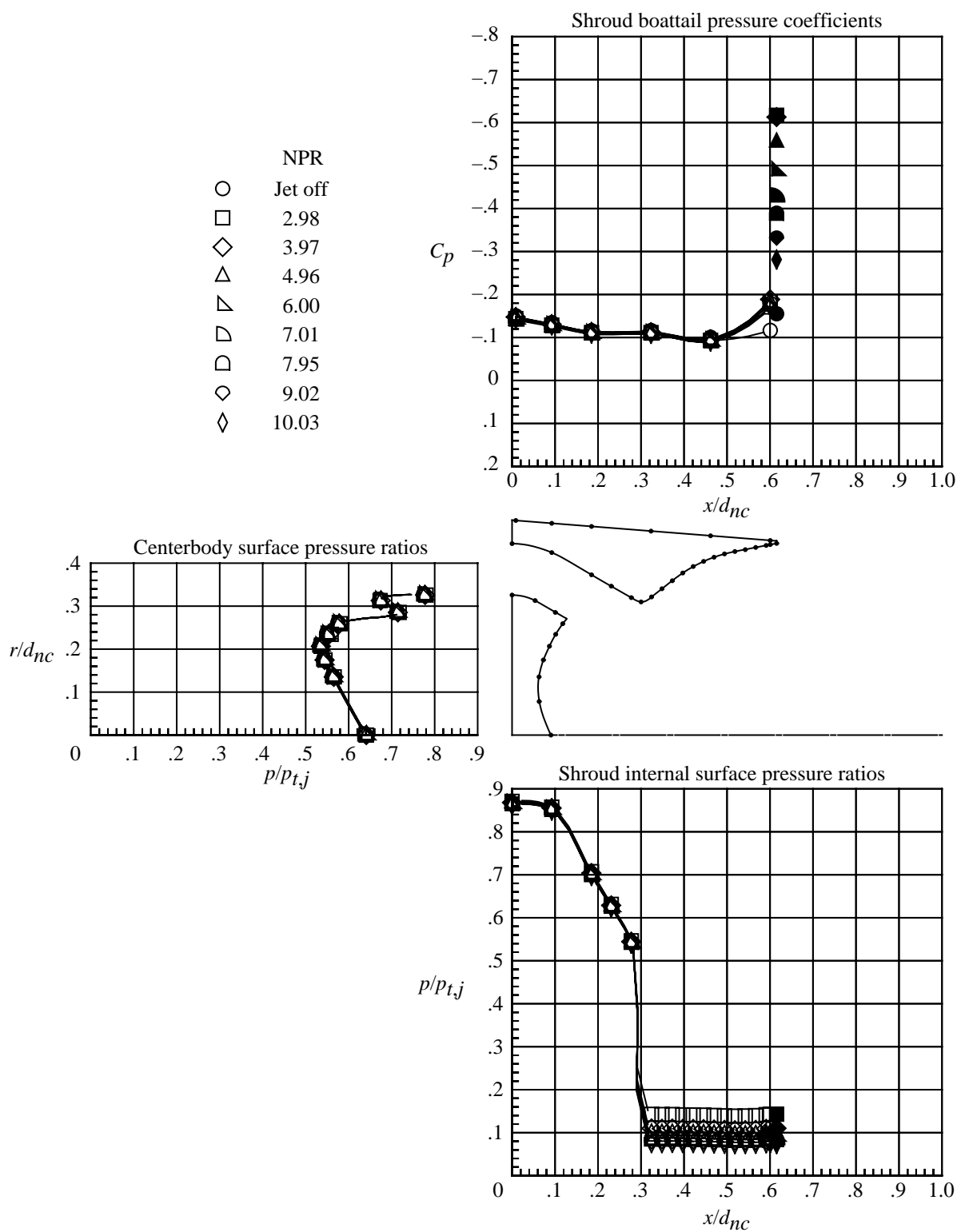
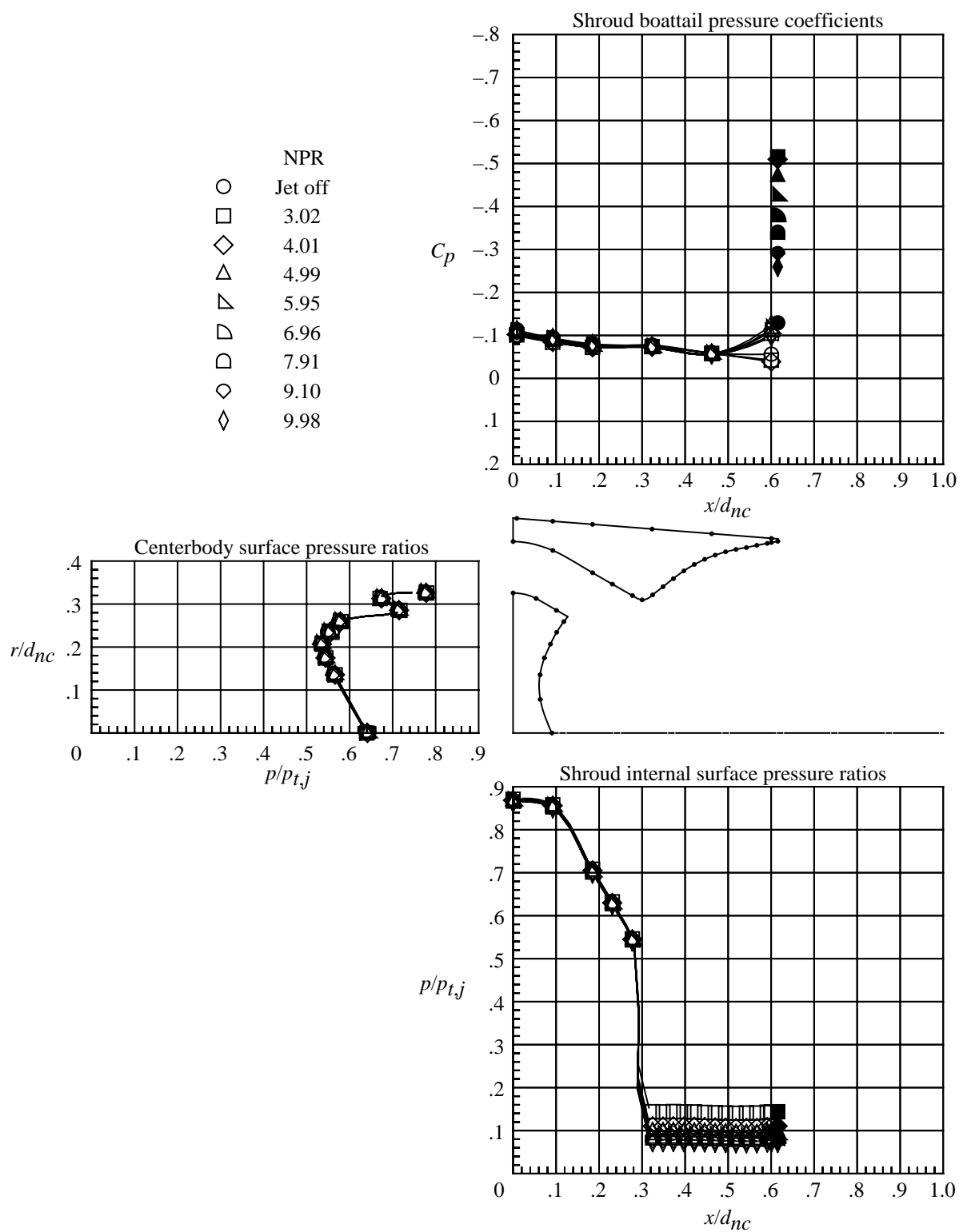


Figure 24. Continued.



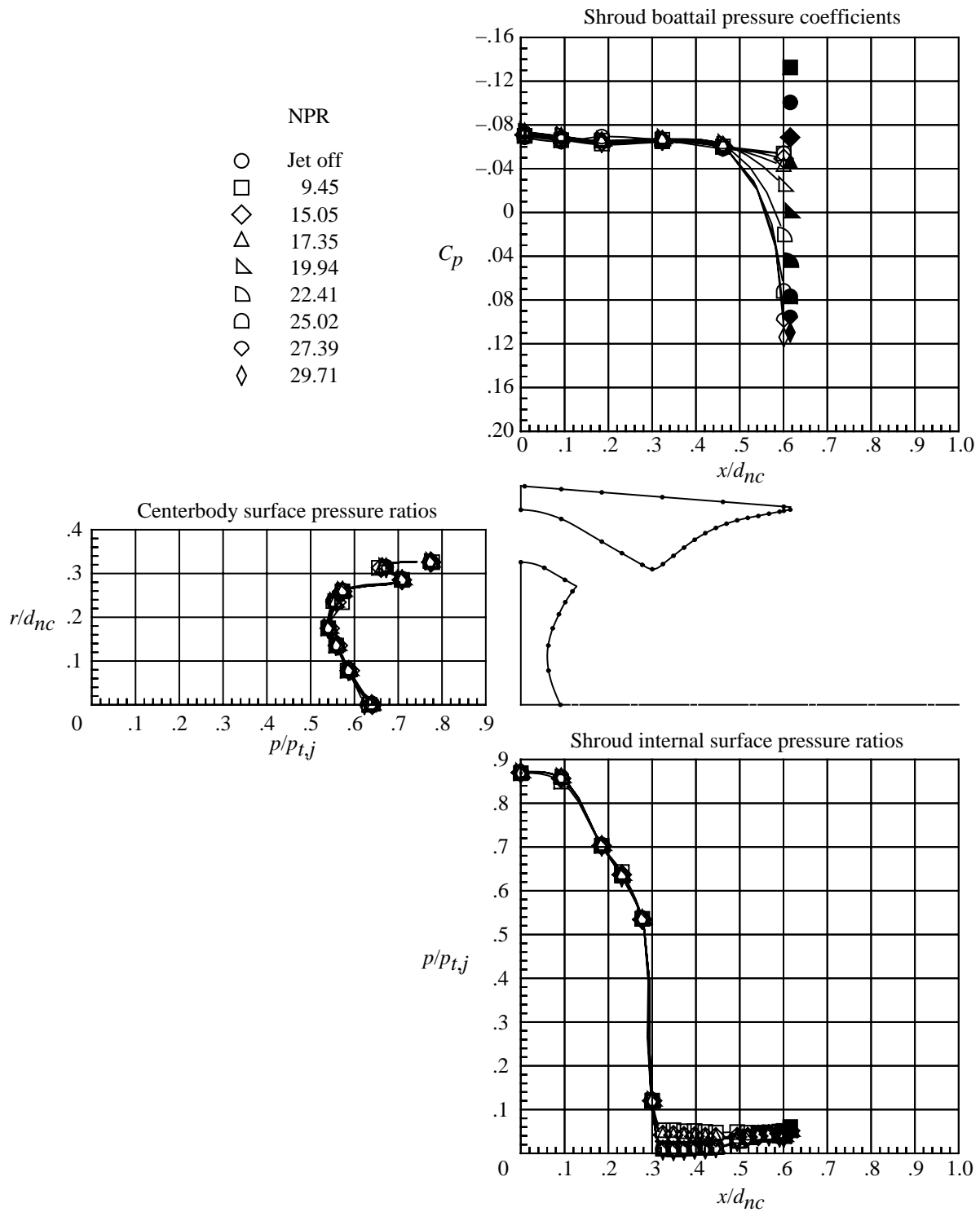
(g) $M = 1.15$.

Figure 24. Continued.



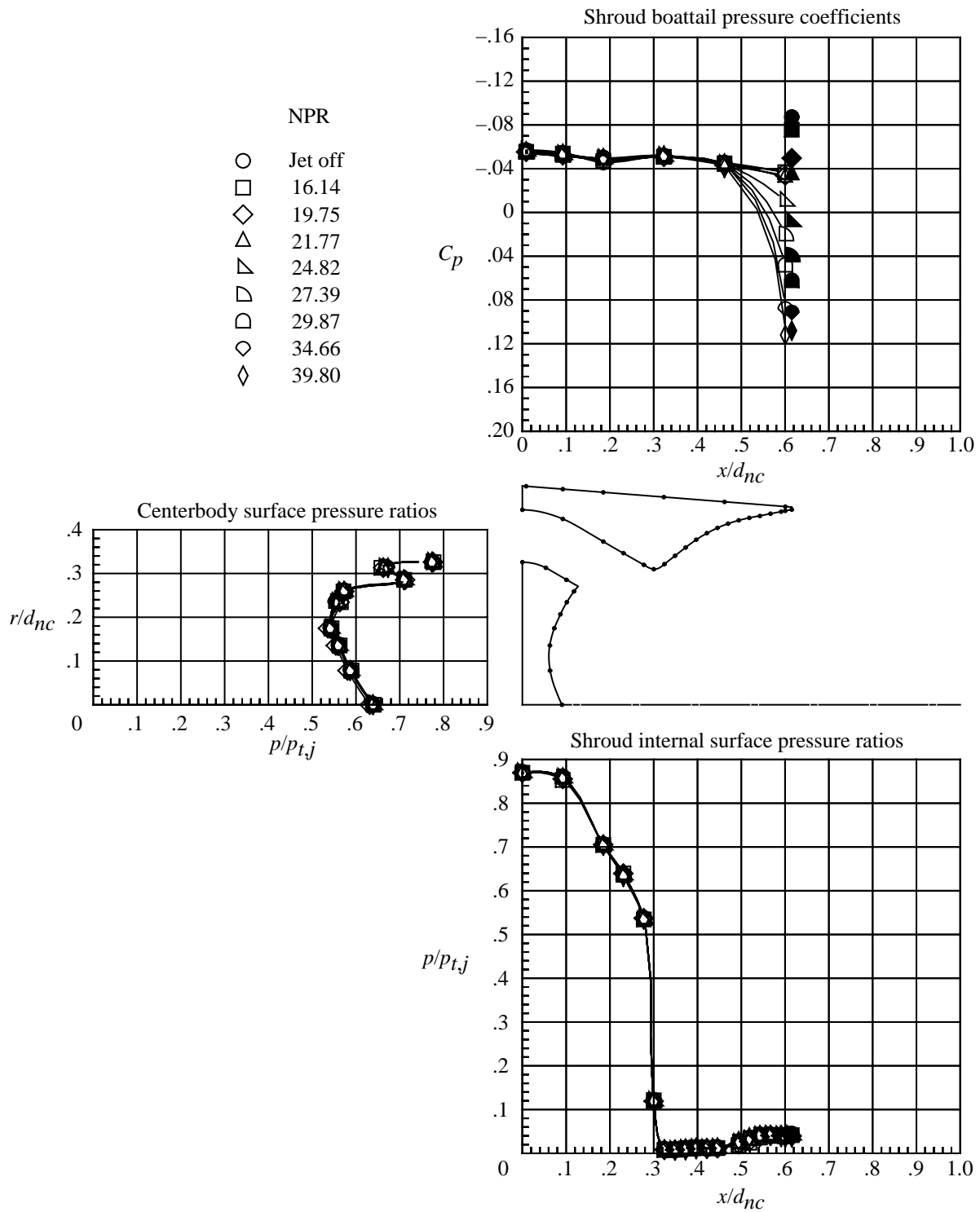
(h) $M = 1.25$.

Figure 24. Continued.



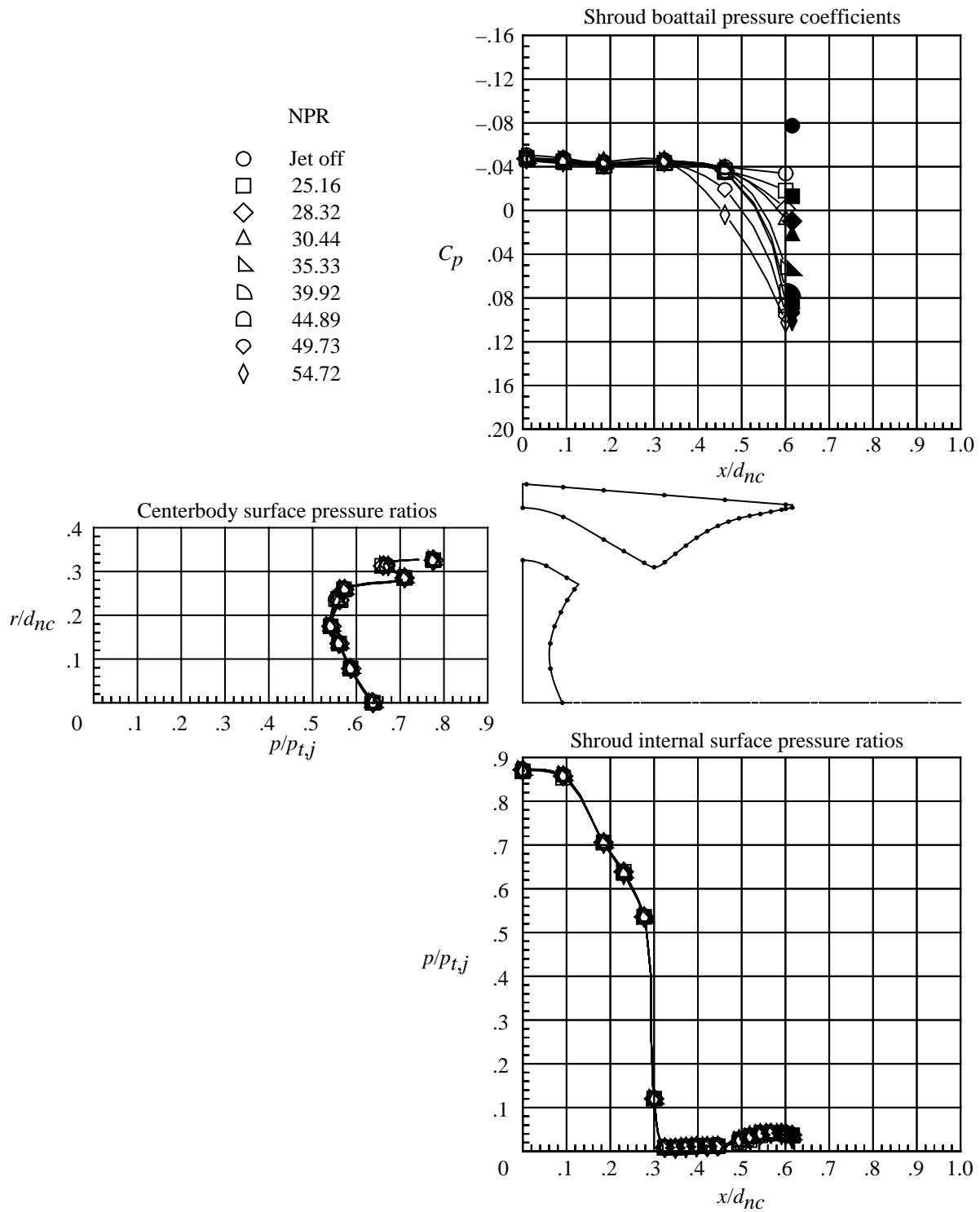
(i) $M = 2.16$.

Figure 24. Continued.



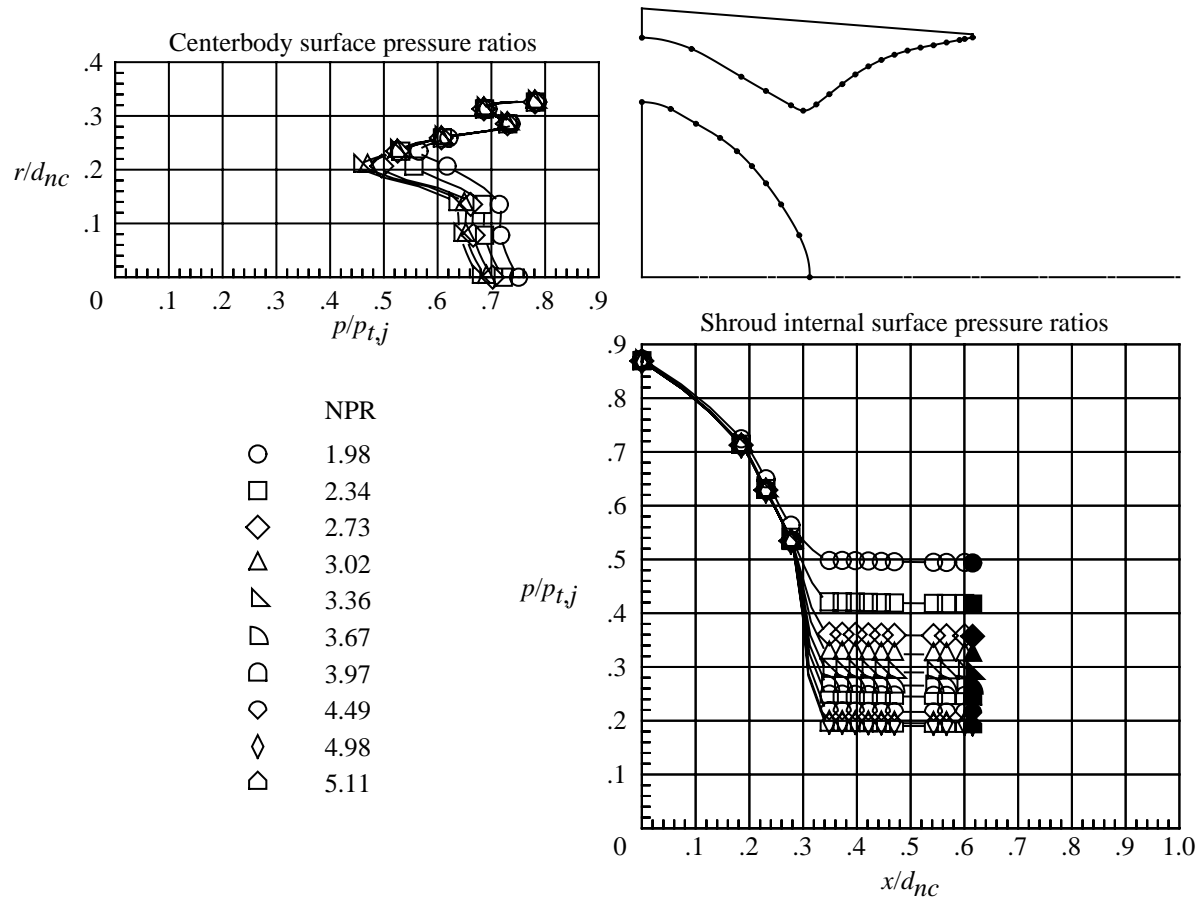
(j) $M = 2.50$.

Figure 24. Continued.



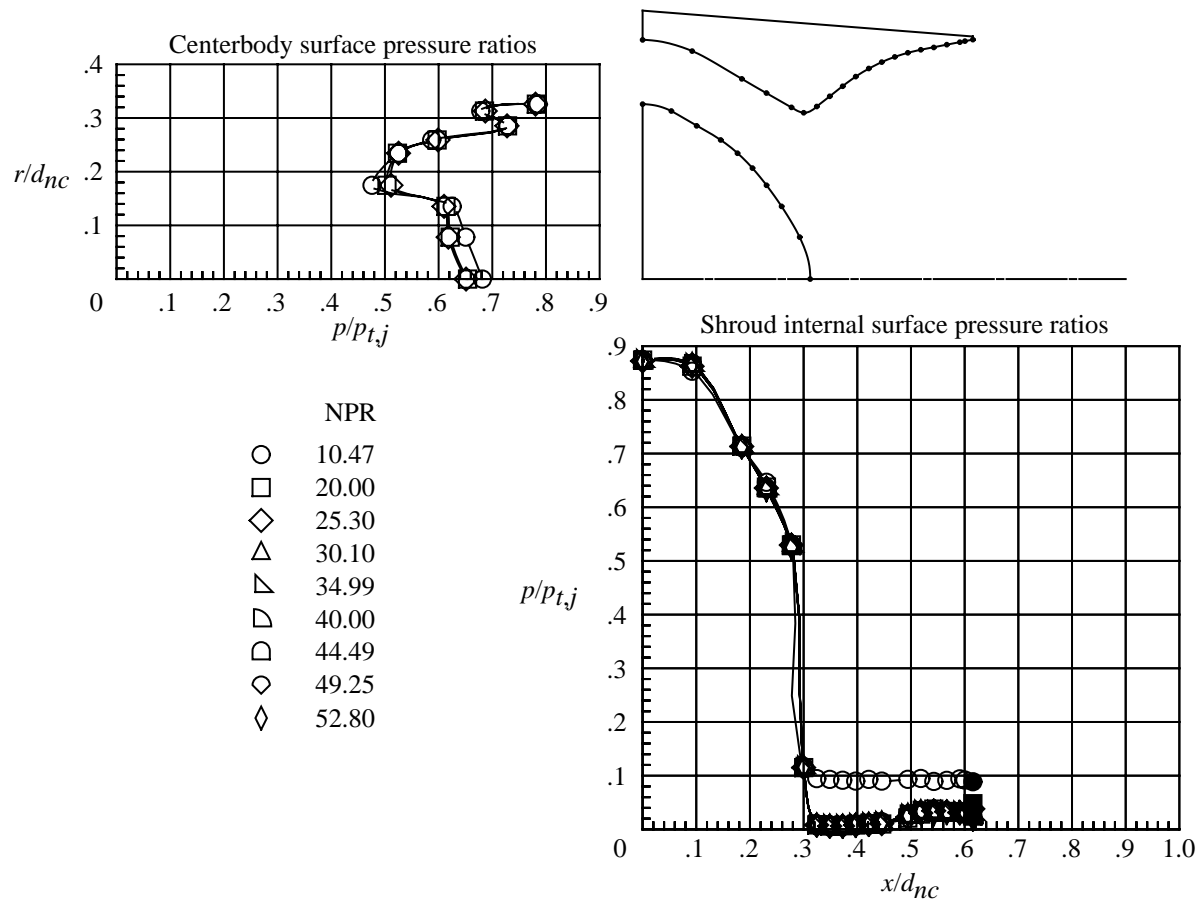
(k) $M = 2.86$.

Figure 24. Concluded.



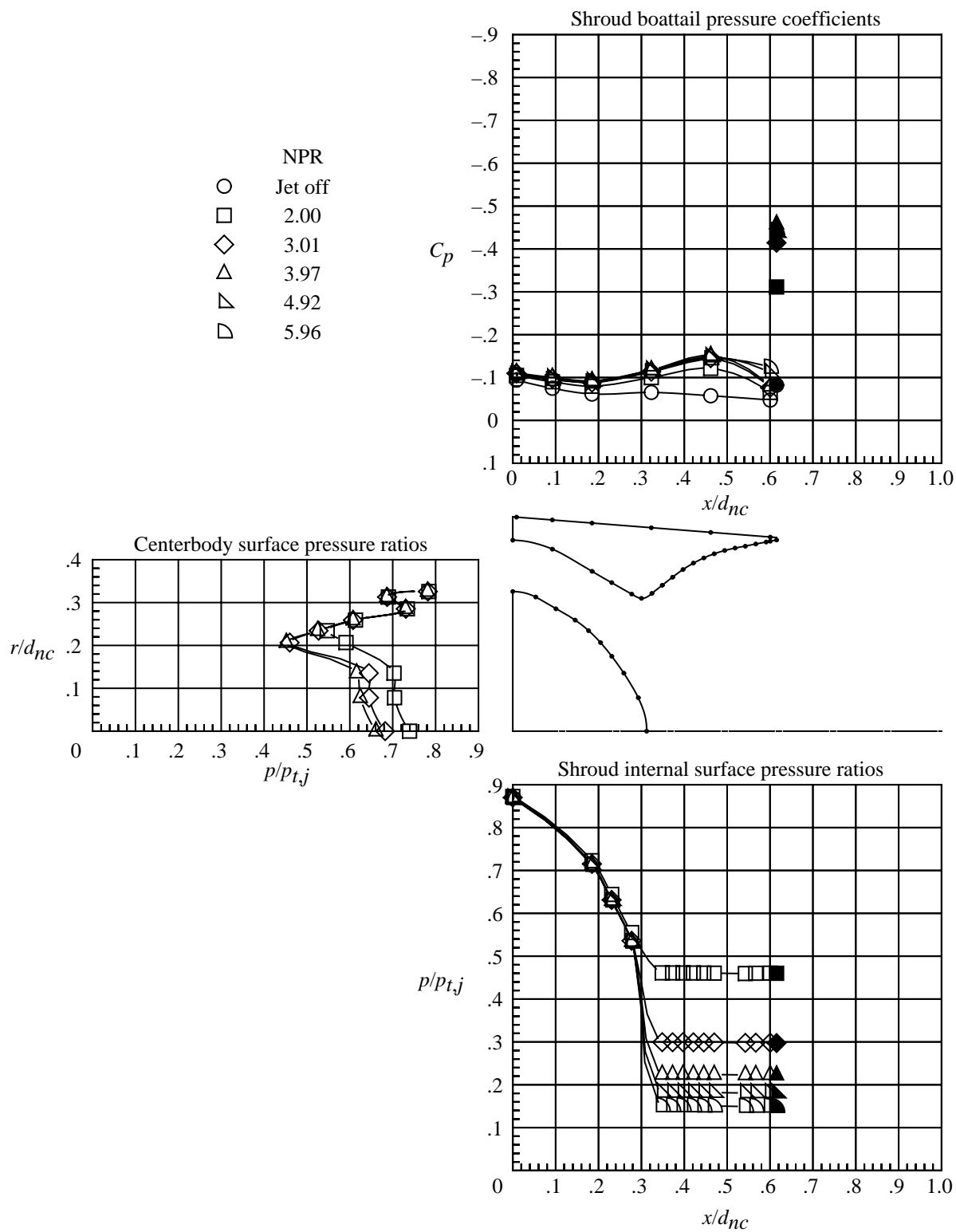
(a) $M = 0$; low nozzle pressure ratios.

Figure 25. Internal and external pressures on nozzle with short unvented shroud and convex centerbody. Solid symbols indicate data at shroud base. Dots on nozzle sketch indicate pressure orifice locations.



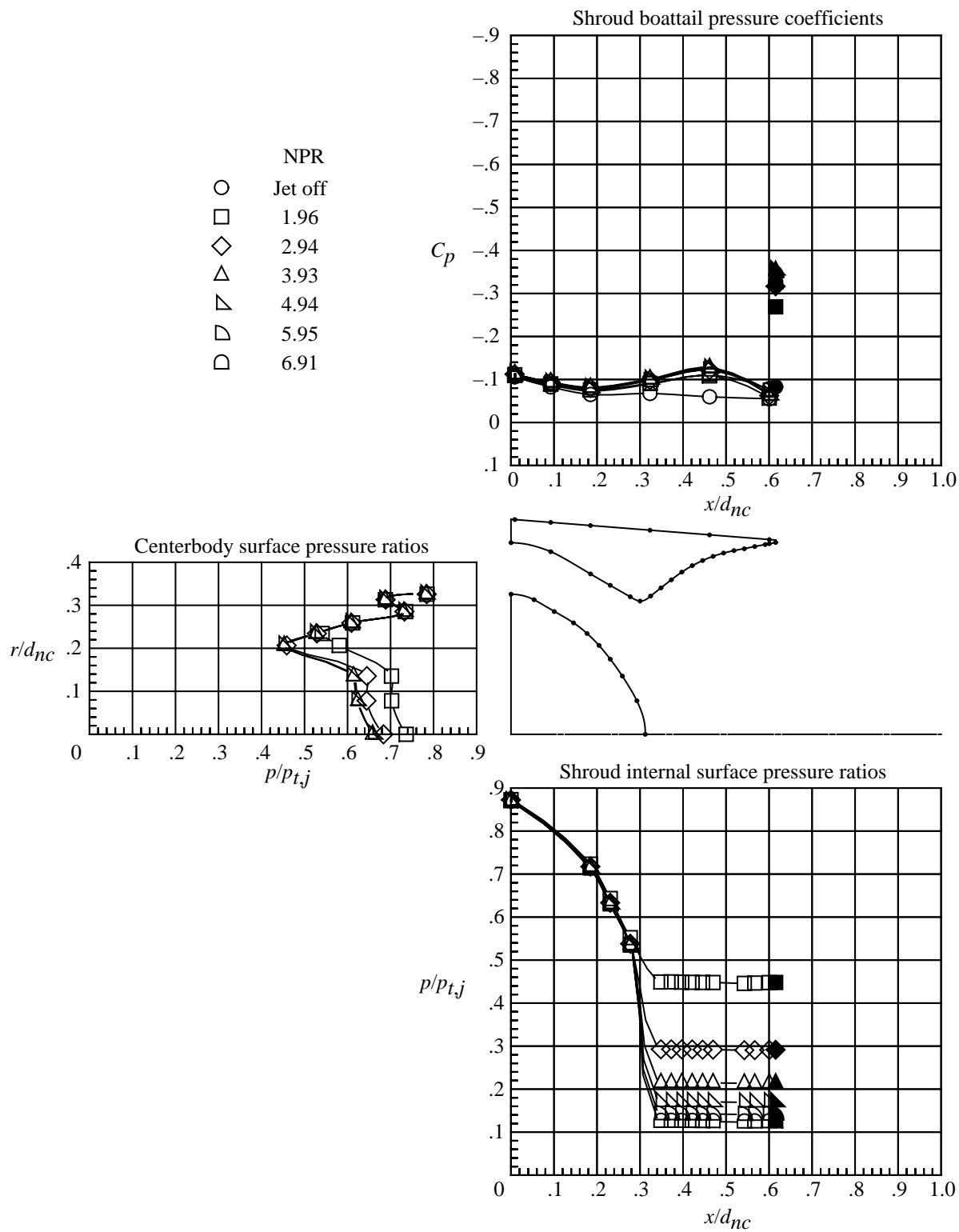
(b) $M = 0$; high nozzle pressure ratios.

Figure 25. Continued.



(c) $M = 0.60$.

Figure 25. Continued.



(d) $M = 0.80$.

Figure 25. Continued.

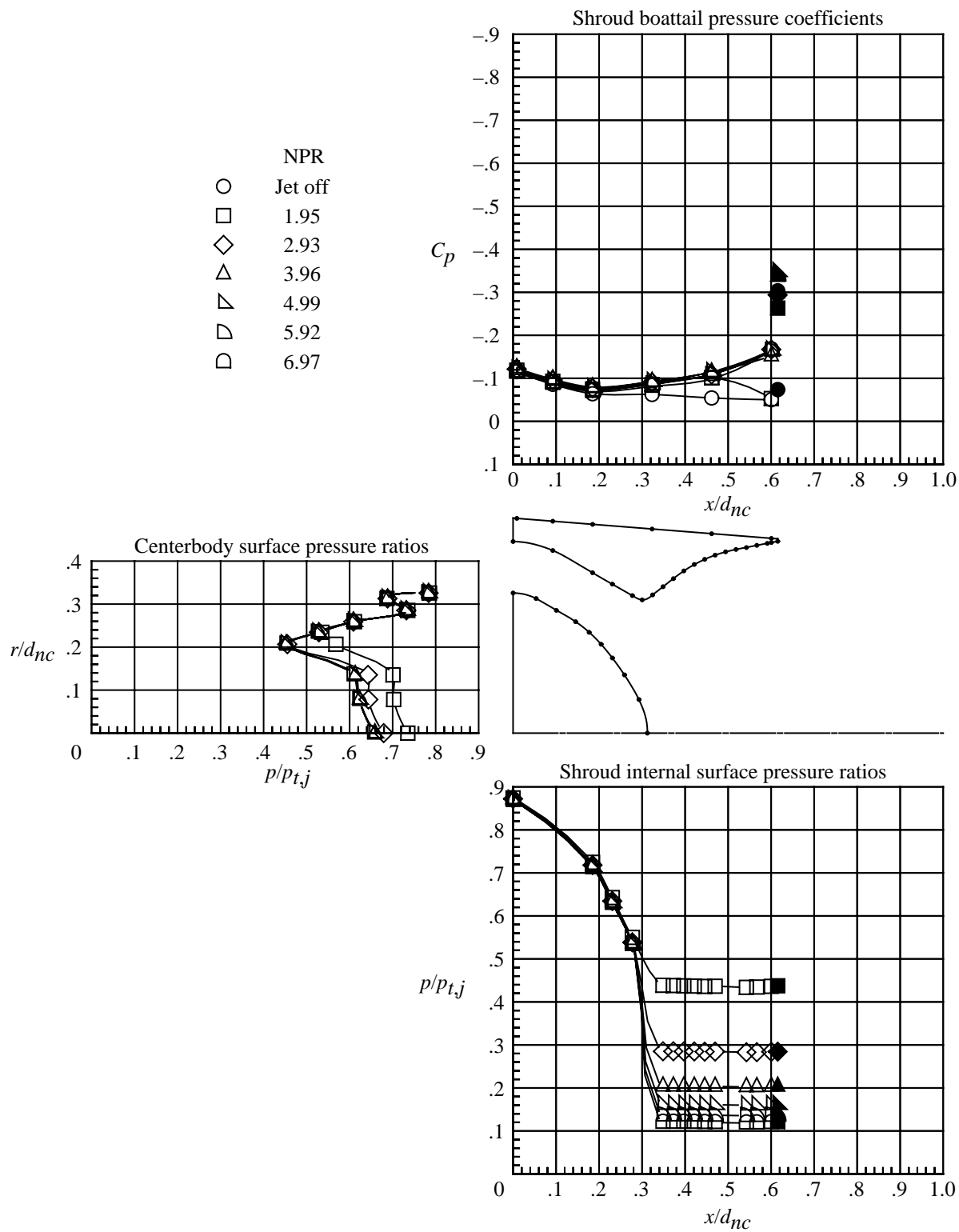
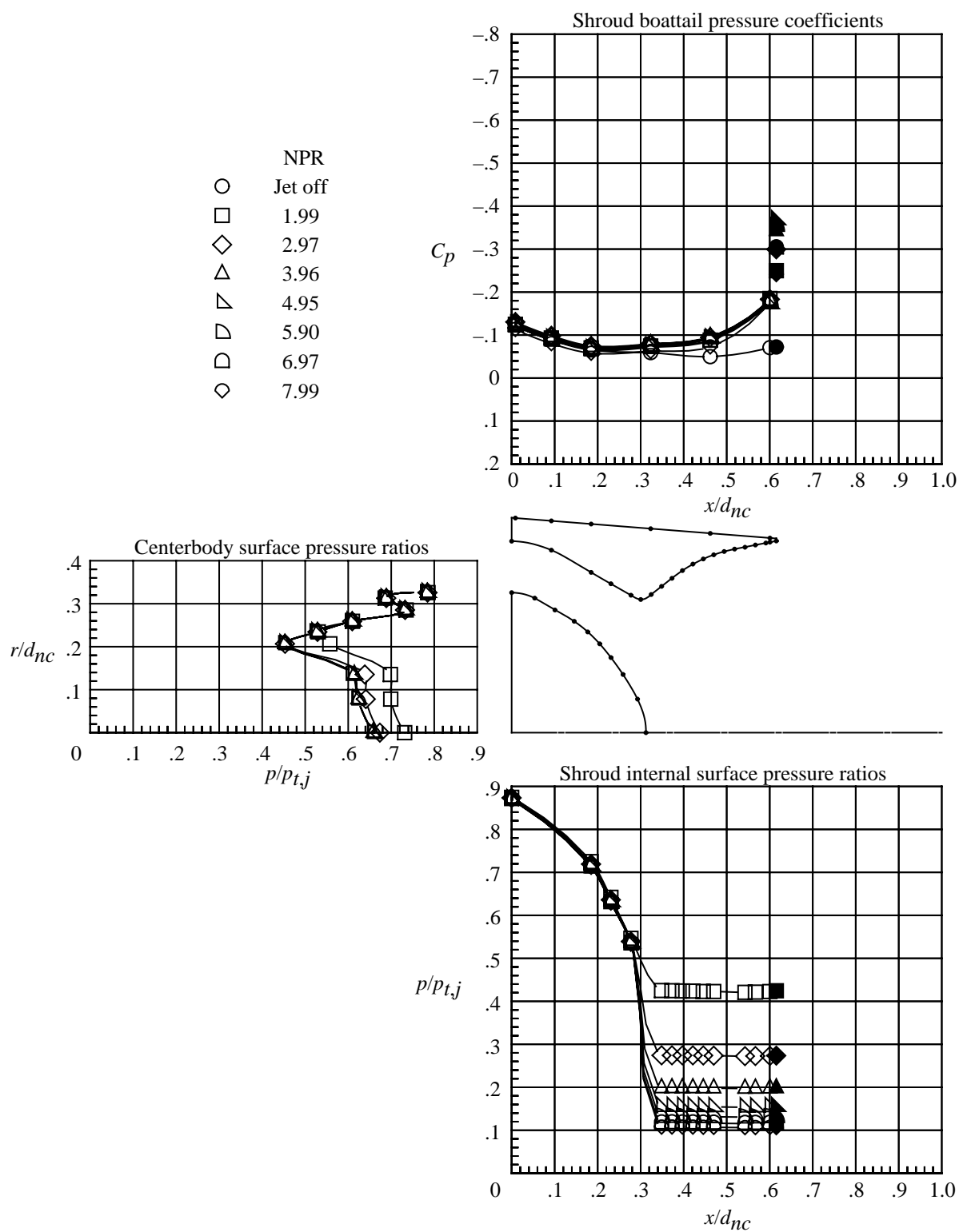
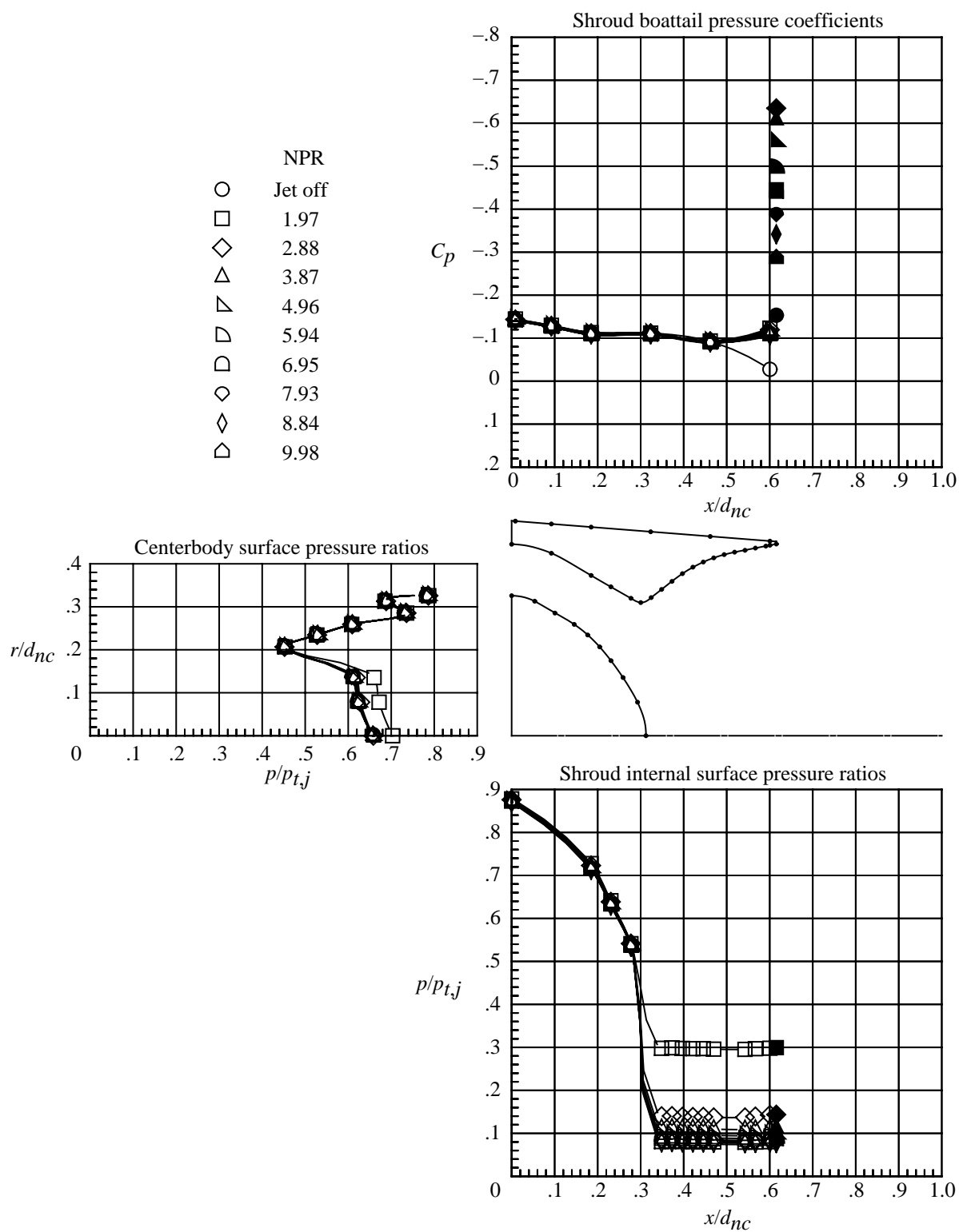


Figure 25. Continued.



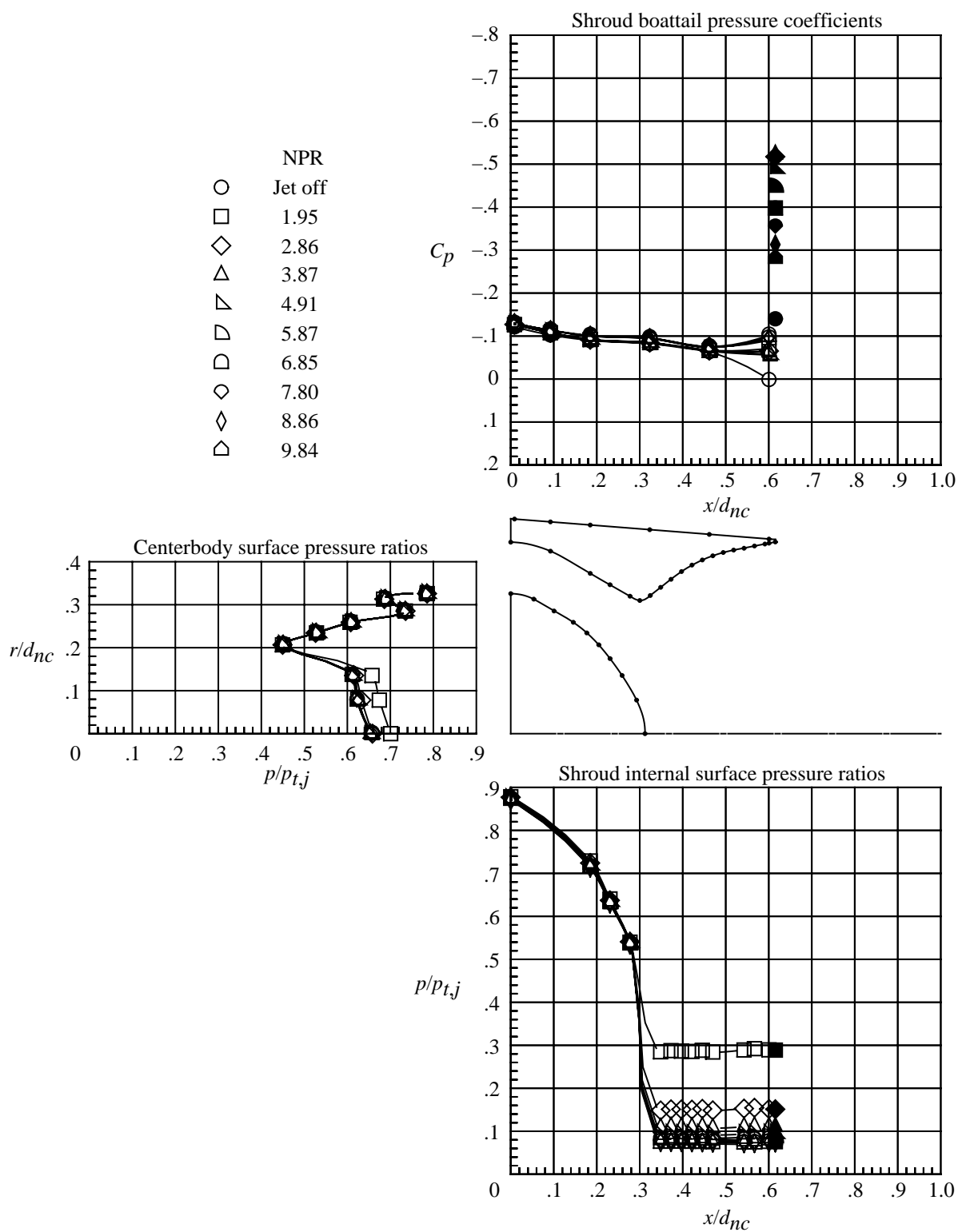
(f) $M = 0.95$.

Figure 25. Continued.



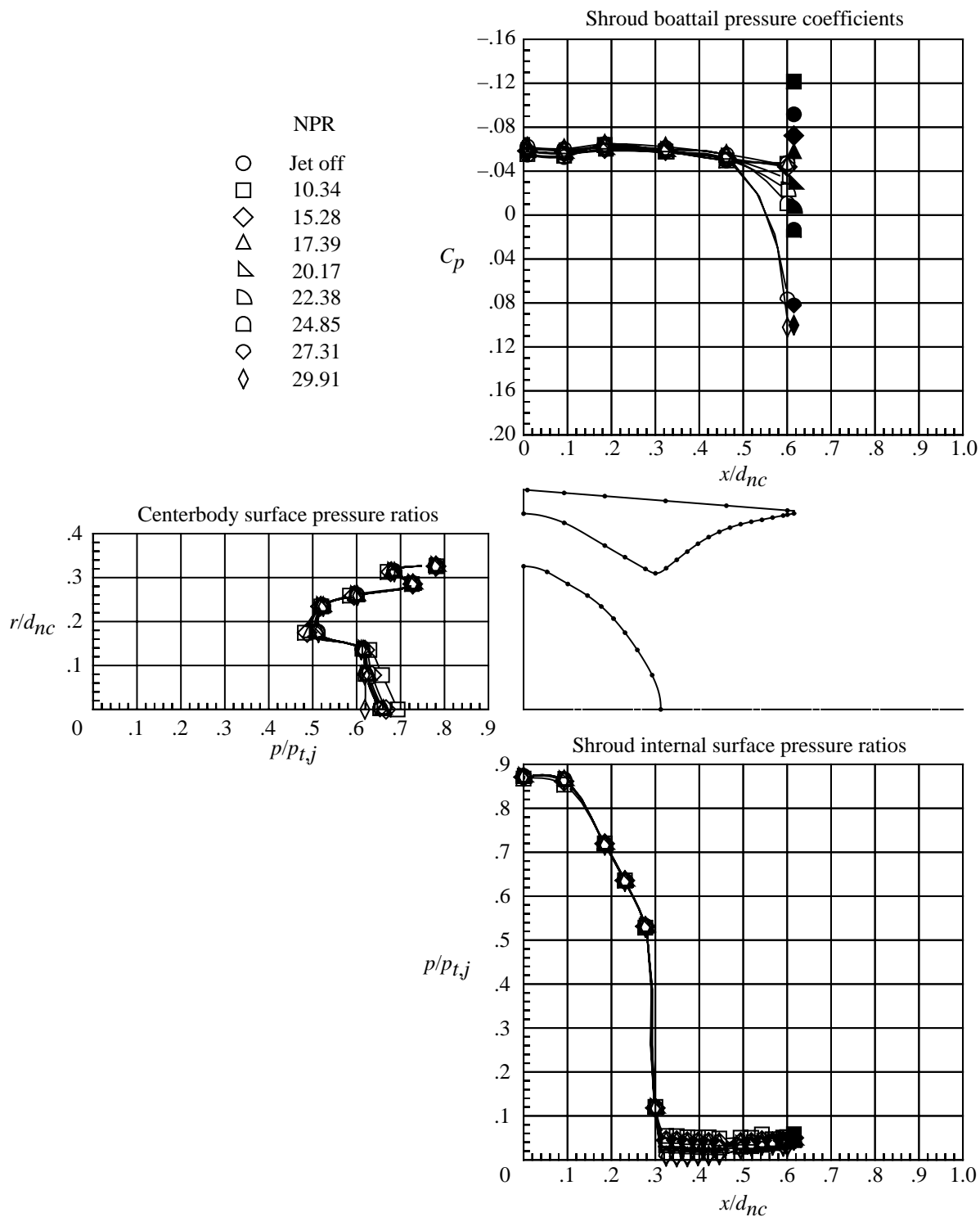
(g) $M = 1.15$.

Figure 25. Continued.



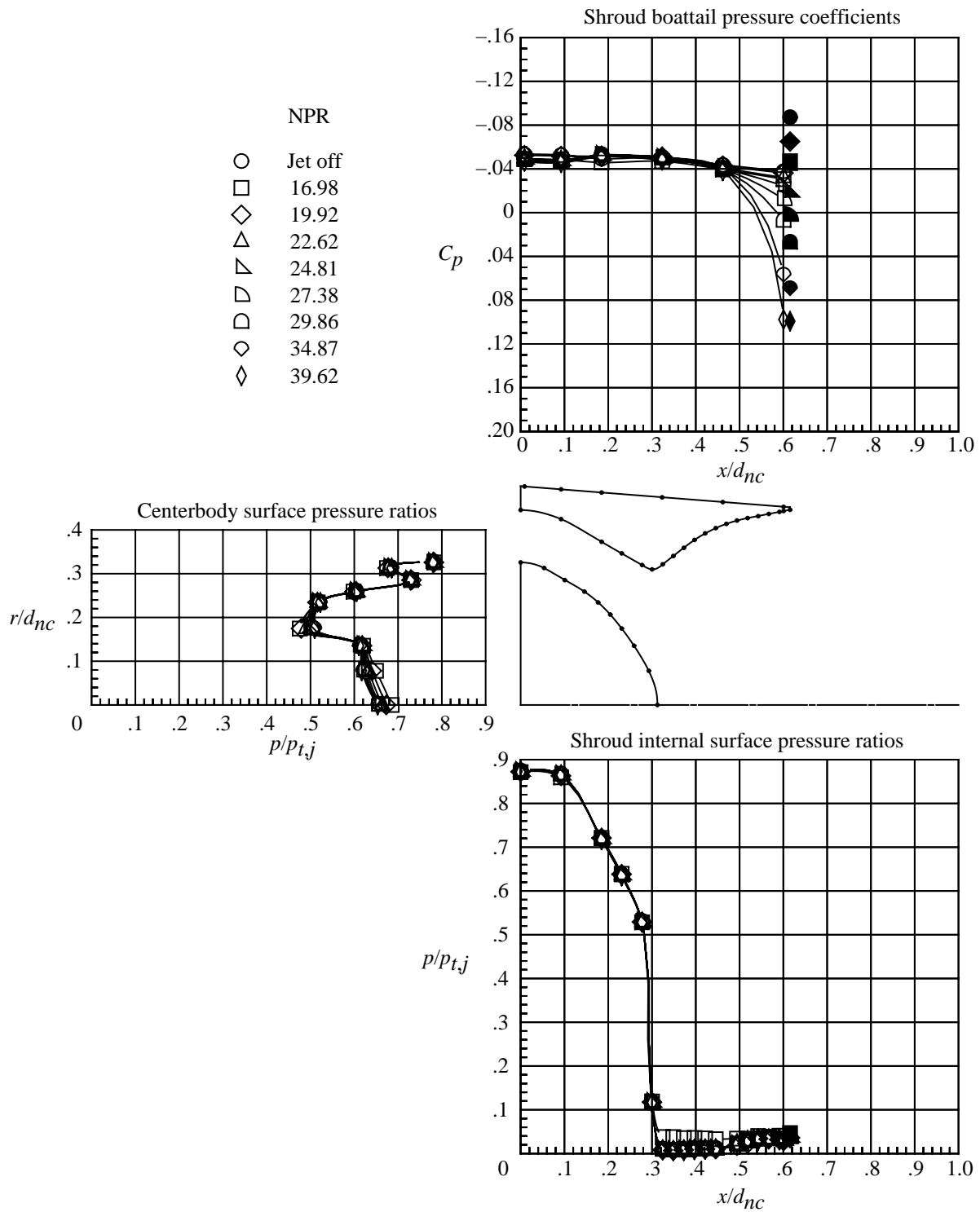
(h) $M = 1.25$.

Figure 25. Continued.



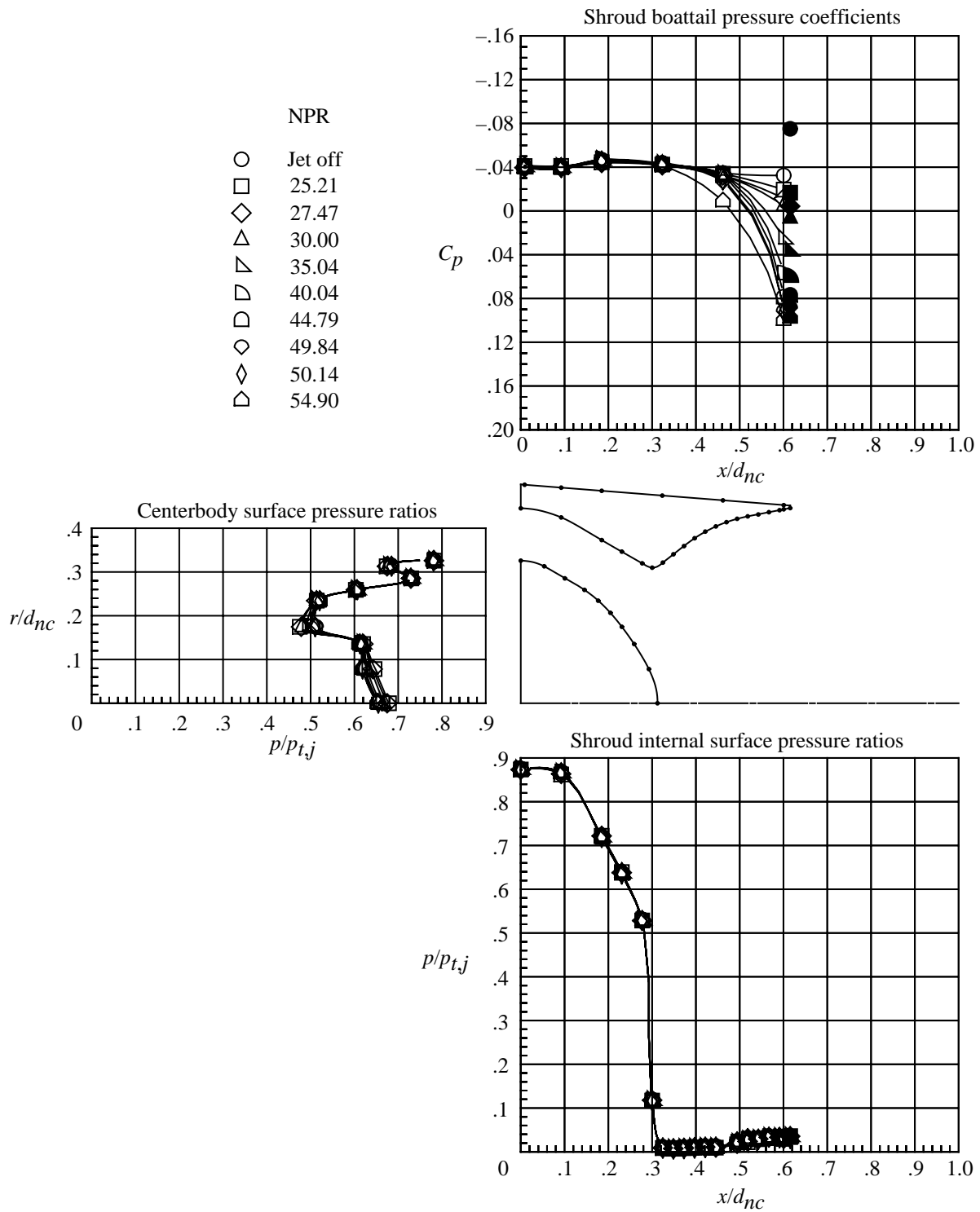
(i) $M = 2.16$.

Figure 25. Continued.



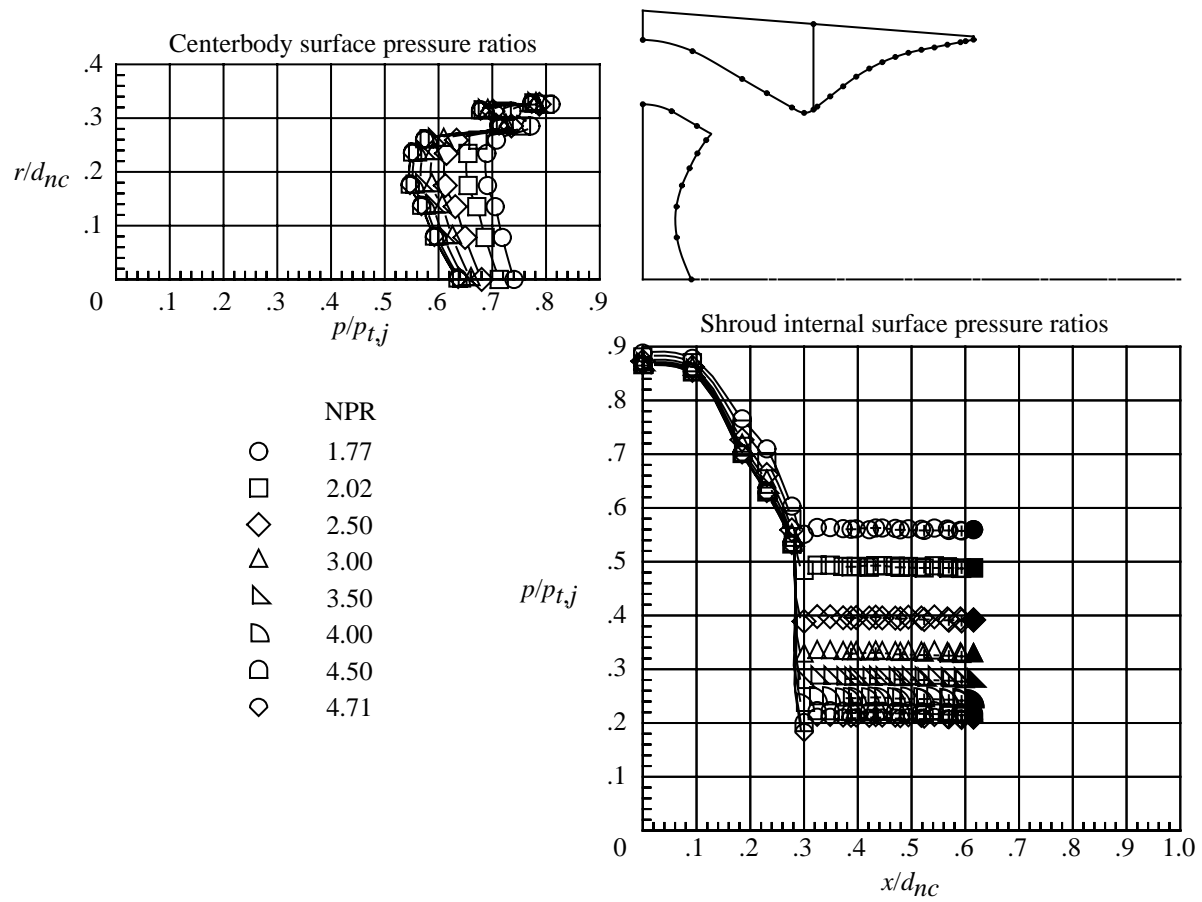
(j) $M = 2.50$.

Figure 25. Continued.



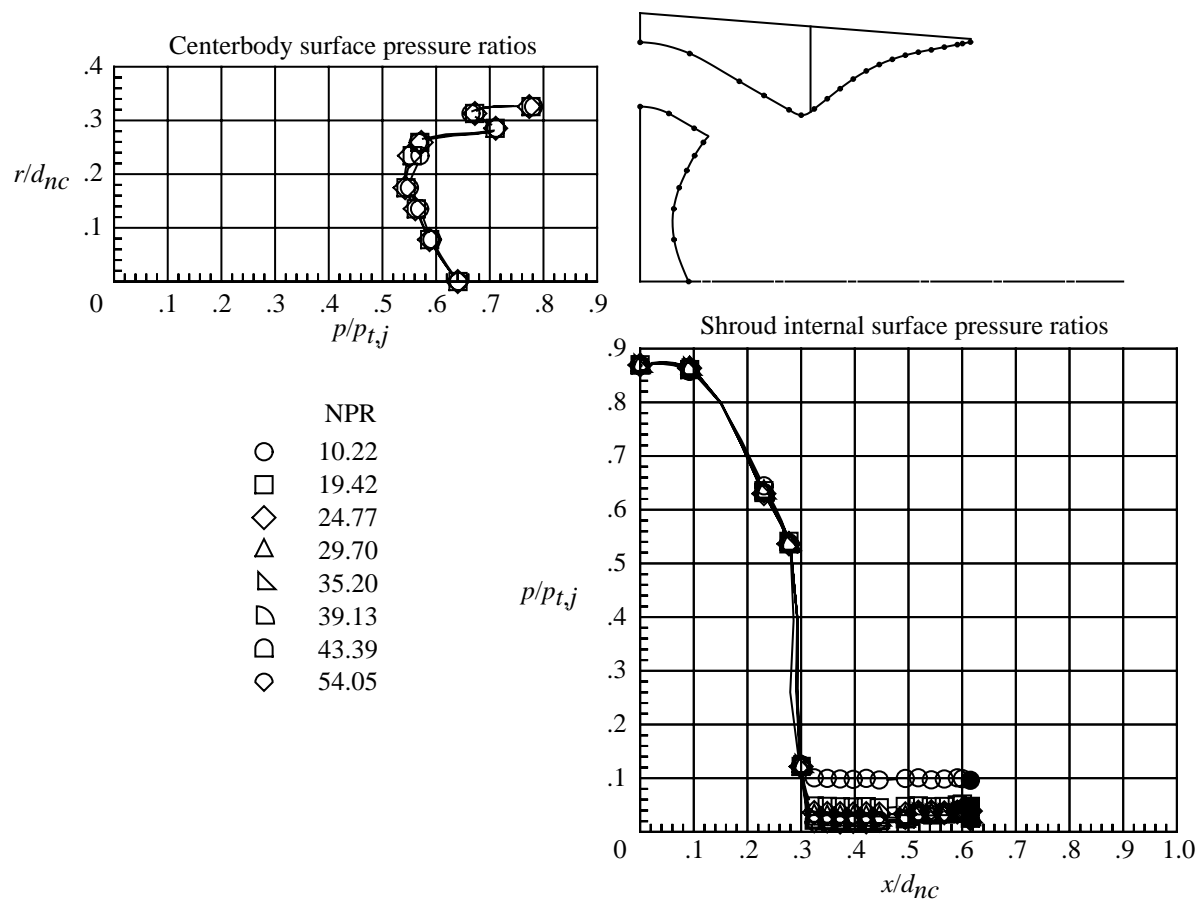
(k) $M = 2.86$.

Figure 25. Concluded.



(a) $M = 0$; low nozzle pressure ratios.

Figure 26. Internal and external pressures on nozzle with short axially vented shroud and concave centerbody. Solid symbols indicate data at shroud base and plus signs in symbols indicate data on walls of vent. Dots on nozzle sketch indicate pressure orifice locations.



(b) $M = 0$; high nozzle pressure ratios.

Figure 26. Continued.

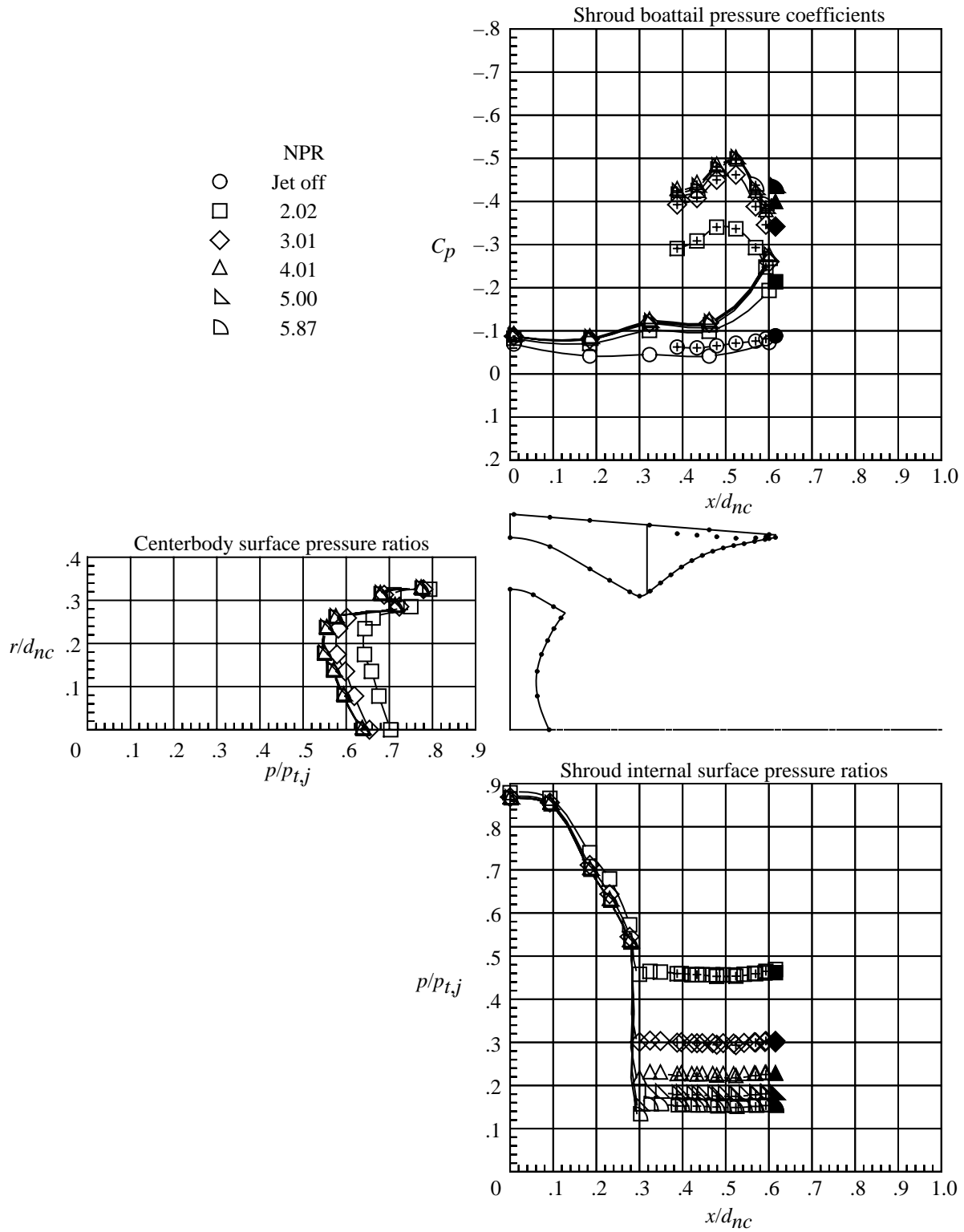


Figure 26. Continued.

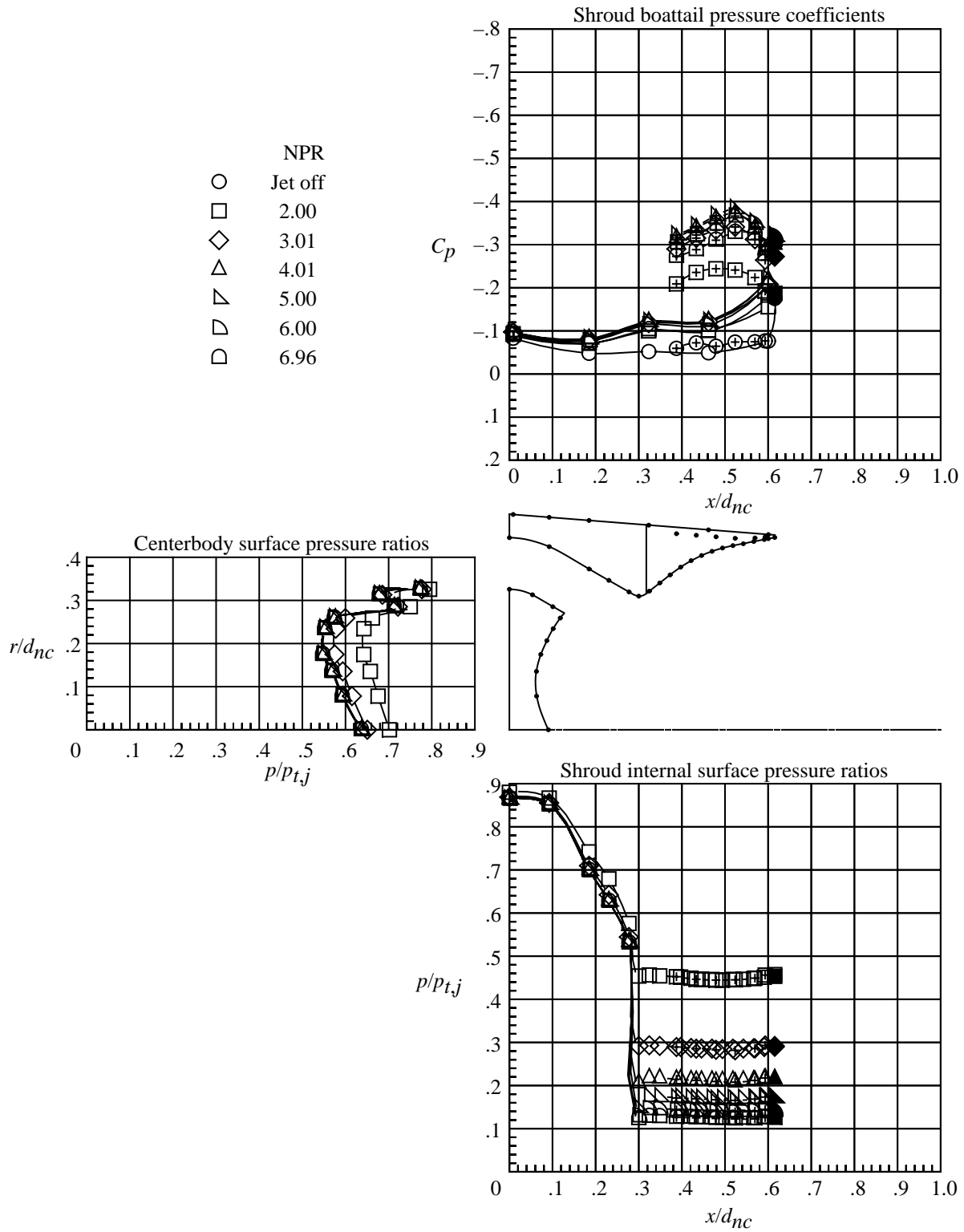
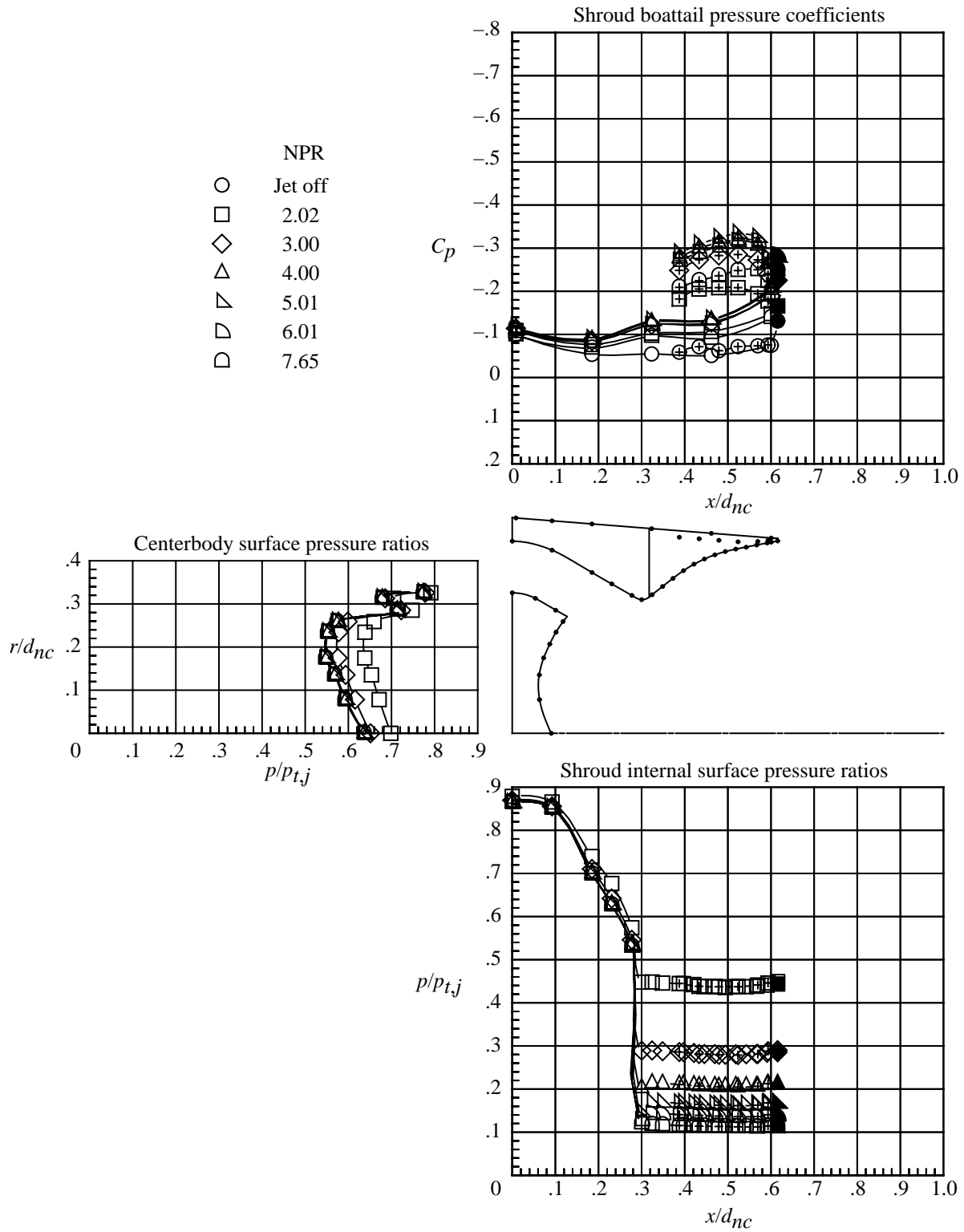


Figure 26. Continued.



(e) $M = 0.90$.

Figure 26. Continued.

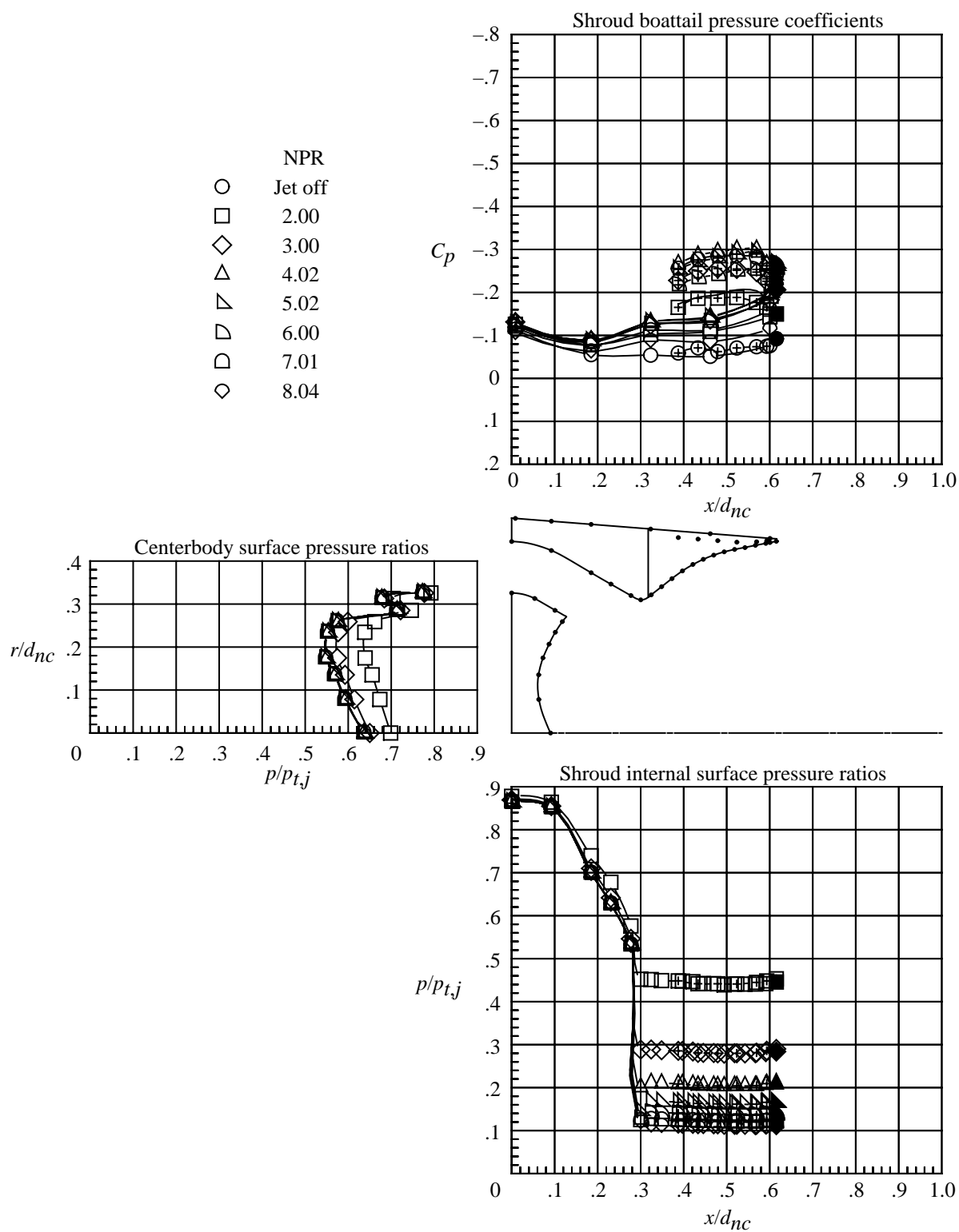
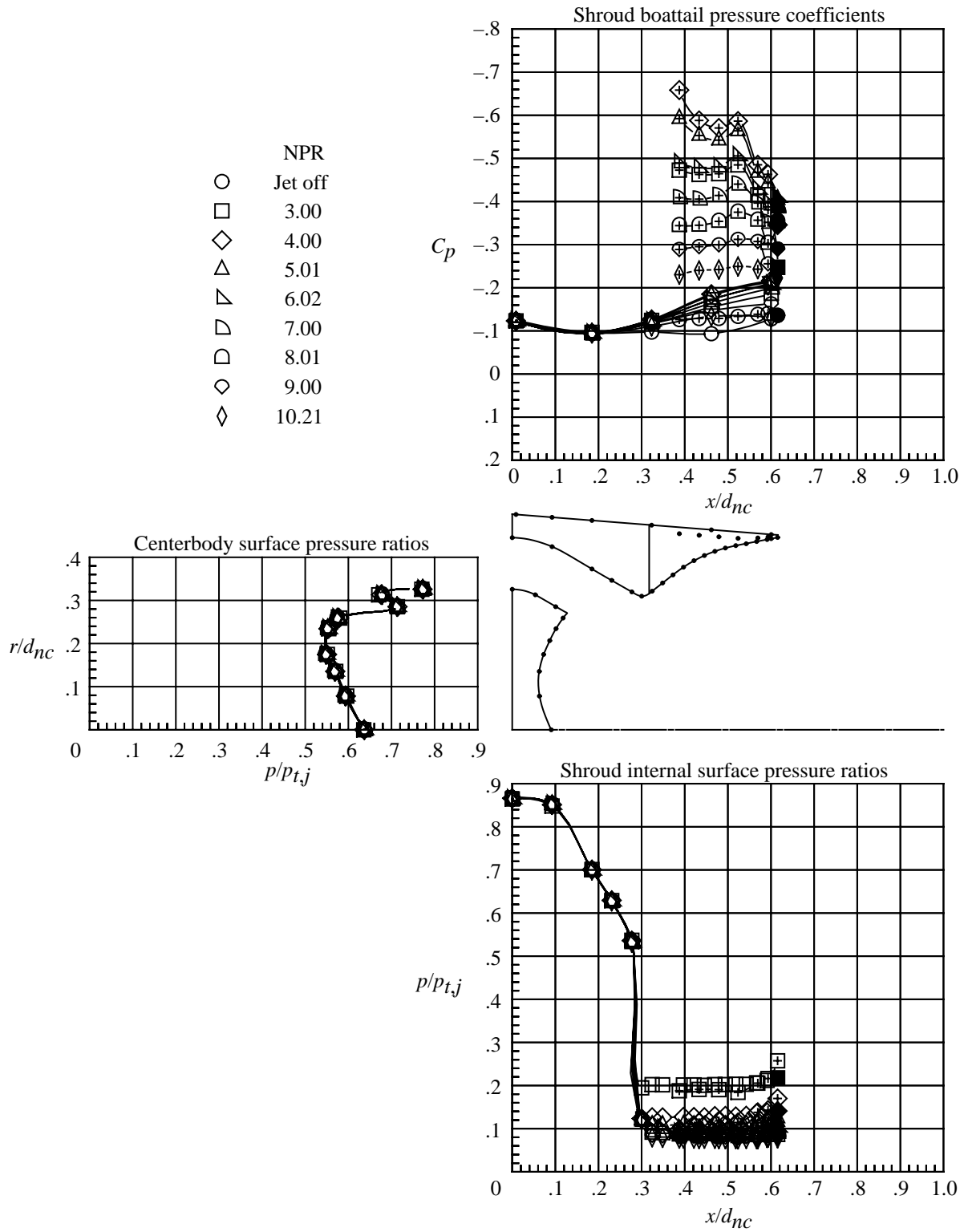
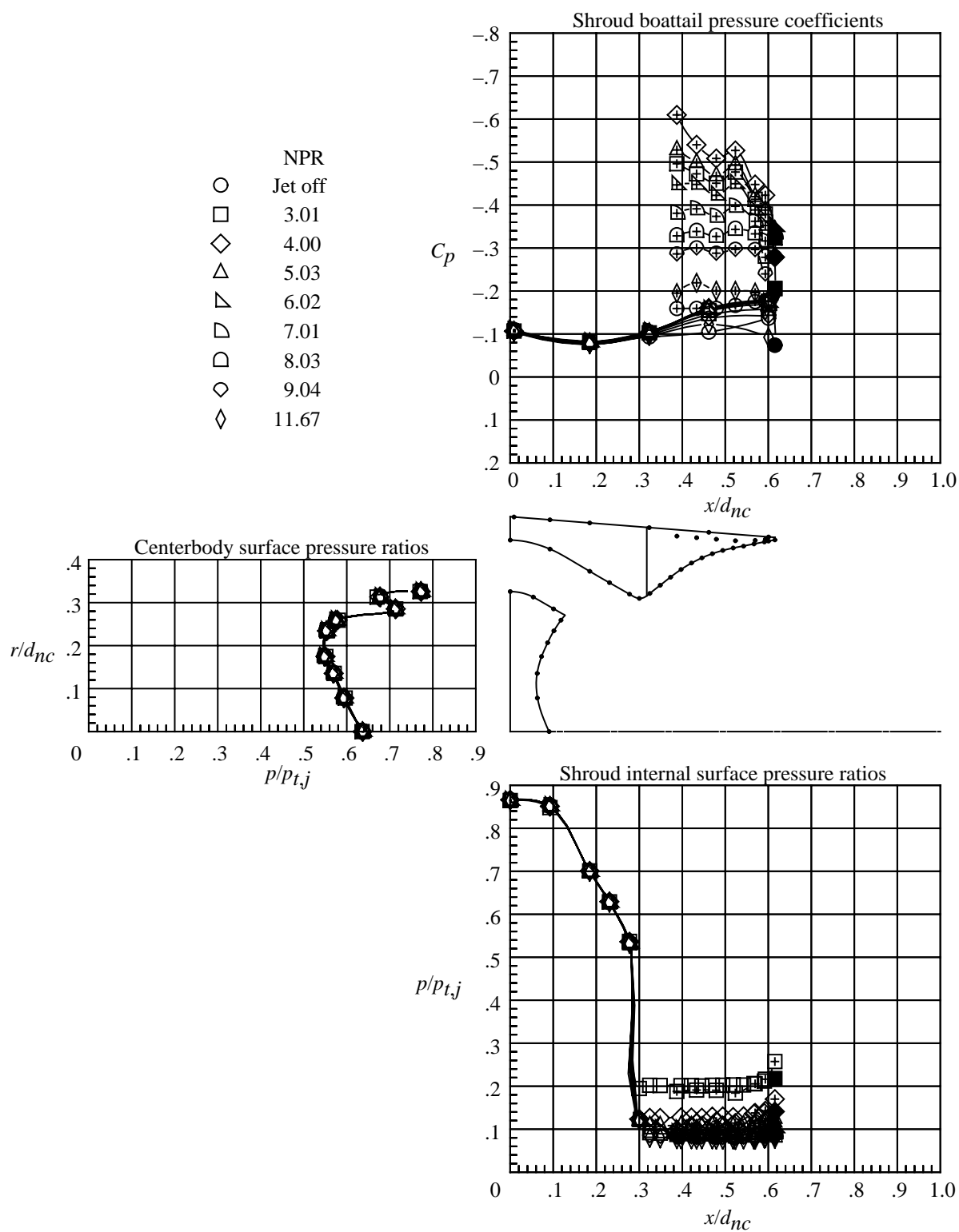


Figure 26. Continued.



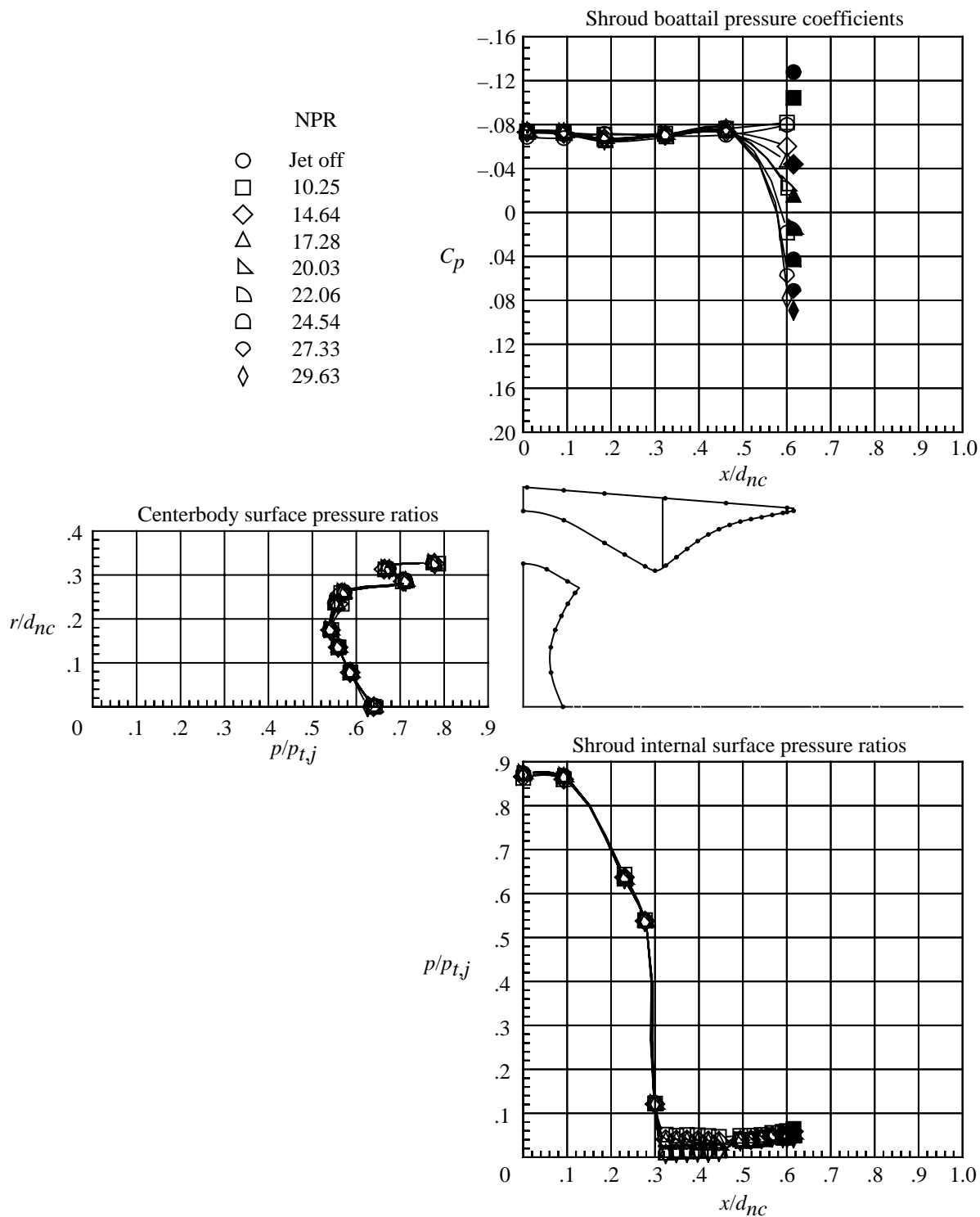
(g) $M = 1.15$.

Figure 26. Continued.



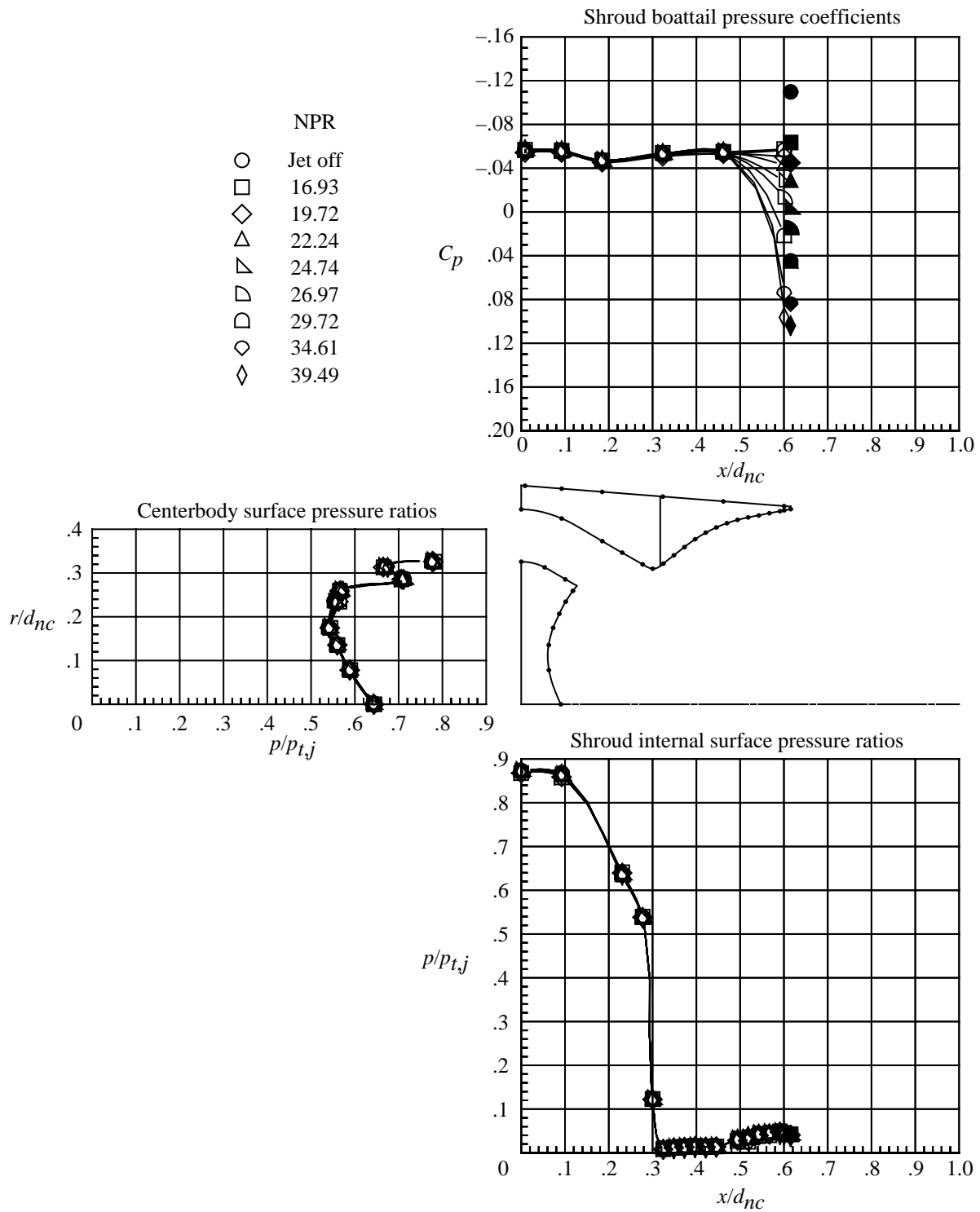
(h) $M = 1.25$.

Figure 26. Continued.



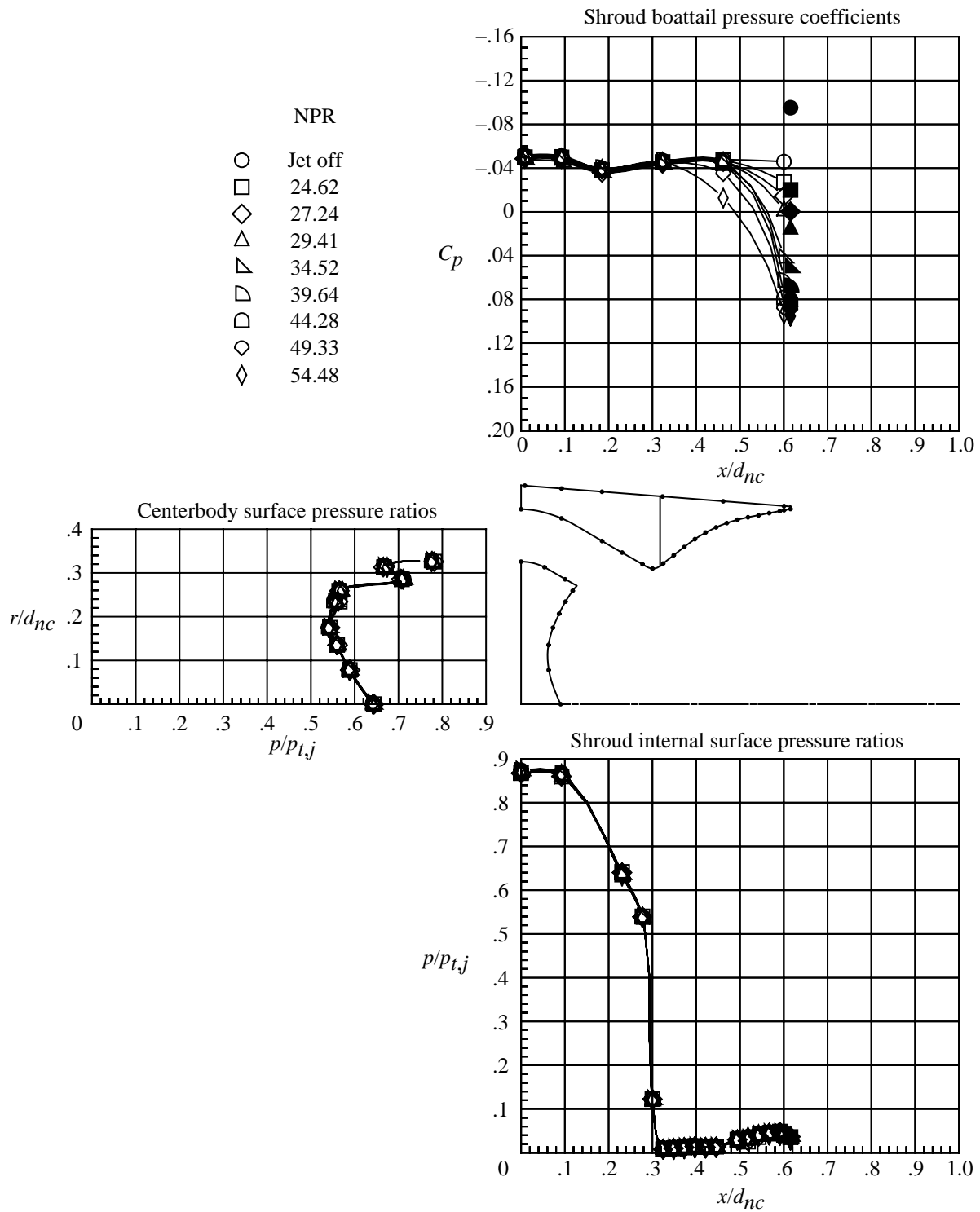
(i) $M = 2.16$.

Figure 26. Continued.



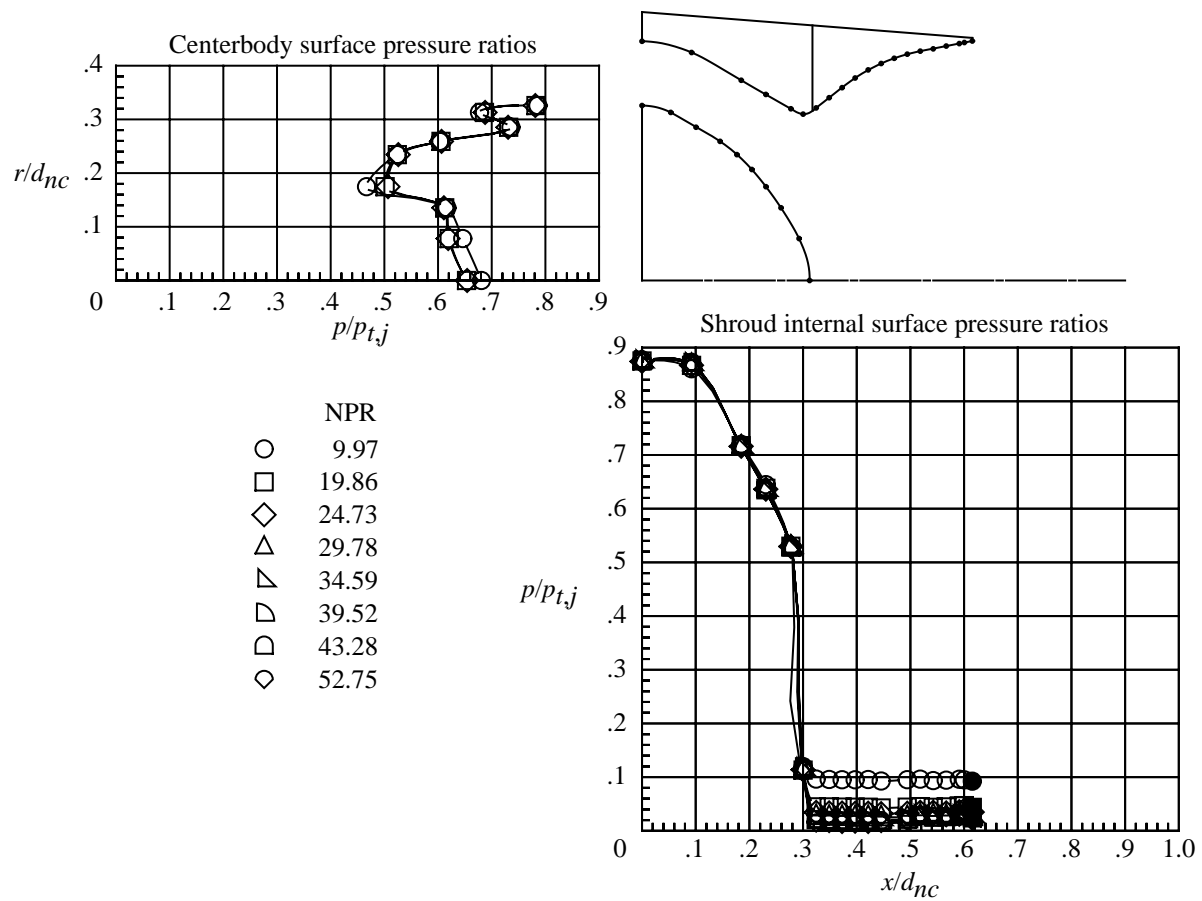
(j) $M = 2.50$.

Figure 26. Continued.



(k) $M = 2.86$.

Figure 26. Concluded.



(b) $M = 0$; high nozzle pressure ratios.

Figure 27. Continued.

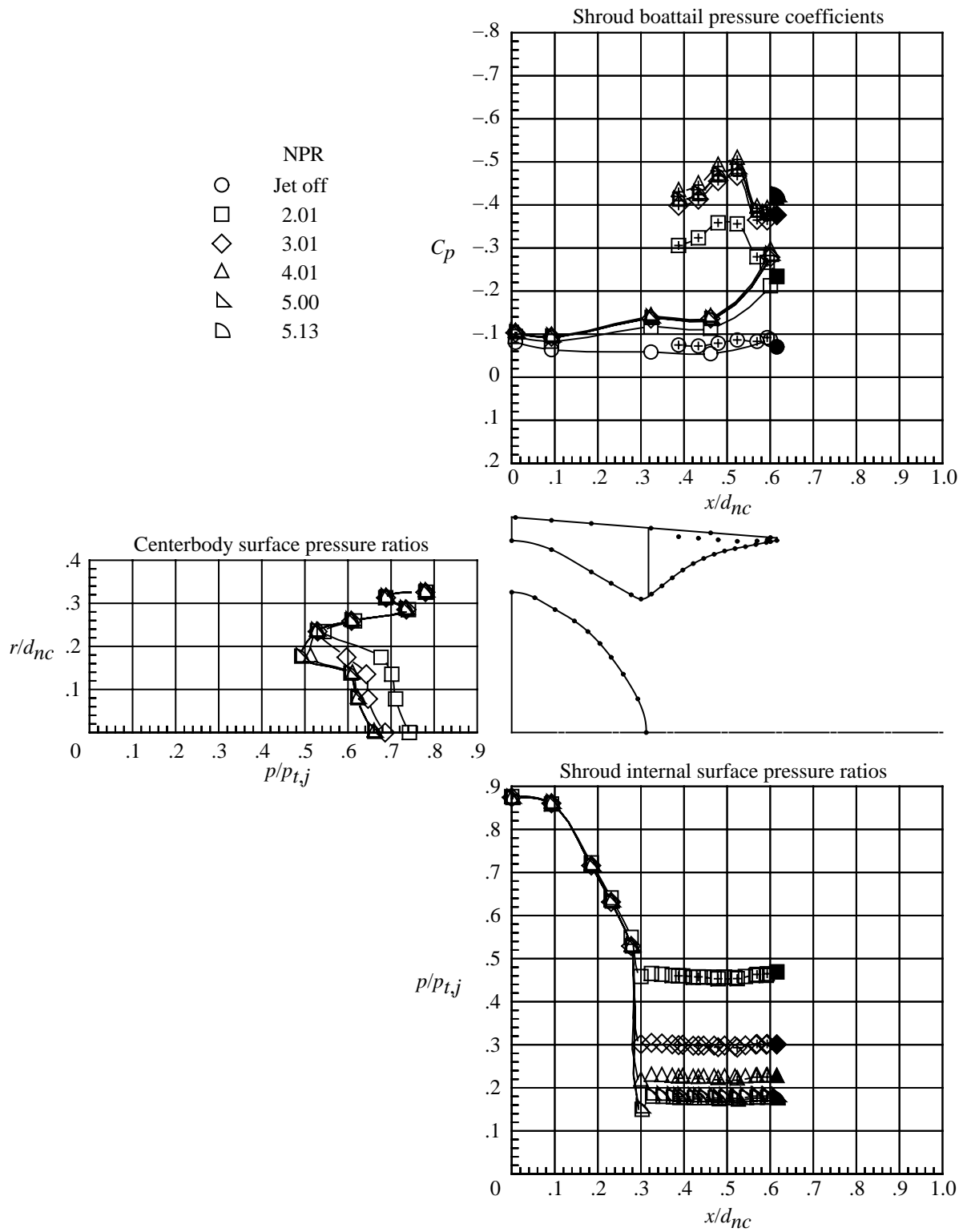


Figure 27. Continued.

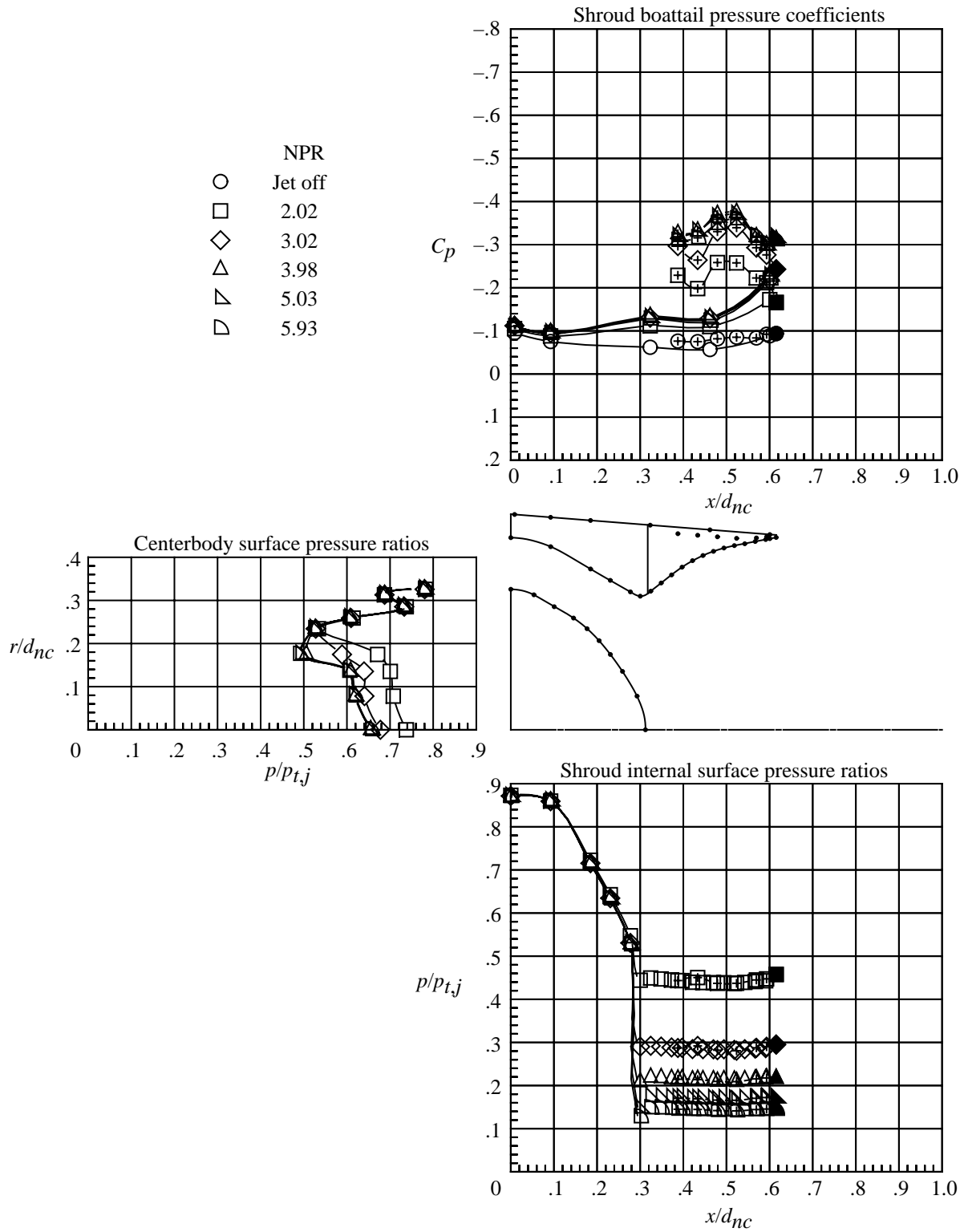


Figure 27. Continued.

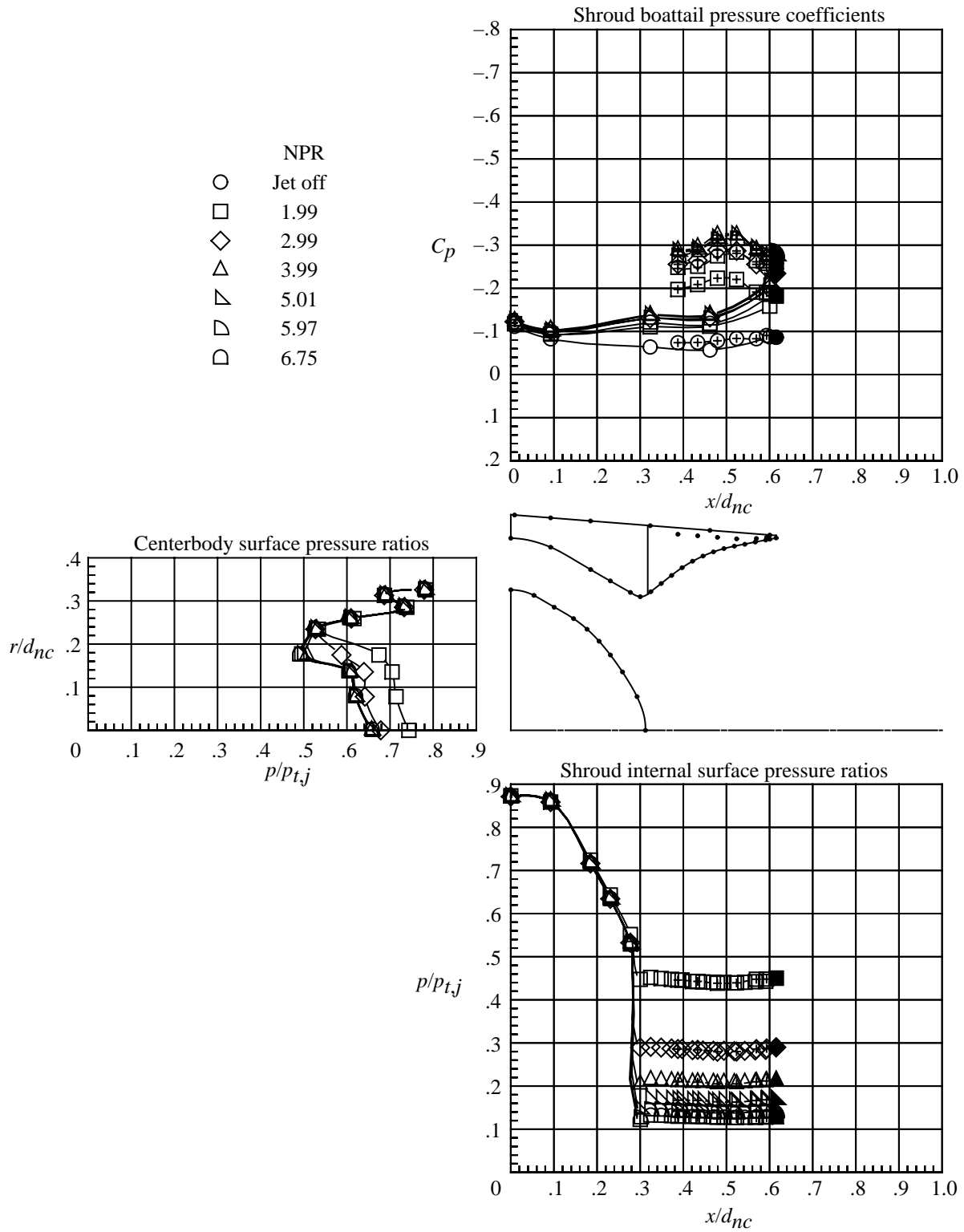


Figure 27. Continued.

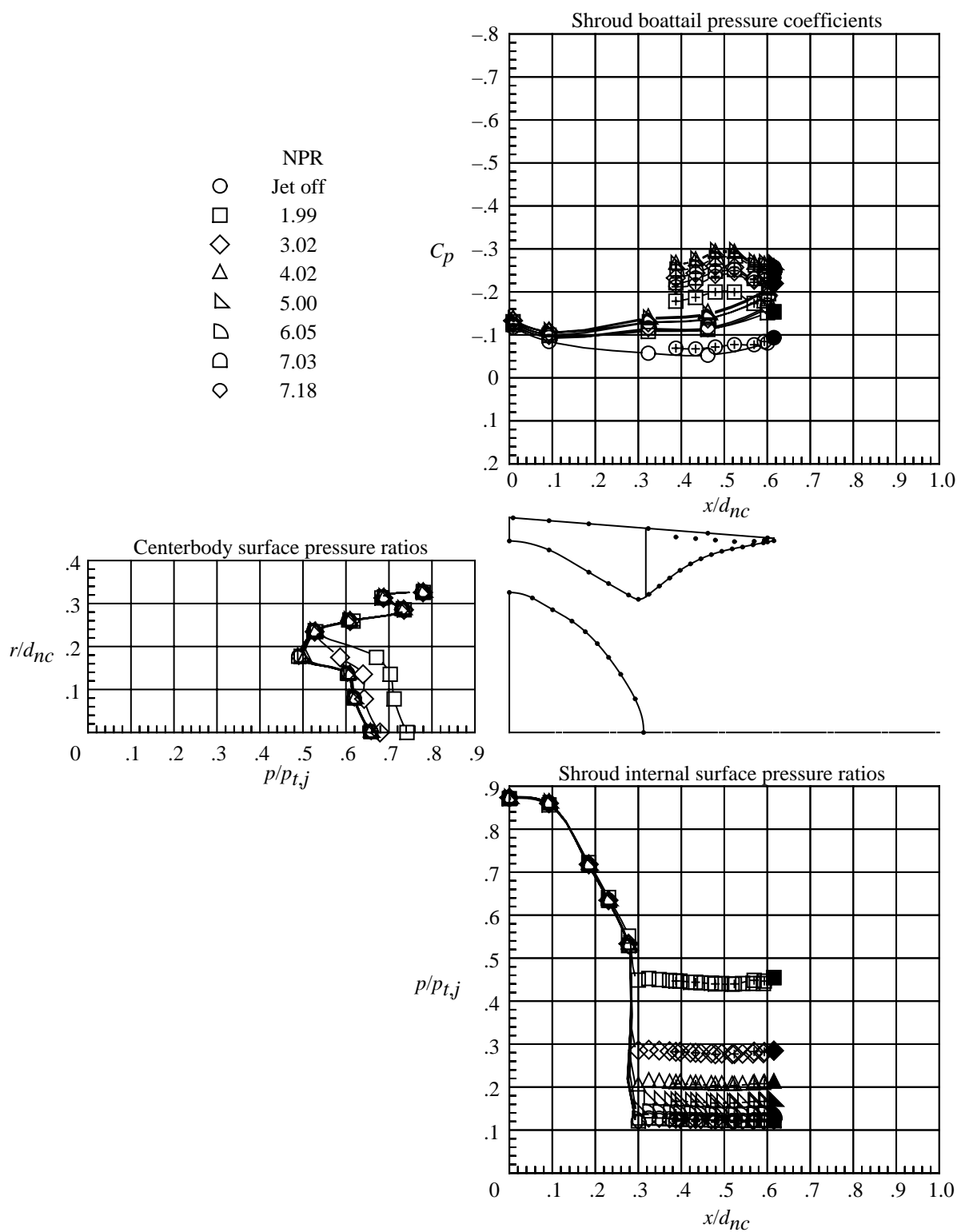
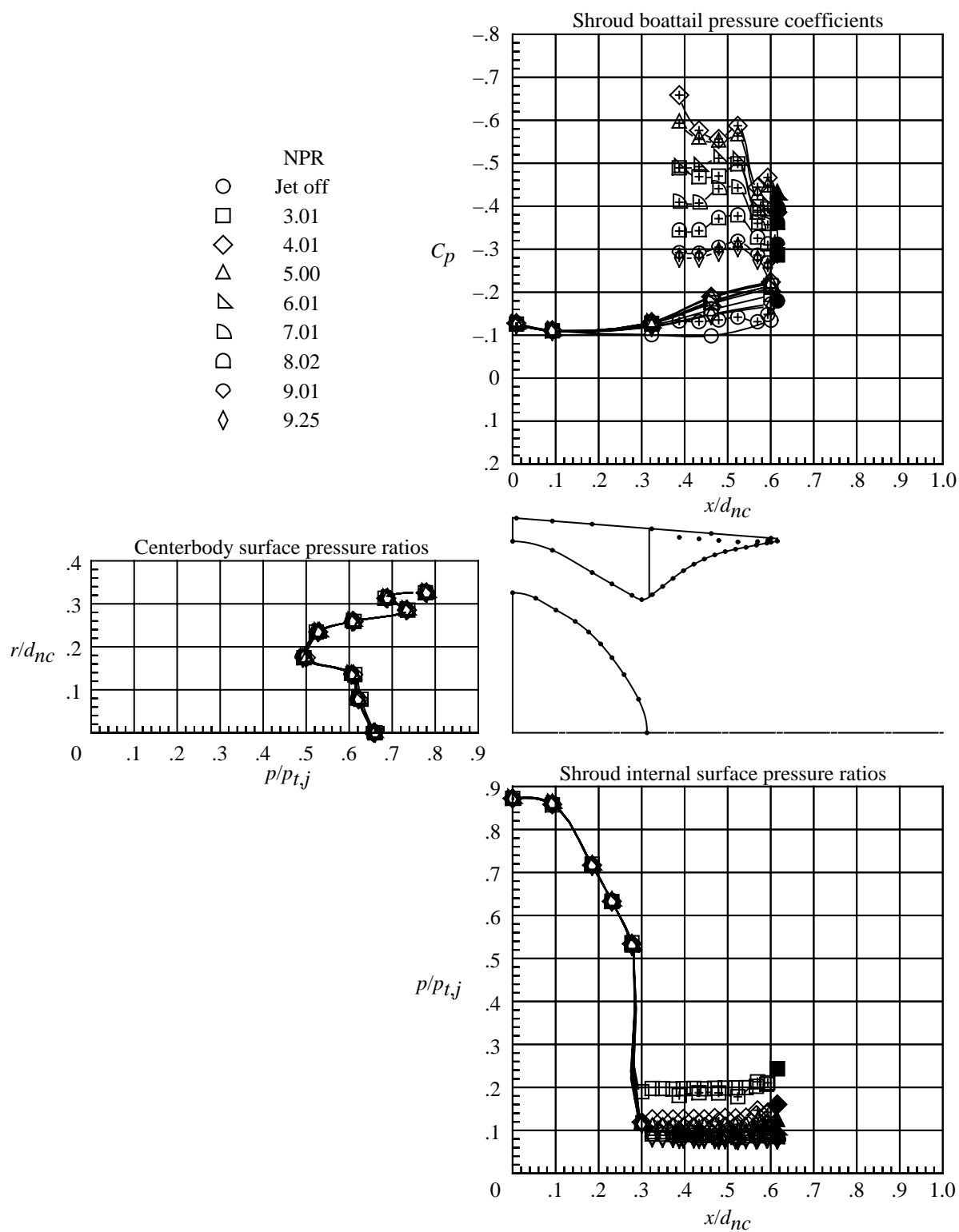
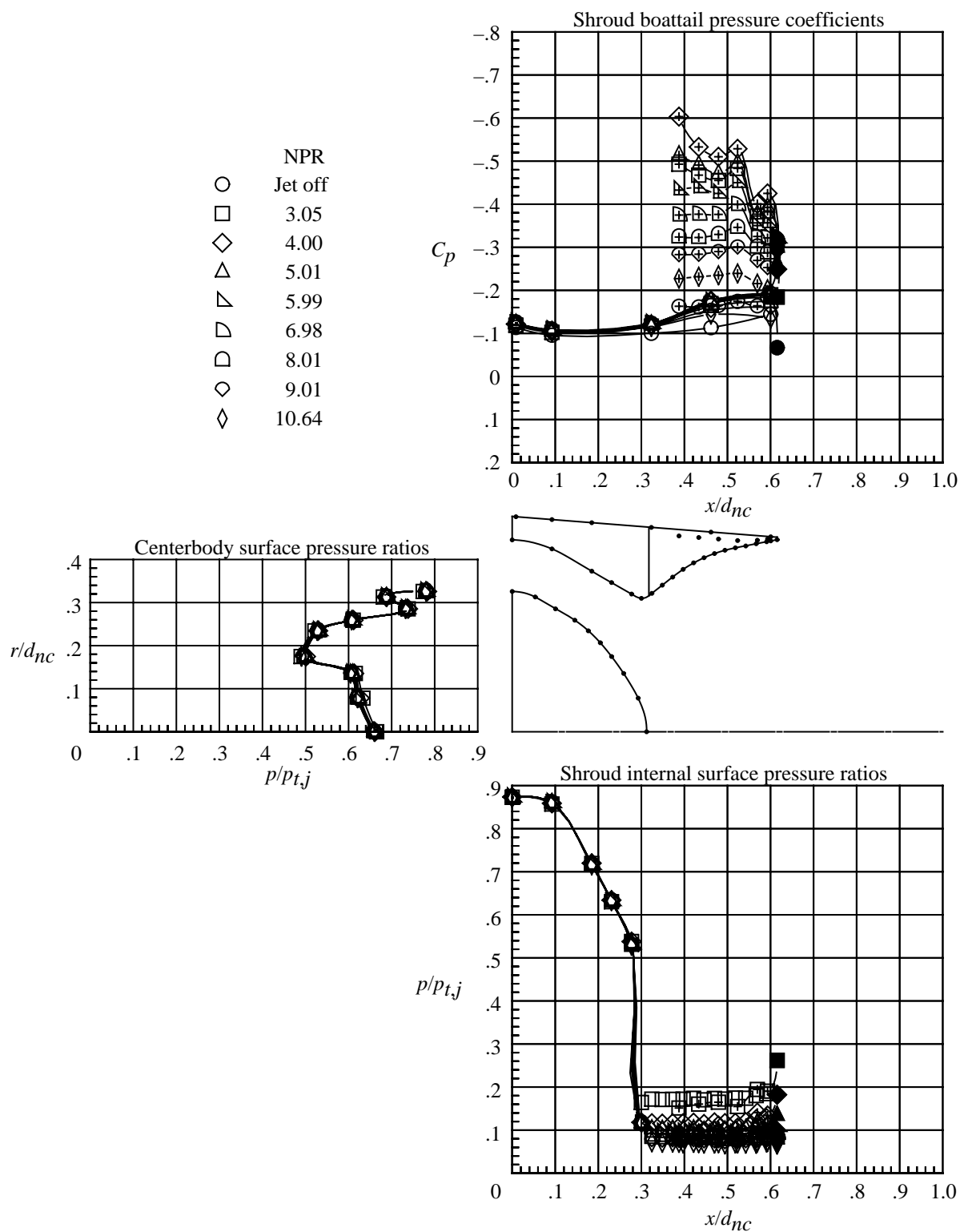


Figure 27. Continued.



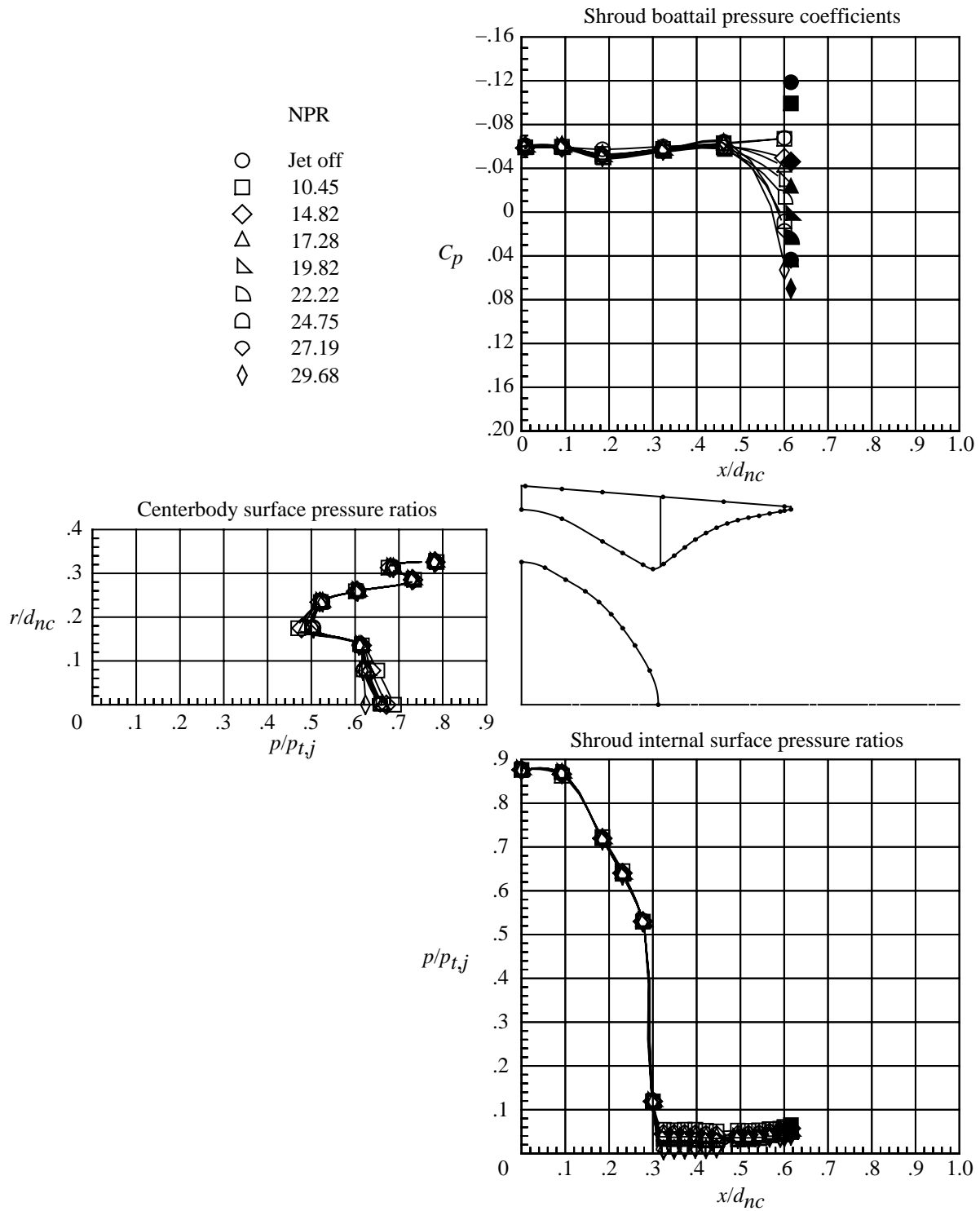
(g) $M = 1.15$.

Figure 27. Continued.



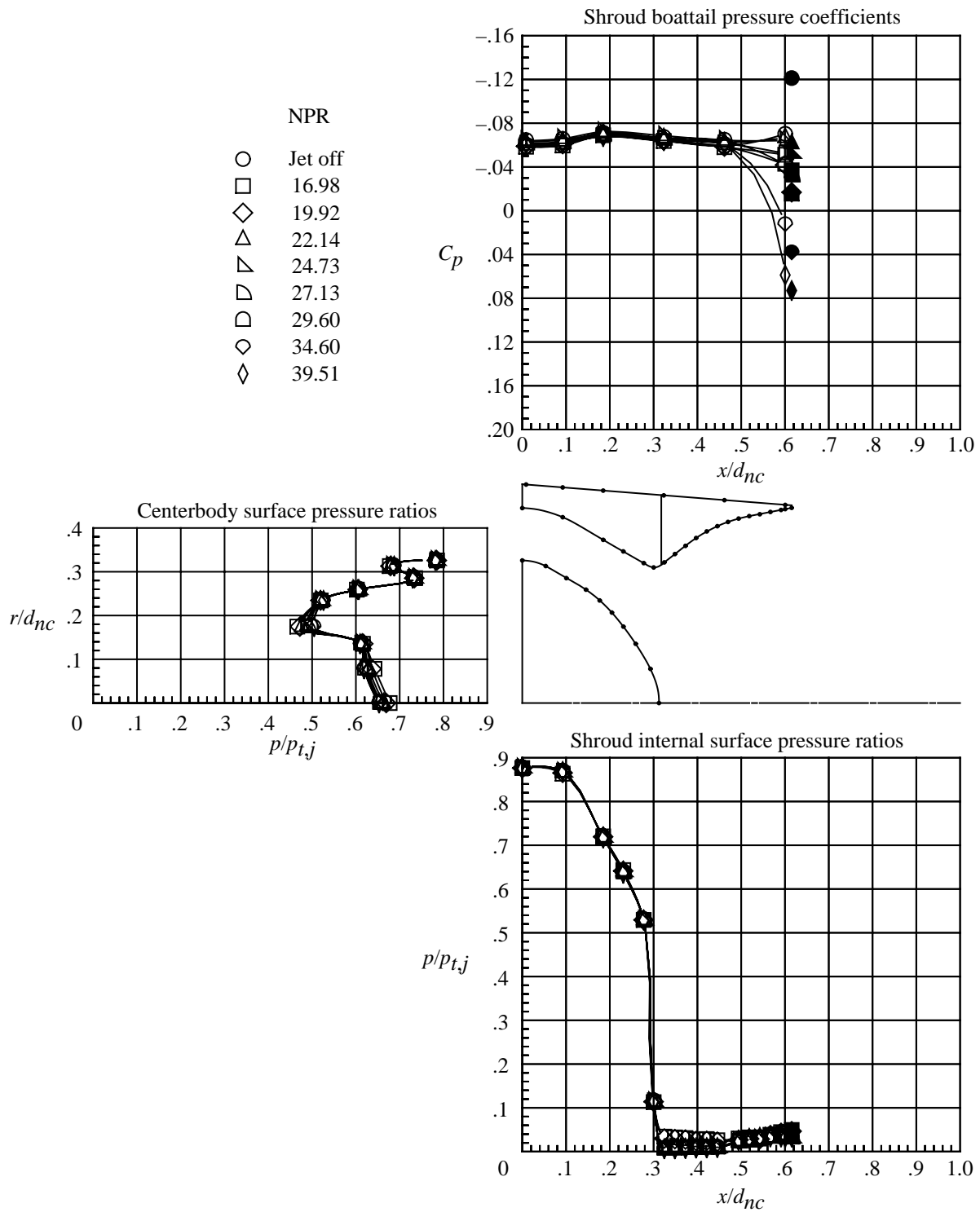
(h) $M = 1.25$.

Figure 27. Continued.



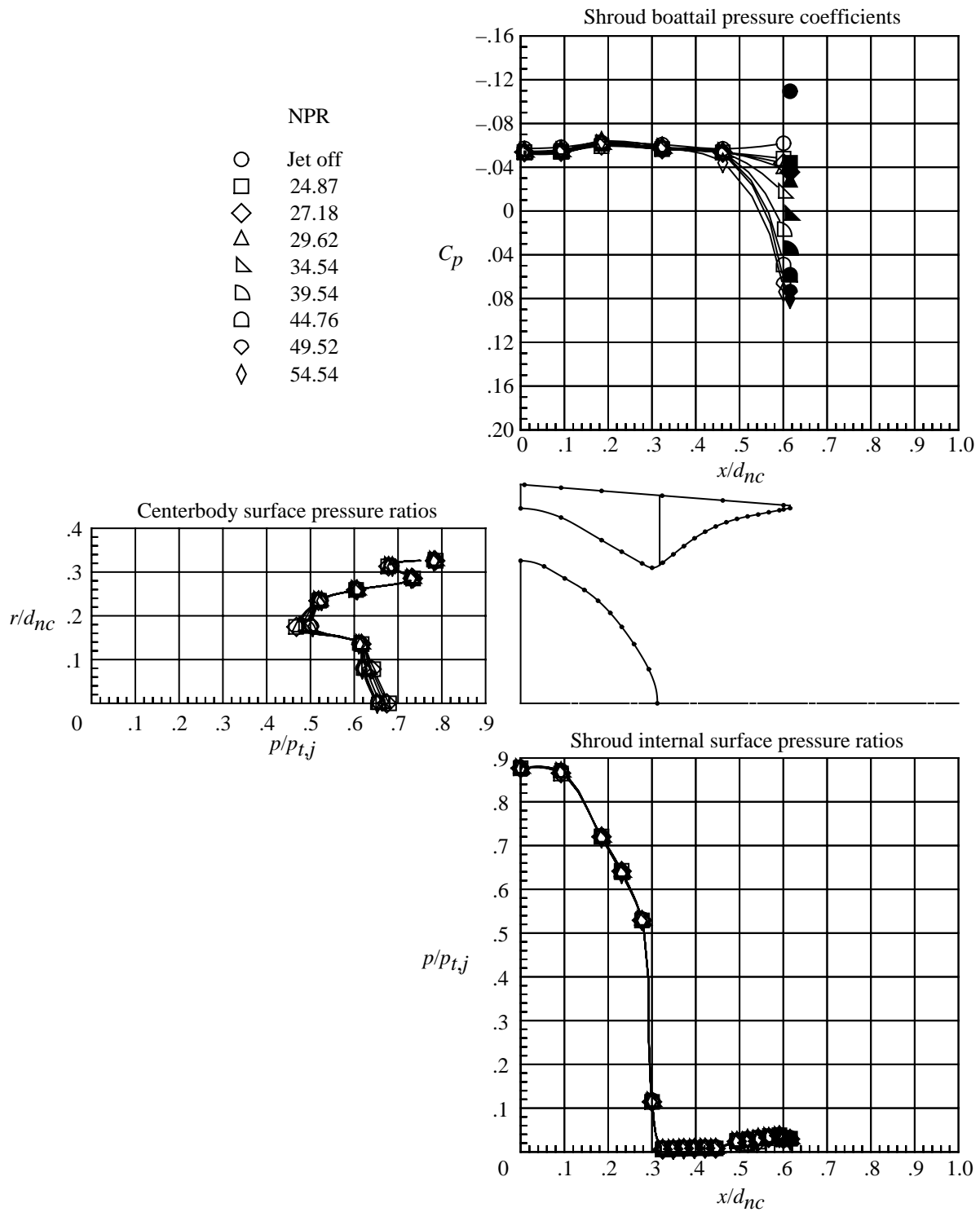
(i) $M = 2.16$.

Figure 27. Continued.



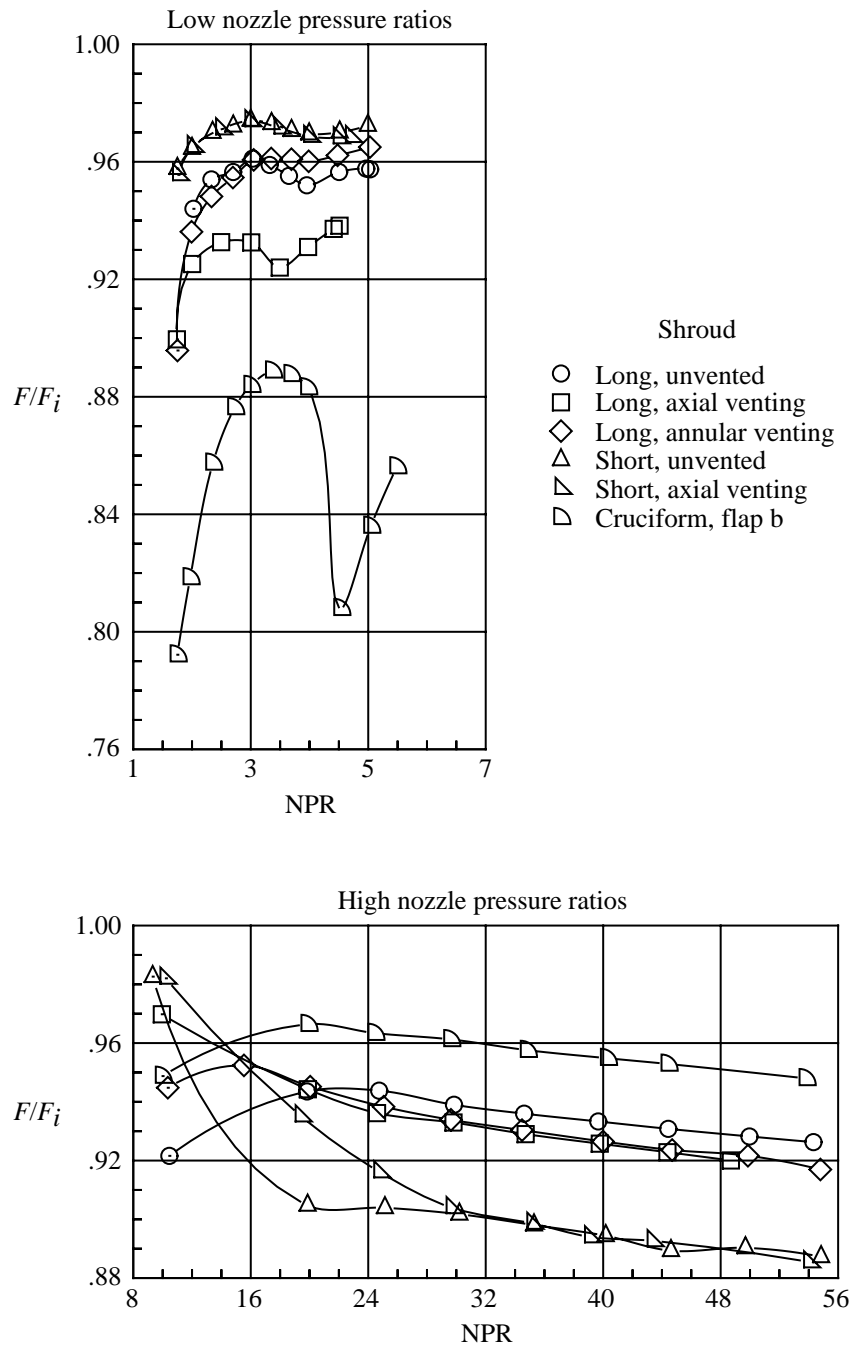
(j) $M = 2.50$.

Figure 27. Continued.



(k) $M = 2.86$.

Figure 27. Concluded.

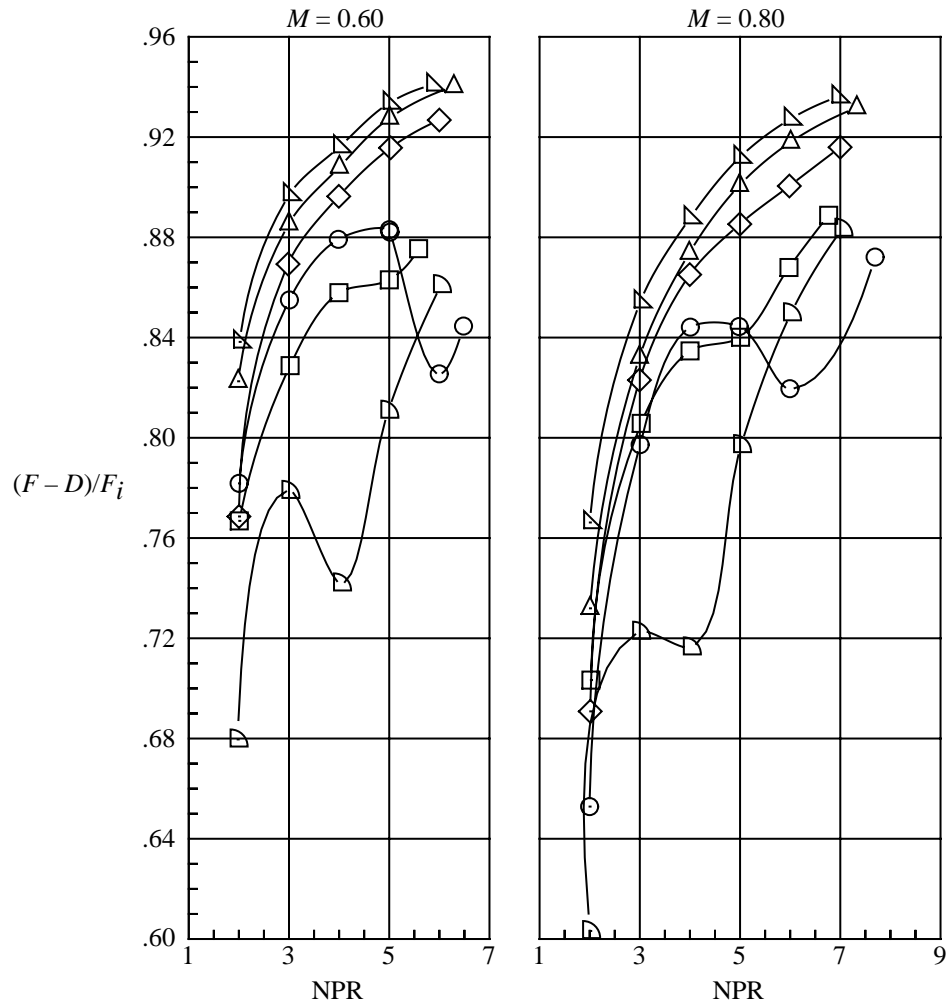


(a) $M = 0$; low nozzle pressure ratios.

Figure 28. Comparison of thrust ratio and thrust-minus-drag ratio performance over range of nozzle pressure ratios for model with six different shrouds and concave centerbody base.

Shroud

- Long, unvented
- Long, axial venting
- ◇ Long, annular venting
- △ Short, unvented
- ▽ Short, axial venting
- ◻ Cruciform, flap b



(b) $M = 0.60$ and 0.80 .

Figure 28. Continued.

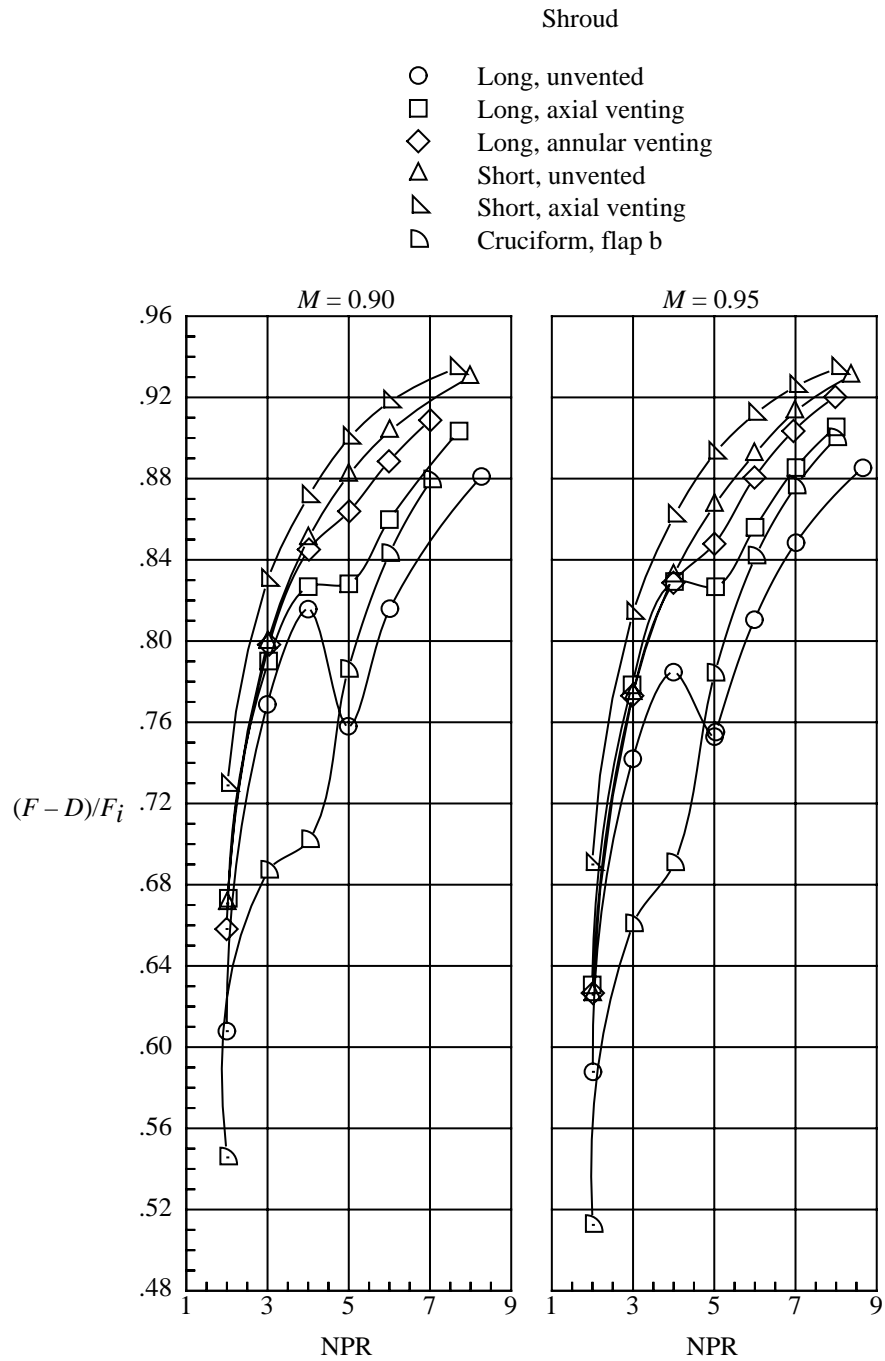
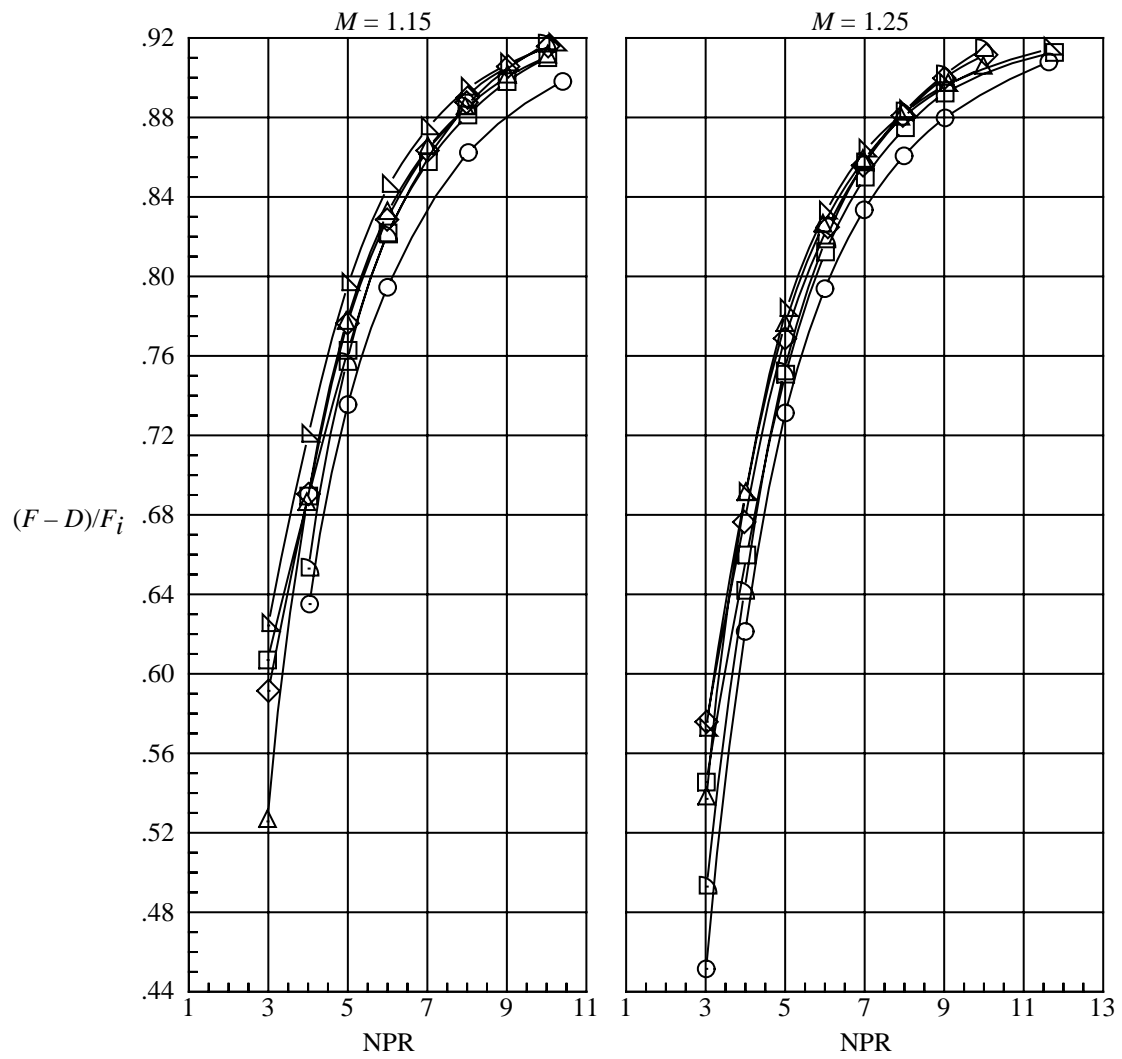


Figure 28. Continued.

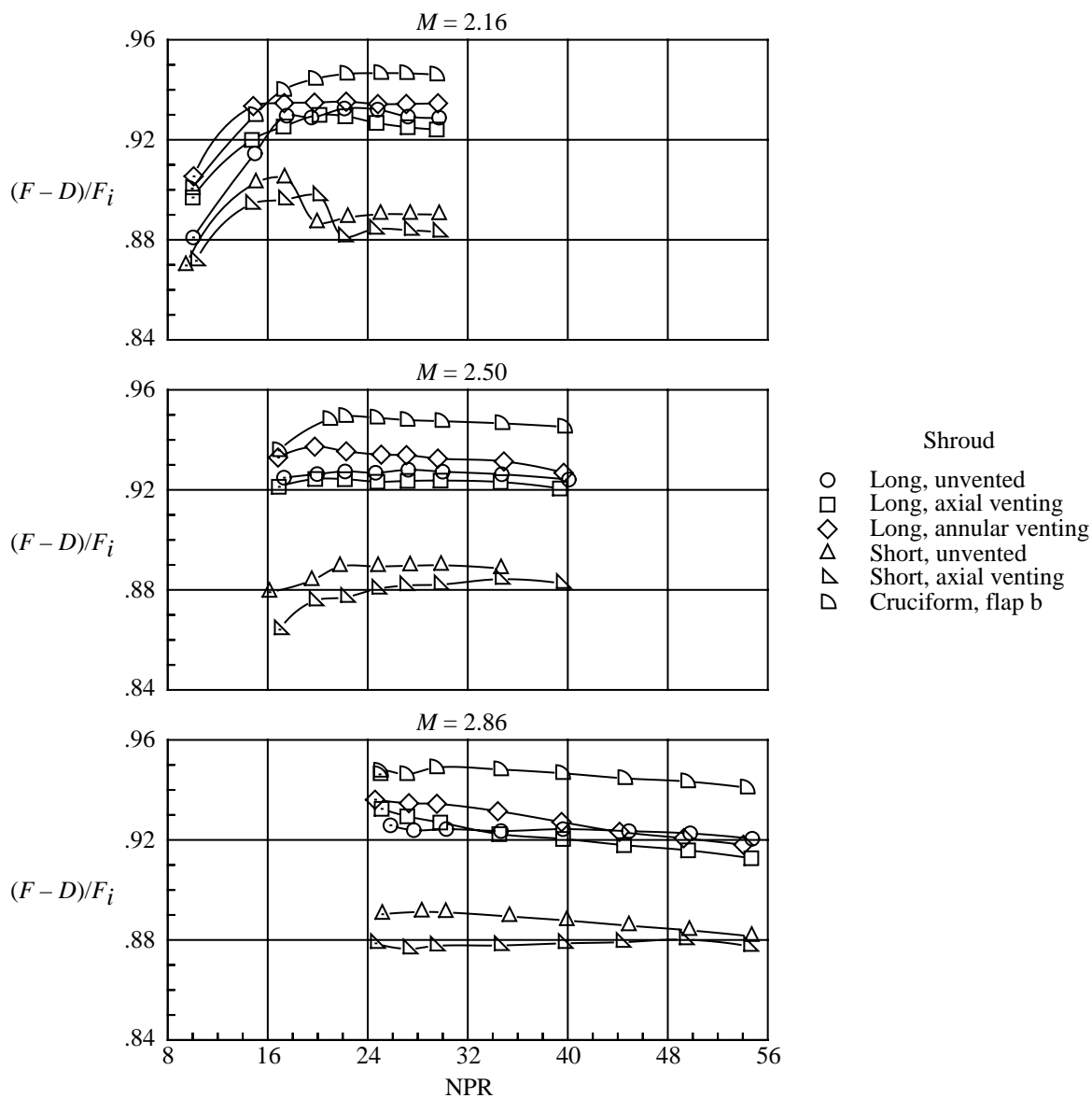
Shroud

- Long, unvented
- Long, axial venting
- ◇ Long, annular venting
- △ Short, unvented
- ▵ Short, axial venting
- ▢ Cruciform, flap b



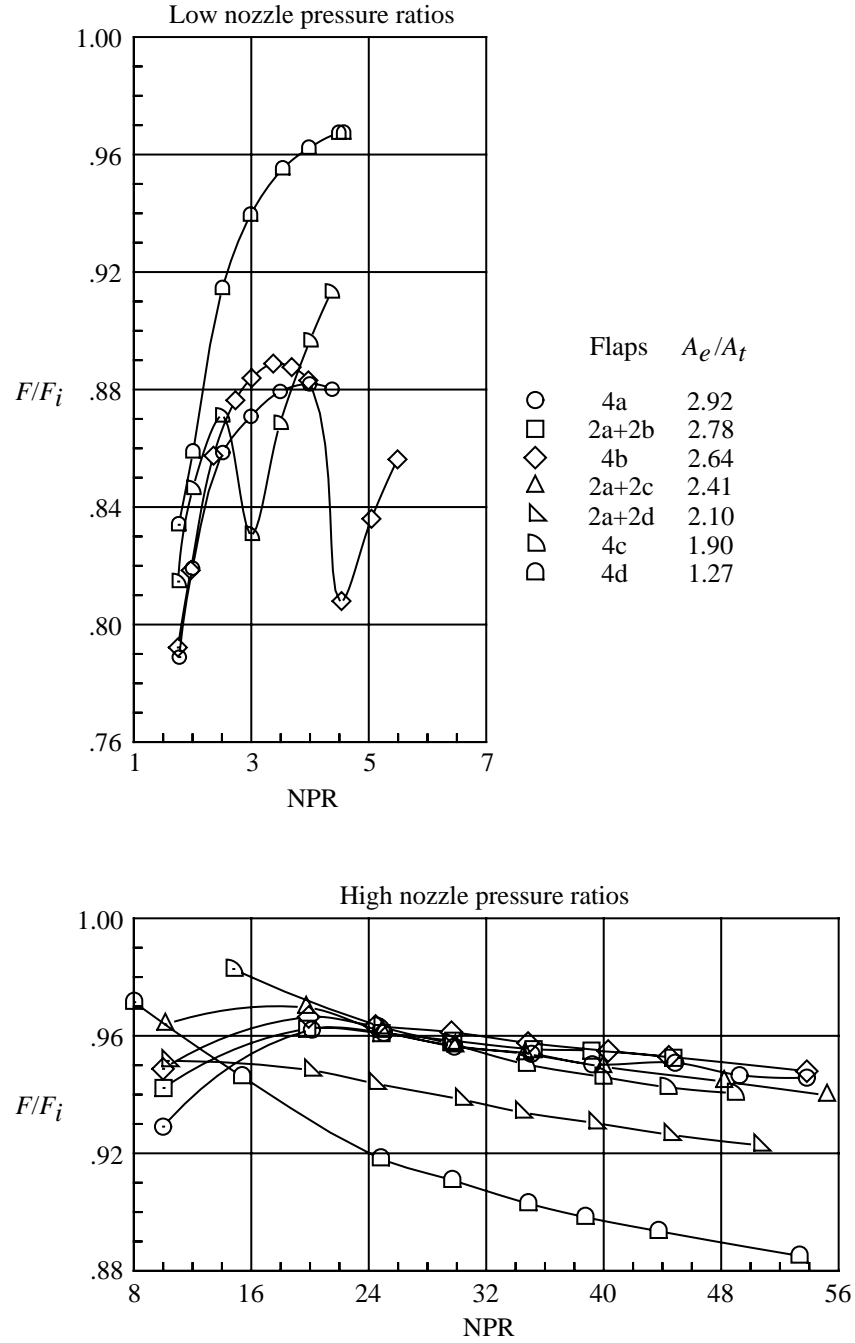
(d) $M = 1.15$ and 1.25 .

Figure 28. Continued.



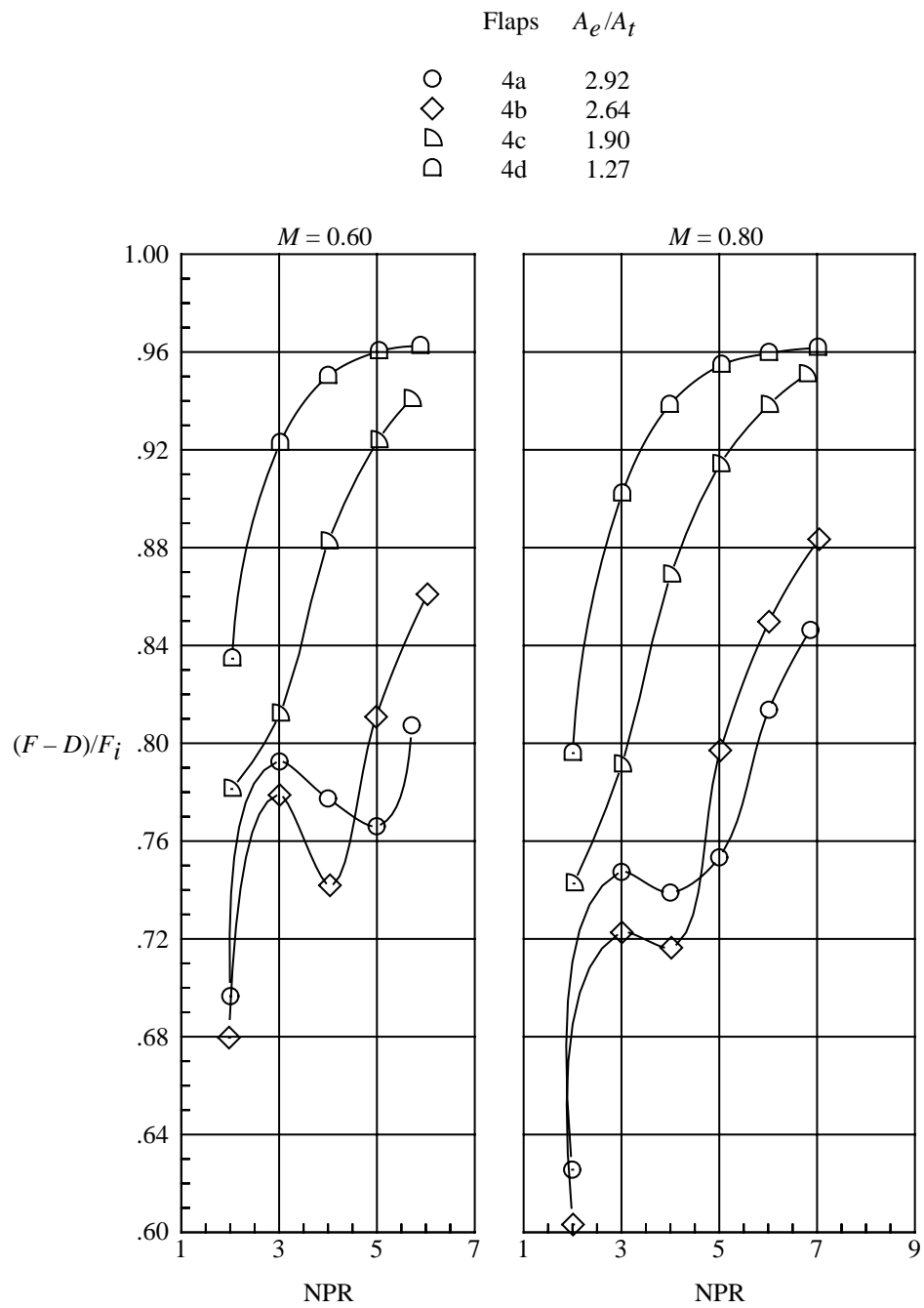
(e) $M = 2.16, 2.50$, and 2.86 .

Figure 28. Concluded.



(a) $M = 0$; low and high nozzle pressure ratios.

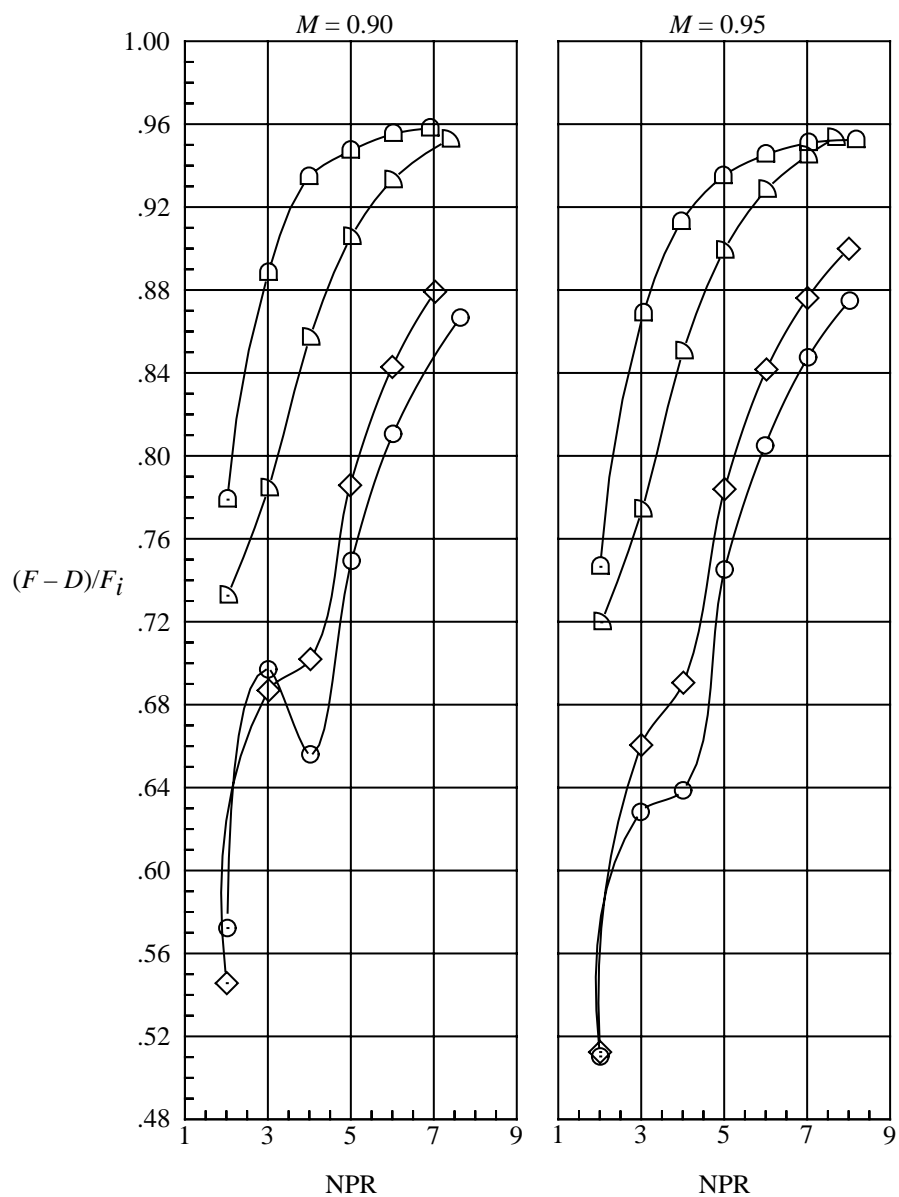
Figure 29. Comparison of thrust ratio and thrust-minus-drag ratio performance over range of nozzle pressure ratios for cruciform nozzle with concave centerbody base and flaps at various positions.



(b) $M = 0.60$ and 0.80 .

Figure 29. Continued.

	Flaps	A_e/A_t
○	4a	2.92
◇	4b	2.64
▷	4c	1.90
◻	4d	1.27



(c) $M = 0.90$ and 0.95 .

Figure 29. Continued.

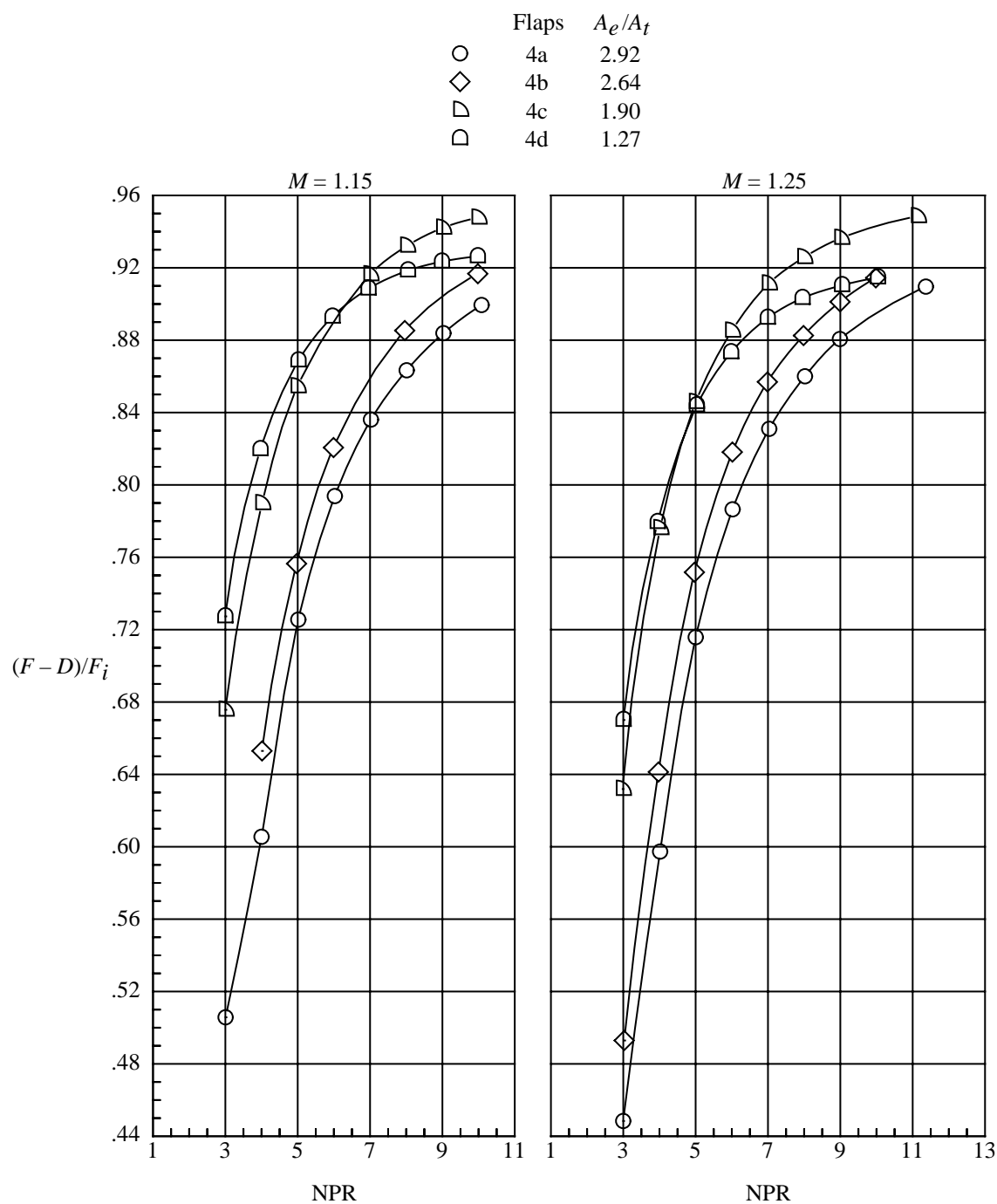
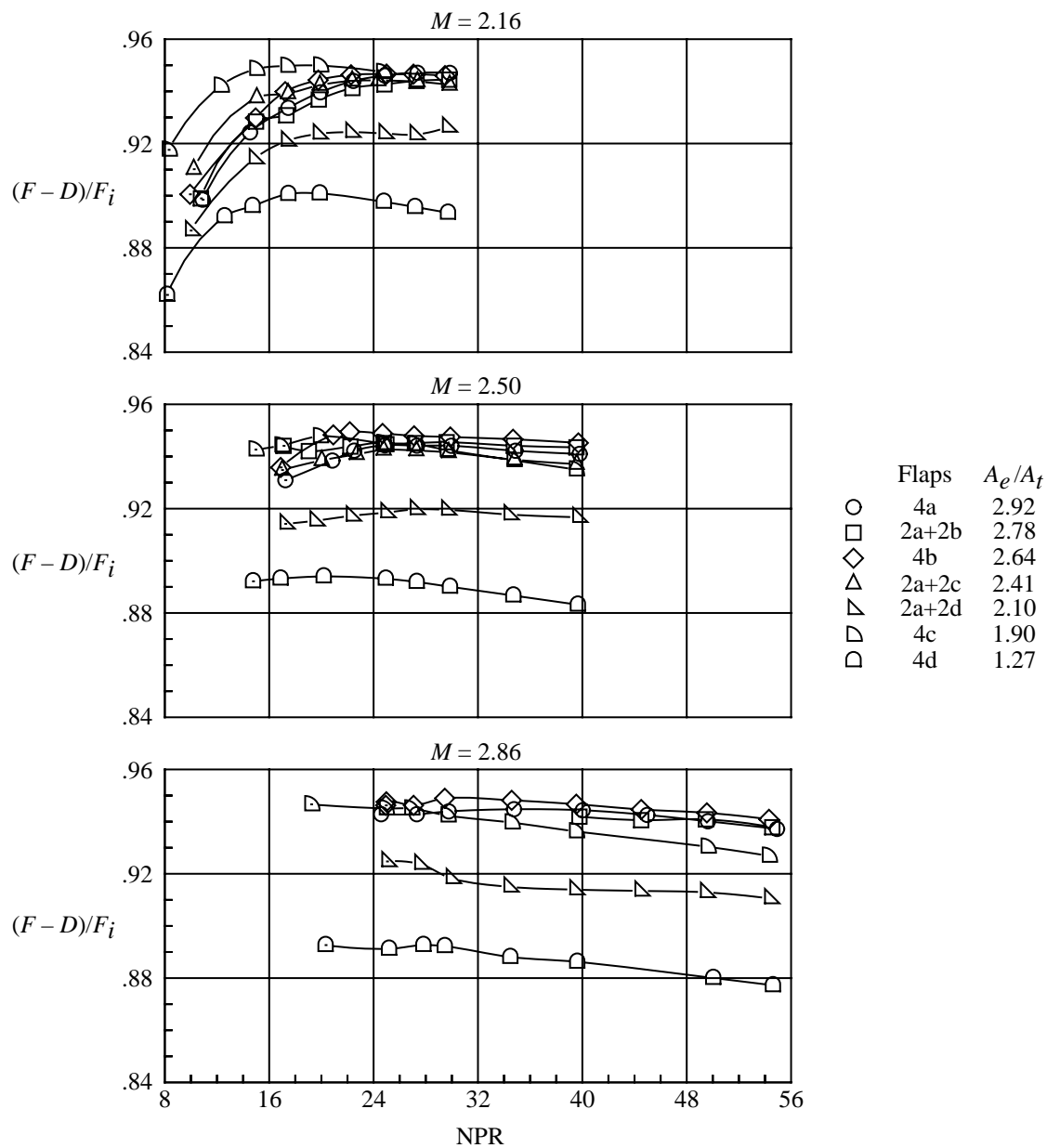
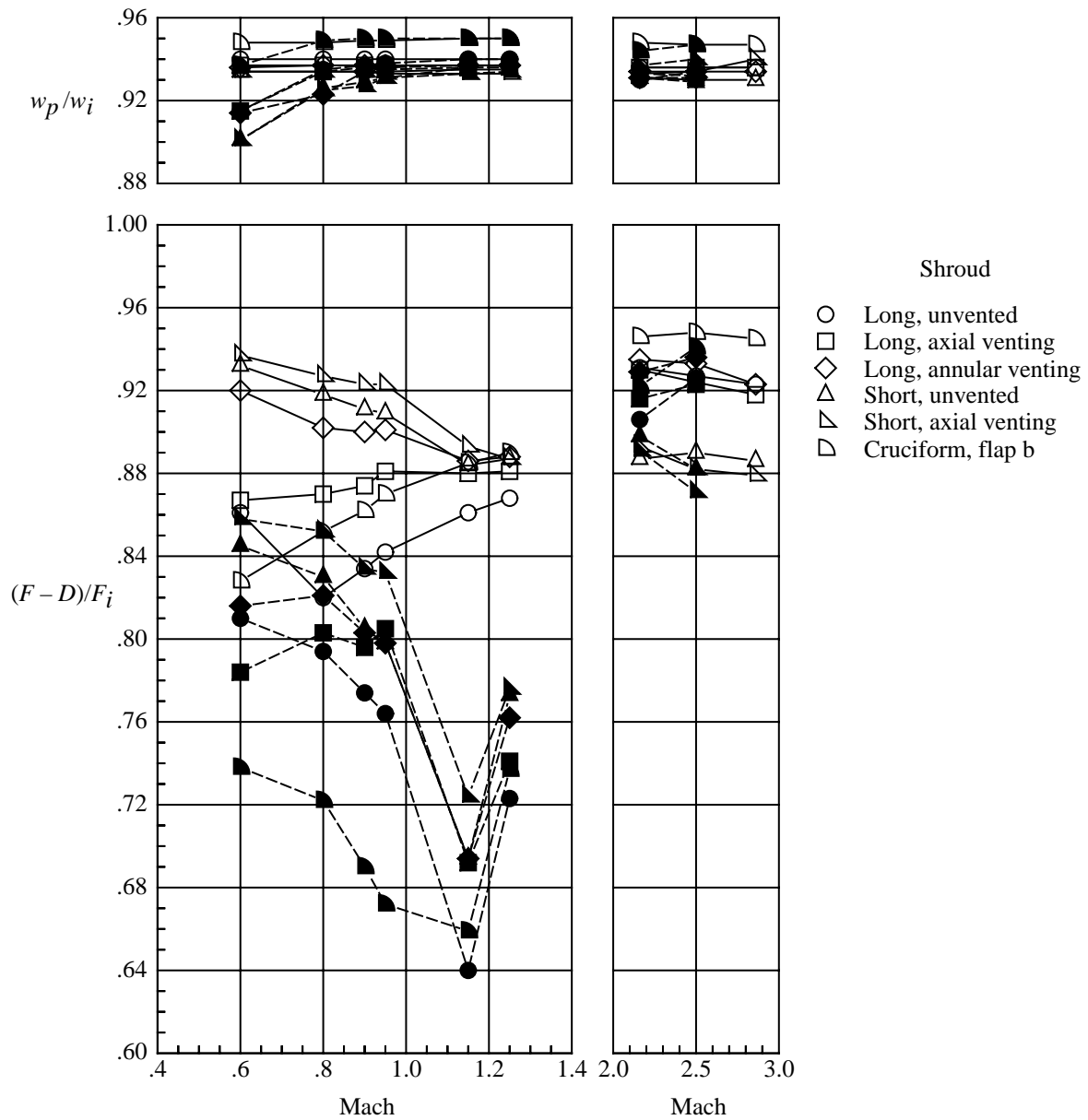


Figure 29. Continued.



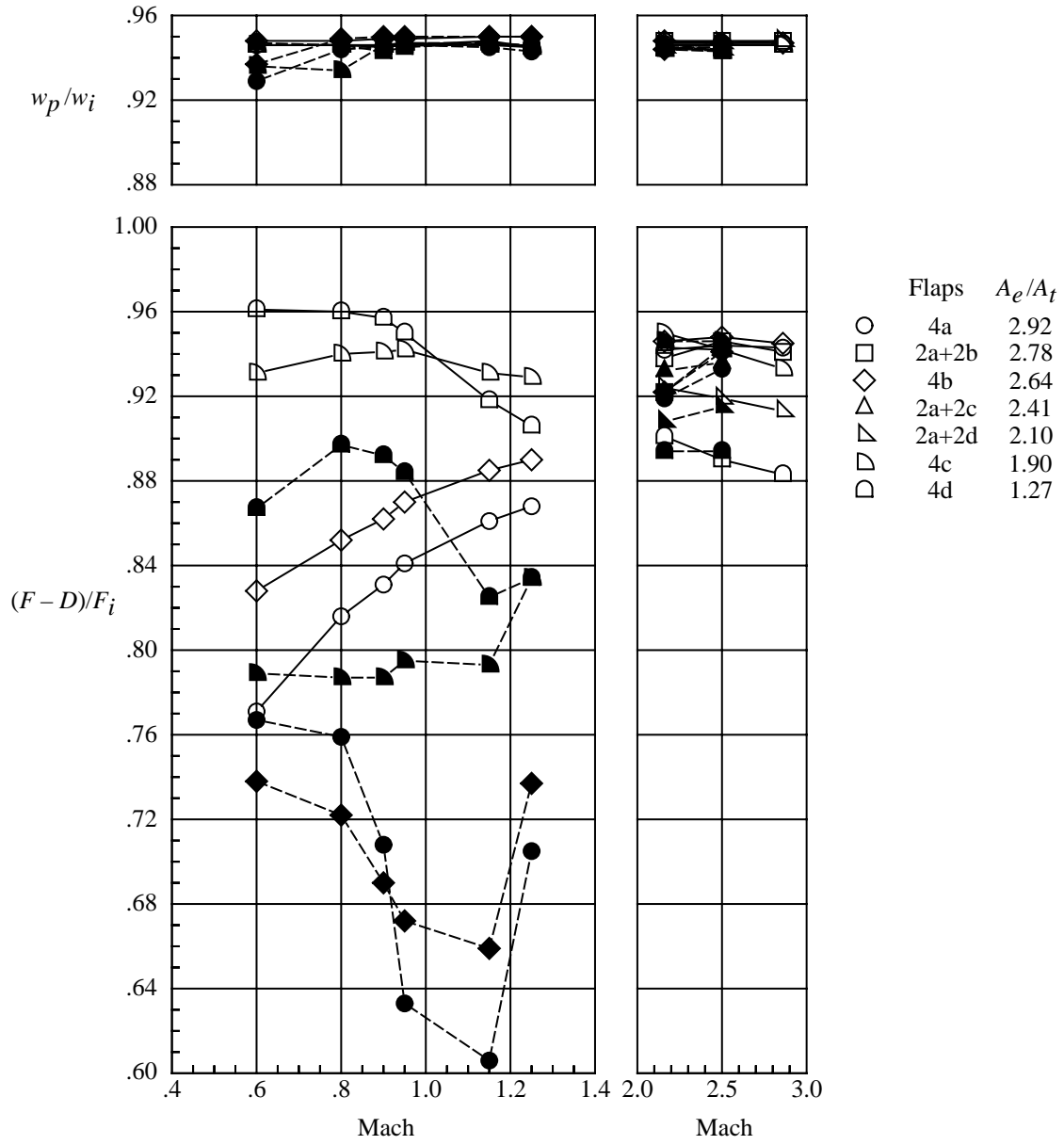
(e) $M = 2.16, 2.50, \text{ and } 2.86$.

Figure 29. Concluded.



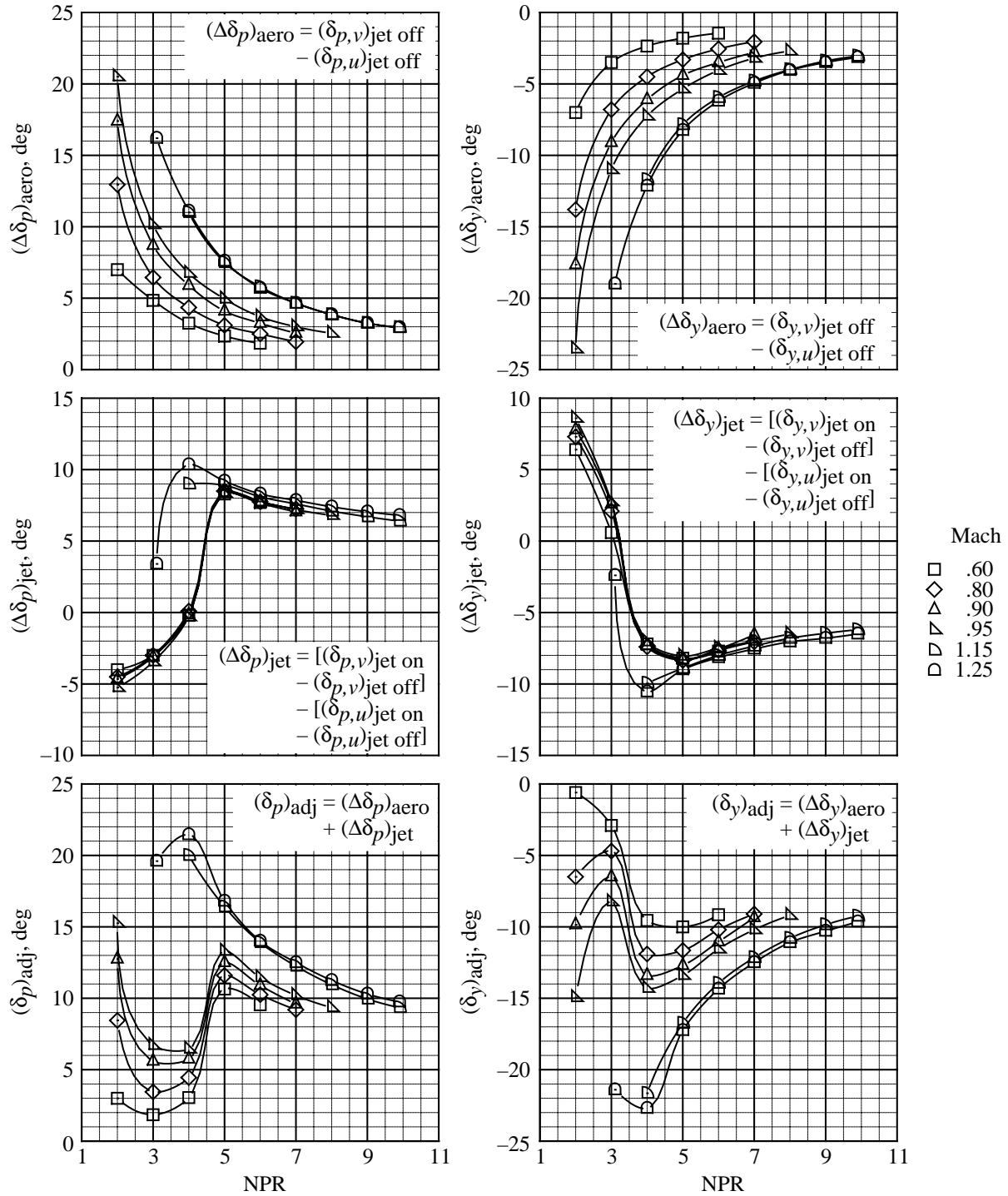
(a) Six shroud configurations having same expansion ratios.

Figure 30. Comparison of thrust ratio, thrust-minus-drag ratio, and discharge coefficient over Mach number range at nozzle operating pressure ratios for high and low altitudes for configurations with concave centerbody. Solid symbols indicate low altitude operating nozzle pressure ratios.



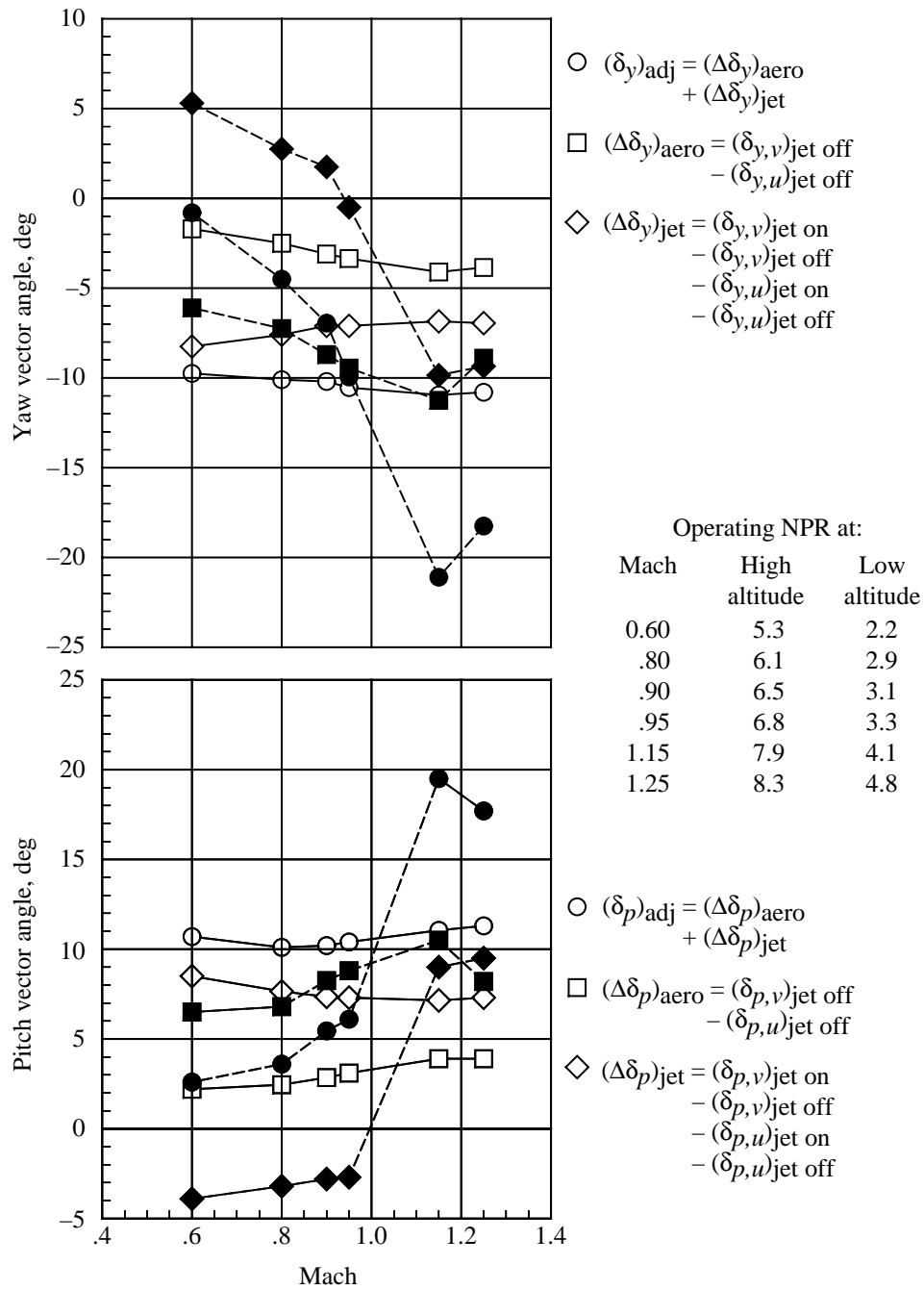
(b) Cruciform shroud configurations.

Figure 30. Concluded.



(a) Adjusted vector angles and vector angle increments over nozzle pressure ratio range.

Figure 31. Cruciform nozzle adjusted vector angles and vector angle increments with flaps in vectored position 2a + 2d over nozzle pressure ratio range and at high and low altitude nozzle operating pressure ratios.



(b) Vector angle increments and adjusted pitch and yaw vector angles. Open symbols indicate high altitude nozzle operating pressure ratios and solid symbols indicate low altitude nozzle operating pressure ratios.

Figure 31. Concluded.

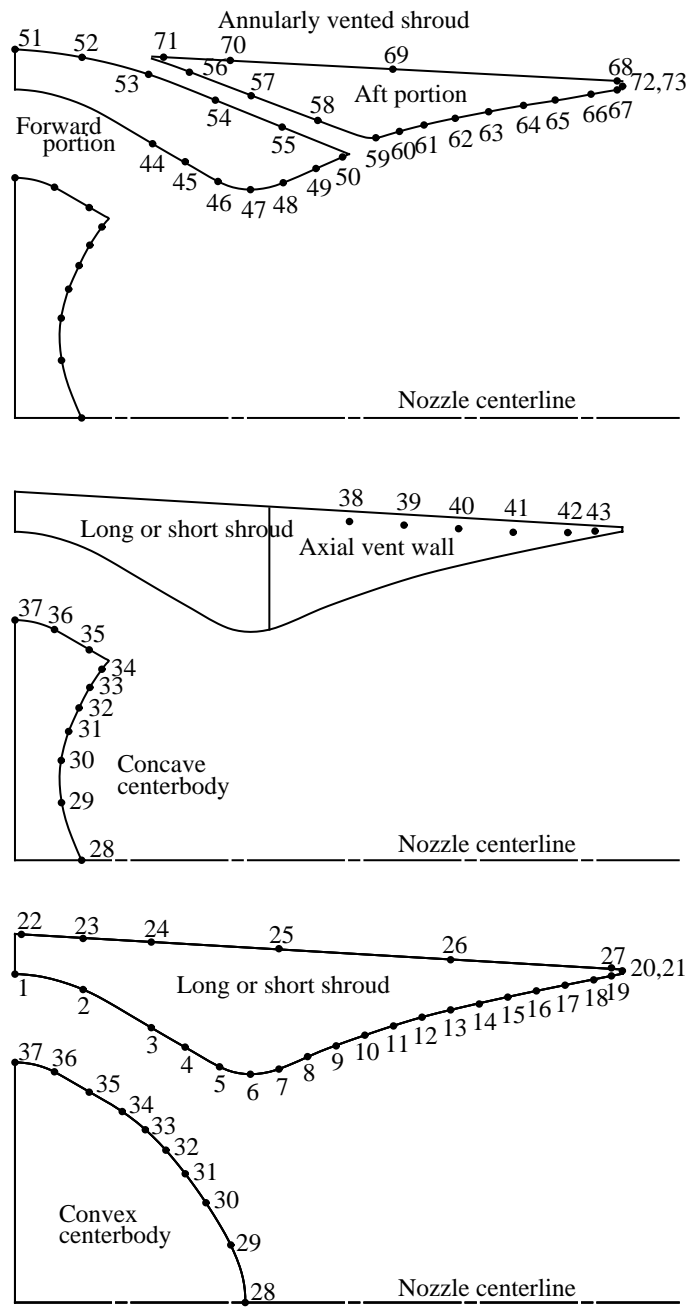


Figure 32. Nozzle pressure orifice numbers for various nozzle components.

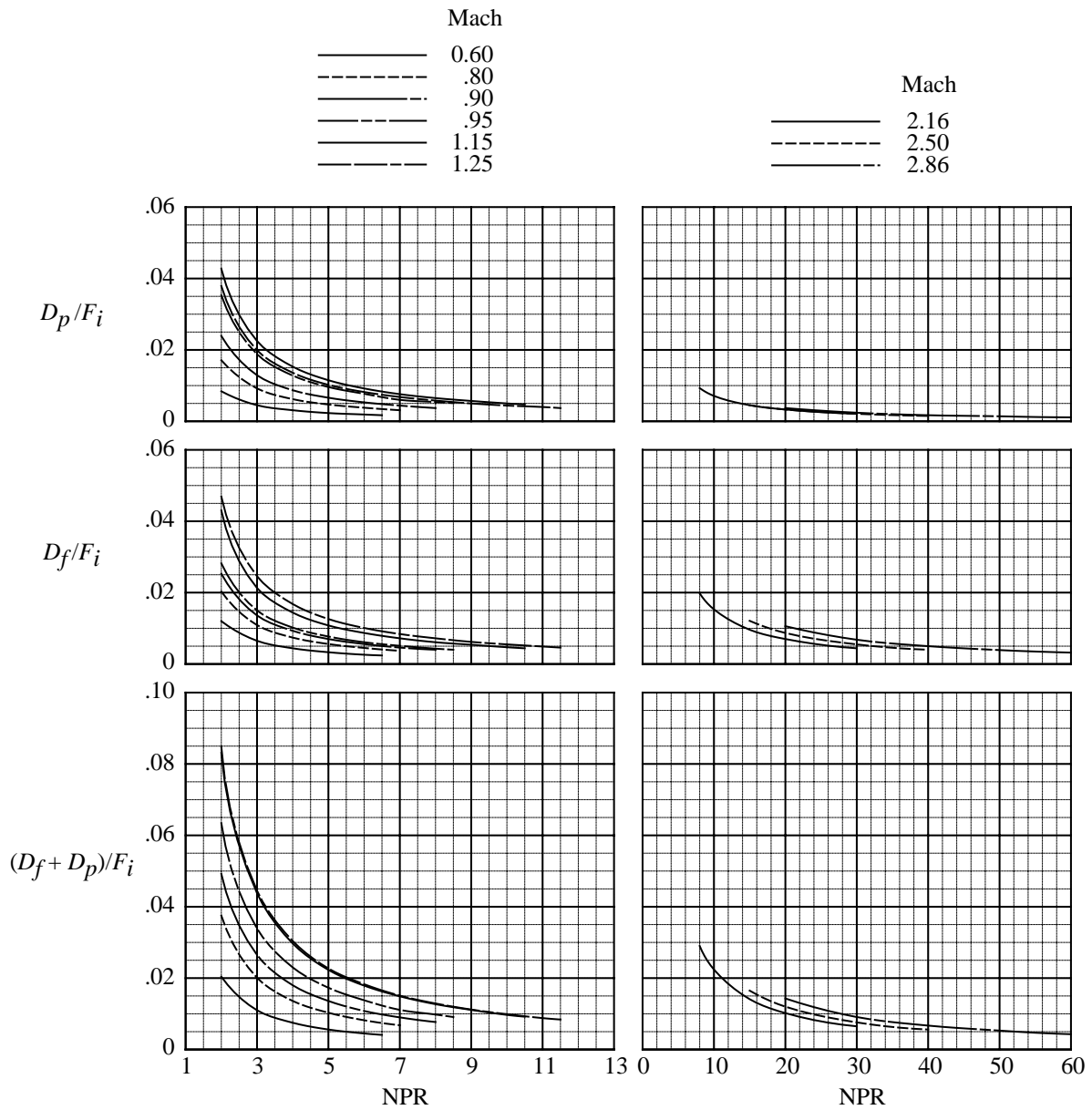


Figure 33. Variation with nozzle pressure ratio of calculated skin friction and pressure drag ratio increments for metric portion of model forward of nozzle connect station for subsonic and supersonic Mach numbers.

REPORT DOCUMENTATION PAGE			Form Approved OMB No. 0704-0188	
Public reporting burden for this collection of information is estimated to average 1 hour per response, including the time for reviewing instructions, searching existing data sources, gathering and maintaining the data needed, and completing and reviewing the collection of information. Send comments regarding this burden estimate or any other aspect of this collection of information, including suggestions for reducing this burden, to Washington Headquarters Services, Directorate for Information Operations and Reports, 1215 Jefferson Davis Highway, Suite 1204, Arlington, VA 22202-4302, and to the Office of Management and Budget, Paperwork Reduction Project (0704-0188), Washington, DC 20503.				
1. AGENCY USE ONLY (Leave blank)		2. REPORT DATE November 2001		3. REPORT TYPE AND DATES COVERED Technical Publication
4. TITLE AND SUBTITLE Isolated Performance at Mach Numbers From 0.60 to 2.86 of Several Expendable Nozzle Concepts for Supersonic Applications			5. FUNDING NUMBERS WU 706-17-21-05	
6. AUTHOR(S) Richard J. Re, Bobby L. Berrier, and William K. Abeyounis				
7. PERFORMING ORGANIZATION NAME(S) AND ADDRESS(ES) NASA Langley Research Center Hampton, VA 23681-2199			8. PERFORMING ORGANIZATION REPORT NUMBER L-17877	
9. SPONSORING/MONITORING AGENCY NAME(S) AND ADDRESS(ES) National Aeronautics and Space Administration Washington, DC 20546-0001			10. SPONSORING/MONITORING AGENCY REPORT NUMBER NASA/TP-2001-211259	
11. SUPPLEMENTARY NOTES				
12a. DISTRIBUTION/AVAILABILITY STATEMENT Unclassified-Unlimited Subject Category 02 Distribution: Standard Availability: NASA CASI (301) 621-0390			12b. DISTRIBUTION CODE	
13. ABSTRACT (Maximum 200 words) Investigations have been conducted in the Langley 16-Foot Transonic Tunnel (at Mach numbers from 0.60 to 1.25) and in the Langley Unitary Plan Wind Tunnel (at Mach numbers from 2.16 to 2.86) at an angle of attack of 0° to determine the isolated performance of several expendable nozzle concepts for supersonic nonaugmented turbojet applications. The effects of centerbody base shape, shroud length, shroud ventilation, cruciform shroud expansion ratio, and cruciform shroud flap vectoring were investigated. The nozzle pressure ratio range, which was a function of Mach number, was between 1.9 and 11.8 in the 16-Foot Transonic Tunnel and between 7.9 and 54.9 in the Unitary Plan Wind Tunnel. Discharge coefficient, thrust-minus-drag, and the forces and moments generated by vectoring the divergent shroud flaps (for Mach numbers of 0.60 to 1.25 only) of a cruciform nozzle configuration were measured. The shortest nozzle had the best thrust-minus-drag performance at Mach numbers up to 0.95 but was approached in performance by other configurations at Mach numbers of 1.15 and 1.25. At Mach numbers above 1.25, the cruciform nozzle configuration having the same expansion ratio (2.64) as the fixed geometry nozzles had the best thrust-minus-drag performance. Ventilation of the fixed geometry divergent shrouds to the nozzle external boattail flow generally improved thrust-minus-drag performance at Mach numbers from 0.60 to 1.25, but decreased performance above a Mach number of 1.25.				
14. SUBJECT TERMS Nozzles; Nozzle performance; Supersonic nozzles			15. NUMBER OF PAGES 199	
			16. PRICE CODE	
17. SECURITY CLASSIFICATION OF REPORT Unclassified	18. SECURITY CLASSIFICATION OF THIS PAGE Unclassified	19. SECURITY CLASSIFICATION OF ABSTRACT Unclassified	20. LIMITATION OF ABSTRACT UL	